Dissertation

Layer formation from perovskite nanoparticles with tunable optical and electronic properties

Martin Kärgell

Univ.-Diss
zur Erlangung des akademischen Grades
"doctor rerum naturalium"
(Dr. rer. nat.)
in der Wissenschaftsdisziplin
"Materialwissenschaften"

eingereicht an der
Mathematisch-Naturwissenschaftlichen Fakultät
Institut für Chemie
der Universität Potsdam
und durchgeführt am
Helmholtz Zentrum Berlin für
Materialien und Energie

Ort und Tag der Disputation:
Potsdam-Golm, 17.06.2020

Martin Kärgell

"Layer formation from perovskite nanoparticles with tunable optical and electronic properties"

Dissertation

Eingereicht: 22.10.2019

Betreuer: Dr. Thomas Unold, Prof. Andreas Taubert

Gutachter der Arbeit:

Prof. Andreas Taubert, Dr. Thomas Unold, Prof. Michael Wark

Disputationstermin: 17.06.2020 (Potsdam-Golm)

Promotionsausschuss:

Vorsitzender:

Prof. Michael Kumke

Gutachter:

Prof. Andreas Taubert

Dr. Thomas Unold

Prof. Dieter Neher

Angefertig am:

Helmholtz-Zentrum Berlin für Materialien und Energie

Abteilung für Struktur und Dynamik von Energiematerialien (ASD)

Hahn-Meitner-Platz 1

14109 Berlin and Berlin

Published online on the
Publication Server of the University of Potsdam:
https://doi.org/10.25932/publishup-47566
https://nbn-resolving.org/urn:nbn:de:kobv:517-opus4-475667

Abstract

Hybrid organic-inorganic perovskites have attracted attention in recent years, caused by the incomparable increase in efficiency in energy convergence, which implies the application as an absorber material for solar cells. A disadvantage of these materials is, among others, the instability to moisture and UV-radiation. One possible solution for these problems is the reduction of the size towards the nano world. With that nanosized perovskites are showing superior stability in comparison to e.g. perovskite layers. Additionally to this the nanosize even enables stable perovskite structures, which could not be achieved otherwise at room temperature.

This thesis is separated into two major parts. The separation is done by the composition and the band gap of the material and at the same time the shape and size of the nanoparticles. Here the division is made by the methylammonium lead tribromide nanoplatelets and the caesium lead triiodide nanocubes.

The first part is focusing on the hybrid organic-inorganic perovskite (methylammonium lead tribromide) nanoplatelets with a band gap of 2.35 eV and their thermal behaviour. Due to the challenging character of this material, several analysis methods are used to investigate the sub nano and nanostructures under the influence of temperature. As a result, a shift of phase-transition temperatures towards higher temperatures is observed. This unusual behaviour can be explained by the ligand, which is incorporated in the perovskite outer structure and adds phase-stability into the system.

The second part of this thesis is focusing on the inorganic caesium lead triiodide nanocubes with a band gap of 1.83 eV. These nanocrystals are first investigated and compared by TEM, XRD and other optical methods. Within these methods, a cuboid and orthorhombic structure are revealed instead of the in literature described cubic shape and structure. Furthermore, these cuboids are investigated towards their self-assembly on a substrate. Here a high degree in self-assembly is shown. As a next step, the ligands of the nanocuboids are exchanged against other ligands to increase the charge carrier mobility. This is further investigated by the above-mentioned methods. The last section is dealing with the enhancement of the $CsPbI_3$ structure, by incorporating potassium in the crystal structure. The results are suggesting here an increase in stability.

Kurzzusammenfassung

Hybrid organisch-anorganisch Perowskite zeigten sich in den letzten Jahren, durch ihren unvergleichbaren Anstieg an Effizienz in der Energiekonversion, als herausragendes Material für die Anwendung als Solarzellen Absorbermaterial. Ein Nachteil dieser Materialien ist allerdings unteranderem ihre Instabilität gegenüber Feuchtigkeit und UV-Strahlung. Eine Möglichkeit, diese Herausforderungen zu meistern, bietet die Nanowelt. So zeigen Perowskitstrukturen in Nanogröße eine dem Schichten überlegene Stabilität. Des Weiteren sind durch die Nanogröße auch Verbindungen bei Raumtemperatur stabil, die als Schicht oder Einkristall nicht darzustellen sind.
Diese Arbeit ist unterteilt in zwei Teile. Unterteilt nach Zusammensetzung, Bandlücke und Form der Nanopartikel, in Methylammonium Blei Tribromid Nanoplättchen und Cäsium Blei Triiodid Nanokuben.
Im ersten Teil werden hybrid organisch-anorganische Perowskite (Methylammonium Blei tribromid) Nanoplättchen mit einer Bandlücke von 2.35 eV auf ihr thermisches Verhalten untersucht. Aufgrund der herausfordernden Eigenschaften der Nanomaterialien, werden mehrere Analysemethoden verwendet und sowohl die Subnanostruktur als auch die Nanostruktur unter Veränderung der Temperatur beobachtet. Dabei wird ein Verschub der Phasenübergangstemperatur zu höheren Temperaturen beobachtet. Erklärt werden kann dieses ungewöhnliche Verhalten durch die Berücksichtigung des organischen Liganden der Nanoplättchen, welcher einen Einfluß auf den Phasenübergang hat.
Im zweiten Teil der Arbeit werden anorganische Perowskit (Cäsium Blei triodid) Nanokuben mit einer Bandlücke von 1.83 eV untersucht. Diese werden als Erstes mittels TEM, XRD und optischen Analysemethoden untersucht und verglichen. Als Resultat stellen sich die Kuben, als Quader einer orthorhombischen Phase heraus. Anschließend erfolgt eine Untersuchung der Selbstanordnung der Schichten auf einem Substrat, welche einen hohen Grad der Selbstanordnung zeigt. Um die Ladungsträgermobilität in den Schichten zu erhöhen, werden verschiedene Ligandenaustauschreaktionen durchgeführt und diese mittels der oben genannten Methoden untersucht. Dabei konnte ein Anstieg der Ladungsträgermobilität um das Sechsfache im Vergleich zur Literatur beobachtet werden. Im letzten Teil wird versucht die Stabilität der Nanokristalle, durch das Einbinden von Kalium in die Perowskitstruktur, zu erhöhen. Die hier vorliegenden Ergebnisse deuten eine Erhöhung der Stabilität an.

> *Stilles und bescheidenes Leben gibt mehr Glück als erfolgreiches Streben, verbunden mit beständiger Unruhe*
>
> — **Albert Einstein**
> Nobel price for discovering the photo electric effect

Für meine Familie und Freunde

Acknowledgement

An dieser Stelle möchte ich mich bei all jenen bedanken, die direkt oder indirekt zur Entstehung dieser Arbeit am HZB und in der Graduiertenschule "HyPerCell" beigetragen haben.

Ich bedanke mich bei Prof. Andreas Taubert für die Betreuung der Arbeit an der Uni Potsdam, für seine freundliche und unterstützende Art und das Vertrauen in meine Arbeit. Weiterhin bedanke ich mich für die DSC-Messungen, die von seiner Gruppe durchgeführt worden sind.
Des weiteren möche ich mich bei Dr. Thomas Unold für die Aufnahme und Betreuung in seiner Gruppe am HZB bedanken. Dies ermöglichte mir mit diverser Geräte und tollen Menschen in Kontakt zu kommen und meine Fähigkeiten auszubauen.

Besonderen Dank gilt Dr. Sergej Levcenko für seine leidenschaftliche Unterstützung und Arbeit mit diversen Messmethoden. Sein Wissen und die Unterstützung durch die interpretation der Messdaten war eine unverzichtbare Hilfe. Auch für seine mentale Unterstützung bin ich dankbar.
Ich möchte mich weiterhin bei Arne Ronneburg und Dr. Luca Silvi bedanken für die schöne Gemeinschaft auch in schlechten Zeiten und die Messungen und interpretation der XRR und NR daten.
Bei Dr. Andreas Ott, Daniel Besold und Hannah Funk möchte ich mich für die Messung der TEM bilder, deren Interpretation und der Diskusionen bedanken.
Bei Dr. Albrecht Petzold möchte ich mich für die Aufnahme, die Datenreduktion und die Auswertung und Diskusion über die erhaltenen SAXS daten bedanken.
Ich möchte mich weiterhin bei Dr.Michael Toward, Rene Grunder und Dr. Alexandra Franz für die Hilfe und Unterstützung bei kristallographischen Fragen bedanken.
Bei Dr. Pascal Becker, Pepe, Lars Steinkopf und Dr. Hannes Hempel möchte ich mich für die Unterstützung im Büro und diverser Messungen bedanken: Gerade die Messung und Auswertung der Terahertz Daten.

Ich möchte mich außerdem bei den vielen lieben Menschen aus anderen Gruppen bedanken für deren Unterstützung und hilfe dazu gehören, Richard, Gregor, Evelin, Sebastian, Enely, Linda, Annegret, Miriam, Nikoline, Karol, Nils, Chemil, Shun, Anastasia, Martin, Rohit, Amran, Luigi, Veronika, Michael, Volkan und Robert. Letzt genannten danke ich sehr für die Durchsicht der Arbeit.

Des weiteren möchte ich mich bei meinem Freunden außerhalb des Arbeitsumfeldes bedanken dazu gehören vorallem Nina, Alex, Georges, Selina und Claudia. Weiterhin gilt besondere Dank Pat, Oli und Martin für das Freizeitprojekt des optischen Aufbaus.

Ganz besonderen Dank gilt meiner Familie, die mir während der gesamten Zeit mit Rat und Tat beiseite Stand und mich in jeglichen Situationen unterstütz und mir den Rücken gestärkt haben.

Contents

1 Introduction **1**

2 Fundamentals **5**
2.1 A brief introduction in solar cells 6
2.2 Perovskite 14
2.3 Nanoparticles and their properties 24
2.4 Synthesis of Nanostructures 31

3 Methods **41**
3.1 Spectroscopy 42
3.2 Scattering of X-Rays and electrons 52
3.3 Thermal analysis 68

4 Phase transition and optical properties of $MaPbBr_3$ nanoplatelets **75**
4.1 Synthesis 76
4.2 Results 78
4.3 Discussion 105
4.4 Conclusion & Outlook 109

5 Enhancing the charge mobility and stability of $CsPbI_3$ nanocrystals **113**
5.1 Synthesis 114
5.2 Investigation of the nanocrystals 118
5.3 Ligand exchange for a higher charge mobility 137
5.4 Further $CsPbI_3$ nanocrystal treatments 148
5.5 Incorporation of potassium into the $CsPbI_3$ quantum dots . . . 156
5.6 Discussion 165
5.7 Conclusion & Outlook 176

Bibliography **193**

1 Introduction

> *The shift to a cleaner energy economy won't happen overnight, and it will require tough choices along the way. But the debate is settled. Climate change is a fact*
>
> — **Barack Obama**
> (44. President of the U.S.A)

The human population and with that, the interest and demand for energy are continually increasing. These days, energy is mostly produced using fossil or nuclear fuels. Both fuel variants are limited and are leading to environmental pollution, in which the fossil fuels further lead to climate change, which we are now starting to experience.[1, 2, 3, 4] Asides from these significant downsides of the energy production, energy generation by combustion and boiling water to generate steam is quite inefficient and outdated.[5, 6, 7]
One of the meaningful challenges in the 21st century is to find a replacement for the energy generation methods mentioned above.[8] A new, efficient, environmentally neutral, combustion-free energy source needs to be found like fusion energy generation. Unfortunately, this energy source is far from being commercially available [9] Despite this fact, Germany is already obtaining about 8.7% of its total energy (about 46 TWh) by a fusion reactor.[10] This fusion reactor is called the sun in the middle of the solar system. The sun radiates a total energy of $3.828 \cdot 10^{26}$ W [11] of which an average of 1050 W/m^2 is reaching earth surface, this is the 1500 times the total of human energy consumption.[12, 13]
Even if the 8.7% of Germany's total energy production is a remarkable achievement, the average solar cell uses these days is with an efficiency of around 17%, which is far from optimal.[10, 14] So the optimisation of solar cells needs to be developed. By this also further disadvantages of the commercially available solar cells could be reduced or even eliminated.

The most widely used material for solar cell applications is silicon.[15] Silicon has a band gap of around 1.1 eV, which fits good to the solar spectrum.[13] However, the production of a silicon solar cell is cost-intensive. Therefore not only the production of highly pure silicon is to be taken into account, but also the material needs to be additionally treated with dopants.[14] Additionally, silicon is an indirect semiconductor. This fact makes it less likely for a photon to get absorbed, which lowers the total efficiency.[15] Additionally from the technical side silicon solar cells are rigid and heavy in weight.[16, 14] Thin-film absorbers might solve these problems.[8]

Besides other materials[8, 17], one material is in a special focus for solar cell development. Solar cells of this material have increased dramatically in efficiency's into the past years, reaching record efficiencies surpassing 23%. [17] The material class is called halide perovskite. Besides the impressive increase in efficiency, this material is cheap in production, no high vacuum or high temperatures are needed, and the production is fairly easy. Furthermore, the band gap is tunable, which gained interest for tandem solar cell devices.[18] These perovskite tandem cells reach record efficiencies of above 27 %. [17] However, perovskite films come with drawbacks. The most investigated and fairly stable perovskite are heavy metal-based, which could lead to environmental pollution and challenges for their disposal.[19]

Furthermore, the long term stability of these perovskite structures under atmospheric conditions [20] or with the influence of light[21], is not known. A solution for both problems might be found in the nano size. Perovskite nanoparticles show an increase in stability.[22]

Furthermore, at room temperature, none stable phases could be obtained, if the nano size is reached.[23, 22] Additionally, the band gap of those particles is not only tunable by their composition, but also by their size.[23] With that, a band gap adjustment without a phase separation of the mixed perovskites[24] is accessible. Asides from the application for solar cells, perovskite quantum dots are an interesting material for optical and electronic applications i.g. LEDs[25] or optical sensors.[26, 27]

As briefly shown, the perovskite nanocrystals are superior over the bulk material in a variety of fields. Additionally to the nanosize, things seem to be possible, which are not for the bulk material, e.g. the room temperature stable $CsPbI_3$ phase.[23] Nevertheless, nanomaterials as such are challenging to analyse.[28] As their beneficial properties are different from the bulk

material, so are their other (often unknown) properties.
This thesis will investigate the unusual phase transition of the $MaPbBr_3$ nanoplatelets. Furthermore, the $CsPbI_3$ nanocrystals are investigated towards their structure, layer formation and their charge mobility. In addition, the charge mobility and stability of the $CsPbI_3$ is enhanced. Moreover, the changes in the material are investigated, which might lead to a better understanding of the perovskite nanoparticles and might improve their applications.

1.0.1 Outline and aims of this work

This thesis is investigating the properties of perovskite nanocrystals. With that, this thesis is divided into six parts. The first chapter is the introduction and motivation chapter and the sixth and last chapter is the experimental part and will not be further outlined here.

Second chapter The second chapter is dedicated to fundamentals of the application (solar cells), the material perovskite, perovskite nanocrystals and their synthesis. This chapter should form the foundation and further the motivation for the investigation of the nanomaterial.

Third chapter The third chapter discusses the used analytic methods in this thesis. For this purpose, this chapter is divided into three parts. The first part is discussing spectroscopic methods. Afterwards, scattering methods are discussed. At the end of this chapter, the thermoanalytical methods are introduced and discussed.

Fourth chapter The fourth chapter is investigating the nontemplate methylammonium lead tribromide nanoplatelets towards their temperature-dependent phase transitions. Because of the challenging character of these nanoplatelets, a single measurement method is not suitable for investigating the properties and behaviour of this material. For this reason, thermal analysis, temperature-dependent X-ray diffraction, temperature-dependent small-angle scattering and temperature-dependent photoluminescence is used. These methods reveal the temperature-dependent processes and a shift of the phase transition towards higher temperatures.

Fifth chapter The fifth chapter is focusing on the full inorganic $CsPbI_3$ quantum dots. This material is usually as a bulk material at room temperature in the non-perovskite δ-phase. In contrast to the bulk material, the quantum dots are showing a stable perovskite phase at room temperature. Here, the $CsPbI_3$ quantum dots are investigated by TEM, XRD and their arrangement on a substrate by XRR. Further investigations were conducted with the goal of an increase in charge carrier mobility in the layer of the arranged quantum dots. Lastly, the enhancement of the phase stability by the incorporation of potassium in the crystal lattice is investigated.

2

Fundamentals

> *All physical theories, their mathematical expressions apart ought to lend themselves to so simple a description 'that even a child could understand them.*
>
> **— Albert Einstein to Louis de Broglie[29]**
> (Physicists)

In this chapter, the basic principles and the foundation of this thesis shall be discussed. The focus of this thesis is on semiconducting nanoparticles based on halide metal perovskite as a material. The main focus of research on halide metal perovskite is further done for the sake of improving the absorber material for solar cells applications. For this reason, a brief introduction to solar cells should be given. Here, the essential parts of the solar energy conversion are discussed.
After the brief introduction into solar cells, the benefits and challenges of the perovskite as an absorber material will be discussed. At the end, a discussion of the perovskite nanoparticles and a general part about the synthesis of nanoparticles or nanocrystals will be given.

2.1 A brief introduction in solar cells

The sun in the middle of our solar system provides radiative energy with a total energy of around 3.828 $\cdot 10^{26}$ W by a fusion reaction.[30] In this process, hydrogen atoms are fused into a helium atom. The fusion inside the sun is following Einsteins relation $E = m \cdot c^2$ which leads to a direct conversion of mass into energy.[31] By this process photons are emitted and radiated towards the earth.[31]
The light generated by the sun can be converted by a semiconductor into electric energy. This process is based on the photoelectric effect, first discovered by Becquerel [32]and later explained by Einstein [33].
Before the explanation of the photoelectric effect, the first solar cell was build in 1885 based on gold-coated selenium.[34] The first silicon solar cell, with silicon as the best-known and widespread semiconductor [15], was presented by Chapin et al. in 1954.[35] In 2009 Kojima et al. first discussed halide perovskite as a possible absorber material for solar cell applications.[36]

2.1.1 Solar radiation

The sun can be seen as a black body with a surface temperature of 5800 K. A black body is an idealised physical body, in which all incoming light is absorbed, and no light is reflected. Hence the sun is following Planck's law. This leads to a specific spectrum.[37, 38]The energy transmitted towards earth atmosphere is around 1360 W/m^2.[13] This solar spectrum is called the AM 0 solar spectrum (AM = Air mass). If light passes through the atmosphere, losses are observable. These are caused by scattering by atmospheric particles and absorption of atmospheric gases, mainly caused by H_2O, O_2, O_3 and CO_2.[37] If the sunlight is passing the atmosphere perpendicular towards the earth surface, the spectrum is called the AM1 solar spectrum. Because of the tilting of the earth and to standardise the conditions for solar cell tests, the 1.5 AM solar spectrum is introduced. By this an incident angle of 48.2° is used, resulting in 1000 W/m2.[13, 37] The resulting spectra of a black body, the solar spectrum of AM 0 and AM 1.5 are shown in Figure 2.1

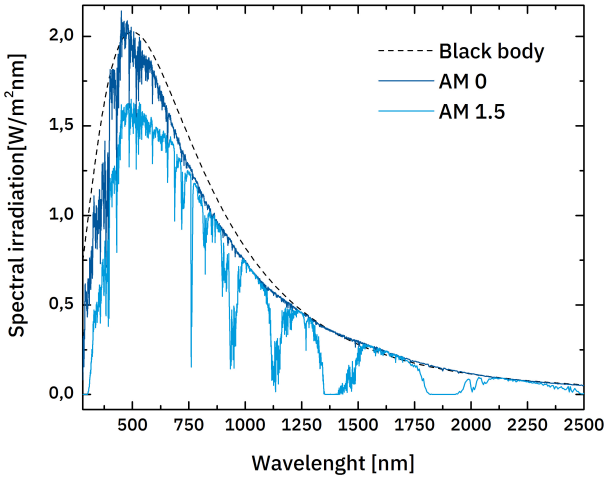

Fig. 2.1: Black body radiation at 5800 K, solar radiation without air mass (AM 0) [39], Solar radiation with an air mass of 1.5 (AM1.5) in an adaptation of [40]

2.1.2 Working principle of a solar cell

The solar cell converts directly light into electric power. A fundamental element of this process is the semiconductor, with its characteristic band gap. The process of the energy conversion is the photovoltaic effect, in which photocurrent and photovoltage is produced.[38] The photovoltaic energy conversion consists of two steps. First, the generation of free electron-hole pairs in the absorber material, and second, the collection of the charges at the contacts.

Semiconductor Materials can be divided into three main groups by their specific resistance. A subdivision of conductors (10^8 S/cm $<\rho<$ 10^4 S/cm), semiconductors (10^4 S/cm $<\rho<$ 10^{-8} S/cm) to insulators (10^{-8} S/cm $<\rho<$ 10^{-18} S/cm) can be made.[41] An explanation for this behaviour can be found by their energy gap (E_{Bg}) for the electronic excitations the so-called *band gap* (Bg). Besides insulators ($E_{Bg} > 3eV$) and conductors ($E_{Bg} \approx 0eV$), semiconductors have a band gap in a typical region of $0 < E_{Bg} > 3eV$.[15] This band gap is in the energy region of the sun spectrum ($E_{400nm} = 3.1eV$ and $E_{2500nm} = 0.5eV$), so an interaction with sunlight and semiconductor is likely.[38]

The band gap is a material-specific property and can be explained by the *linear combination of atomic orbital* (LCAO) theory. Electrons of a single atom can only occupy distinct orbitals or energy levels. In between these energy levels, the probability of the presence of an electron is zero, so the energy levels between the orbitals are forming forbidden states.[42] If two atoms are forming a bond, an emergence of a molecular orbital is observed. Yet the total amount of orbitals needs to be consistent. A linear combination of the atom orbitals leads to bonding and anti-bonding molecular orbitals. Due to the electronic interaction of the molecular orbitals, the energy of the antibonding orbital is raised, and the bonding orbital is decreased.[42] By the addition of more atoms, i.e. in a crystal, the energy levels of the molecular orbitals are merging and forming a continuous band. The molecular orbitals are filled from the lowest state towards the highest state. Only the highest occupied and the lowest unoccupied orbital is of interest for the band gap, for this reason, the lower core electrons are negligible.[15, 42] The bonding orbitals are occupied with fixed, valence electrons, which is forming the valance band. If an electron is excited to the unoccupied, antibonding band, it can be described as a quasi-free moving particle, also described as electron gas and therefore this band is called the conduction band.[15]

The now formed bands can be filled with electrons.[15] Therefore two assumption needs to be made. Firstly, their occupational states need to be present. Secondly, Pauli's exclusion principle needs to be fulfilled. This exclusion principle dictates that only one electron can occupy a given quantum state. As a result, the density of states is energy-dependent and is described approximatively by a square root function for a 3D material in thermal equilibrium. In a non-equilibrium, the description of the electron and hole population is described by the Fermi-Dirac distribution. Thus the chemical potential of the electron can be described as temperature-dependent.[42, 43]

From the explanation of the LCAO model, one could assume, that a band diagram of a semiconductor is straight bands edges. This is not the case. A dispersion function represents the band structure of a semiconductor. With that, the energy is plotted against the reciprocal space. The dispersion function further contains local extrema.

A band-band transition of an electron always occurs from the highest unoccupied to the lowest occupied state. Due to the material properties, these extrema can be shifted in the reciprocal space leading to a so-called direct (if

the extrema are not shifted) or indirect band gap.[15, 44, 45]
A different approach for explaining and calculating the band gap can be made by solving the Schrödinger equation for the wave functions of electrons. For a solid with around 10^{23} atoms/cm^3, this is very complicated.[15] So approximations and simplifications need to be done. Moreover, a solution can be found by using group theory. However, this will be for the sake of completion only be mentioned here. A more profound discussion can be found in literature.[15, 44, 42]
The band gap is strongly temperature-dependent and leads to a widening of the band gap at lower temperatures. So even a semiconductor can become an insulator at low temperatures.[42] The temperature-dependence can be explained by the electron-phonon interaction. With lower temperatures, the interactions will be stronger, and the band gap will be increased. As a secondary effect, for lower temperatures, the thermal contraction of the crystal lattice is an influence. This effect also contracts the band gap with decreasing temperatures. The last-mentioned effect also applies to an increase in pressure on the crystal lattice, which further results in a decrease in the band gap.[44, 46, 47, 48]

Charge generation in a semiconductor: The generation of electron-hole pairs in semiconductors is based on the internal photoelectric effect. Therefore incident photons with an energy higher then the band gap of the absorber material excites electrons from the valence band to the conduction band. By this process vacancies are also known as *holes*, are left in the valance band. The excitation to the lowest state of the conduction band is the ideal case. After an excitation into higher states, a relaxation process towards the conduction band edge occurs.[37] During the process, the excess energy is transferred to the crystal lattice by electron-electron, and electron-phonon interaction and heat is generated.[15] As mentioned earlier, a distinction between indirect and direct band gap can be made. For semiconductors with an indirect band gap e.g. silicon, the excitation of electrons into the conduction band is not only determined by the change of energy but also momentum to reach the minimum of the conduction band starting from the maximum of the valance band. The momentum of a photon is negligible, so the change in momentum is provided by the absorption or emission of phonons from or to

the semiconductor.[42] As a result, the photon absorption is less likely.[38] In a direct semiconductor, no change in momentum is required, so the energy conversion is more efficient.
Excluding the fact of a direct or indirect band gap, the generated electron-hole pairs attract each other by the Coulomb force caused by their opposite charge. The formation of a hydrogen-like quasi-particle, the exciton can be observed if the excitation energy is insufficient for the electron to escape the Coulomb force.[42, 15] The binding of the electron and holes leads to exciton states below the conduction band, which leads to a narrowing of the band gap.
The binding of an exciton is dictated by the Coulomb-attraction. This attraction is correlated with the dielectric constant of a material.[49] Materials with a low dielectric constant, e.g. organic dye's ($\epsilon_r = 2 - 4$)[50] are more likely to form exciton with binding energy, higher than the thermal energy at room temperature. While inorganic materials like silicon, with relatively high dielectric constants ($\epsilon_r < 10$)[51] the exciton binding is lower than the thermal energy at room temperature, and an occurrence is unlikely. In general, two kinds of exciton can be observed. The small, strongly bonded Frenkel-exciton and the in this thesis observed big, weakly bonded exciton the Wannier-Mott exciton.[42, 52] The properties of a Wannier-Mott exciton can be calculated with the effective mass theory. Within this theory, the electron and hole are seen as two particles moving with the effective masses of the conduction and valence bands, respectively. [15, 23] An exciton can transport energy through a crystal lattice, but no charge, since it is electrical neutral.[42]

Collection of charges carriers Following the photogeneration, the generated charge carriers have to be collected efficiently for electrical power generation. The general purpose is to collect the charge carriers and prevent recombination. This process underlies a combination of several factors. The absorber thickness and the absorption coefficient determine the overall charge generation and are immobile factors. The charge carrier mobility and the charge carrier lifetime are limiting the recombination process and are properties of the mobile charge carriers. In addition conduction inside the absorber material needs to be provided by the absorber material.[38]
Indirect semiconductors like silicon with several hundred-micrometre thick

absorber layers, therefore, need to provide sufficiently high carrier mobility and/or a lifetime in comparison to direct thin-film absorbers like GaAs or Perovskites.[13] The charge carrier collection is facilitated by establishing an asymmetric i level by doping the silicon.[38] This is done by adding impurities like boron or indium for a p-doping and phosphorus arsenic for an n-doping. A different possibility can be achieved by applying selective contacts, which transfers in the ideal case one type of carrier.[38] An intrinsic material property of the selective electrodes is a significant difference in conductivities of the electrons and holes within the selective electrodes.[38, 53] The overall process of the charge generation and the charge collection is shown in Figure 2.2

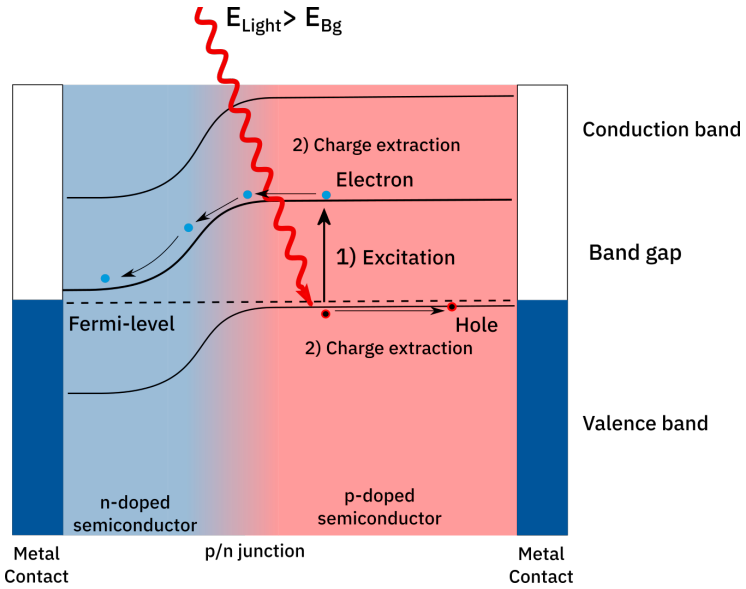

Fig. 2.2: Basic working principle of a solar cell. An adaptation of [54]

Here a simple band diagram of a silicon solar cell is shown. On both sides, metal contacts are applied. In between these contacts, the n and p doped semiconductor (marked with blue = n-doped and red = p-doped) with a so-called p/n junction is present.[38]
Step one shows the excitation of the electron from the valance band to the conduction band. This step is only possible if the energy of the incident light surpasses the energy of the band gap ($E_{light} > E_{Bg}$).[15, 38]

Recombination process The charge carrier recombination is the reverse process to the charge carrier generation. By this process, the energy of the excited electron is released in a radiative or non-radiative way. This process is unwanted in solar cells because the generated charges are lost. For other applications, e.g. LEDs this is the main light-generating process and is a wanted phenomenon.[15]
Nevertheless, these recombination processes are giving an insight into the working principle of the absorber material and furthermore an idea of preventing losses inside an absorber material. A collection of these processes is shown in Figure 2.3

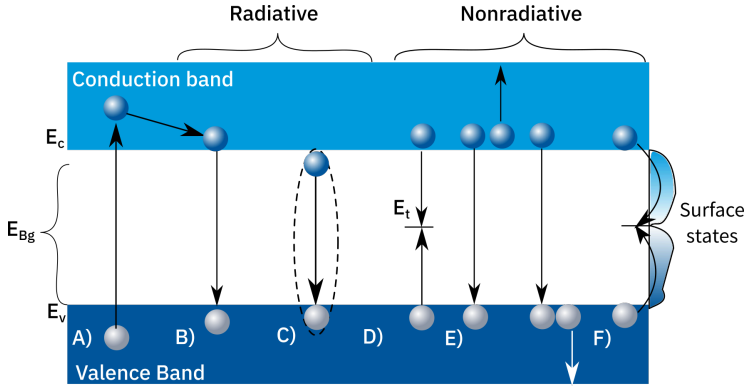

Fig. 2.3: Recombination pathways A) Excitation and ring down B) Band-Band transition C) Excitonic transition D) SRH- Recombination E) Auger recombination F) Surface recombination Adapted from [15, 13]

Figure 2.3 shows the valance and conduction band with the band gap. Furthermore, several recombination processes are divided by their radiative and non-radiative recombination.
In Figure 2.3 A) a excitation of an electron from the valance band to a conduction band followed by a ring-down process in which the excess energy of the photon is non-radiatively transferred to the crystal lattice is shown. Eventually the electron reaches the conduction band edge.
With B in Figure 2.3 the radiative band-band transition also called direct recombination, is shown. The band-band transition is the direct inverse process of the photoelectric effect. The electron and the hole are recombining radiative, emitting a photon with the excess energy. Both charge carriers are involved in the recombination process, and therefore, the recombination rate is proportional to the densities of charge carriers. This is expressed by $R_{rad} = B \cdot n \cdot p$ where B is the radiative recombination constant, n and p the

density of electrons and holes. The density of electrons and holes is further proportional to the absorption coefficient of different materials.[13]
In Figure 2.3 C the special case of an exciton is shown. Here the recombination from a lower state as the conduction band edge is observable. This results as discussed earlier in a decrease in the band gap.
Besides the radiative recombination, other recombinations can be found.[13, 55] [56] The first nonradiative recombination is shown in Figure 2.3 D) A perfect semiconductor has no electronic states in the forbidden band gap. Imperfections of the semiconductor crystal lattice lead to defect states in the forbidden band gap of a semiconductor. These are known to be trap states and cause the Shockley-Read-Hall recombination.[13, 57, 58]
Illustrated recombination in Figure 2.3 E shows the Auger recombination. This non-radiative recombination is observed in charged semiconductors. For this process, two electrons are always necessary (in total 2 electrons and a hole are involved). During this process, an excited electron gets further exited to a higher vibrational level by a second recombinational electron. In comparison to bulk material, this process is more likely to occur in quantum dots.[59]
A last mentioned non-radiative recombination is the surface recombination shown in Figure 2.3 F. The surfaces of a crystal terminates the ordered crystal lattes immediate. This leads to so-called dangling or non-saturated bonds.[13] These dangling bonds imply a high density of electrons with a broad distribution in the band gap. With the high surface to volume ratio, the number of dangling bonds is comparatively high in quantum dots.[60]
The total recombination rate is described by the sum of the reciprocal free charge carrier lifetimes.[13]

$$\frac{1}{\tau_{Total}} = \frac{1}{\tau_{rad}} + \frac{1}{\tau_{Auger}} + \frac{1}{\tau_{SRH}} + \frac{1}{\tau_{surface}} \tag{2.1}$$

The fastest process is thereby the limiting step in the total lifetime of the photogenerated free charge carriers. For a photovoltaic absorber, the charge carriers has to be extracted faster, than the fastest recombination process.[13]

A good solar cell As discussed there are several features the absorber, and the selective contacts need to provide.
At first, the absorber material needs to have a band gap. This band gap should be in an energy region, fitting to the solar spectrum. For an idealized single-junction solar cell this is usually described by the Shockley-Queisser limit.[61] This theory describes the losses of photons, with energies lower than the band gap for a solar cell. Moreover, the losses caused by recombination and thermalization.[62] The majority of the incoming photons should be absorbed. A reflection or transmission should not be the case. The formed charge carriers should have a sufficient lifetime and a high charge carrier mobility to reduce recombination.[62] The high charge carrier mobility is connected to the charge carrier transport. A high charge carrier mobility is one of the main challenges for quantum dot solar cells because of their size, the material is often interrupted by air, vacuum or even by non conducting surfactants.[63]
The charge carrier lifetime and the charge carrier mobility should be high. The band alignment with the selective electrodes or other phases should be given.[64]
Additional to the technical facts, solar cells should be cost-efficient and efficient in manufacturing to compete with the other energy generating sources. Furthermore, solar cells should provide sufficient stability. The decomposing of the solar cells should be easy and non-toxic. Moreover, leakage of eventually toxic material should be prevented.

2.2 Perovskite

These days, the name of perovskites as an absorber material for solar cell applications is widely spread.[65] Perovskite is not describing a single material, but a crystal structure, with the stoichiometry ABX_3.[66, 67, 68]
The A-side is mono or bivalent alkaline or alkaline earth metal or an organic compound with a twelvefold coordination. The B-ion is a bivalent metal with sixfold coordination. And the X-side is a bivalent chalcogen, a monovalent halide or a monovalent pseudo halide. The metal (B) and the halogen (X) are forming an octahedral. In this octahedral heteropolar bonds (mixed ionic and covalent) with the BX_6 sub-lattice are formed. In the origin of this a

strong orbital overlap (hybridization) between the two ions is observed.[69] Eight of these octahedrals are surrounding the A side ion.[69, 70] The A-side ion is less strongly bonded to the lattice by hydrogen bonds for the organic methylammonium ion.[71] The general perovskite crystal structure for the highest symmetry, the cubic perovskite structure is shown in Figure 2.4

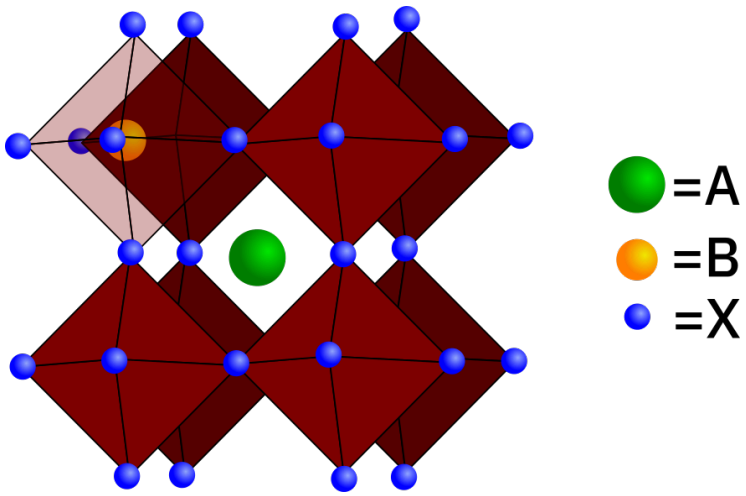

Fig. 2.4: General cubic perovskite structure ABX_3

This stoichiometry shows already the highly versatile and chemical diversity of this crystal family, which results in about 1600 known perovskites.[72] Although a wide variety of perovskites are known, not every *ABX* element system is forming a perovskite structure. The ionic radii and the Goldschmidt-formula can give an empiric prediction for the formation of perovskites at room temperature.[73]

$$t = \frac{r_A + r_X}{\sqrt{2}\,(r_B + r_X)} \tag{2.2}$$

Whereby r_A is the radius of the A-cation, r_B is the radius of the B-cation and r_x is the radius of the anion. The tolerance factor is derived in four different regimes. For a tolerance factor t> 1, a formation of a hexagonal or tetragonal phase is likely. Here the difference can be found in the tilting of the octahedral structure of the perovskite. The second regime can be found between 0.9 < t < 1. In this region the formation of a cubic crystal structure is likely. With a value of 0.71 < t < 0.9, the orthorhombic/rhombohedral structure occurs. Tolerance factors of t < 0.71 a non-perovskite structure

is likely.[74] It should be mentioned that the ionic radius for organic ions is difficult to estimate, for this reason, the Goldschmidt factor is difficult to calculate for bigger organic molecules, e.g. formamidinium.[75]
The different phases are not only determined by material composition. In addition to material composition, outer influences like temperature[70, 76, 77] or pressure [78] may have an influence on the phase. With that, the dominant crystal structure is starting from the highest symmetry the cubic to the tetragonal and orthorhombic crystal structure. These are shown in Figure 2.5

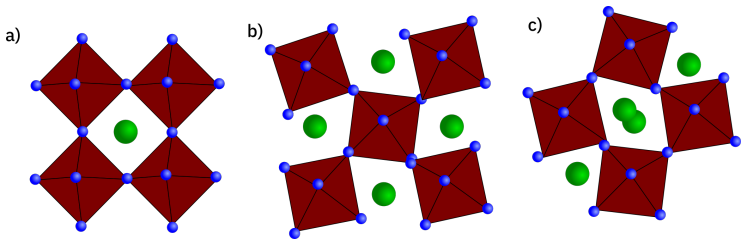

Fig. 2.5: a) Cubic b) tetragonal c) orthorombic [79]

Besides the described perovskite crystal structures, other crystal structures with the stoichiometry mentioned above are observed, one example is the double-perovskite or elpasolite crystal structure, which should just be mentioned here.[80]
Besides a lot of compounds and their useful applications, one group of perovskite forming compounds are highlighted these days.[65] The group of metal-halide perovskites. Here A is usually an organic molecule like methylammonium, formamidinium, guanidinium but also an inorganic molecule like caesium or rubidium. B is a two charged metal of the carbon group, like lead, tin or germanium. And C is a one charged halide, pseudo halide or a formiate.[81]

2.2.1 Halide Metal Perovskite

Methylammonium lead iodide, the most famous among the group of halide metal perovskites, was first described by Weber et al. in 1978.[70]. The attention of the halide metal perovskite for solar cell applications was focused more than 30 years later in 2009 with the publication of the group of *Yasuo* with an efficiency of 3.8% [36]. In 2012 *Nam-Gyu Park* [82] published already an increased efficiency exceeding 9%. From there on the number of publications with the topic perovskite for solar cell application and other optical applications like photodetectors[26] and LEDs [83] exploded. Moreover with that an impressive increase in solar cell efficiencies, leading to record efficiencies exceeding 23%.[17] (As an example of the dramatic increase in interest in the perovskite structure for solar cell applications, the search results of "Web of science" is shown in Figure 2.6)

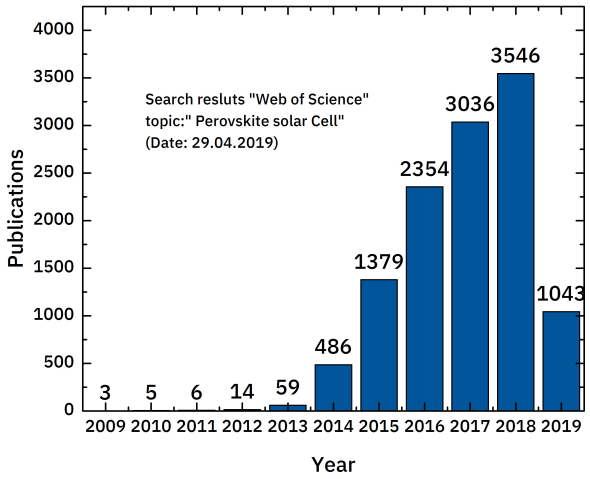

Fig. 2.6: Search results "Web of science" Topic: Perovskite solar cell Date: 29.04.2019

As discussed earlier, the crystal structure perovskite is formed by three ions. For the halide metal perovskite, there is usually the ABX_3 stoichiometry predominant.*Methylammonium triiodoplumbate(II)* as an example for the hybrid organic-inorganic perovskite is illustrated in Figure 2.7

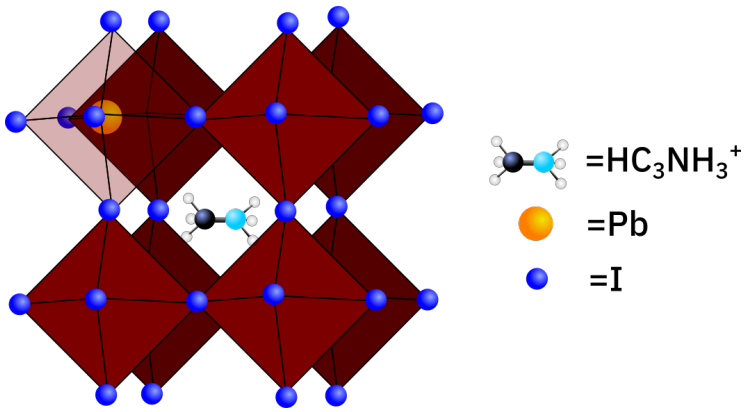

Fig. 2.7: Methylammonium triiodoplumbate(II) or $MaPbI_3$ structure

With A as methylammonium B as lead and X as iodide. However, several other combinations are known, e.g. the change of the organic anion A to formamidinium or even guanidinium (at least partly)[84]. Additionally to the hybrid perovskites also fully inorganic perovskites or their alloys are known. One example is the Caesium lead triiodide ($CsPbI_3$)[85]. Furthermore, there is a considerable variety of perovskite mixtures, with all kind of different compositions are known, e.g. $FA_{0.75}Cs_{0.25}Sn_{0.5}Pb_{0.5}I_3$ [86] , which expands the ABX_3 possibilities.

The single ions in the perovskite structure have a dedicated role in the perovskite structure. The group of Hoffmann [87] suggest that the A ion (methylammonium, formamidinium, caesium and others) does not contribute to bands near the Fermi level. However, the A-ion is, with its 12 fold coordination, essential for the symmetry, stability and therefore for the properties of the perovskite.[88] Regarding stability, it is suggested, that the organic ions improve the separation of photo carriers but decreases the structural stability, and it is further suggested, that both phenomena are correlated.[89] Furthermore, investigations on the lattice vibrations were made. The methylammonium ion in the crystal lattice has several directions for a movement besides the vibrational modes of the six hydrogen atoms, there are also four rotational axes, which transfers the vibrations on the whole crystal lattice.[90] The main focus for the optical and electronic properties of the perovskite is on the metal-halide bond, which is forming the structure of the octahedral [69] shown as red in Figure 2.7.

For supporting this assumption, the band gap tunability of the perovskites is demonstrated by the different emission of the different mixed halide perovskites. Interestingly also partly exchanged halides seem to affect the band

gap, so the full range of colours from blue towards deep red is adjustable. An outstanding example for tunability by halide exchange are the nanocrystals, with their very high quantum yields, shown in Figure 2.8.

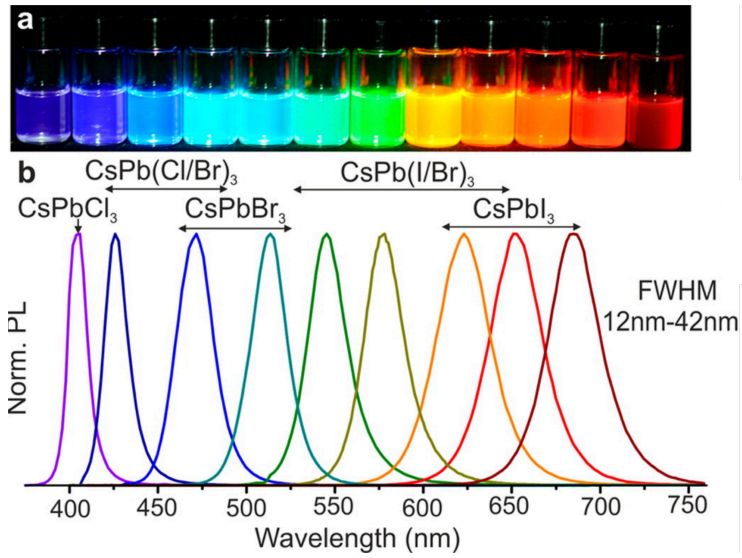

Fig. 2.8: a) $CsPbX_3$ nanoparticles in dispersion, with different Halides and Halides mixtures under Uv-Illumination b) Different measured Pl spectra,indicating different band gaps with permission of ACS publication ref.[23]

Besides the high versatility, a direct band gap and the tunability of the band gap, perovskite as an absorber material can also have more promising benefits.

Charge carrier mobilities were found in the region of $\mu \approx 200\ cm^2/V \cdot s$.[91] In comparison to Si or GaAs, these charge carrier mobilities are one to two orders of magnitude lower.[51] However, additional to the charge carrier mobilities, the comparable long lifetimes (up to 3 ms in single crystals [92]), leads to diffusion lengths in perovskite thin-films of 10 μm and single crystals up to 175 μm which exceeds the typical 1μm thin-film thickness.[92, 93]

Further investigations are showing a high intrinsic defect tolerance of the absorber material. The point defects of the perovskite seem to be inert, so a conversion of the energy to thermal energy is unlikely.[94, 95] More harmful seems to be the extended defects occurring at the grain boundaries or the surface. These defects are supposed to limit the overall electronic properties.[96]

Furthermore, based on the low non-radiative recombination losses and the high recombination rates in the perovskite, an intrinsic reabsorption of the

radiative emitted photons can be observed. With that, reabsorption of the emitted photons into the perovskite can lead to a build-up of the free charge carrier density. With that, a photon recycling is possible.[97]
Besides all these benefits, the material is easy and cheap to produce, even printing seems to be an option.[98] No high vacuum or other expensive techniques are needed.[99]
All these benefits combined led to a rapid increase in efficiency over a few years up to a power conversion efficiency of 23,7%.[100] The potential maximal solar power conversion for $MaPbI_3$ is around 30.5%.[101]
Regarding the perovskites, there are two major challenges.
The first to be addressed is the toxic heavy metal elements Pb and Sn and their compounds. Even though the release of heavy metal, e.g. by a broken solar cell into the environment is negligible [19] the disposal of the solar cells and the public acceptance of the heavy metal technology might hinder the commercial competitiveness of this new material. A solution for this challenge could provide heavy metal-free perovskite, e.g. so-called double-perovskites. For these perovskites In^+,Ag^+ and Sb^{3+} Bi^{3+} are interoperated into the perovskite structure to form an $A_2B'B''X_6$ crystal structure.[102, 103, 104]
The second and even more profound challenge for perovskite is their long term stability.[105] The above-mentioned weak bonds and the high dynamic of the methylammonium ion [90] result in a low decomposition energy barrier of 0.1 eV for $CH_3NH_3PbI_3$.[106] As a result, this indicates, that the material and its precursors (PbI_2 and MaI) are close to a phase coexistence.[106]
Adding up the organic cations are likely to be sensitive to heat, with evaporating temperatures as low as 85°C for the Ma-ion.[107] Furthermore, a known challenge is the degradation under the influence of moisture[20] or UV-light[21]. Not only the intrinsic degradation is a challenge, but also extrinsic processes, like the metal interdiffusion from the electrodes are reported.[108]
Interestingly despite the fact of the low stability concerning moisture and UV-radiation, hybrid perovskite was showing a high resistance towards proton radiation and furthermore a self-healing effect by ion redistribution within the material.[109, 110]
Although promising strategies towards the long term stability by protecting

the absorber material with a protective extrinsic coverage against the environment with, i.e. fluoropolymer [111], surfactant [112] or metal oxides [113], the intrinsic material stability is not increased. Therefore as a first step, the volatile organic compound might be substituted against less volatile organic compounds like e.g. formamidinium. However, the pure formamidinium lead triiodide ($FaPbI_3$) with a tolerance factor > 1.1 is forming a non-perovskite, photo inactive phase.[75] The solution here is a smaller cation like caesium, which is incorporated into the perovskite structure. Even though the pure, bulk $CsPbI_3$is not forming a perovskite at room temperature.[114], in combination with the formamidinium, a stable, photoactive perovskite is formed.[75] As mentioned the pure inorganic $CsPbI_3$ is not forming a perovskite like structure at room temperature .[114] With changing the size to nano size of the material, also the phases are stable, even at room temperature.[23] Additionally, the surfactant is adding up to the stability. The high surface tension of the nanoparticles might even lead to perovskites, which are not forming as a bulk material.

2.2.2 Metal-Halide Perovskite Nanoparticles

The first metal-halide perovskite nanoparticles or nanocrystals were mentioned in an article from Kojima et al.[36] In this article the authors described the formation of 2-3 nm $MaPbI_3$ and $MaPbBr_3$ nanocrystals in a template of mesoporous TiO_2 films by spin coating the precursor solution on the TiO_2 film. Later on also nanocrystals in Al_2O_3 films and nanowires where found.[115, 116] In 2014 the group of Schmidt et al. reported the non-template synthesis of 6 nm methylammonium lead tribromide ($MaPbBr_3$) perovskite nanoparticles.[117] In 2015 the Feldmann group[118] further investigated the previous of Schmidt et al.[117] described nanoparticles and found, that the described 6 nm nanoparticles were lead bromide nanoparticles surrounded by methylammonium lead tribromide platelets. The further investigated the size-adjustable thickness of the nanoplatelets by the ratio of ligand to oleic acid.[118] In 2015 the Kovalneko group published a synthesis of $CsPbI_3$ nanocrystals in a perovskite structure, which are stable at room temperature.[23] This is remarkable since the bulk $CsPbI_3$ undergoes a phase transition from the perovskite to the non-perovskite, yellow phase

at 320°C.[114] A reason for the phase stability of the nanocrystals could be the higher surface tension of the nanocrystals and in addition further stabilization properties of the ligand.[23] The challenging character of the nanocrystals concerning the XRD and HRTEM analysis leads to the conclusion of the cubic $CsPbI_3$ perovskite phase. *Bertolotti* et al. revised the cubic α-phase so, it was shown, that the nanocrystals are in an orthorhombic phase within locally ordered subdomains.[119] TEM-Images and an example for the high quantum yield of the $CsPbI_3$ quantum dots is given in Figure 2.9

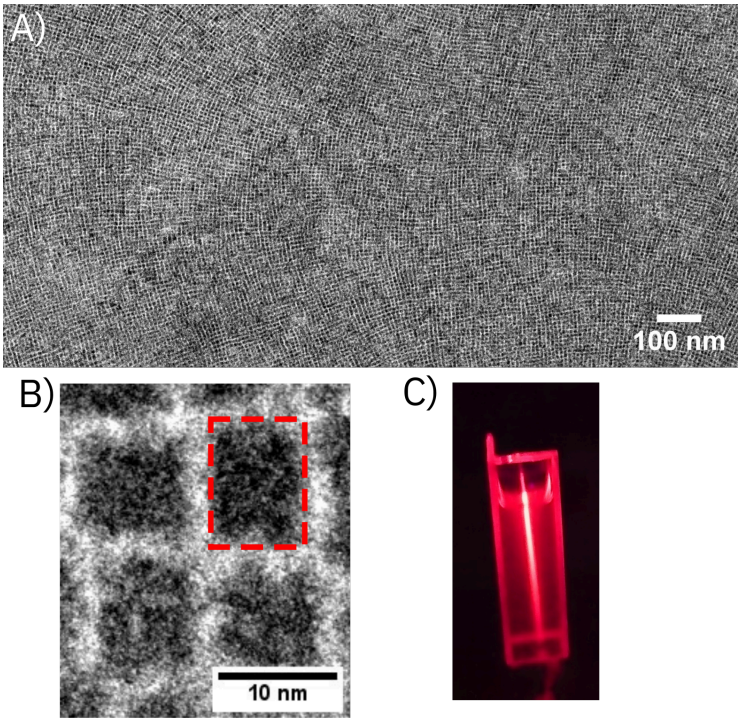

Fig. 2.9: A) $CsPbI_3$ quantum dots in an array (an overview TEM-Image) B) Magnification of the $CsPbI_3$ quantum dots, the rectangular shape of the nanocrystals is shown C) Laser beam in a dispersion of $CsPbI_3$ quantum dots with high quantum yield

An overview TEM-Image of an array of $CsPbI_3$ quantum dots is given in Figure 2.9 A. A magnification shows, the rectangular shape of the nanocrystals is shown in Figure 2.9. Additionally the Figure 2.9 C is showing the high quantum yield of the $CsPbI_3$ quantum dots, by excitation of a quantum dot dispersion with a laser.

The change of size towards nano sizes leads to further interesting properties of the nanocrystals in comparison to the bulk material. One very well

known and investigated property is the size-dependence of the band gap for semiconducting nanocrystals.[23, 120, 121] With sizes below the exciton Bohr radius, the band gap of the nanocrystals gets tunable by the size.[23] The size-dependent band gap is allowing the adjustment of the band gap without changing the material composition. So a phase separation of the mixed halide perovskites [122] can be avoided by using phase-stable perovskite compositions with a designed size, resulting in the desired band gap.[22, 123] Furthermore, the PL emission lines for the nanocrystals ar narrow, which leads to a high colour purity.[23, 124] In combination with the band gap tunability, this leads to a wide colour gamut, making the material aside from solar cell applications appealing for screen technology.[23, 125] Additionally to that, the photoluminescent quantum yield (PLQY) of perovskite nanocrystals is remarkably high. This property might lead by photon-recycling ,which increases the efficiency of the solar cell and possible reaching the Shockley-Queisser limit for a single-junction device.[22, 126] By manipulating the size of the A cation, the formation of a 2D Structure or a 1D structure can be observed.[127] By reducing the dimensions, the material properties, e.g. the high PLQY, stability and the desired band gap still achievable, but also the challenge of the ion migration and phase segregation is reduced.[22] Furthermore, the change of dimension influences the optical and electronical properties of the material. For example in a 2D inorganic material, the excitons are usually more confined due to a larger exciton binding energy, than in a 3D structure.[22] But not only the size and the dimensions can be limited. Also, exotic nanostructures can be achieved by changing the material composition and the surfactant, e.g. Ruddlesden Popper perovskites (Stochiometrie: $A_{n+1}B_nX_{3n+1}$). With this structure, a quantum well in the material is formed and nanostructures are generated. This should just be mentioned and is further discussed elsewhere.[22, 127] In comparison to the thin-film device fabrication, the steps for the absorber or emitter material can be separated. This leads to a more controllable and purer material. Additional methods like printing can be used.[128, 129, 130] Even though the stability of nanocrystals exceeds those of the film or single crystal, long term stability is not achieved yet. Furthermore, the problem of the toxic heavy metal elements is still involved in the formation of the perovskite nanocrystals. The small size and the organic ligands might further lead to better absorption of the heavy metal elements.[131, 132] Addition-

ally,l in the literature the arrangement of a single layer of quantum dots is described, but not in a 3D arrangement.
One major disadvantage of nanocrystals as an absorber material for solar cells or as emitting material for LEDs is the limited charge carrier transport. The cause for this can be found in the stabilizing surfactant, with a small dielectric constant and therefore insulating character.[22]

2.3 Nanoparticles and their properties

Nanoparticles are occurring in a variety of sizes and shapes composed of a multitude of materials. However, the definition of nanoparticles is defined if one dimension of the structure is in a size between 1 nm and 100 nm or 10^{-7}m-10^{-9}m.[133]
[134, 135] To put the nanosize in perspective the scale from a metre to a nanometre is 10^{-9} m (1 m=1.000.000.000 nm), it is the same as comparing a tennis ball with the earth.[133, 134, 135] This small size leads to a remarkable change in material properties. The origin of these properties can be explained by two effects, the surface- and the quantum confinement effect.
A typical example of the change in properties is gold. The shiny, "golden" colour changes if the size goes below the size of 100 nm the gold nanoparticles dispersion is purple, and if the particles are getting smaller (towards around 10 nm), the colour is changing to red.[136]
Another well-known example of the change of properties is the melting temperature of gold (melting point for bulk gold $t_{melt} = 1064°$C). If the size is falling short of 10 nm, the melting temperature is falling exponentially. At the size of 1.4 nm, the melting temperature is at around $500°$C.[137] These effects are attributable to the size effect.
For very small particles a different effect is observable. Especially semiconductors are affected by the so-called quantum confinement. As a consequence a size-dependent shift of the band gap is observable. Furthermore, the electronic states are getting quantised.[137]

2.3.1 Surface Matters (The Nanosize Effect)

The nanosize effect can be explained by the different kind of atoms of the same element inside a structure. For an explanation, a model of a liquid is discussed. Here a distinction between *surface atoms* and *volume atoms* is made. In the (bulk) volume, every atom can interact with their surrounding neighbour atoms in every direction. The cohesive bond energies are evenly distributed. This is not the case for the surface atoms. Some neighbouring atoms are missing, so the cohesive bond energies are not evenly distributed like for the volume atoms. This is leading to surface tension and the special properties of interfaces.[138] An illustration of the surface and volume atoms (in solid called bulk atoms) with their resulting forces is given in Figure 2.10

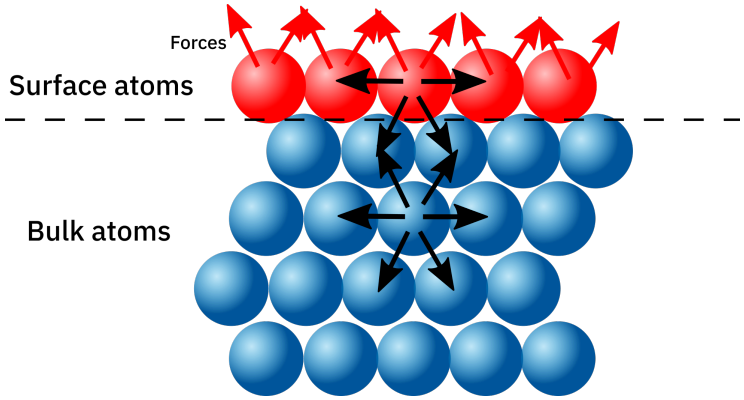

Fig. 2.10: Surface tension formation due to Interaction in the volume and surface

In this illustration, the bulk atoms with their evenly distributed forces are shown. On top, the red surface atoms with their forces in a non-equilibrium are shown. This leads to the above mentioned higher surface tension.[138] This explanation is transferred to solids and explains nanoparticle properties e.g. catalysis[139], reactivity[140] and surface plasmon[141].[142]
The increase of surface atoms in comparison to the bulk atoms for different shapes is shown by geometrical calculation in Figure 2.11.

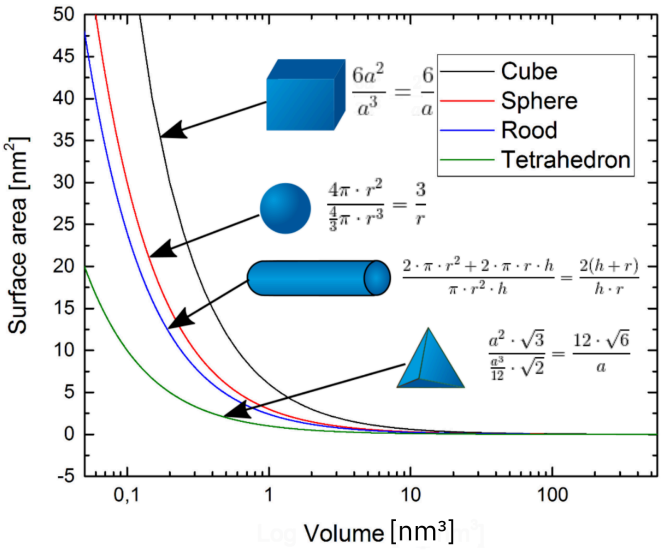

Fig. 2.11: Surface to volume ratio for different shapes

Here the surface against the volume of the different shapes is plotted to show the rapid increase in surface atoms. If the nano size of around 100 nm is reached, the surface atoms are starting to dominate. At around 10 nm with only several hundred to thousand atoms, this effect gets dominant. An example of such small particles are quantum dots.

2.3.2 Quantum dots (quantum size effect)

Quantum dots consist of semiconducting material and are found at the lower end of the nanoscale. Measuring 1-10 nm in diameter, quantum dots consist of several hundred to thousand atoms.[121] This very small size provides these particles with unique properties, close to quantum mechanical systems like single atoms. If the size of the quantum dots is below the exciton Bohr radius of the material, the band gap of the quantum dot increases with a smaller quantum dot size.[15, 54, 143] This effect can be explained with the confined electrons in the quantum dots, which leads to the quantum confinement. As described earlier, the formation of the bands are reasoned by the LCAO. The lower the amount of overlapping molecular orbitals are

overlapping[144], the lower the continuous character of the band structure is becoming. An illustration is given in Figure 2.12

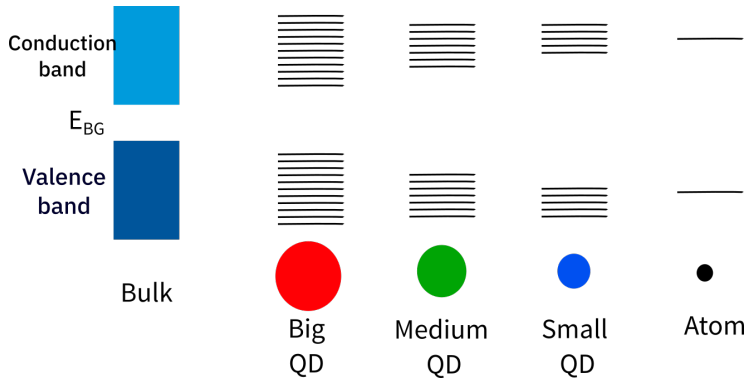

Fig. 2.12: Band gap change with the size of the particle below from a bulk material to a single atom in an adaptation of [145]

For calculating the quantum confinement energy in a semiconductor nanoparticle, the effective mass approximation can be used.[15, 23, 22]

$$\Delta E = \frac{\hbar^2 \pi^2}{2m * r^2} \tag{2.3}$$

Where m* is the reduced carrier mass, and r is the particle radius. In the case of quantum confinement, a blue shift with the confinement energy ΔE is observable.[15, 22]
In a bulk semiconductor, the bands are continuous. Each of the atoms is contributing to its atomic states to the individual band. So the width of the band is dependent on the number of atoms. Therefore the density of states (DOS) is within the band proportional to the number of atoms, which contributes to the band-like state.[137] The density of states for an expended crystal is describing a parabolic function. If the space for the wave function gets reduced in dimensions, this is changing. A 3D structure with a parabolic function is becoming a step function if the dimensions are reduced to a 2D structure (like a quantum array) system.[63] If the dimension is further reduced to a 1D system (nanorod) the function is becoming a peak function (a δ-function).[143] A further reduction to a quasi 0D structure like in quantum dots leads to discrete energy levels like found for single atoms. A further discussion can be found in literature at[121, 143, 146, 147]An

illustration of the density of states in different confined dimensions is given in Figure 2.13.

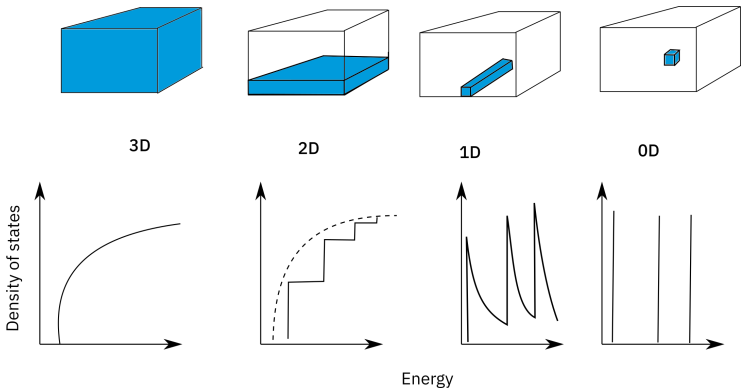

Fig. 2.13: Density of states with reduced dimensions in an adaptation of [121]

Both of the effects mentioned above, leads to the properties, observed in quantum dots. The quantised energy levels resemble more those of an atom than a bulk semiconductor with continuous bands.[143] As a result, the band gap of the quantum dots gets tunable not only by their composition but also by their size.

Another effect, which is interesting for a solar cell application, is a higher intrinsic dipole momentum, which leads to a more rapid charge separation.[143, 148]

Furthermore, it has been found, that quantum dots can emit up to three electrons per incoming photon, which is called multiple exciton generation.[143, 149]

An additional effect occurring in quantum dots is the broadening of the photoemission spectra. The effect is illustrated in Figure 2.14, and an example measurement found in literature [150] of a single quantum dot is shown.

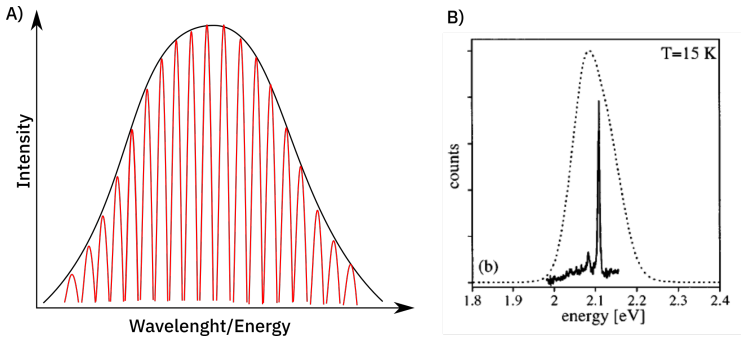

Fig. 2.14: A) Illustration of a nanoparticle photoluminescence spectrum with the resulting broadening. B) A Low temperature measurement of CdSe/CdS core-shell nanocrystal (solid line) emission of ensemble (dotted line) [150]with permission from AIP Publishing

In Figure 2.14 A an illustration of the photoemission spectrum is shown. Thereby the broad signal is underlaid by a multiplicity of several narrow signals. An experimental result of Banin et al.[150] is shown in Figure 2.14 B. Here, a single CdSe/CdS core-shell nanocrystal is measured. As a comparison, an ensemble of quantum dots is shown as a dotted line.
The small volume of the quantum dots leads to an unusual excitation of the semiconducting material. If a beam of light is emitted on a one cm^3 solid quantum dot, the typical charge carrier density is around 10^{14} [151] if the size is now reduced to 10 nm^3, the charge carrier density rises to 10^{18}. But not only the optical effects of very small nanoparticles like quantum dots are affected. It is known, that the crystallinity of the quantum dots is very high, without defects.[152] One further interesting effect is the melting point depression, which is also correlated to the quantum dot size. And will be discussed in the following section.

2.3.3 Phase transition and Nanoparticles on the example of melting point depression

A classical phase is defined as *An entity of a material system which is uniform in chemical composition and physical state*"(p.588)[153].
A phase transition to a different phase can be observed if the environment of the present phase is changed. A common example is the melting of ice a solid-liquid transition. During this process, heat is introduced into the system.

But not only heat as the temperature is an external condition, which leads to phase transitions.
Furthermore pressure, the activity of a component, a magnetic, electric or stress field can also lead to a phase transition.[153]
A phase transition is in most cases defined by symmetry breaking.[43] With this process, the system is experiencing a change in free enthalpy, enthalpy, entropy, volume, heat capacity and chemical potential. This is noticeable by an abrupt increase in the first derivate of the above mentioned physical property during a constant increase in temperature or pressure.
For this reason, the phase transition is defined by Ehrenfest as a first-order phase transition.[154]
Furthermore, a system is always assumed to the lowest Gibbs free energy to a minimum in a closed system. This relation is described by the Gibbs-Helmholtz Equation (Equation 2.4).

$$\Delta G = \Delta H - T \cdot \Delta S \tag{2.4}$$

Where G is the Gibbs free energy, H the enthalpy, T the temperature and S the entropy of a system. At the phase transition, ΔG equals zero.
In this thesis, solid/solid phase transitions are investigated. Thereby a change of crystal structure is observable. As a change in the ordering parameter, the crystal lattice transition is observed. In this case a change from orthorhombic to tetragonal to the high-temperature cubic phase.
The phase transition for a bulk material is sized independent.[155] However, if a certain size is surpassed and the surface to bulk ratio reaches a point in which the surface is dominating the bulk, the phase transition temperature dramatical drops. This property was observed for the solid-liquid phase transition and should form here the foundation for the explanation for other phase transitions.[137, 156, 157, 158, 159, 160] Instead of the expected phase for bulk material, the nanomaterials occur in a different phase. This phase is sometimes several hundred degrees in terms of temperature shifted from the expected bulk phase.[160, 161, 162] The above mentioned higher surface can explain this behaviour to volume ratio in nanoparticles. With that, the surface atoms are surrounded by fewer neighbouring atoms and the cohesive energy of the surface atoms is lower. The cohesive energy is directly related to the thermal energy required to free an atom from a

solid. Therefore the phase transition temperature becomes proportional to its cohesive energy.[163, 164] Most models for determining the melting point depression, are applied on metal nanoparticles or model systems.[163, 164, 165] For semiconductors with covalent bonds, this behaviour is less dominant. The covalent character of the bonds counteract the lack of cohesive energy.[163] This phase transition is also to apply to crystal solid-solid phase transitions, as shown in literature.[161, 162]

2.4 Synthesis of Nanostructures

As described in the previous chapter, the size of nanoparticles typically range from 1 nm up to 100 nm ($1 \cdot 10^{-9}m$ - $1 \cdot 10^{-7}m$) [133, 134, 135]. This leads to the challenge of synthesising and stabilising the nanostructures.
In general, the nanoparticles synthesises techniques are divided into two main approaches, the top-down and the bottom-up synthesis.[166] The top-down method starts with macroscopic, bulk material and by mechanical forces like ball mining the bulk is reduced until the desired size is reached. On the other hand, there is the bottom-up method, in which the starting material are molecules or clusters. For the bottom-up method, solution-based synthesis methods are used. An example for this method is the hot injection method, which will be discussed later.[152, 167] An illustration of both approaches is given in Figure 2.15.

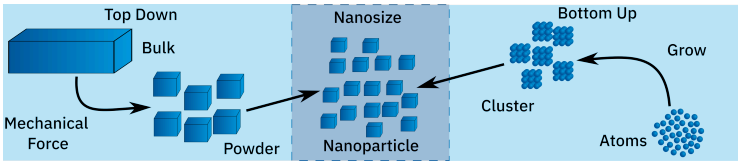

Fig. 2.15: Approach for nanostructures manufacture

The purely synthesised nanostructures are likely to aggregate or coagulate. During this process, a loss of the nanoparticle size and therefore, of their desired properties is observed. Particles are usually stabilized by charge or by surfactants for preventing the aggregation or coagulation.[138] Additionally, to the stabilisation properties of the surfactant, these molecules are essential for the size and shape control of the nanoparticles.[168] A surfactant is commonly known as soap and consists fundamental by of a hydrophilic head

and a hydrophobic tail.[138] For a better understanding of the described surfactant model, oleylamine as an example for a surfactant is shown. (see figure 2.16). Besides a simple surfactant like oleylamine, a huge variety of surfactants with different properties and functionalization exists, so a proper overview cannot be given here and the description is limited to oleylamine (shown in Figure 2.16).[169, 170, 171]

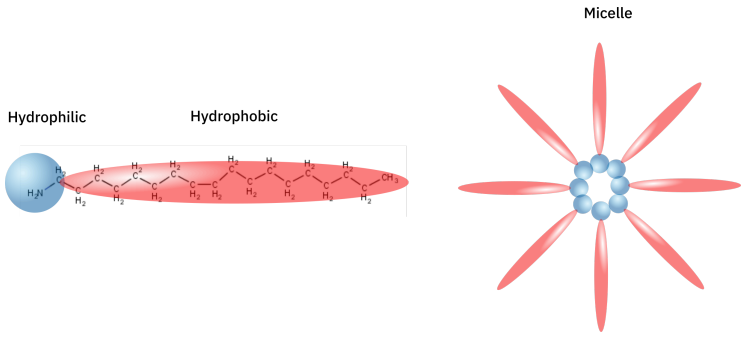

Fig. 2.16: Example of a surfactant (Oleylamine) and idealized formation of a reverse micelle

In a non-polar solvent, the surfactant molecules will form, above the critical micelle concentration (CMC), reverse micelles.[168, 172, 173] (idealized shown in figure 2.16). From a thermodynamic point of view, the micelle formation is based on the Gibbs-Helmholtz Equation.

$$\Delta G_m = \Delta H_m - T\Delta S_m \tag{2.5}$$

ΔG_m stands for the change of the free Gibbs energy of the micelle formation, ΔH_m stands for change in the enthalpy of the micelle formation, T the absolute temperature and ΔS_m is the change of the entropy of the micelle formation, under constant pressure. At room temperature, the process only shows a small positive enthalpy and a significant positive entropy. This behaviour is unusual because no system will have a positive entropy without any force or activation.[174] The formation of micelles is only possible if the solvent molecules, are taken into account, which are interacting with the surfactant molecules. During the formation of the micelles, the solvating hull of the molecule is stripped off. By this process, the total entropy of the system will turn positive, and the formation of the micelles is thermodynamically possible.[138, 175] In this now formed cavity nanoparticles can grow to a

specific size and depending on the chosen surfactant, a shape could be formed. During this process, the micelle can be seen as nanoreactor with an inner polar region, in which a polar precursor can react. The cavity, in this case, is polar and the nucleation, and growth of the nanoparticles can occur.[168] The geometrical shape of the surfactant further influences the shape of the micelle and further on the growth and shape of the nanoparticle.[168]

2.4.1 Nucleation and growth of nanostructures

Nucleation and growth are essential steps in synthesising nanoparticles. For this reason, this subsection discusses nucleation, growth and ripening of nanoparticles. It should be mentioned that the monitoring of the nuclei formation is nearly impossible, so theoretical or model system approaches are made.[176]

To describe and understand the nucleation and growth of nanoparticles, LaMer and Dinegar investigated the growth of sulphur, commonly called "*milk of sulfur*". In the paper [177] of LaMer and Dinegar, both observed the formation of sulphur. Sulphur has a high solubility in ethanol but is indissoluble in water. The precipitation of sulphur is observable by adding water to a sulphur/ethanol solution. At a certain point, the saturation of the solution is reached, and nanoparticles are observable. With this observation, they described a kinetical model for the growth of nanoparticles, called *LaMer-Model*.[177] (shown in Figure 2.17)

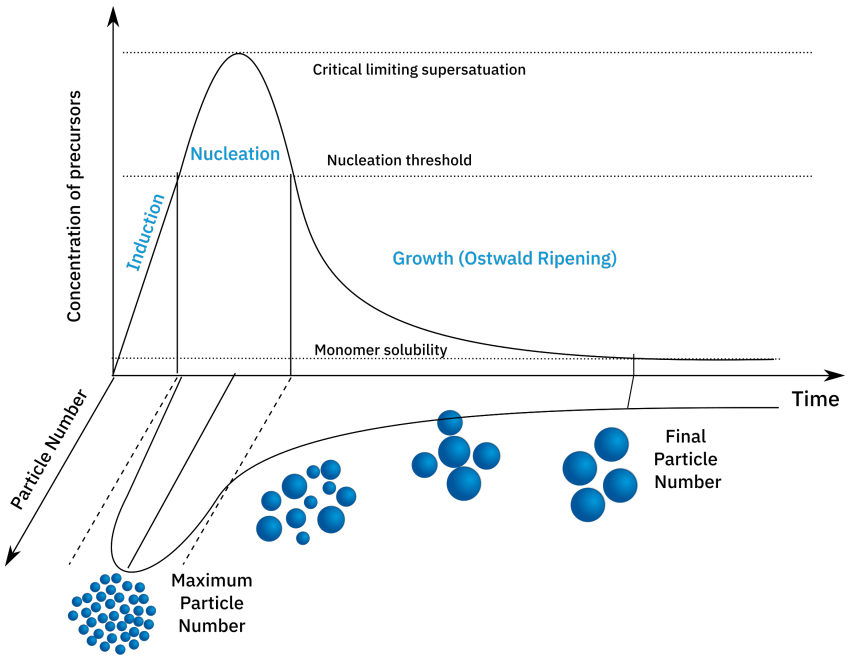

Fig. 2.17: Modified LaMer Model [177, 178] with particle number and Ostwald ripening

The observation can be divided into three steps. The induction step, the nucleation step and the growth step (Ostwald ripening).[179] In the first stage, the formation of nuclei is not observed, and just monomer is present until a threshold is reached. If this threshold is surpassed, nucleation starts. This is shown in Figure 2.17 by the spheres (nuclei) at the bottom of the LaMer-diagram and the rise of the particle number. From that point on the nucleation starts and reaches the upper limit of the nucleation at the critical limiting supersaturation. The particle number is decreasing since the monomer is consumed. At a certain point, the system is passing the critical nucleation concentration. No new particles are formed and the third phase, the growing phase is initiated.[180]

The classical nucleation model is purely thermodynamic. The nucleation theory applies that the system tends to minimise the Gibbs free formation energy. This is done by a phase transition, forming a new phase.[181] The Gibbs free formation energy consists of a sum of negative and positive terms. Here the negative term implements the bonding between a monomer and nuclei. This is described as a decrease in bulk free energy.

On the contrary, the positive term describes the unfavourable bonding between monomer and nuclei. The last term is described by an increase of the

Gibbs free surface energy. For a spherical particle, the Gibbs free formation energy of nuclei can be described as [152, 182]

$$\Delta G = -\frac{4}{3}\pi r^3 \left|\Delta G_v\right| + 4\pi r^2 \gamma \tag{2.6}$$

With ΔG as Gibbs free formation energy, r is the nuclei radius, ΔG_v is the decrease in free energy per volume due to crystallisation. With that, the volume part is described. The surface part is described with the second therm. Here γ the surface free energy per unit of surface area. The resulting graph is shown in Figure 2.18.

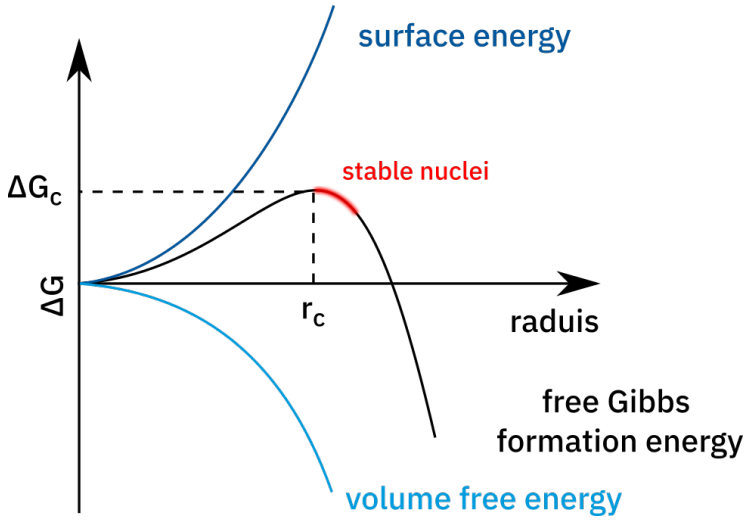

Fig. 2.18: Dependence of the Gibbs free formation energy for the nucleation. In dark blue the positive term of the surface energy, in light blue the negative term for the volume free energy. red marked is the region in which nuclei are formed adapted from[152]

Addition to the above mentioned positive and negative term and the Gibbs free formation energy ΔG, a critical radius r_c at the maximum of the free Gibbs formation energy and activation energy barrier ΔG_c is implemented. The critical radius is corresponding with the activation energy barrier. The formation of nuclei only occurs after reaching the critical radius r_c. Thereby the activation energy ΔG_c is surpassed. Particles smaller than the critical radius get dissolved. The critical radius can be determinate by solving the equation $\frac{d(\Delta G)}{dr} = 0$

$$r_c = \frac{2\gamma}{|\Delta G_v|} \tag{2.7}$$

where γ is the surface tension. The activation energy for the nucleation can be calculated with

$$\Delta G_c = \frac{16\pi\gamma^3}{|\Delta G_v|^2} \tag{2.8}$$

This model focuses on the homogenous nucleation. It is important to mention that the critical radius is almost always far too large for homogenous nucleation to reach. So with just homogenous nucleation, no nuclei would be formed. The homogenous nucleation is generating nucleation seeds, on which monomers further can absorb. This is called a heterogeneous nucleations.[183, 184] In nanoparticle synthesis, both kinds of nucleation are present. Both appear consecutively and parallel during nucleation.
Figure 2.17 shows another important step for the synthesis of uniform nanoparticles. The main growing and ripening process surpassing diffusion growth [185] is called *Ostwald ripening*.[186] Ostwald describes the observation that bigger particles of mercury oxide are favoured over smaller particles.[187] A thermodynamic-driven, spontaneous process is occurring. With that, smaller particles are dissolving. The released monomer is then consumed by the bigger particles which no continue to grow. The driving force is the difference in vapour pressure of smaller particles with higher vapour pressure and bigger particles with lower vapour pressure, generated by the higher surface energy of the smaller particles.[186, 188]
In general, Ostwald ripening leads to a uniform size distribution (focusing).[188] This is also visible in Figure 2.17 by observing the particle number, which correlates with the particle dispersity, as an illustration above the diagram and shown with the z-axis. The overall rate-limiting step of the Ostwald ripening is the diffusion in the dispersion.[189] The diffusion rate, in general, is also temperature-dependent, which means that higher temperature leads to a higher diffusion and, hence, a higher rate of Ostwald ripening.[190, 191]

2.4.2 Hot injection

A more sophisticated method for synthesising mono-disperse nanocrystals is the *hot injection* method.[152, 167]
As described in Nucleation and growth of nanostructures (subsection 2.4.1), the growth of nanoparticles can be divided into three distinct stages. The induction, the nucleation and the ripening/growth stage. The induction is for the general nanoparticle synthesis in this case, not of interest. The focus is on the nucleation and the ripening process. For achieving mono-disperse nanoparticles, it is important to separate the nucleation and the ripening process. The rate of the nucleations needs to be, therefore, high and immediate. A better term for describing the immediate nucleation is *burst nucleation*.[179, 192] Afterwards, the ripening process without any further nucleation should be acquired. The ripening process is in contrast to the nucleation process significantly longer. In Figure 2.19, the hot injection is illustrated with an adapted LaMer diagram. Additional, the moment of the injection is shown in images from the synthesis of $CsPbI_3$ nanoparticles.

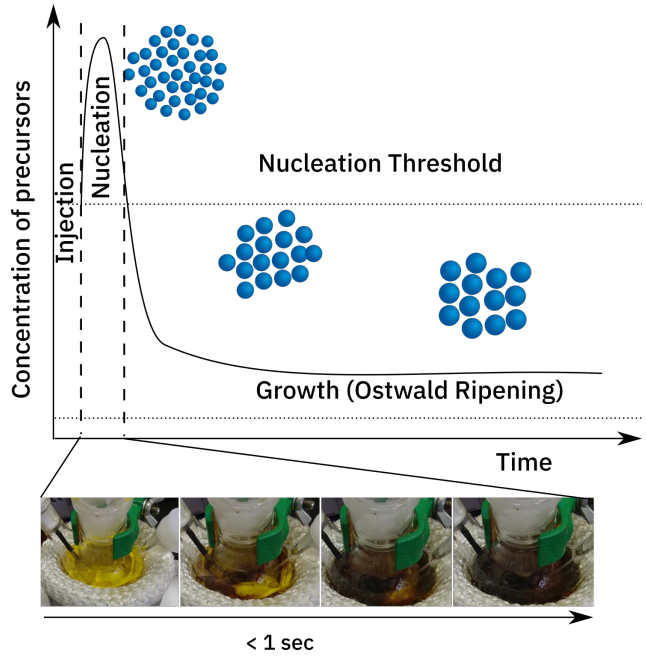

Fig. 2.19: LaMer-diagram of the hot injection. Separation of the nucleation and ripening phase with illustration of the particle formation and photos of the "burst" nucleation (t<1sec.)

The hot injection leads to instantaneous nucleation and rapid cooling of the reaction temperature. Thereby, the reaction temperature drops behind the nucleation threshold, and no further nuclei are formed. A separation of the nucleation and the growth is the result. The classical nucleation theory cannot be fully applied to the hot injection method. First, the nuclei formed by the hot injection are very small. Therefore the Δ G is not a constant but can vary with the size of the particle. Second, the surface tension will also vary depending on the arrangement of the surface atoms and the coordinating ligands. Moreover, last the hot injection method is dependent on the temperature-quenching, so the size of the formed nuclei is not necessarily the size of the critical nuclei given by Equation 2.7.[152] So a solubility product-based model for the hot injection method is used for the description. This is described and can be found in literature [152]

2.4.3 Ligand exchange

For the nanoparticle synthesis stabilizing agents must be present to prevent aggregation, precipitation and conduct self-assembly.[138, 193] These stabilizing agents or capping ligands (surfactants when bond covalent, dative or by ionic bonds) are chosen for their properties in the nanoparticle synthesis. However, these surfactants often lack the properties wanted for the specific application.[129, 193]
A straightforward way of the exchange is the exposure of the capped nanocrystals in dispersion to an excess of the preferred capping ligand. So the new ligand is competing over the previous. By repeating this step several times, a full exchange can be achieved.[193, 194] This approach is limited since the head group affinity for the nanoparticle surface needs to be higher or equal to the original ligand. This limits the number of ligands, which undergoes the exchange. The used solvent polarity and in this connection the relative abundance of the present and exchanged ligand affect the efficiency of the ligand exchange.[176]
Furthermore, the ligand needs also to stabilize the nanoparticle and decomposition due to the ligand should be prevented.
A different way for removing the ligand and merging the arranged nanocrystals is by thermal treatment.[195] During this process, the organic ligand is

decomposed, and the nanocrystals are ligand-free on the surface.
Furthermore, the nanoparticles are sintered and form a conductive layer.[129, 195] This implies higher thermal stability of the nanocrystals than the organic capping ligand.
A third method mentioned here, which is suitable for, e.g. ionic bonded capping ligands, is a washing method. By adding a solvent, which dissolves the ligand but not the nanocrystals, the capping ligand can be extracted. Afterwards, a new, different capping ligand, with the desired properties, can be inserted. By this method, a competition of the ligands is excluded and the exchange is more likely.[196, 197]

3

Methods

> *The greater the contrast, the greater the potential. Great energy only comes from a correspondingly great tension of opposites.*
>
> **— Carl Gustav Jung**
> Swiss psychiatrist and psychoanalyst

This chapter focus on the methods used in this thesis. For discussing this, a short introduction into light and the interaction of light and matter will be given. Later, the spectroscopic methods and the x-ray and electron scattering methods with a small introduction into scattering will be discussed.

Light as such is described as a particle (photon) beam, or as a wave. This unique property puts light as interesting "device" in a special position since depending on the investigated method, the behaviour of light can be explained as a particle beam or a wave.[198] For the investigation in this thesis, a part of the spectrum starting at around 10^{-4}m with the energy of 10^{-2}eV to around 10^{-10}m with the energy of 10^{5}eV was used.
If a beam of light is incident on a material, there are three, distinct pathways for the light emerge. Light can be transmitted, so an Interaction with matter is not observed. The light can interact with a material in a way as to be absorbed and often remitted. As a third observation, the pathway of the light can be changed by, for instance, scattering, diffraction or reflection. In comparison to the transmittance for absorption/emission and scattering/diffraction/reflection, an interaction of light with matter is observed. Depending on the measurement method often several of these interactions are involved, which often leads to challenges.
These three fundamental observations are leading to different pieces of information from the sample. For obtaining the desired information, the

wavelengths of the light must be adjusted to information hidden in the matter. For instance, a band gap excitation can only be observed, if the energy (or wavelength) of the light exceeds the band gap of the material. Furthermore, for scattering processes, the wavelength of the beam of light should be in the range of the size of interest. Through all these methods, different pieces of information of the sample are obtained. These pieces of information often support each other and lead to a conclusive result.

3.1 Spectroscopy

This section is derived from the wavelength or energy-dependent change of light by the interaction with the material. These methods are the absorption spectroscopy, the photoluminescence, and the X-ray fluorescence. Furthermore, time-resolved methods are used for investigating processes in the material. Here the time-resolved photoluminescence and the optical pump terahertz pulse method can be mentioned.

3.1.1 Absorption spectroscopy

Absorption spectroscopy investigates the attenuation of electromagnetic radiation by an absorbing substance.

The method is based on the principle of a light-induced excitation of an electron.[199]
The extinction of light is described by Beer-Lambert's law.[198]

$$I = I_0 \cdot e^{-a \cdot d} \tag{3.1}$$

From that follows for the transmission [200]

$$T = \frac{I}{I_0} = e^{-\alpha \cdot d} \tag{3.2}$$

Where T is for the transmission, I_0 the incident beam, I the transmitted beam, α the absorption coefficient and d the thickness of the sample. For calculating the absorption A, the following relationship is described [174]:

$$A = 1 - T \tag{3.3}$$

Since thin layers are investigated and losses due to scattering or reflection cannot be avoided, transmission and reflection measurements were performed in an integrations sphere. An integrations sphere is a hollow sphere covered with a diffuse reflecting coating.[201, 202] The measurement set-up is shown in Figure 3.1

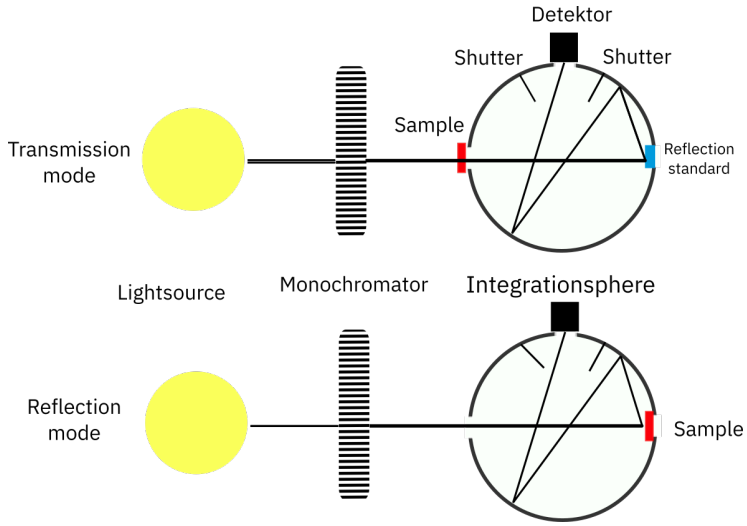

Fig. 3.1: Absorption measurement with an integrations sphere. Shown is only one possible reflection path (besides infinitive others) inside the integration sphere

Here a polychromatic light source (two lamps for a full spectrum) is shown. Lenses are focusing the light and further passing it through a scanning monochromator. This path is constant and not changed in both measurements. Two measurements need to be performed, for obtaining the real incident beam, without surface reflection and scattering.
First, the diffuse transmission was measured. Therefore the light was conducted through the sample in the integrations sphere. The light beam gets diffuse scattered at the reference sample and further inside the sphere (material of the inner sphere). Eventually, the attenuated beam is reaching the

detector. A direct scattered beam observed by the detector is not possible since shutters cover the detector.
As a second measurement, the sample is exchanged against the reference sample. Moreover, another measurement was conducted. This time the diffuse reflection and scattering was investigated.
With these measurements, the incident beam is determined, and the transmission of the sample can be determined.
Of the resulting spectra, the first derivative was formed. With the local minimum of the derivative, the absorption onset was determinate. With the absorption onset, the band gap of the sample can be estimated.[203]

3.1.2 Photoluminescence

As discussed in the Recombination process, the excited electron is likely to fall back to the ground state. This process is often combined by the emission of light and is usually done at the band edge of the conduction band. From this point on, there are several pathways for a radiative and a non-radiative transition to the ground state. A short overview of some processes is given in Figure 3.2

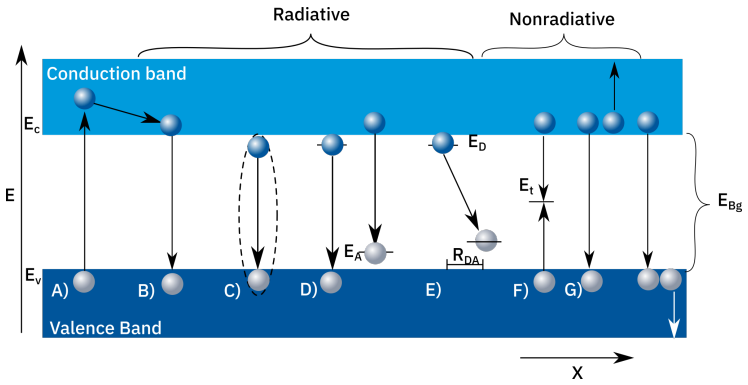

Fig. 3.2: PL pathways A) Absorption and ring-down to lowest excited state B) Band-Band transition C)Electron hole-pair transition D) Band-Defect recombination E) Donor-acceptor pair recombination F)Shockley-Read-Hall recombination e) Auger recombination in an adaptation of [15]

The measured photoluminescence can be divided into radiative and non-radiative recombination processes. For the radiative B) the band-band transi-

tion, C) the electron-hole pair transition, D) band-defect transition and E) Donor-Acceptor recombination can be named. For the non-radiative examples are the Shockley-Read-Hall F) and Auger recombination G). The later processes, are not detectable by direct photon detection and therefore not directly observable with photoluminescence. A more in-depth discussion of the recombination processes can be found in literature.[15, 204]
The radiative band-band transition occurs if recombination from the lowest conduction band to the highest valance band is observed. This transition has a high probability for semiconductors with a small number of defects. These transitions are well observable at higher temperatures. In this case, the exciton is dissociated and defect states not occupied.[15] Another way of recombination is the exciton recombination. In this state, the electron and the hole are still interacting by Columb interaction and forming an exciton. As shown in Figure 3.2, the exciton transition is not occurring from band to band. The recombination is occurring from a lower state as the lowest conduction band state.[15] This transition is found and described in metal halide perovskites [205] and mentioned above (see section 2.1.2). The last here mentioned transition is the defect transition. In general, a defect can be seen as a microscopic internal surface, which is producing a continuum of states. This model of a defect has a strong temperature dependence.[204]
The following illustration is showing the setup for the here performed steady-state photoluminescence measurement. (See Figure 3.3)

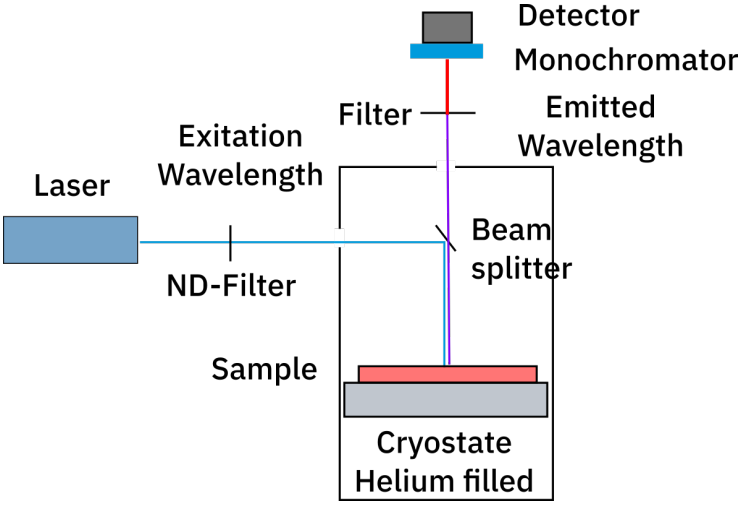

Fig. 3.3: Schematic illustration of the steady-state photoluminescence set-up

Thereby a laser (E_{em}> E_{Bg}) is used. The beam is passed through a neutral-density filter (ND-Filter) to adjust the fluence. The beam is directed on the sample. From the sample on the emitted light gets directed towards the beam splitter. A bandpass filter extracts the emitted and scattered light. The beam then passes a monochromator into a detector. Alternatively, in this case, a diffraction grating on a line detector. With the last-mentioned method, scanning with a monochromator is not required. For temperature-dependent measurements, the sample can be placed in a Helium cryostat.
With temperature-dependent measurements, changes in the material can be observed, and therefore changes in the photoluminescence are expected. The full width at half maximum (FWHM) will be narrow at low temperatures, and a broadening at higher temperatures will be observable.[15] Furthermore, if a material is cooled, the lattice parameter will narrow, and with that, the band gap is expected to shift to higher wavelengths (lower energies). This behaviour can be described with a fundamental based approach for analysing the band gap with a function of temperature which is given by [206, 207]:

$$E_{BG} = E_{BG}^{0} + \frac{\partial E_{BG}}{\partial V}\frac{\partial V}{\partial T}T + A\left(\frac{2}{\exp\left(\frac{E_{ph}}{k_B T}\right) - 1} + 1\right) \tag{3.4}$$

where is E_{BG}^{0} is the band gap at 0K ,$\frac{\partial E_{BG}}{\partial V}$ is the band gap expansion coefficient, $\frac{\partial V}{\partial T}$ Is the thermal expansion coefficient, A is the strength of the electron-phonon coupling, E_{ph} is the average photon energy, k_B is the Boltzmann constant and T the crystal lattice temperature.
The quantum yield gives an insight into the recombination properties of a sample to convert the absorbed photons into emitted photons. The competing radiative or non-radiative processes in a semiconductor previously mentioned limit this process.[208] The quantum yield is defined by [209]:

$$\Phi = \frac{\#photons\ emitted}{\#photons\ absorbed} \tag{3.5}$$

For the measurement of the quantum yield, a different set-up was used. This set-up is shown in Figure 3.4

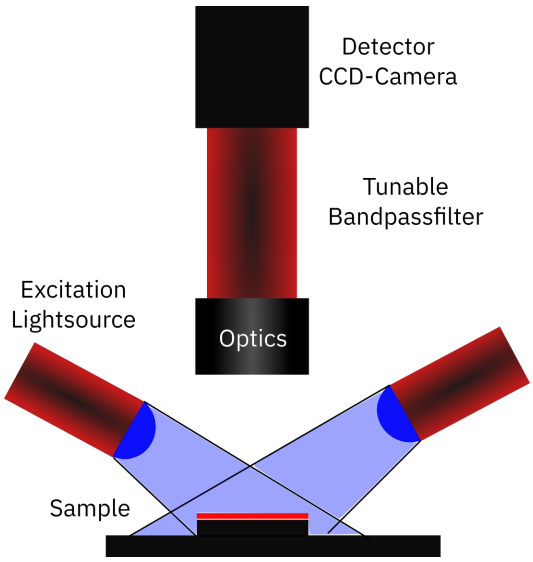

Fig. 3.4: Calibrated photoluminescence quantum yield set-up

LED light sources illuminate the sample with a wavelength of 455 nm and are equal to one sun. The sample gets excited and emits lights towards the optics. These optics are focusing and directing the light trough a tunable bandpass filter to adjust the emission wavelengths of the sample. The detector a, CCD-Camera, is detecting the intensity of the light.
The set-up is calibrated to the known current of a reference solar cell. By the current of the reference solar cell, the incoming photons are known, and the quantum yield can be determined.[208, 210]

3.1.3 Time-resolved photoluminescence

As discussed above the ground state is the thermally equilibrated state. If a light pulse interferes with a sample, electrons get excited to the excited state. There the electrons stay some time and fall back to the ground state. The typical time for the light absorption is around 10^{-15} s and can be seen as instantaneously. The scattering process or ring down process to the lowest excited level is occurring at around 10^{-12} to 10^{-10} s.[15] Both described processes are significantly faster than the here observed radiative lifetime which is in a range of 10^{-9} to 10^{-3} s.[15] Furthermore, competing non-radiative processes like Shockley-Read-Hall and Auger recombination can distort the results of the measured lifetime.[56] In addition to these also

surface recombination and interface recombination might occur. However, this shall just be mentioned and can be found elsewhere.[211]
A pulsed source is needed for investigating the time-dependent radiative decay process. These pulses need to excite the sample and need to be short enough to not interfere with the measured signal. The process is repeated several million times for a sufficient signal to noise ratio. The here used set-up is illustrated in Figure 3.5 A. Additionally an illustrated time-dependent measurement signal is given in Figure 3.5 B.

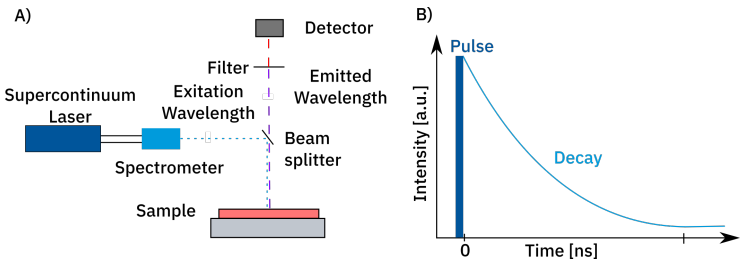

Fig. 3.5: A) Time-resolved photoluminescence set-up B) Illustrated decay

For the excitation, a pulsed supercontinuum laser [212, 213] is used. For adjusting the excitation wavelength, a spectrometer or filter are placed in the beam path. The pulsed, monochromatic beam is directed on the sample. The sample gets excited and emits light. The light is guided through a beam splitter and towards a bandpass filter. The bandpass filter eliminates the scattered light from the source. A single-photon detector is counting the decay. As a result, the time-resolved signal is shown in Figure 3.5 B. Here the pulse is illustrated as dark blue and the decay as light blue.
The general approach to investigate these decays might be in a first attempt to fit the decay with a single or bi-exponential function. For semiconductors especially for quantum dots, this is often not possible. Therefore the potential decay needs to be modelled, and a potential fit function needs to be found. Further information can be found in the literature.[56, 211, 214]

3.1.4 Optical pump terahertz probe

The optical pump terahertz probe (OPTP) is a pulsed method for characterising the absorber material and investigating the charge mobility. Since a time-dependent process is observed, the method is pulsed on a femtosecond timescale. The general set-up is shown in (Figure 3.6)

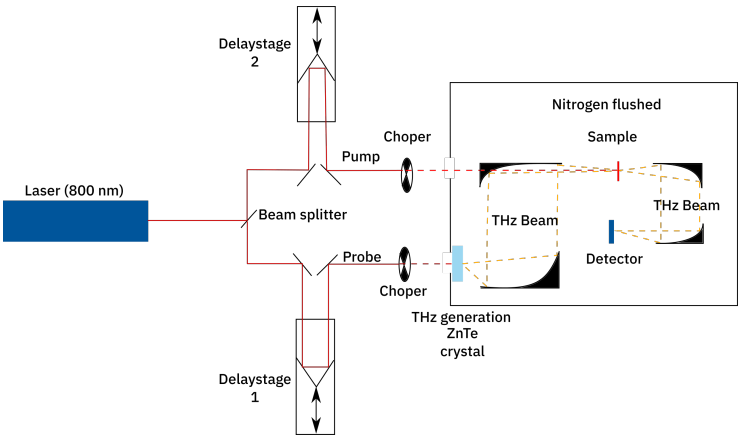

Fig. 3.6: Schematic illustration of the pump probe terahertz set-up

Here an 800 nm femtosecond pulsed laser is used. The laser is divided by a beam splitter into two paths. Both paths are directed into separate delay stages for adjusting the signal, so that the principle mentioned above can be applied. Afterwards, both beams pass a chopper wheel for adjusting the pulse length. The first beam passes a zinc telluride crystal, and terahertz radiation is generated.[215] The terahertz radiation gets absorbed by water in the atmosphere.[216] Therefore, the whole spectroscopy needs to take place in a nitrogen environment. The generated terahertz beam gets directed and focused by parabolic mirrors on the sample.
Meanwhile, the pump beam of the 800 nm laser is directed on the sample. Both beams, the pump, and the probe beam are overlayed on the sample. The transmitted terahertz radiation gets refocused and directed on to the detector. To obtain information about the charge carrier dynamics, the OPTP is divided into three steps. The first step is a terahertz pulse (energy a few meV) in transmission, which observes the sample in the ground state. Then a pump pulse (energy for exciting the electrons typically a few eV) of a femtosecond laser is generating charge carriers in the sample. The excited sample then gets probed by the second terahertz pulse (energy few meV). This process is illustrated in Figure 3.7.

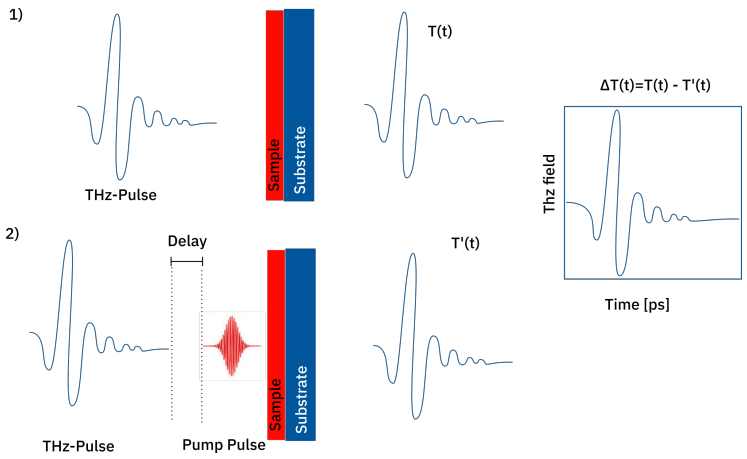

Fig. 3.7: 1) First teraherz probe pulse 2) Pump pulse with slightly delayed teraherz probe and the resulting pulse

The differences of the terahertz signal are Fourier transformed to generate a spectrum. From the resulting spectrum, the charge mobility can be extracted by extrapolation to 0 THz. More information and the modelling can be found in the literature.[217, 218, 219, 220]

3.1.5 X-ray Fluorescence

If a high energy light beam (e.g. UV, X-ray or an electron beam) interacts with electrons of an atom, the ejection of the electrons from the electron shell is observable. By this process, the atom gets ionised. The inner shells of the atom will get filled with electrons from the outer shells. This transition emits light as described in Photoluminescence subsection 3.1.2 but with a characteristic wavelength (typically X-ray) and is dependent on the energy difference of the initial to the final orbital. The emitted wavelength is element-specific, so a characteristic spectrum is generated.[221, 222, 223] The process is illustrated in Figure 3.8.

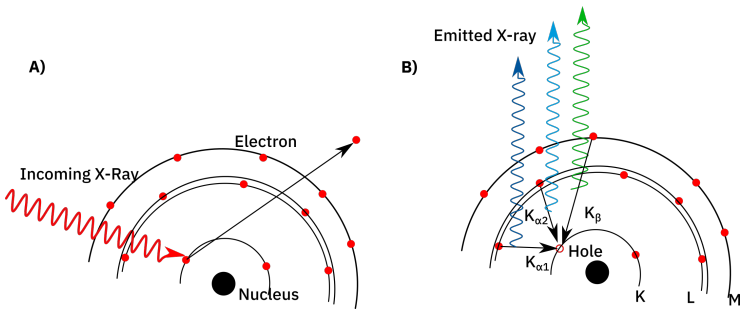

Fig. 3.8: A) Incident beam (red) leads to a ejection of an electron from the inner shell of an atom B) hole filling of electrons from higher shells like L and M shell with their characteristic energies represented by different colours

As shown in Figure 3.8, a limited number of electrons can fill the resultant hole. The main transitions are $L \rightarrow K$ transitions and $M \rightarrow K$ transitions. These are described as K_α and K_β. Also, other transitions are possible. An X-ray can also eject an L electron, so a $M \rightarrow L$ transition becomes possible which is named L_α transition. In addition, more than one signal can come from a $L \rightarrow K$ transition. These signals can be explained with the L-Shells properties of quantum number N=2. So multiple line emissions occur for electrons in a quantum state with N>1. The quantum state N>1 leads to the characteristic splitting of the K_α line into $K_{\alpha 1}$ and $K_{\alpha 2}$ of copper in a copper X-ray tube. This principle is also used in generating X-rays (see section 3.2 (see subsection 3.1.5).[198, 222, 224] The atomic number gives a general trend for the energy released by the filling of an ejected electron. An example is shown in Table 3.1 with elements investigated in this thesis.

Tab. 3.1: Elements used to analyse in this thesis in atomic number (Z) order with selected emission lines in keV [225]

Element	K_α	K_β	L_α	M_α
Potassium	3.314	3.590	-	-
Iodine	28.612	32.294	3.938	-
Cesium	30.973	34.982	4.285	-
Lead	74.970	84.939	10.551	2.342

As shown in Table 3.1 in heavy atoms like caesium, iodine or lead, also higher shell atoms can be excited. The X-ray fluorescence is here not limited to a transition from a higher shell to the K-Shell. Also, a transition from an N $\rightarrow$ M for the element lead is possible and results in an energy of 2.342 keV.[225] XRF is a qualitative, semi-quantitative and a relative method. The calibration

is usually done by a reference material, with the same composition. If no reference material is present, the error for the quantitative measurement will rise. One reason for this observation is the overlap of the emission lines of the elements.[223] Furthermore, the emitted X-ray from one transition of an inner electron shell can also eject another electron from a higher shell, which can be described as an inner, non-radiative Auger-Effect. The emitted radiation from the transition to the newly formed hole, will often be in the lower energy region and also not detected. This process can also occur in between atoms of a sample. Additionally, the Auger-Effect is more likely for light atoms up to an atomic number of around 30 (Zinc).[226, 227]
In addition, the sensitivity of the measurement method is reduced due to surface roughness, water content and grain size variations of the material.[223]
Asides these challenges and the fact of the semi-quantitative method, a general overview of the composition of the sample can be made, and first insights with this fast and non-destructive method can be made.

3.2 Scattering of X-Rays and electrons

In the following section, the used X-ray and electron scattering methods are described. Therefore first a subsection about X-rays and their generation will be given, and the general idea behind the scattering will be discussed briefly. The here used methods are then segmented into reflection methods (XRD and XRR) and transmission methods (SAXS and TEM).

3.2.1 X-rays and scattering

X-rays are an electromagnetic wave characterised by energies ranging from several 100 eV to 100 keV with wavelengths of aground 10 nm to 0.001 nm. X-rays only differ from infrared, visible and UV-light by the energy.[228]
X-rays are generated by the acceleration of electrons in a vacuum in an electric field and focussed towards an anode (here copper target). If the electrons collide with the anode, their kinetic energy is released. This continuous spectrum is called the bremsstrahlung. The bremsstrahlung emerges if an electron is forced to change its direction.[222, 228] A typical X-ray

spectrum of an X-ray tube is composed by bremsstrahlung and further by the characteristic X-ray emission lines.[198, 228] The characteristic X-ray emission lines originate from the copper target. These emission lines underlay the principle of the ionisation of the copper target by the electron beam and the filling of the vacancy by a different core electron under the emission of X-rays, described in X-ray Fluorescence subsection 3.1.5.[228]
In this thesis the copper $K_{\alpha 1}$ radiation is used with a wavelength of 1.5406 Å with an energy of 8.04 keV.[198] Copper is giving the characteristic K_{β} =1.39 Å, $K_{\alpha 1}$ =1,540 Å and $K_{\alpha 2}$ = 1,544 Å of which in most cases $K_{\alpha 1}$ is used. This is done by filtering the K_{β} with a nickel filter (absorption edge 1.49 Å [225]).[222, 228]
One disadvantage of the X-Ray tube is the low yield of X-rays with 1-2%, which often is not sufficient for some investigation methods.[229] Another more efficient way of generating X-ray radiation is the usage of a synchrotron. Electrons are generated by a cathode and accelerated in a vacuum in a loop accelerator. This loop accelerator is called a synchrotron, in which further acceleration takes place. At a certain acceleration level, the electrons are injected into an electron storage ring. As mentioned above particles emit a continuous spectrum of light if they are deflected. The bremsstrahlung in a storage ring is generated by special, magnetic devices ((undulator or wiggler).
The intensity of the light, the brilliance, and the possibility of pulsing the light is extraordinary in comparison to a lab size x-ray tube.(x-ray tube =10^{7} - 10^{11} $\frac{N_{Photon}}{s \cdot mrad^2 \cdot mm^2}$; Synchrotron up to 10^{21} $\frac{N_{Photon}}{s \cdot mrad^2 \cdot mm^2}$) [222, 229, 230]
The electromagnetic wave is characterised by an electric field, vibrating at a constant frequency, perpendicular to the direction of its movement.[228]By an interaction with matter, electrons as charged particles of the outer layer of an atom, are interacting with the electromagnetic wave in a sinusoidal change with time at the same energy. As a result, X-rays are released and with that X-rays are scattered on the electron shell of an atom.[228]
In general, scattering can be distinguished in two kinds of scattering, the elastic and inelastic. The difference in the inelastic and elastic scattering is in the energy transfer to the scattering centre. For the here discussed and observed elastic scattering, no (or negligible low) energy transfer is observed (Thompson scattering).[228, 231]
Since the general scattering process is considered to be magnitudes faster

than the process of moving particles or even crystal lattice vibration, the Born approximation is applied.[232, 233] The general process of scattering is shown at the scattering triangle shown in Figure 3.9

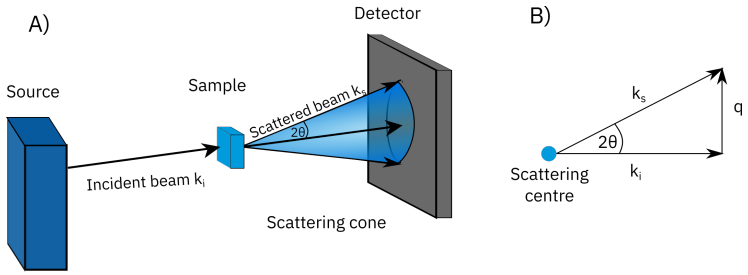

Fig. 3.9: A) Scattering in a transmitting device with scattering cone B) Scattering triangle with the scattering vector

In general, the incident beam interacts with the scattering centre and gets scattered. Both beams are considered as wave vectors wave vector for the incident beam (k_i), and the scattered beam (k_s) and the scattering vector q can be defined as[228, 234, 235].

$$\vec{q} = \vec{k_s} - \vec{k_i} \tag{3.6}$$

$\vec{q}$ is described in inverse length scales with units Å^{-1} or nm^{-1}. The scattering vector q can be further expressed as a function of a photon with the incident wavelengths λ, which scatters at a sample at an angle of 2θ.[228, 234, 235] This eliminates the need for a vector direction of $\vec{K_s}$and $\vec{K_i}$. With that a comparison with different incident wavelengths is possible.

$$\vec{q} = |q| = \frac{4\pi \sin\theta}{\lambda} \tag{3.7}$$

$\vec{q}$ can be further described in the direct space as:

$$\vec{q} = \frac{2\pi}{d} \tag{3.8}$$

Here d is the interplane spacing in a structure or crystal. Equation 3.8 shows, the relationship of smaller angles, and expanded structures. Also, vice versa higher angles with smaller structures. After the scattering event, the

X-ray beams can interfere constructively or destructively. The constructive interference is described by the Bragg equation:

$$n\lambda = 2d \cdot sin(\theta) \tag{3.9}$$

If the Bragg equation or better Bragg condition is fulfilled, a constructive interference is observable.[202] With that, the amplitude of the wave gets amplified.[228] An explanation for this observation is given in Figure 3.10

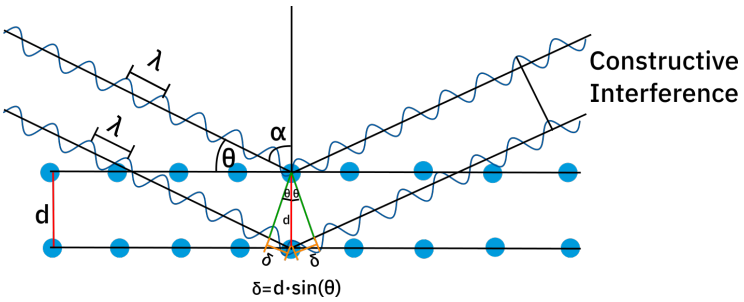

Fig. 3.10: Crystal lattice with incident beams which interfere constructively

A crystal lattice with the lattice distance d is shown. Two incident beams with a wavelength λ get scattered at the crystal plane with an incident angle α (seen as perpendicular to the plane). The resulting scattering angle is described as θ. The path difference (orange) is described as $2\delta = n\lambda$. The forming rectangular triangle (green orange, red) is here describing the angle-dependent path difference with $\delta = d \cdot sin(\theta)$. Both expressions combined are giving the Bragg condition (Equation 3.9).[236]
One advantage of scattering is shown in Figure 3.11. With the scattering methods, the whole sample can be analysed and investigated in comparison to other methods, which investigate only fractions of a sample. In Figure 3.11 A different methods are compared. In Figure 3.11 B a sample as an example for the sample size is shown.

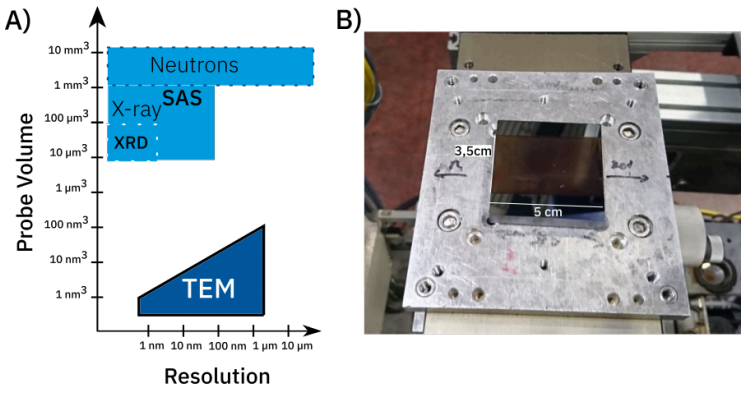

Atomprobe

Fig. 3.11: A) Overview of the used sample size and resolution by different methods in an adaptation [237] B) Example for the size of a sample here Neutron scattering

3.2.2 X-Ray diffractometry

X-ray diffractometry (XRD) is a tool for identifying the crystal structure of a solid material, a powder or a single crystal. For this method, the scattering theory is applied to crystal lattices. Here, the used X-rays have the wavelength of the crystal lattice distance and are scattered quasi-elastic at the electron hull of the lattice. With that, the inverse scattering vector matches the typical crystal plane distances.[228, 229] The main assumptions of the X-ray diffraction should be listed:

- Atoms in a crystal lattice should be arranged periodically
- The X-ray wavelength is around the same magnitude of the interatomic distance inside a crystal
- X-rays are elastically (or quasi-elastically) scattered
- The crystal should be seen as infinitivly thick (or thicker, than the penetration depth)

Besides other X-ray powder diffraction methods (like, e.g. Guinier or Debey-Scherrer) the most used method today for analysing the crystal structure is the Bragg method with a *Bragg-Brentano* Gonimeter.[238] Here a goniometer with an X-ray source and a detector is used, and the reflected X-rays are observed.[228] The benefit of this method is the possibility to implement

detector optics and reduce unwanted diffuse scattered signals or eliminate other wavelengths generated by, i.e. X-ray fluorescence of the sample with a filter. Additionally this geometry enables further measurement techniques like, i.e. X-ray reflectivity. Furthermore, a good resolution and high intensities are achieved.[228, 229] A schematic image of the Bragg-Brentano Goniometer is shown in Figure 3.12

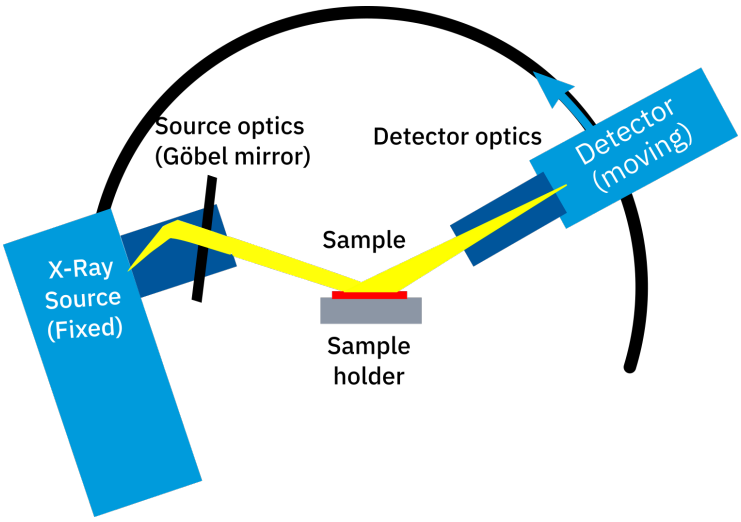

Fig. 3.12: XRD Goniometer equipped with a Göbel mirror[229].Here in an ansymetric mode with a fixed source and a moving point detector is shown.

For investigating thin films by a symmetric XRD technique, with a limited thickness of around 200-1000 nm, the penetration depth of an X-ray beam is surpassed and also signals from the substrate will be visible. Besides the additional signals from the substrate, the sample peaks will have a low intensity, and a poor peak to background ratio.[239, 240]So an asymmetric XRD technique needs to be used. In this technique, the X-ray source is kept fixed at a low indecent angle (usually α<3°), and the detector is moving at the goniometer (see Figure 3.12). To illuminate the whole sample a Göbel mirror for the parallel beam focus is used.[229] In addition the beam is limited and directed by the source optics. For this technique, the detector needs to be a point detector for analysing the line focus of the incident beam. The method is called the gracing incident X-ray diffraction (GIXRD).[222, 229, 239, 240] Atoms in a crystal are not at a fixed point. Atoms are constantly in a fluctuation, which is temperature-dependent.[228] Furthermore, temperature-dependent phase transitions are occurring. These mentioned events are observable in the XRD pattern. The atomic fluctuation leads to a reduction

of intensity.[228, 229] Furthermore, an influence on the lattice parameter (or unit cell size) is observable. With that on the peak position in an XRD pattern is shifted towards lower angles with higher temperatures. (Shown in Figure 3.13)

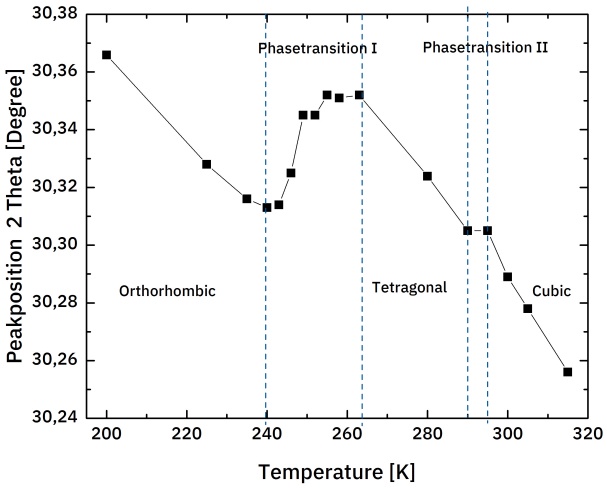

Fig. 3.13: Example for a phase transition and the merging of 2 signals

Here the peak position is shown as a function of temperature. A linear peak shift towards lower angles with increasing temperature is observable. Furthermore, this linear peak shift is discontinued by the phase transitions. A phase transition is usually characterised by a decrease in the number of signals towards higher temperatures. The origin can be found in a higher symmetry with increasing temperature for a high-temperature phase.[241] To evaluate the resulting data, at first, they can be compared to literature data. In a more sophisticated step, with the knowledge of the phase and the space group, the Lebail method can be used to determine the unit cell, the profile parameters and the peak intensity. For this purpose, an algorithm is used, which fits the measurement with the preset, expected phase.[242] An even more sophisticated method is the Rietveld refinement. Additionally to the profile parameters, it is used to separate overlapping signals, and fit the multiple phases in one system.[243] So also, the preferred orientation can be determined. If the phase is unknown or additional unknown phases are involved, the refinement methods are not suitable. One additional way of investigating a known phase with unknown overlapping phases is to use the known Miller indices (hkl) and calculating the lattice parameters a,b,c.

For the cubic crystal structure (in this case the highest order and for this reason the most straightforward pattern) this can be done by the following formula.

$$d_{hkl} = \frac{a_0}{\sqrt{h^2 + k^2 + l^2}} \tag{3.10}$$

A different method for analysing the phase transition of similar crystal structures (like, i.e. the perovskite structures) is the pseudocubic approach.[244] In this approach, one is assuming, that the overall change in the crystal structure is sufficiently small, so a transition from orthorhombic to tetragonal to cubic can be seen as an increase in the volume of the phase with the highest symmetry (cubic phase). As a result, one is obtaining by excluding the phase transition region a straight line, which represents the continuous lattice expansion.
As mentioned above, one of the major assumptions of the XRD concerns the theoretical infinitive thickness of the crystal. A nanoparticle is limited in size and in a crystal lattice, which leads to a reduction in parallel lattice plains. This causes a decrease in the correlation between nearby atoms as their separation increases, which leads to a peak broadening.[245] Furthermore, the particle and crystal distribution adds up to a further broadening of the signal.[246] For crystal sizes L< 100 nm, the Scherrer Equation is given by [246] [247]

$$L = \frac{K \cdot \lambda}{\Delta\,(2\theta) \cdot \cos\theta_0} \tag{3.11}$$

Where L is the size of a crystal, perpendicular to the lattice plane, K is the Scherrer-form ($K_{cubs/cuboids}$=0.89) factor, λ the used wavelength and θ_0 the Bragg angle).[246]
With its high detection angles, the XRD is a powerful method for determining the crystal structure under different conditions at an atomic level. For investigating expanded structures, other methods with smaller angles need to be used like X-ray reflectivity or small-angle x-ray scattering.

3.2.3 X-ray reflectivity

In comparison to XRD, in X-ray reflectometry, small angles of the incident and detected X-rays are investigated. The X-ray reflectometry delivers information about the Z-axis of the sample. Here, the surface or interface of a material and in general expanded structures in comparison to the XRD is of interest. The basic idea is the measurement of the reflected intensity as a function of the reflected angle. Withal solely the specular reflection of the X-rays is considered, so the incident angle and the reflected angle are assumed to be equal.[233, 248] Similarly to the XRD the different pathways of the reflected beams can interfere constructively or destructively and can be described by the Bragg condition.[233] For the measurement, a Bragg-Brentano goniometer with a Göbel mirror is used, similar to the GIXRD measurement. Additionally a point detector and low angles (typical 0.05-5°) are used.
If a light beam passes through the material into another material with a different refractive index, the light reflects partly and transmitted at the interface. Here the Fresnel law describes the reflection.[198]
For the X-ray reflectivity (XRR), the same principle is applied. For X-rays, the refractive index is generally less than 1.[233, 248] A influence on the refractive index is derived from the scattering length. For this reason, the focus of X-Ray scattering is on the difference in scattering length, which further is responsible for the contrast in this method.[233, 249] The scattering length (b) is an element-specific coefficient, which describes the scattering power of X-rays or neutrons.[233] Furthermore, the scattering is dependent on the physical density of the material. Therefore the coefficient is called the scattering length density (SLD).
If a material consists of multiple atoms, the relationship of the $SLD_{1,2}$ can be described for a two-atom system with:

$$SLD_{1,2} = \frac{V_1 \cdot SLD_1 + V_2 \cdot SLD_2}{V_1 + V_2} \tag{3.12}$$

Here V is the volume of the atom 1 and 2 in a unit cell and the SLD of each of the atoms (1& 2).
The basic principle of reflectometry is described for an infinitive, thick layer and with that a single interface with no roughness in Figure 3.14. With

that, the incident beam $\overrightarrow{K_i}$ gets reflected under the incident angle α_i at the interface of the material. One part of the beam gets transmitted $\overrightarrow{K_t}$ into the sample, and the other gets under the scattering angle α_s reflected $\overrightarrow{K_s}$. The observation here is perpendicular towards the sample and described as scattering vector $\vec{q_z}$ (the relationship is described with $q = \frac{4\pi sin(\theta)}{\lambda}$) see Equation 3.7). The scattering at the surface is illustrated for a single layer without roughness in Figure 3.14

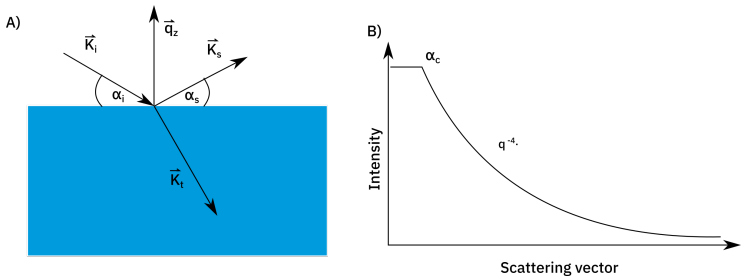

Fig. 3.14: A) Example for an infinitively thick sample layer with a single interface and no roughness. With the scattering vector K_i as incident beam,K_s as scattered beam, K_t as transmitted beam, q as scattering vector and the angles α_i and αs as indecent and scattered angle B) the resulting measurement described as an intensity over the scattering vector with a ideal case of a decay of q^{-4}

The reflection can be further described with the Snell's law, which is given with [198, 202]

$$n_1 \cdot \cos\alpha_{in} = n_2 \cdot \cos\alpha_{tra} \tag{3.13}$$

Here n is the refractive index (in a vacuum n=1) and α the incident and transmitted angle. At angles below the critical angle, α_c the beam gets completely reflected. (see Figure 3.14) This condition can be described with $\alpha_{tra} = 0$ (and the assumption of the incident beam is in a vacuum, so the refractive index $n_1 = 0$) which leads to:

$$\cos(\alpha_c) = n \tag{3.14}$$

So the critical angle of a one-layer system is only dependent on the refractive index of the material.
For a multilayer system, the reflection inside the material is observed. An

intrinsic reflection and oscillation can be used to obtain information about the interfered layers. With that thickness, interlayer roughness and the SLD of the different layers are accessible. Systems of that kind are more sophisticated than a single layer. An example of a multilayer system with its oscillating wave is shown in Figure 3.15

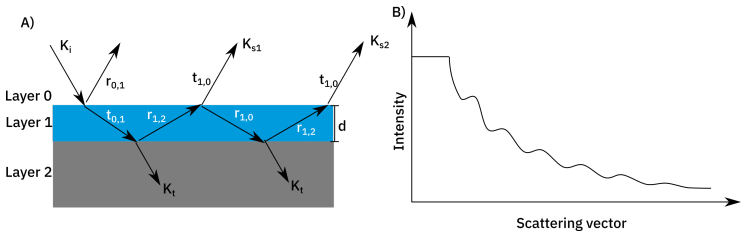

Fig. 3.15: A) Multilayer system i.e. air, sample, substrate with the propagation of the reflection B) resulting reflectometry pattern

The first pathway of the incident beam until the reflection at K_{s1} ($r_{K_{s1}}$) can be described as the following [222]:

$$r_{K_{s1}} = r_{0,1} + t_{0,1} \cdot r_{1,2} \cdot t_{1,0} \cdot \exp\left(-2ik_1 d\right) \tag{3.15}$$

the vectors of the reflection $r_{n,m}$ and transmission $t_{n,m}$ can be seen in Figure 3.15.Here, n is the origin layer and m is the incident layer. Additional the exponential of $(-2ik_1 d)$ describes the change of the wave vector by passing mater. Which includes the wave vector $k_1 = \frac{2\pi}{\lambda}$, and d the thickness of the sample. As a result, the Parratt algorithm [250, 222] is derived as :

$$r'_{N-1,N} = \frac{r_{N-1,N} + r_{N,N+1} \cdot exp(2ik_N d_N)}{1 + r_{N-1,N} \cdot r_{N,N+1} \cdot exp(2ik_N d_N)} \tag{3.16}$$

By that Parratt considered the multilayer system as a single layer system and assumed, that only the reflected signals are adding to the resulting diffractogram. Afterwards, an iteration to higher layers is executed to form the whole diffractogram.[250, 233]
No surface is perfectly smooth. Therefore a surface roughness needs to be taken into account. This roughness leads to a falsification of the results. The influence of the surface roughness on the reflectivity r_{rough} can be described as.[233]

$$r_{rough} = r_{smooth} \cdot \exp\left(-2K_i \cdot K_t\sigma^2\right) \tag{3.17}$$

With r_{smooth} the reflection of a perfectly smooth surface, K_i as the incident vector, K_t as the transmitted vector and σ the roughness.[233]

With all this background, the analysis of the data is challenging. The illustrated limitation of Figure 3.15 shows a two-layered system with two different scattering length densities. The beam intensity scattered at the first surface with the path K_{s1} and the beam scattered at the second surface with the path K_{s2} are convertible. By this, the resulting diffractogram will show the same for both cases. Therefore no unique solution can be found. Previous to the analytical method a simulation needs to be run for limiting the fit parameters.[222, 251] The X-ray absorption for heavy atoms may lead to an error. This can be verified by a complementary method with a non-absorbing incident beam, like in neutron reflectometry. An additional challenge by analysing the data is found in the uncertainty of the source of the signal.[252] A complementary method for this method is neutron reflectometry.

3.2.4 Neutron scattering/Neutron reflectometry

Neutrons are neutral elementary particles, which are found besides protons in the core of every atom. By radioactive decay of the element ^{235}U in a nuclear reactor or the target bombardment of protons at a spallation source, free neutrons are generated and can be used as a beam for investigating materials.[229] These neutrons are moderated. For the interference with the matter, thermal or cold neutrons are used. In nuclear fission, hot neutrons are generated, by passing them through a cold source like 20 K deuterium, the neutrons lose parts of their energy by inelastic scattering. A distribution of cold neutrons is the result. These free neutrons than are conducted to the experiment by a beamline.[229] The wavelength of a neutron is determined by the expression $\lambda = \frac{h}{m \cdot \mu}$ with h as Planck's constant, m the mass of a neutron and μ the velocity of a neutron.[249] Neutrons are neutrally charged particles, so electromagnetic interference is not possible. To access a monochromatic

wavelength either a chopper or a monochromator (single crystal with Bragg reflection in a defined angle) are used.
Neutron scattering is a complementary method for X-ray scattering and in this case for X-ray reflectometry. The scattering of neutrons is comparable to the scattering of X-rays. However, in comparison to X-rays, neutrons get scattered at the nucleus of an atom. Since the possibility of a scattering event on a nucleus is by some magnitudes smaller, that the scattering on an electron shell, the penetration depth of the neutrons is significantly higher.
As for X-rays, the difference in scattering lengths of different elements is responsible for the contrast in the diffractogram. A scattering relevant difference between X-rays and neutron is the difference in scattering length. For example, the X-ray scattering length for hydrogen at a wavelength of λ= 1.5 Å is b= $0.431 \cdot 10^{-12}$ cm. For neutrons, on the other hand, the scattering length is wavelength-independent and has a value of b= $-0.374 \cdot 10^{-12}$ cm. Additionally to that the scattering length is further dependent on the isotope. The most famous example is hydrogen and deuterium.[249] The absorption of neutrons is usually much smaller than the absorption for X-rays. For the here investigated elements, the absorption of neutrons can be seen as insignificant.[249]
The detection of neutrons is more challenging than the detection of X-rays. Direct detection of neutrons is because of their non-ionising properties not possible. The detection can only occur indirectly. For this purpose, a tube is filled with ^{3}He. A neutron is interacting with the ^{3}He according to the following equation [253]

$$^3_2\mathrm{He} + ^2_0\mathrm{n} \longrightarrow ^3_1\mathrm{He} + ^1_1\mathrm{p} \tag{3.18}$$

The resulting proton is then detectable by a discharge.
With that, the scattered neutrons are detected, and the resulting diffractogram can be compared to the complementary X-Ray method.

3.2.5 Small-angle X-ray scattering

Small-angle X-ray scattering (SAXS) is investigating materials up to the 100-nanometre scale often in dispersion.[237] In contrast to the previously

discussed methods, the SAXS measurement here is performed in a transmitted mode. For this measurement, the incoming beam should be monochromatic, coherent and collimated to a point focus or line focus. The point focus benefits in comparison to other methods in easy, understanding of the method, data reduction, and analysing procedure but a less intense primary beam.[237]. For reaching this spot focus pinhole collimation or a Kratky collimator can be used. The last-mentioned collimates the beam with rectangular blocks of metal. The Kratky collimator further makes also a line-shaped focus possible.[254, 255] To reduce scattering of the atmosphere the collimation section is kept under vacuum.
The sample is filled in a closed capillary and placed in the sample environment in which the desired condition (i.e. temperature) is kept constant for the measurement. After the primary beam passes the sample environment, the evacuated sample-to-detection section or flight tube is entered. This part is necessary to reach a sufficient separation of the primary beam and the scattered signal. After this passage, the primary beam is blocked at a beam stop to prevent the detector from damage. The scattered beam gets detected on a 2D-CCD-Detector. The result is shown in Figure 3.16 on the detector side. The black spot results from the beam stop and the slightly smeared scattering signal is forming a circle around the shadow of the beam stop. (See Figure 3.16)

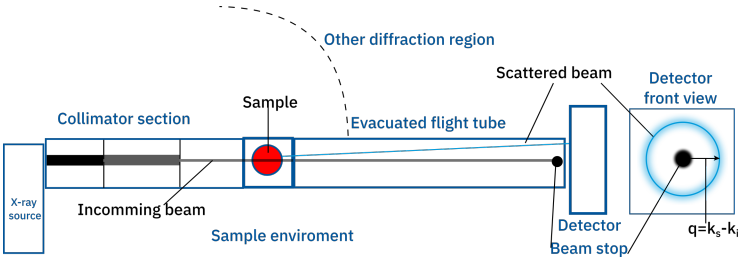

Fig. 3.16: Scheme of a SAXS instrument with X-ray source, collimator, sample environment, flight tube and detector additionally the angle of different scattering methods (i.e. XRD) are shown. In a adaptation of [237]

After the data collection, the signals are averaged and transformed by area integration from a 2D SAXS diffraction pattern to a 1D diffraction pattern. Even with the best available instrumentation, several data correction steps need to be performed to recover the true scattering cross-section. These errors result from the general properties of the sample and the detection system. Typical corrections are spherical correction, polarization correction

and the sample self-absorption. To name more significant correction the background correction, dark current, dead time correction and scaling to absolute units should be mentioned.[237] The general process of the data reduction should be just mentioned at this point. In order to perform the process of the data reduction and correction "*...a high level of instrument understanding and characterizations is needed, which cannot be provided by a casual user.*"[[237], page.7, paragraph 3] The results of the process are shown in Figure 3.17 where A) represents the raw data and B) the reduced and corrected data and C) represents the last step of analysing the SAXS data, the data normalization and the subsequent fit.

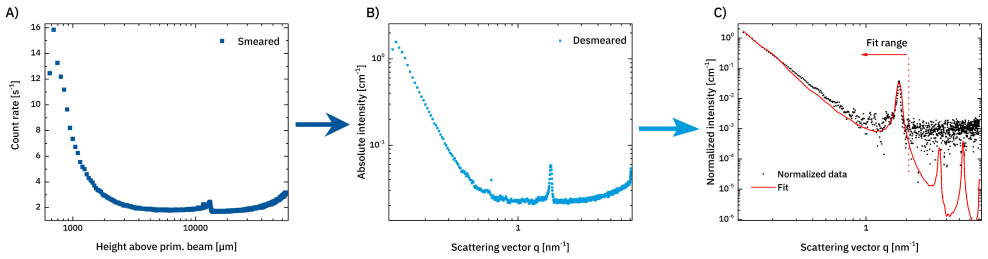

Fig. 3.17: Data redurction example A) Raw Data B) fully corrected and reduced data of the raw data C) normalized and fitted dat

To now analyse the reduced and corrected data, the data first has to be normalized to the fit. The choice of fit is based on previous measurements to determine, i.e. the size, shape, and the surface of the sample. The decay, eventual peaks and other features give information about the sample. The full diffractogram can be divided into three main fitting regions, the Guinier, Fourier and Porod region. Each of the regions contains different information about the investigated sample.[235, 256] The software SASfit executed the data reduction and the fitting with its fitting algorithm. A further description can be found in literature.[257]

3.2.6 Transmission electron microscope

Even though on first sight microscopy has seemingly no connection with x-ray or neutron scattering, the principle of electron scattering underlays a similar background. The electron scattering is based on the matter-wave theory.[258]

The used wavelength limits the general resolution in microscopy. Visible light could therefore not resolve sizes beneath 200 nm.[259] A transmission electron microscope (TEM) is using therefore electrons with wavelengths depending on the acceleration voltage (e.g. commonly used acceleration voltages 200 kV = 2.5 pm ; 300 kV = 1.9 pm). By this method resolution of nanostructures and even atoms up to around 0,045 nm are possible.[260] A limiting factor of this method is optical aberration.[261]
The working principle of a TEM should be briefly discussed in the following. A more profound description can be found in literature.[262, 263, 264] As the name of the method name suggests, the basic concept is resolving the transmitted electrons of a sample in an imaging method. The sample needs to be thin enough (typical 100 nm) for the electrons to transmit or the arrangement of nanoparticles needs to be in a monolayer.
The main structure of a TEM is usually constructed in a high-vacuum tube. At the top of the tube is the electron source, a cathode. The Wehnelt-cylinder with a negative potential, surrounding the cathode is focusing the electrons towards a hole in the cylinder. An anode is accelerating the electrons. An electron beam is generated. The now generated electron beam becomes further focused by the electron lenses towards the sample.[262]
The sample is prepared on a so-called TEM grid, a metal grid covered with a layer of carbon. The majority of the electrons are transmitted through the sample. However, a portion of electrons is interacting with the atoms of the sample. This interaction is divided into elastic, inelastic scattering and secondary effects.[265, 266] In this process, an attenuation or a deviation of the electrons is observable, and contrast is generated. It is to mention that the inelastic scattering is dependent on the atomic number of the atom. A higher number results in a stronger and more probable scattering.[262] The scattering of the electrons leads to a contrast. Stronger scattered regions appear darker in the resulting image.
After the interaction with the sample, the electron beam gets directed and collimated towards a fluorescent screen. An image becomes visible. For permanent detection, a photo film or these days a CCD-Camera is used.
By applying a fast Fourier transformation (FFT) on the regularly arranged sample, the scattering information is getting revealed. So information about the size and shape of an array of nanocrystals can be made. This is shown in Figure 3.18

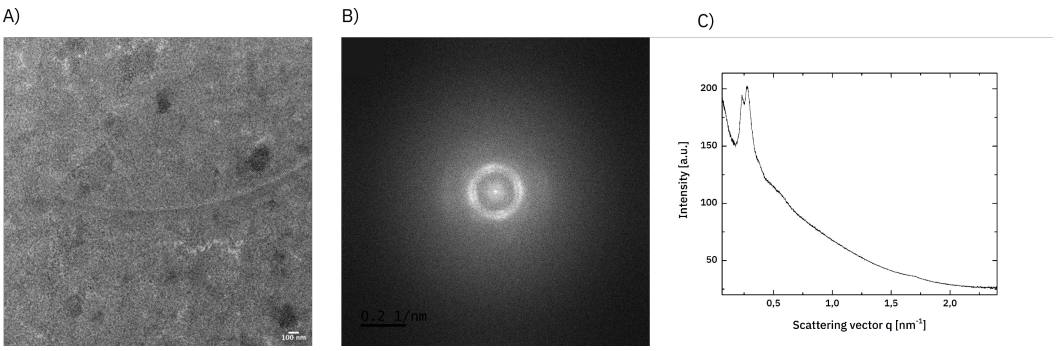

Fig. 3.18: A) TEM-Image of cuboid nanocrystals B) The resulting FFT C) The resulting area integral of the FFT

The process for analysing the shape and size of nanocrystals is shown in Figure 3.18. The resulting integral resemble a typical scattering pattern. This shows the similarity of this method to the other here mentioned small-angle scattering techniques. Furthermore, in a higher resolution, the FFT can be used for getting information about the interatomic distances and reveal information about the crystal structure.[262]

3.3 Thermal analysis

In this section, the thermal analysis methods will be discussed. With these methods, the temperature-dependent behaviour of a material is investigated. For example, phase transitions or thermal decomposition of a sample can be observed. It is essential to mention that with the thermal analysis, often only quantitative results are acquired, so further supporting methods are needed.

3.3.1 Thermogravimetric analysis

The thermogravimetric analysis (TGA) is commonly the first measurement method for analysing the thermal properties of a sample. The purpose of this method is here the determination of the decomposition temperature and obtain first insights into the behaviour of the material. These data are beneficial for further thermal investigation methods, to prevent decomposition

and contamination of other devices. The general observation of this method is the temperature-dependent weight change under a constant temperature ramp or scan rate ($\frac{dw}{dt}$).[267] Therefore the TGA is equipped with a sensitive balance and a furnace. The whole measurement is carried out under a constant gas stream. Resided protective gases like in this case, nitrogen. (See Figure 3.19 A) Before the measurement, the weight of the crucible and the sample is defined as accurately as possible. Afterwards, the furnace is flushed with protective gas, and the temperature program is started. The temperature program is usually a linear heating curve to a high temperature (here up to around 550°C). At a constant weight, the thermogram will show a horizontal portion or plateau. At a specific temperature, a change of the sample may occur, and this will lead to a change in the sample weight. In the thermogram, this will show a decrease in weight against temperature. Often a second plateau is reached, which indicates a stable intermediate compound at this temperature. In most cases, not all elements in a sample are volatile, and after reaching the preset temperature maximum, the crucible contains non-volatile decomposition products.[267](See Figure 3.19 B))

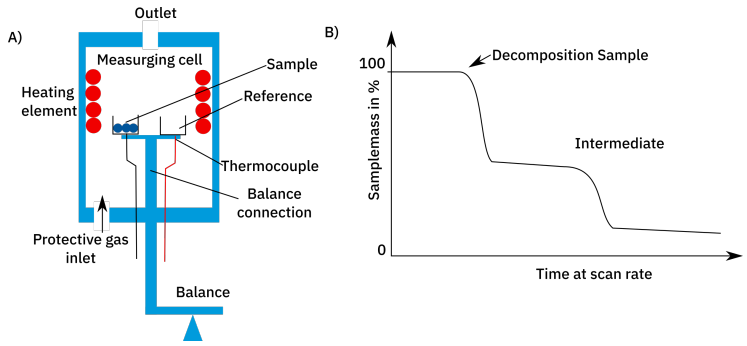

Fig. 3.19: A) Cross section of a thermo balance B) schematic thermogram

To get more insight into the behaviour of the sample, commonly a *differential thermoanalysis* (DTA) is implemented. Therefore the change in heat flux between the sample and an empty reference holder is measured during the whole temperature program. With this method, an endothermic or exothermic behaviour of the sample can be detected.(For more details see subsection 3.3.2 Differential scanning calorimetry)[267] An even more sophisticated system is the combination of the TGA/DTA with a mass spectrometer or an infrared spectrometer, to directly detect the released chemicals of the reaction passing the outlet. However, this should be just mentioned at this point and was not used in this thesis.[267, 268]

3.3.2 Differential scanning calorimetry

The differential scanning calorimetry (DSC) or scanning heat flux calorimetry is a subsequent method for analysing the thermal behaviour of the sample. The purpose of a DSC analysis is to get information about the thermal behaviour of the samples and their reversibility.
In comparison to the TGA, not one linear temperature is used, but several cyclic temperature programs are used. With that, the reversibility of the thermal-behaviour is investigated. Furthermore, in focus of this temperature program is the avoidance of the material decomposition. During the measurement, the heat flux of the system in comparison with a reference is measured, similar to the DTA measurement (mentioned in subsection 3.3.1). In Figure 3.20, a schematic drawing of the sample chamber is given.

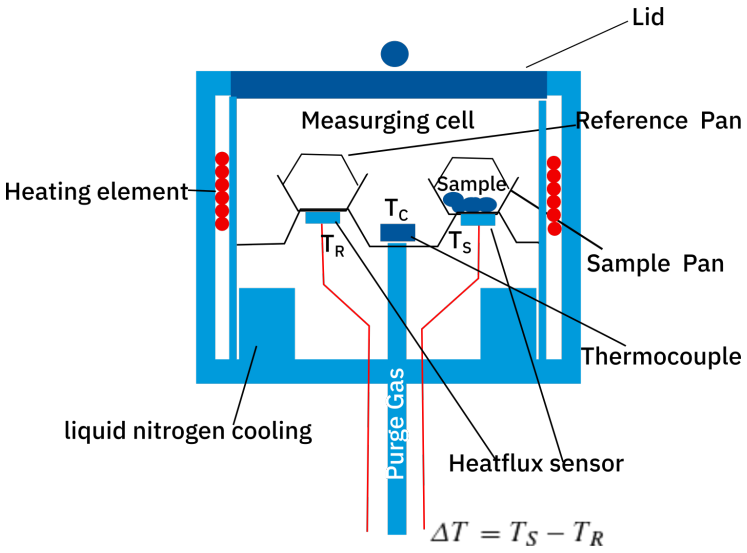

Fig. 3.20: Schematic illustration of a heat flux DSC cross-section

In Figure 3.20 is a reference crucible and a sample crucible and the thermocouple of the measurement cell (T_C) to monitor the temperature inside the chamber represented. The elementary parts of the DSC are further illustrated with the heating and cooling elements and the heat flux sensor. The last mentioned sensors are the core of the measurement system, the heat flux sensors (marked as T_R and T_S) will monitor the heat flux over the temperature program and will result in $\Delta T = T_S - T_R$.
The sample and the empty reference cell is placed in the measurement cell, and a temperature program is started. The temperature will now increase or

decrease with a previous program scan rate and the temperature change in the measuring cell will then be linear in time. Thereby the heat capacity of the sample is described as a proportionality factor with C_p, and the heat flux is described as Φ_{Cp}.[269]

$$\Phi_{C_P} = C_P \cdot \frac{dT}{dt} \tag{3.19}$$

The measured heat flux depends on the differential heat capacity and the scan rate. Thereby additional to the heat flux of the sample $\Phi_r(T,t)$ two more terms are included in the measurement result. The first is the asymmetry of the DSC $\Phi_0(T)$ and the second is caused by the difference in heat capacity of the sample and the reference sample (in this case an empty crucible).[269]

$$\Phi\left(T,t\right) = \Phi_0\left(T\right) + \Phi_{Cp}\left(T\right) + \Phi_r\left(T,t\right) \tag{3.20}$$

The first two terms are defined as "baseline". The temperature gained from the heat flux sensor is an estimated temperature since the sample is placed in a crucible and has no direct contact with the heat flux sensor.[269] So the accuracy of the measurement will be dependent on the heat conductivity of the used crucible. Furthermore, are small temperature gradients inside the temperature chamber observable, which further leads to an asymmetry of the difference calorimetry. The asymmetry of the DSC $\Phi_0(T)$ is set to zero by measuring the reference crucible against an empty sample crucible previous the first sample measurement.[269]
The heat capacity of the sample Φ_{Cp} can be assumed to be constant (insufficiently small temperature changes) and additionally in comparison to most phase transitions or reaction signals turns out negligible. Furthermore, Φ_{Cp} got no significant time dependence.[270] So the Φ_r is the only variable, which is changing over time. As a result, a signal in the thermogram is present.
In Figure 3.21 A) an illustration graph of the signals of the heat flux sensors and the resulting measurement curve B is given.

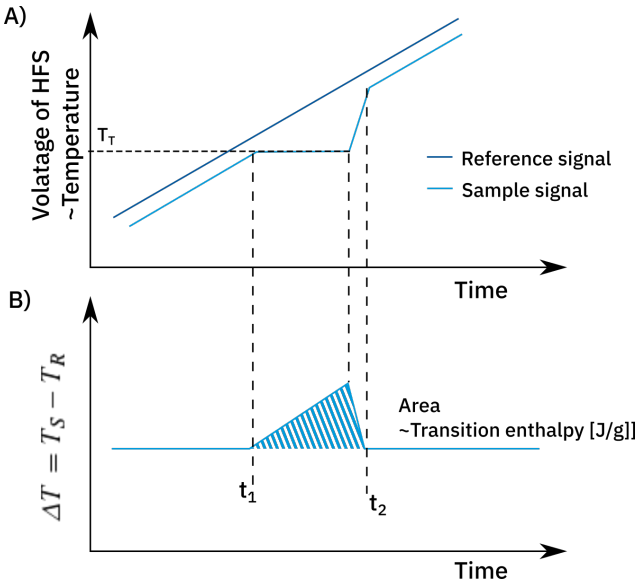

Fig. 3.21: A) Voltage change in the heat flux sensor (HFS) (propotional to the temperature) against time (by a given scan rate) marked T_T transition temperature B) The resulting signal in on the scan with t_1 as temperature onset and t_2 as temperature offset) in a adaptation of [269, 271]

Here a change in the voltage of the heat flux sensor (HFS) which is proportional to the temperature at the transition temperature (T_T) of a substance at a certain time in the temperature scan is observable. This can be translated into the Figure 3.21 B) a graph with ΔT against time, with a clear signal with a transition onset (t_1) and a transition offset (t_2).[269]
The detected heat flux is caused by the release or absorption of enthalpy of the analysed substance. Therefore endothermic or exothermic processes could be observed. In Figure 3.21B) this is indicated by an increase of temperature in the sample in comparison to the reference crucible. The DSC measurment gives two main informations about a sample. There is first the temperature at which the phase transition is occurring and secondly the amount of heat flux, which resembles the enthalpy of a substance. For determine the temperature two significant points of a peak can be used, the peak onset and the peak maximum. The peak onset temperature (t1 in 3.21) is used for the determination of the phase transition for highly pure substances. In broad signals caused by materials containing several different elements, the peak onset cannot be determined. In this case, the peak maximum is used for determining the phase transition temperature.[269]. The area beneath the peak resembles the total heat flux in mW/mg, which can be further used for calculating the transition enthalpy in J/g.

With the *Gibbs-Helmholtz equation* $\Delta G = \Delta H - T\Delta S$ the entropy of the system can be calculated. This is possible, since by definition at a phase transition $\Delta G = 0$.[269]
The peak shape and position is furthermore mass and scan rate dependent. The reason for the signal shift with different scan rates can be found in the general property of a phase transition. Phase transitions need time. The higher the scan rate, the less time is present for the sample to undergo a phase transition in comparison to the reference crucible. Additional to that the heat needs to pass through the whole sample, which is not the case during a high scan rate.
Nevertheless, the effect of the peak shift is a linear phenomenon.[269] The heating and cooling cycles additionally have another source of information. With that, the reversibility of a system can be seen. Additional information about a thermodynamic hindered process can be made. For example, if the melting point in a heating curve differs a lot from a crystallisation point in a cooling point a thermodynamic hindered phase transition (i.e. supercooling) might be the explanation.[269]

4

Phase transition and optical properties of $MaPbBr_3$ nanoplatelets

> *The road to hell is paved with good intentions*
>
> — **Samuel Johnson**
> English writer

The main focus of this chapter is on the methylammonium lead tribromide ($MaPbBr_3$) nanoplatelets. The bulk material is at room temperature in the cubic structure with a band gap of around 2.3 eV[272]. This band gap is not optimal for the usage in solar cell applications, but applications like LED's or photodetectors are described in literature [273, 274, 275]. Nevertheless, it is an advantageous material for investigating the properties of the perovskite structure in nanosize dimensions. The synthesis of the nanoplatelets is fairly easy, and the stability in comparison to the methylammonium lead triode layer or bulk material is fairly high.[276]
In this chapter, the focus is on the investigation of the phase transition of the described nanoplatelets analysed by thermoanalytical methods and temperature-dependent x-ray diffraction. Temperature-dependent photoluminescence measurements are provided to support these findings. All measurements lead to the result of an unusual shift of the phase transition to around 100 K higher temperatures in comparison to the bulk material. Considering the nanosize of the material, phase transitions towards lower temperatures are expected. Quantum confinement could not be found, even though the size in one direction is limited to a single layer of perovskite surrounded by the surfactant. This hybrid structure might lead to the explanation for the surprising observation of the phase transitions.

4.1 Synthesis

This section is dedicated to the synthesis of the nanoplatelets and the corresponding precursors. Before the synthesis of the nanoplatelets, the corresponding ammonium precursors and ligands need to be synthesised and purified. In a second step, the nanoparticle synthesis via precipitation and further purification steps could be applied, resulting in perovskite nanoplatelets.

4.1.1 Ammonium precursor and surfactant synthesis

The ammonium precursors the methylammonium bromide and N-octylammonium bromide were synthesised in the same way, by an acid-base neutralisation reaction.

For the synthesis of the ammonium compound, the corresponding amine compound was dissolved in water (for the N-octylamine in acetonitrile), and slowly hydrobromic acid (HBr) was added dropwise into the reaction mixture. Then the solvent was evaporated using a rotational evaporator.[117, 277] The resulting white crystalline powder was then dissolved in as little methanol as possible and precipitated in a significantly bigger amount (around 200 times) of diethyl ether. The precipitate was filtered and dissolved in water for a further freeze-drying process. Since a strong acid is used, the reaction is quantitative.[278] The reaction is shown in Figure 4.1

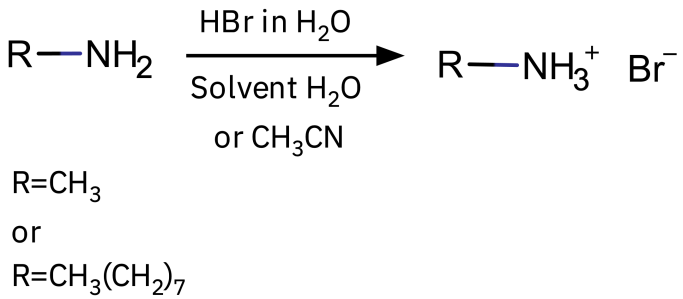

Fig. 4.1: Acid-Base reaction to form alkyleammonium bromide

4.1.2 Nanoplatelets synthesis

The general nanoplatelet synthesis was carried out after a protocol found in literature.[117, 279] Slight changes were applied by to the purification method. For the synthesis oleic acid and the previously synthesised N-octylammonium bromide (OA) was dissolved in 1-octadecen and stirred in a round bottom flask under nitrogen at $80°$C. The precursors lead(II)bromide $PbBr_2$ and methylammonium bromide (MaBr) were dissolved in N,N-dimethylformamide (DMF) and added to the reaction mixture. The molar ratio of the ammonium salts (organic surfactant and methylammonium bromide) and the lead bromide was equal. Afterwards, the temperature was reduced to $60°$C to prevent the evaporation of acetone. Subsequently, acetone was added, and a yellow precipitate was produced. In addition to the procedure described in literature [117], the reaction flask was immediately cooled in an ice bath. The precipitate was separated by centrifugation (7000rpm) at $10°$C. The yellow precipitate was redispersed in toluene and precipitated a second time with acetone. After the redispersion in toluene, the yellow dispersion was stored under a nitrogen atmosphere at room temperature.
The nanoplatelets synthesis is a solvent-induced precipitation method, similar to the described method in *Nucleation and growth of nanostructures*(subsection 2.4.1). The precursors are soluble in the solvent, by adding a precipitation agent (here acetone), precipitation of the product occurs.[22] The perovskite expansion is in 2 dimensions. The long chains of the surfactant are hindering the surfactant from incorporating the perovskite structure. By the surfactant, the growth of the perovskite structure is limited into two dimensions and platelets are formed.[22] Asides the limiting factor, the surfactant further enables the perovskite nanoplatelets to be dispersible in a variety of organic, in polar solvents.[118, 280]

4.2 Results

4.2.1 Transmission electron microscope analysis

As the first method for analysing the synthesised material, transmission electron microscope (TEM) images were recorded and analysed[1]. TEM-images are shown in Figure 4.2

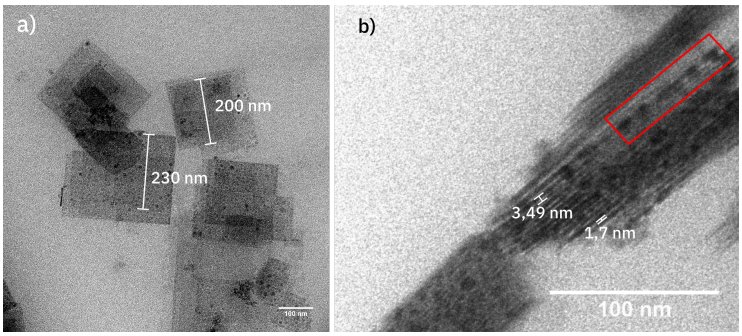

Fig. 4.2: a) TEM images of Nanoplatelets with a size of 200nm-230nm b) Nanoplatelets standing perpendicular to the TEM Grid observable dark and light lines. In the red box spherical ($PbBr_2$) nanoparticles are visible

In Figure 4.2 a) nanoplatelets with a size of 200-230 nm are shown. This is comparable to the findings in literature.[117, 279] Furthermore, it was possible to find a nanoplatelet structure standing perpendicular to the TEM grid. (See Figure 4.2 b) The resulting image is showing light and dark areas in an alternating way. The sizes of the areas were estimated even if the resolution is limited. The estimation results in light areas of around 1.7nm and dark areas of 3.49 nm. It is assumed that the dark areas might belong to the perovskite phase, and the light areas are the organic surfactant (octylammonium). This assumption is based on the consideration of the atomic number of the used elements.
Lead and bromide, as elements of the perovskite structure, have a higher atomic number and a higher possibility to scatter electrons. Therefore fewer electrons pass through the layer, and the image appears dark at this area. In comparison to that, the organic structure of N-octylammonium consists of light elements (hydrogen, carbon and nitrogen) has a low electron density, and the image appears light at the area of the film. In total the contrast

[1]The TEM images were measured by Dr. Andreas Ott

between both layers is high, which leads to a suitable distinction of the layers.[281] (see subsection 3.2.6)
Furthermore, in Figure 4.2 quasi-spherical structures are visible. These were suggested to be perovskite nanocrystals by Schmidt et al.[117] but later the *Feldmann* group suggested the quasi-spherical structures are lead bromide, which further develops due to electron beam damage.[118] Melting of the nanoparticles in the TEM beam [282] and therefore decomposition of the material cannot be excluded. An illustration of the nanoplatelets without the lead bromide particles is given in Figure 4.3

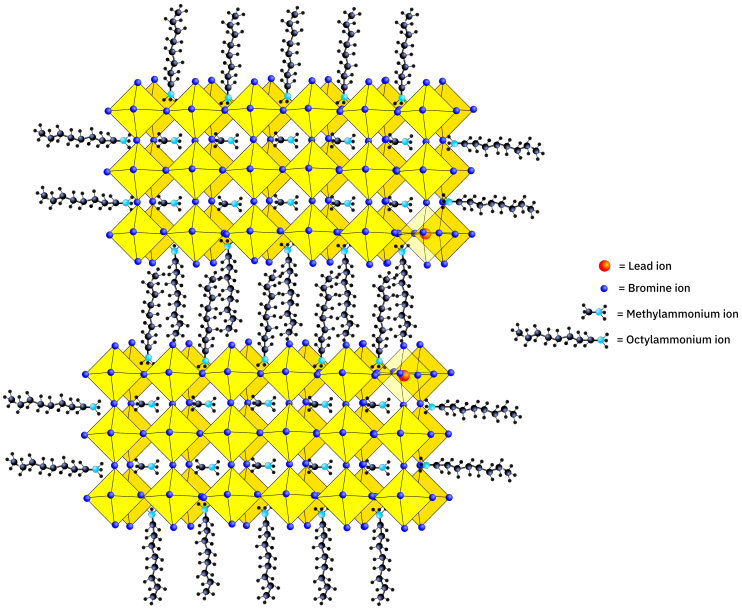

Fig. 4.3: Illustrated image of the perovskite nanoplatelets structure. An extract of two perovskite layers with the surrounding surfactant

Figure 4.3 represents the perovskite structure with the surrounding surfactant octylammonium. The perovskite structure is consists of an octahedral structure, formed by a lead ion as a central atom and surrounded by six bromine ions (shown in Figure 4.3 in the lower corner of the upper nanoplatelet). Four of these octahedra are forming with a methylammonium ion in the centre of the characteristic perovskite structure. Three layers of perovskite octahedra are forming one nanoplatelet. This assumption is made with the knowledge of the typical unit cell size of $a_{Pm3m} = 5.901$ Å [283]. The perovskite structure is surrounded by octylammonium ligands, which fits partly with the "head"-group (ammonium) into the perovskite structure, similar to the methylammonium. Representative of a bigger stack the two structures

show a general interaction between the nanoplatelets and the surfactant. This layer formation is known for the ammonium alkyl structures on nanoparticles [284] and further for the organic surfactant in combination with a perovskite structure [285]. What could not be illustrated, due to the limited dimensionality of a printed thesis, is the Z-axis. Furthermore, not shown is a realistic expansion of the nanoplatelets with a rectangular size of about 200-230 nm in the x-direction.

4.2.2 Thermal analysis

For further investigation, the temperature-dependent stability of the nanoplatelets thermogravimetric analysis (TGA) was carried out first. Subsequently, differential scanning calorimetry (DSC) was accomplished for investigating the reversible, temperature-dependent phase transitions.

Thermogravimetric analysis To determine the decomposition temperature of the sample the TGA was set up with a temperature program in the range of 298-818 K (25-550°C) with a heating rate of 10 K/min under a nitrogen atmosphere was conducted. The resulting thermogram is shown in Figure 4.4

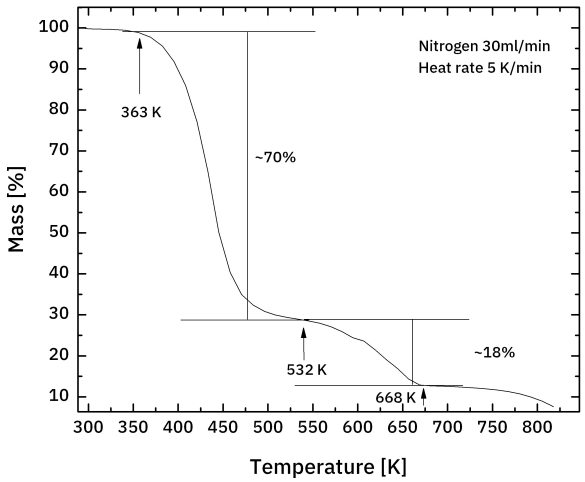

Fig. 4.4: TGA signal with mass loss in precent over temperature

The decomposition of the perovskite nanoplatelets is divided into two distinct steps. The first decomposition occurs with a loss of mass of around 70% starting at 363 K. Subsequently, the loss of around 70% at 532 K a plateau is reached, after which a further decomposition of 18% occurs until 668 K. From 750 to 800 K, a further decomposition is detected, but this shall not be further discussed here.
The decomposition at 363 K with a loss of 70% can be assigned to the decomposition of the perovskite nanostructure and the loss of octylamine, methylamine and hydrobromic acid. With that, a loss of potential water out of the system seems unlikely, but cannot be excluded. It could be assumed that the perovskite layer is not stable without the surfactant and will degenerate to lead(II)bromide. The lead(II)bromide seems to form a stable intermediate phase and degrades further under a release of bromine at around 580 K. This temperature seems to be low for $PbBr_2$ decomposition(literature decomposition: 836 K [286]).However, with a decomposition temperature of 836 K for $PbBr_2$ this might explain the last observed decay. This might be explained by the observed formation of quasi-spherical $PbBr_2$ nanoparticles.[118]
Moreover, as described in subsection 2.3.3 *Phase transition and Nanoparticles on the example of melting point depression* nanoparticles tend to have a temperature shifted phase transition. Additionally, the uncertainty of a possible volatile lead compound formation remains. This might lead to a lead compound with a lower evaporation point, than pure lead bromide.
From the literature [279] a TGA measurement shows that, the results differ from the here observed. This can be explained, by the use of dispersion in octadecane in the literature reference.[279] The process described in [279] would lead to a later decomposition of the sample and a different decomposition process.
In comparison to that, the investigated sample in this thesis was used as a dried, pure powder and not in dispersion with additional octadecane and oleic acid.
Furthermore, the synthesis protocol in this thesis was adapted to form less quasi-spherical $PbBr_2$ nanoparticles, than the described particles found in the literature. This might lead to a different decomposition mechanism.
In comparison to the bulk material, the group of *Nagabhushana* et al.[287] showed the decomposition of the bulk $MaPbBr_3$ at around 570 K and a

loss of around 20% which seems to be similar to the observation made in the measurement above. In general this decomposition might occur, but to determinate the pathway of decomposition by just the weight change of a sample against time at a scan rate with no further information is here not possible. The main focus on this measurement was to determine the decomposition of the sample ($T_{decomposition} = 363$ K).

Differential scanning calorimetry With the knowledge of the decomposition temperature obtained by the TGA, the DSC measurements were carried out. The temperature region between 150 and 360 K was investigated, and a scanning rate of 10 K/min chosen. The measurement was carried out under an nitrogen inert atmosphere, and aluminium crucibles were used. In Figure 4.5 the results of the DSC measurement of the bulk $MaPbBr_3$ powder [2] (from now on referred to as bulk) (black), and the $MaPbBr_3$ nanoplatelets (red) are shown with a heat rate of 10 K/min. The cooling curves are neglected to enhance visibility.

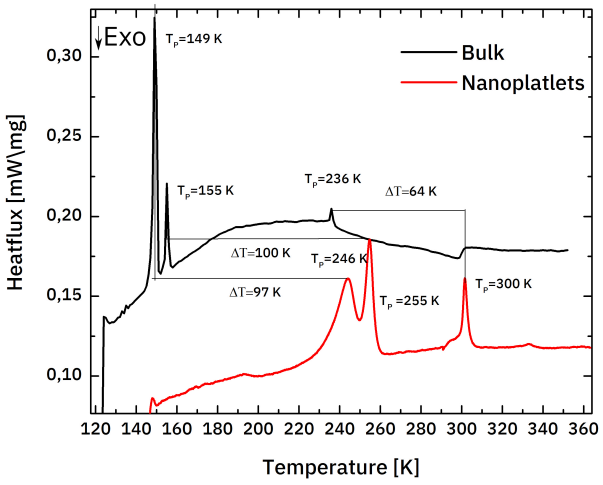

Fig. 4.5: DSC measurement of powder (Bulk) $MaPbBr_3$ and $MaPbBr_3$ Nanoplatelets

On first sight, the phase transitions of the $MaPbBr_3$ nanoplatelets resemble the phase transitions of the perovskite bulk. The bulk shows a phase transition at T_p = 149, 155 and 236 K, which is comparable to the findings in literature [283, 288]. For the nanoplatelets, the phase transition occurs at T_p

[2] Frederike Lehmann provided the results of the powder measurement

= 249, 255 and 300 K. The phase transition, are shifted to around ΔT_p= 97 and 100 K for the first transition and for the second ΔT_p= 64 K. In the DSC measurement of the perovskite nanoplatelets no signal at low temperatures is observable.
The orthorhombic phase (Pna2) is described as the low-temperature phase $T_p < 144K$.[283, 289, 288] In the intermediate phase, the tetragonal phase (I4/mmm) or phases are determined, with a phase transition at $T_p = 149$ K. The tetragonal I phase (I4/mmm) further undergoes a phase transition towards the tetragonal II phase (I4/mcm) of this system. This incommensurable phase [290] has a temperature range of $T_p = 150 - 155$ K to the tetragonal II phase of (I4/mcm) .[283, 288] The high-temperature phase is described as cubic (Pm3m), $T_p > 236$ K.[283, 288] The same profile of the curves are observable for the nanoplatelets. The following Table 4.1 resulting enthalpies and entropies could be found by integrating the transition DSC-Signal.

Tab. 4.1: Phasetransition Enthalpy and Entropy (calculated as described in 3.3.2Differential scanning calorimetry)

Material	Temperature [K]	Enthalpy $\left[\frac{J}{g}\right]$	Entropy $\left[\frac{J}{K \cdot g}\right]$
Bulk	149	-2.14	$1.438 \cdot 10^{-3}$
	155	-0.40	$0.262 \cdot 10^{-3}$
	236	-0.12	$0.005 \cdot 10^{-3}$
Nanoplatelets	246	-2.99	$1.215 \cdot 10^{-3}$
	255	-2.11	$0.827 \cdot 10^{-3}$
	300	-0.89	$0.297 \cdot 10^{-3}$

Table 4.1 implies that, not only the phases are shifted to higher temperatures, but also the enthalpy and entropy for each phase transition are increased. The phase transition of the perovskite seems to be thermodynamically hindered.
This behaviour can be explained by adding the surfactant to the thermodynamic observation. The surfactant is directly bonded to the perovskite structure [22] and for this reason, is adding enthalpy and entropy terms to the phase transition. To elaborate on the results of the DSC measurements further in Figure 4.6, a measurement of the nanoplatelets are shown. During this measurement, the same conditions, as mentioned above, were used. Also, cooling curves are implemented to observe a reversible change.

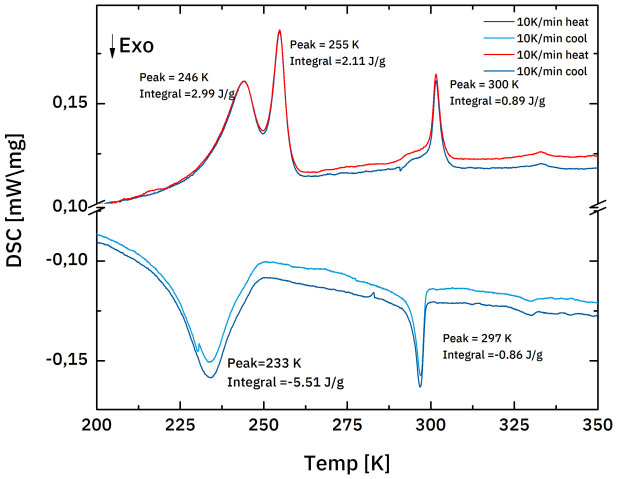

Fig. 4.6: DSC measurement of the nanoplatelets heating and cooling cycle

The DSC-measurement reveals heating and cooling curves which are overlaying each other in large parts of the course. The phase transition temperatures mentioned-above, are also found in this heating curve. Additionally in the cooling curve, the described phase transitions are observable. These are shifted towards lower temperatures.
The overlaying of the signals reveals reversible process of the phase transition. With that irreversible processes like evaporation, decomposition or chemical reactions can be excluded. Furthermore, the shift of the cooling cycle towards lower temperatures is expected.[269]
For the first phase transition at around T_p=246 and 255 K, the possible incommensurable phase is observable. This is not the case for the cooling curve. Nevertheless, the released heat flux can be seen as equal. For the cooling cycle, the incommensurable phase seems to be omitted. Interestingly the phase transition from the tetragonal to the orthorhombic phase (surpassing the incommensurable phase) is shifted towards lower temperatures by around 22 K in comparison to the heating curve. This reveals a stronger thermodynamically hindering of this phase transition and might be in connection with the incommensurable phase.
The phase transition from tetragonal to cubic and vice versa appears at around the same temperature (shifted by around 3 K, which can be explained with the heating rate and the used method see subsection 3.3.2) and the heat flux can be seen as equal. This phase transition seems not to be further

thermodynamically hindered.
For investigating the possible influence of the surfactant on the phase transition, the pure surfactant N-octylammonium bromid was measured under identical conditions. This measurement is shown in Figure 4.7

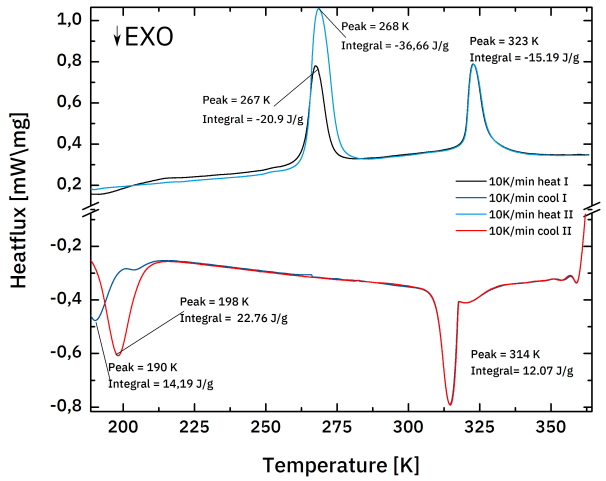

Fig. 4.7: DSC measurement of the surfactant N-octylammonium bromide

The DSC-measurement of the surfactant shows two (around 70 K) shifted phase transitions and two narrow shifted phase transitions. Nevertheless, the phase transitions seem to be reversible. The melting point of N-octylammonium bromide is described in the literature with 408-409 K (207-208°C[291]) and can be excluded to be present in this measurement. The low-temperature phase transition seems to form a supercooled state. This is a known phenomenon for organic molecules with alkyl chains especially for alkyl ammonium bromides.[292, 293] In such a case the movement of the alkyl chain dominates the thermodynamic processes.[294] By reheating the material, energy needs to be transferred to the ordered chains. With that, the shift towards higher temperatures can be explained. The now relative unordered system is more likely to obtain a different phase, with a lower temperature, if further heated. This explains the second signal at 323 K and the cooling curve at 314 K. During the heating and cooling cycles the alkyl chain will orient itself more, so the shift of the phase transition temperatures will narrow down to a single phase transition temperature.
The phase transitions of the surfactant and the perovskite are close. This might add up to the observed phase transitions. In comparing to the phase

transitions of the perovskite nanoplatelets, the pure surfactant has not reached the phase transition temperature yet. However, the overall perovskite/surfactant structure might contain enough energy, so a phase transition from the perovskite might surpass the energy needed for a transition adding the phase transition of the surfactant. As a result, the phase transition of the perovskite nanoplatelets is shifted towards higher temperatures in comparison to the pure perovskite. The opposite is the case for the surfactant. Here the phase transition is shifted towards lower temperatures because the perovskite is forcing the surfactant to undergo a phase transition.

To conclude this part, the decomposition temperature of the perovskite nanoplatelets could be determined. Furthermore, a possible decomposition pathway is described. A comparison to the literature concerning the decomposition was not direct possible since the described TGA measurement of the literature was conducted as a dispersion with additional compounds.
The phase transitions are well defined in the DSC measurement. The thermal behaviour of the nanomaterial strongly resembles the thermal behaviour of the bulk material. The heating and cooling signals are shifted slightly, which indicates zero or a little thermodynamical hindrance of the phase transitions itself. The incommensurable phase, described in the literature, is also visible, but only in the heating curve. For the cooling curve, the incommensurable phase is bypassed. Furthermore, the signal of the orthorhombic $\rightarrow$ tetragonal (containing the incommensurable phase) is shifted in the cooling and heating curve of around 22 K. This indicates a slight suppressed thermodynamically event, which might be explained by the incommensurable phase in which the system bypassed. Comparing the phase transition of the bulk and the nanoplatelets signals concerning their position, the phase transitions of the nanoplatelets seem to be strongly suppressed. A phase transition occurs 100, 97 and 60 K shifted towards higher temperatures.
The big difference between both systems is the interruption of phase transition by the organic surfactant, which leads to the observed differences. The ten-fold higher energies for the phase transitions of the surfactant add up to the conclusions. Furthermore, the surfactant undergoes phase transitions close to where the nanoplatelets phase transition is observed. The surfactant N-octylammonium likely hinders the possible phase transition of the nanoplatelets. This further gets supported by the higher phase transition

energies of the ligand.
However, it needs to be mentioned that the thermal analysis only gives quantitative results and leaves space for interpretation. Other methods need to be chosen to determinate the qualitative results to investigate the material further,

4.2.3 Structural analysis by X-ray diffractometry

In this section, the sub nanosize, crystal structure should be investigated. For this purpose, X-Ray diffraction as a method was used. Furthermore, the temperature-dependent change of the crystal structure is elaborated. Even though nanostructures, have their challenging character in determining the crystal structure, this method delivers essential insights into the previously observed, unusual phases transition shifts to higher temperatures.

For analysing the crystal structure of the synthesised material, the crystal structure was determined by X-ray diffraction (XRD). For this purpose, the powder sample was prepared on a zero background sample holder. A Bragg Brentano XRD (Bruker D8) was used. A region of 10-80° 2θ was investigated.The result are shown in Figure 4.8 A with sharp signals. Additionally for comparison a XRD pattern of nanoparticles synthesized according to a literature protocol is shown.[117, 279] (see Figure 4.8 B) This pattern consists of broad signals, with narrow peaks on top.

Figure 4.8 A, shows the here synthesised and used nanoplatelets. Furthermore, the XRD-pattern of the synthesised nanoplatelets by the protocol found in literature [117, 279] is shown in Figure 4.8 B. The slight change in the synthesis protocol seems to increase the purity of the $MaPbBr_3$ nanoplatelets. The signals of the here (Figure 4.8 A) synthesised nanoparticles are not overlaid by broad signals like in the synthesised nanoparticles by the protocol found in the literature(Figure 4.8 B). The difference between the measurement can be explained by the lower amount of $PbBr_2$ in the here synthesised nanoplatelets.
This fits well with the previous observations made in the TEM-images. (see subsection 4.2.1) The TEM-Images reveal nearly no quasi-spherical $PbBr_2$ nanoparticles.

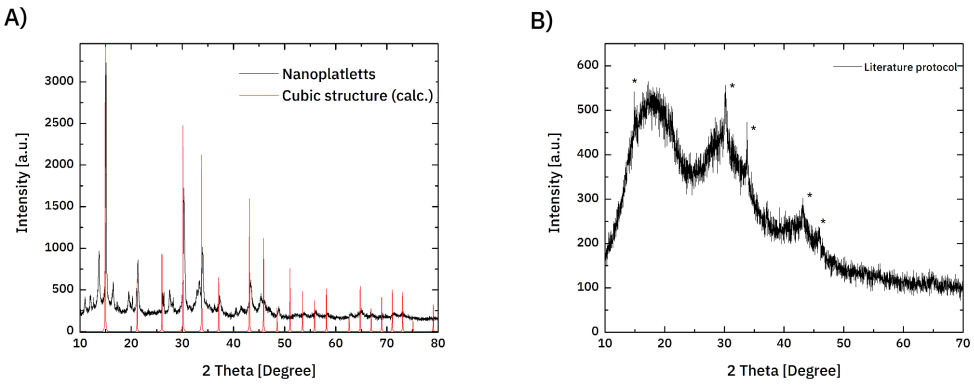

Fig. 4.8: A)Room temperature XRD measurement of the nanoplatelets sample (black) with the calculated structure of the cubic phase (red)[283] B)Room temperature XRD measurement of the nanoplatelets synthesized with the protocol, found in literature [117, 279] * makes possible $MaPbI_3$ signals

The cubic perovskite phases serve as an example structure to analyse the following data. This is done to simplify the analysis of the system. The cubic crystal structure is the highest order in the perovskite crystal structure family, and therefore the simplest resulting pattern for the example-structure. Furthermore, the cubic crystal structure is formed at room temperature. In addition, the tetragonal phase and the orthorhombic phase differ only slightly in structure and can be discussed in comparison to the cubic perovskite crystal as pseudo cubic structures.[244] [283, 295, 296] The cubic-phase (α=5.901 Å, Phase= Pm3m) described in the literature [283] agrees with the XRD pattern of the nanoplatelets. It seems that the peaks of the measured sample are shifted to higher angles.

Nevertheless, in the presented XRD-pattern here, more signals than expected are visible. These signals could not be assigned or found in the literature. However, as is known from the TEM-Images and the SAXS measurement (discussed later), the structure features a contrast in scattering of electrons and X-rays, which indicates the presence of the surfactant. Therefore measurement of the pure surfactant was performed, even though the arrangement in lamellar structures of the surfactant cannot be recreated without the perovskite as a template. (see Figure 2.16)

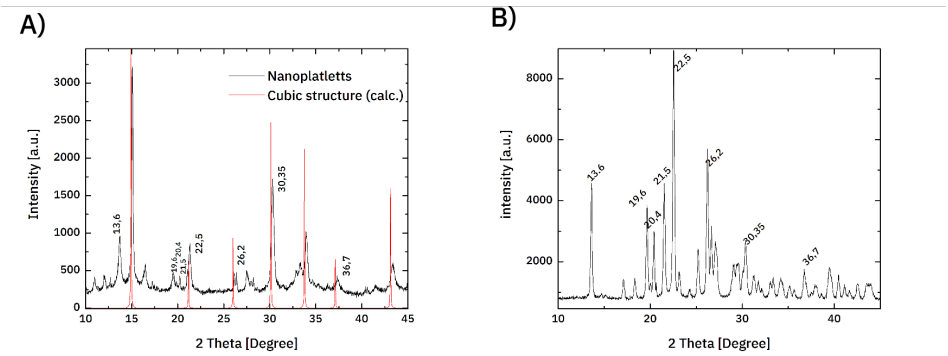

Fig. 4.9: A) XRD pattern with included calculated cubic perovskite pattern taken from Figure 4.8 B) The pure surfactant N-octylammonium bromide with significant signals marked in degree 2θ

The surfactant and the perovskite structure are presented as two patterns To simplify the evaluation of the XRD pattern. At first sight, the surfactant Figure 4.9 B shows a high amount of signals distributed over the whole detected region. The in Figure 4.9 B shown significant signals, could also be found in the perovskite nanoplatelets pattern. Inconveniently the signals of the surfactant and the signals of the perovskite are overlapping in many positions. The most significant signal of the perovskite structure the 100 signal at 15° seems to be at room temperature unaffected by the surfactant reflections. Besides the here discussed signals, more signals in the XRD-pattern of the nanoplatelets can be found. These could not be assigned to another unknown phase. An explanation could be found by the consideration of the formation of a bilayer of the surfactant. In this case, the chained structures of the surfactant will form a structure, which differs from the crystal structure of the pure surfactant. This consideration gets supported by the fact that at lower angles, more signals are appearing. This indicates that a bigger structure, like a bilayer, is formed. This hypothesis gets supported by the previous measurements and by the literature.[285, 297] The structure of the precursor methyl ammonium bromide [298] could not be assigned. Noticeably a peak shift towards higher angles of the assigned perovskite signals is observable. (See Figure 4.10)

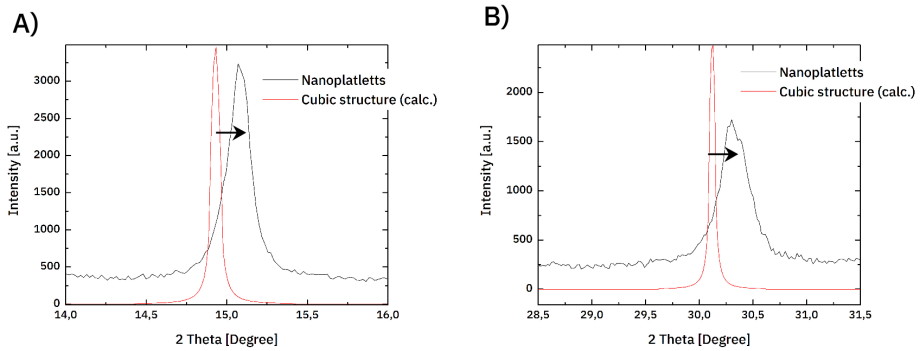

Fig. 4.10: A) XRD Pattern extract of the 15° signal with calculated signal B) XRD Pattern extract of the 30.51° signal with calculated signal

A constant shift in the here shown XRD signals to higher angles can be observed (See Figure 4.10). This might come from a smaller size of the unit cell. This can be explained by the different species of ammonium ion inside the crystal structure. Moreover, the higher surface energy in comparison to the bulk material. For a better understanding, an illustration is provided. In Figure 4.11 the $MaPbBr_3$ structure is given.

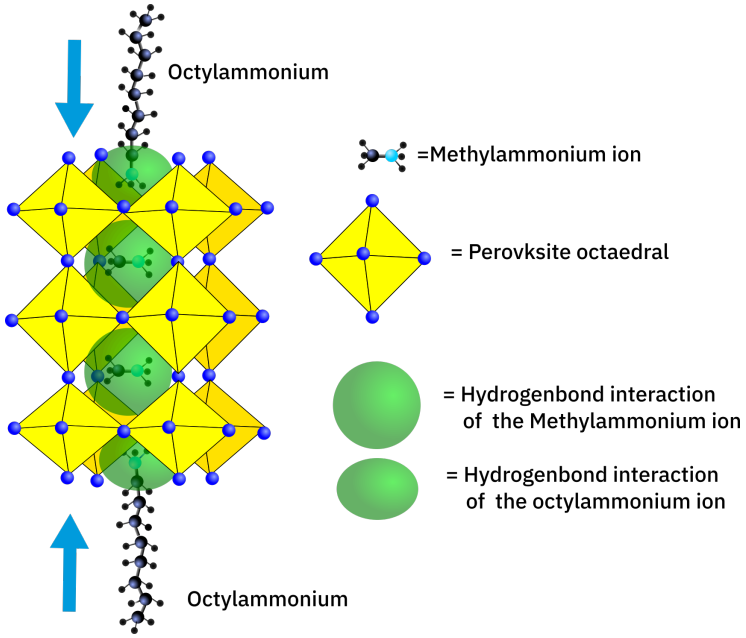

Fig. 4.11: Excerpt of the $MaPbBr_3$ structure with additional N-octylammonium ligands on the top and bottom of the structure, additionally the interaction radii of the amines are drawn in green

The lead ion is located in the middle of the octahedral and is not visible here. Additionally N-octylammonium as surfactant is drawn at the $MaPbBr_3$ crystal

structure. Furthermore, an interaction sphere of the ammonium is drawn in green. The arrows illustrate the pressure on the unit cell. As discussed in "*Surface Matters (The Nanosize Effect)*" (subsection 2.3.1) surface atoms behave differently than bulk atoms, since the forces at a surface are unevenly distributed in comparison to the bulk material. More interaction between surface molecules and surfactant are observed. Additionally to those properties, the N-octylammonium ion can take the same place as the methylammonium ion in the crystal structure.[22, 285] However, due to its size (mainly alkyl chain), the perovskite structure is not formed around the N-octylammonium ion like it is the case for the methylammonium ion.[22] Furthermore, it is known that the hydrogen bonds of the methylammonium ion play an essential role in the stabilisation of the crystal structure [299]. For the N-octylammonium half of the supporting perovskite structure is missing, so the ammonium group is more deeply involved in the structure since the hydrogen bonds are stronger. This is leading to a compressed unit cell, at least for the outer surfactant/perovskite layer. To support this hypothesis, the signals at higher angles (>40 2θ) gets broader, which indicates the compressed unit cell. The size change of the unit cell under pressure is documented for the bulk $MaPbBr_3$.[78] With that, the shift towards higher angles is explainable with the nanosize effect and a lattice compression. Because of the unknown phase of the surfactant and the possible underlying signals of the $PbBr_2$, a refinement was not possible.

To investigate the effects of the temperature on the crystal structure, the temperature-dependent XRD was measured. This was done at the synchrotron *BessyII* (HZB, Berlin, Germany) at the beamline KMC2.[3] An intensity attenuated photon energy of 8.048 keV (represents Cu $K_{\alpha 1}$=1.5406 Å)was used. The temperature was controlled by a closed-cycle cryocooler under a beryllium dome. Rotation of the sample was not possible during the measurement. A temperature range of 200-315 K was used, after a comparison of the DSC data, with a particular interest in the phase transitions. An analysis of the synchrotron data was only possible to an angle of 45°. The reason here is the used beryllium dome, which is adding signals to the XRD pattern starting

[3]The measurement and the merging of the data were performed by the beamline scientist *Dr. Daniel Többens*

at an angle of 46°. For a comparison between laboratory and synchrotron measurement Figure 4.12 is shown.

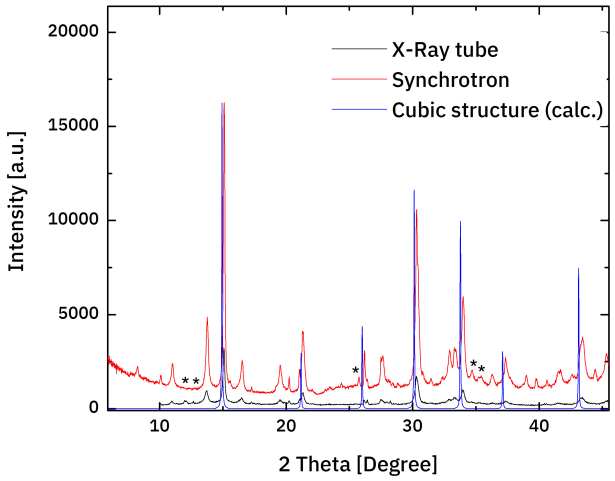

Fig. 4.12: X-ray diffraction pattern of the laboratory device (X-Ray tube) and the synchrotron measurement at room temperature (300 K) in addition the calculated pattern.[283] * marks additional or missing signals

Even if a range up to 80° 2θ is detected, the collected data up to 45° can only be used, since the beryllium dome of the cryocooler also adds reflection signals starting at around 46°. The synchrotron and the laboratory measurement shows a nearly identical XRD-pattern (Figure 4.12). The synchrotron shows higher intensities, because of the higher photon flux in comparison to the X-ray tube of the lab device. Every perovskite signal can be assigned to the high-temperature cubic crystal structure. In general, the same discussed properties of the measurement performed on the laboratory device done previously, can be applied here. The only differences are missing or additional features of the surfactant, which are visible because of the absence of the sample spinning. (See Figure 4.12 marked with *)
Besides a room temperature (300 K) measurement, further temperature-dependent measurements were performed at the synchrotron. These are shown in Figure 4.13.

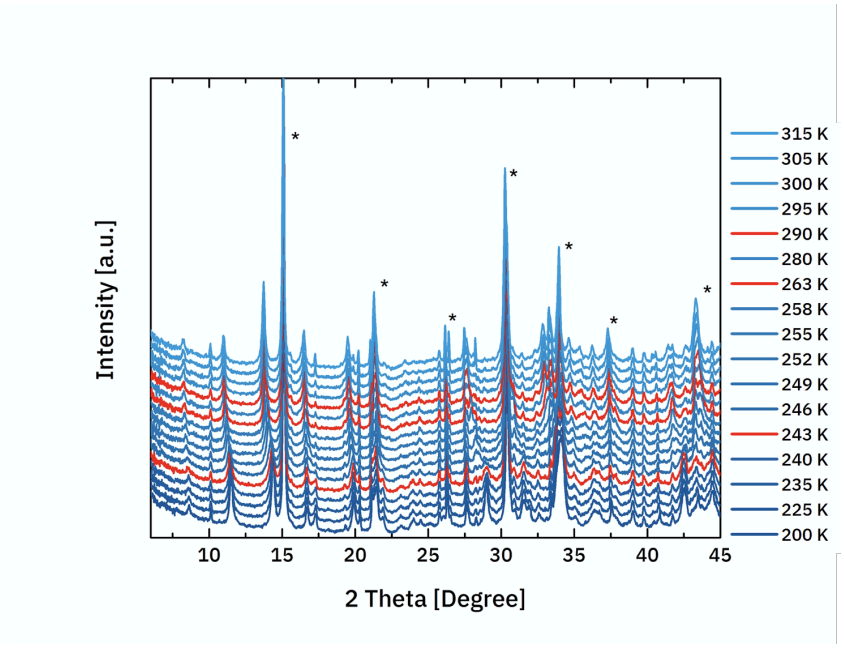

Fig. 4.13: Temperature dependent XRD-measurements with temperature scale. The *marked signals can be assigned to the perovskite cubic crystal structure found in literature.[283]

Here the *-marked reflexes are assigned to the high-temperature cubic perovskite crystal structure. Besides these, more signals are appearing, these are, as mentioned above, assigned to the N-octylammonium surfactant.
Furthermore, a temperature-dependent signal splitting of the assigned perovskite peaks is observable. This shall be discussed in detail later. Unfortunately, the signals from the surfactant are also changing their position in relation to the temperature and also merging with the signals of the perovskite. A temperature-dependent measurement for the surfactant, for comparison, cannot be provided. In addition to that, the outer perovskite layer seems to be tilted, which is originated by the interaction of the surfactant N-octylammonium.[300]For this reason, the crystal structure and its temperature-dependent behaviour cannot be fully investigated. Further information for refinement are missing, so an analysis of the phases by a refinement method cannot be applied.
To further analyse the resulting data, in the following selected signals of the perovskite shall be presented and discussed. For this reason, in Figure 4.14 the 100 signal at around 15° of the cubic high-temperature phase is shown, additionally the calculated XRD-Pattern of the in the literature described orthorhombic and tetragonal phase is shown.[283]

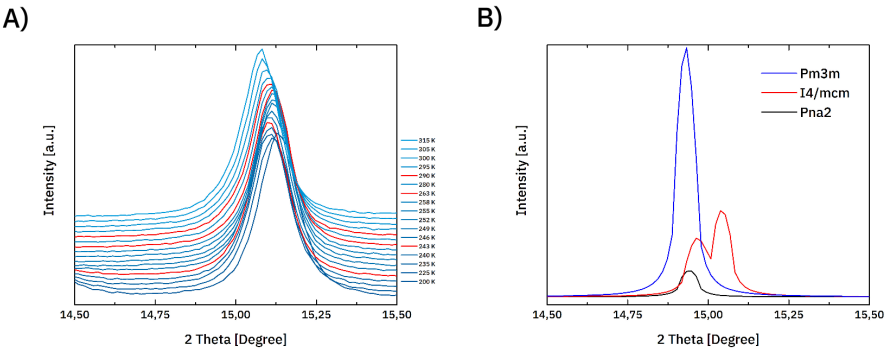

Fig. 4.14: A) Temperature-dependent XRD-measurement with an extract of the 15° signal with red marked phases transition onsets B) Calculated structures found in literature [283]

The temperature-dependent XRD-patterns show changes in the signal position and intensity as a function of temperature. At 243 K, the phase transition is expected (see Figure 4.5 marked in red). Towards this temperature, the signal reduces constantly in intensity with a slight shift to lower angles. This is related to the thermal expansion of the unit cell. At 243 K the signal is getting broad. At this temperature a phase transition from orthorhombic → tetragonal phase is expected (see Figure 4.5). Splitting can be interpreted, but a clear separation of the signal in the tetragonal (I4/mcm) phase cannot be observed (compare Figure 4.14 B). The reason for that might be the peak broadening of the signal resulting from the nanostructure, which even in a synchrotron measurement gives a low intensity and an overlay of otherwise separate signals. The incommensurable phase (in literature described as tetragonal I phase or γ phase [283]) cannot be distinguished.(see Figure 4.5) After the phase transition orthorhombic → tetragonal phase at 263 K, the temperature-dependent expansion of the unit cell is continuous, as expected. At 290 K, the tetragonal → cubic transition is occurring, and this is getting visible by a change in peak intensity. As shown in Figure 4.14 B a phase transition tetragonal → cubic undergoes a signal merging and an increase in peak intensity. This can also be observed at the 15° signal. Although the peak at 15° seemly undergoes a temperature-related change in intensity and broadness, a clear separation of the signals and therefore a separation of the expected phases (i.e. orthorhombic → tetragonal, singlets to doublet or from tetragonal → cubic, doublet to singlets (see Figure 4.14 B)) is not possible. Furthermore, a dramatic change of this signal is not expected, since the symmetry change of the system is at the represented size not as dramatic

as in smaller regions. For this reason, higher angles need to be observed. An example for this can be the 200 signal at around 30° shown in Figure 4.15. At the 30° peak the temperature-dependent changes of the signal are more clearly visible.

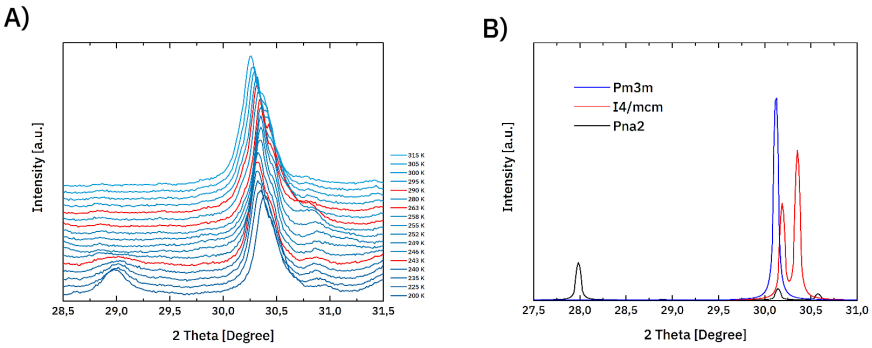

Fig. 4.15: A) Temperatur-dependend XRD measurement with a extract of the 30° signal with red marked phases transition onsets B) Calculated structures found in literature [283]

The orthorhombic phase can be assigned to the calculated structure. The signal at 28° 2θ in the calculated pattern is shifted to higher degrees at 29° 2θ in the at 200 K measured pattern. The same applies for the other two signals at 30.1° and 30.6° 2θ shifted in the measurement to respectively to 30.4° and 31° 2θ. Even though the peak position is comparable to the calculated, the intensities are changed. The explanation can be found in the shift of the surfactant incorporated in the perovskite, resulting in a lattice compression of the above-mentioned perovskite structure. With that, the surfactant and the perovskite are forming a different perovskite layer, which becomes visible in the change of the signal intensities(see Figure 4.11. If the temperature increases the peak at 29° 2θ vanishes at the temperature of 243 K. The peak at 31° 2θ is flattening out at a temperature of 243 K. The peak at around 30,5° 2θ is increasing in intensity and decreasing in angle towards the phase transition orthorhombic $\rightarrow$ tetragonal. This is assigned with the calculated XRD-pattern in Figure 4.15 B. The 29° 2θ signal is not further present to be discussed since this signal is not included in the tetragonal or cubic structure. The signal at 31° 2θ is increasing in intensity and is moving towards the signal of 30.5° 2θ at a temperature of 263 K to form a doublet. The signal at 30,5 ° 2θ is increasing in intensity. For the next phase transition (tetragonal $\rightarrow$ cubic), the doublet of the tetragonal phase is merged into one

single signal. The signal of the cubic phase can be observed at around 30.25° 2θ.This can also be observed in the temperature-dependent measurement (seeFigure 4.15).
For a better observation of the temperature-dependent phase behaviour, the peak maximum of the 30° 2θ signal is plotted against the temperature. With that the phase transitions are visible (see Figure 4.16)

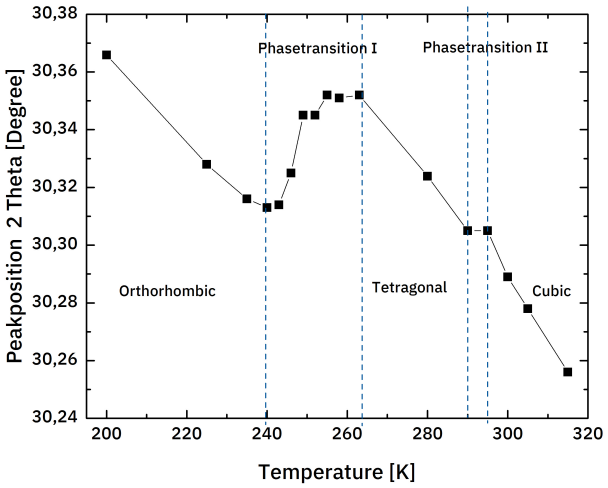

Fig. 4.16: Peak position of the 30° peak plotted against temperature. The expected phase transitions known from the DSC measurement are implemented

As discussed earlier, the thermal expansion of the unit cell will shift every signal to a lower angle on the 2θ scale. This is visible for the orthorhombic, tetragonal and cubic phase. During the phase transition, this is not the case.The first phase transition (orthorhombic $\rightarrow$ incommensurable $\rightarrow$ tetragonal) shows first an increase in peak position depending on the temperature between 243 and 249 K. Between 249 and 252 K, a plateau is reached. After that there is a slight increase in the peak position between 252 and 255 K, which might indicate a second phase transition. The change in peak position is only minor, so it gives a hint about the incommensurable phase (described in [283]). Starting at 263 K, the tetragonal phase is reached until the second phase transition at 290 K tetragonal $\rightarrow$ cubic at 295 K is reached. The cubic phase behaves as a linear expansion of the unit cell. Even though the phase transition can be described and observed, a refinement of the structure is (due to the complexity of the system) not possible. From the extracted peak position, the cell parameter can be extracted and converted into the cell

parameter of the cubic cell.[296, 244] In the following the cell parameter, a is plotted against the temperature.(see Figure 4.17)

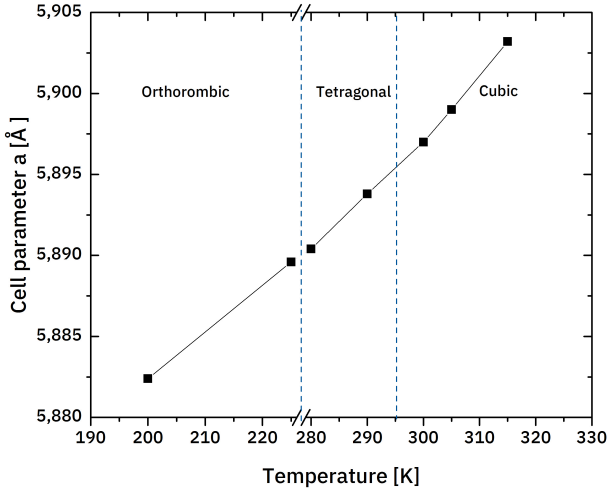

Fig. 4.17: Linear expansion of the pseudo cubic unit cell (the phase transition are excluded)

Here the phase transitions are excluded, to show the continuous, linear thermal expansion of the unit cell and no further change in the crystal structure. The parameter b and c are excluded, since the uneven expansion of the unit cell caused by the incorporation of the surfactant into the outer perovskite layer, is leading to an error. Furthermore, the outer layer of the perovskite seems to be tilted, as suggested by Sichert et al.[300]
Nevertheless, the expansion of the unit cell can be followed and appears linear.

To conclude, a change on a sub nanosize level is observed. The expected crystal structure change can be observed and compared to the DSC measurements. This gives qualitative information to the other temperature-dependent measurements. A quantitative analysis of the observed behaviour is made. An evaluation with a refinement like the Rietveld or Le Bail method was not possible due to the complexity of the system and the additional phases, caused in the surfactant system of the perovskite nanoplatelets. Furthermore, an explanation for the peak shift towards higher angles is given. This could be explained with the unit cell compression originated from the nanosize

effect. Asides the sub nanostructure, it is also known, that the nanostructure may undergo a temperature-dependent structural transition. For this reason, smaller angles need to be investigated. This is covered in the following section with small-angle X-ray scattering.

4.2.4 Small angle X-ray scattering investigations

For investigate the temperature-dependent properties of the material on the nanoscale, temperature-dependent small-angle X-ray scattering (SAXS) was performed. For this purpose, the perovskite nano sheds were dispersed in toluene (0.1 mg/mL). The dispersion was sealed in a capillary and placed in the sample environment. The measurements were performed at the tetragonal $\rightarrow$ cubic phase transition at 288, 293, 298 and 303 K. Afterwards a background measurement of the pure toluene was performed. For the data correction and the data reduction, a transmission correction, a correction for empty cell scattering and a normalisation for absolute intensities were performed. Subsequently, the results were desmeared with the *Strobl* algorithm.[301] [4] The corrected data can be seen in Figure 4.18

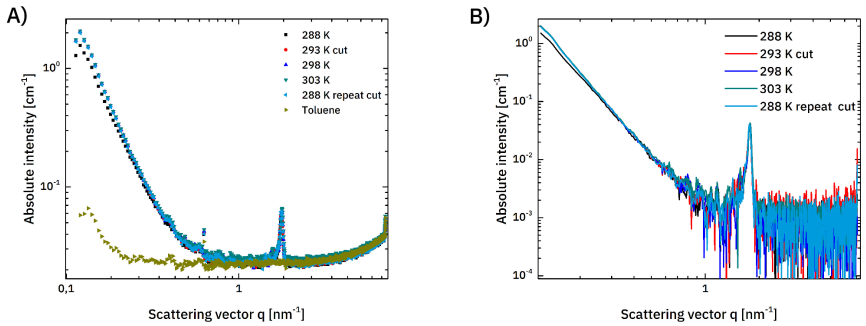

Fig. 4.18: A) Full desmeared SAXS data (the with "cut" marked measurement are reduced of spikes which may result from the surfactant, but could not further be investigated and did not apply informations for the investigated system) B) Zoom on the peak at 1.7 nm^{-1}

In Figure 4.18 a decay into the background (toluene) is shown. Furthermore, a signal at 1.7 nm^{-1} is detected. A temperature-dependent shift of the peak

[4] The data reduction and correction were carried out by the SAXS expert *Dr. Albrecht Petzold* with his support, expertise and help the fits with SASfit were carried out

at 1.7 nm^{-1} is not observable. This is shown in Figure 4.18 B) with no change in the peak size or position at different temperatures. The control measurement at 288 K shows no change, so an irreversible change of the sample on a nanoscale range, can be excluded.
The signal was further investigated by a fit using the software *SASfit*.[257] The size of the nanoplatelets of 200 nm is to expand, to be observed in the SAXS-measurement. For this reason, the shape of the nanoplatelets is negligible, and a simple, cylinder as a plain model can be chosen. Additionally the TEM images (Figure 4.2) revealing a lamellar structure, so an assumption of a lamellar system was made. The TEM-Image further shows alternating for the lamellar structure with light and dark contrast. This leads to the assumption that the material can be seen as a paracrystalline material. Which is defined by having a short or medium range ordering but lacking a long-range order at least in one direction.[302] The fit is shown in Figure 4.19. Here the signal at 288 K is chosen. Since the variation of the peaks at different temperatures are not significant, the signal at 288 K can be seen as representative for all SAXS measurements.

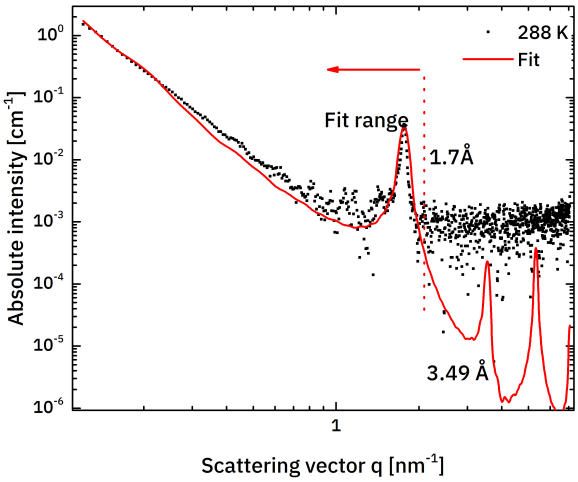

Fig. 4.19: Resulting SAXS Fit is shown with a peak at 1,7nm^{-1}

The above-mentioned model was applied to the fit, and the results of 1.7 nm^{-1} match the measured size of the TEM images.(see Figure 4.2) The fit was further continued into the background. A small variation in the background noise is still visible at the signal around 3.49 nm. This also fits very well with the TEM images, as a centre to centre distance.(see Figure 4.2)

Furthermore, the number of layers in a 0.1 mg/mL solution could be determinate. The perovskite nanoplatelets are forming a 9-12 layer cluster on average in dispersion with a concentration of 0.1 mg/mL in toluene. A temperature effect on a nanoscale size can be excluded, no change of the structure was visible. Furthermore, no single quasi-spherical particles could be observed by SAXS.

4.2.5 Temperature dependent analysis of optical properties

In this section, the optical and electronic properties of the synthesised nanoplatelets will be investigated. Besides obtaining more information about the system and the surprising shifted to higher temperatures of phases transitions, the optical and electronical properties of the nanoplatelets are also of interest. The section is structured by firstly to describing the room temperature measurements and continue to the temperature-dependent measurements. This adds further information about the system because a more expanded temperature range between 17 up to 319 K is covered. [5]

In Figure 4.20 a absorption spectrum of the perovskite nanoplatelets is shown. In addition a fit with the Elliott model, describing in crystalline material the excitonic and continuum contributions is given.[303] This was done by a suggestion from the literature.[304]

With applying the fit an excitonic binding energy (E_B) of 60 meV could be determined. Furthermore, a broadening parameter (Γ) of 55 meV, the band gap (E_{Bg}) of 2.36 eV and non parabolic conduction and valance band parameter close to 0 eV^{-1} were collected by using the analytical expressions by Saba et al [304]. These values correlate well with the findings in literature for $CH_3NH_3PbBr_3$ thin films with ($E_B = 60meV$, Γ= 50 mev and a non parabolic parameter of 0.11 eV^-1 .
Normalized temperature-dependent (17-319 K) photoluminescence (Pl) data with an excitation level of 4 $\frac{W}{cm2}$ are shown in Figure 4.21.

[5]The measurement and the fitting of the data were performed by Dr. Sergiu Levcenco

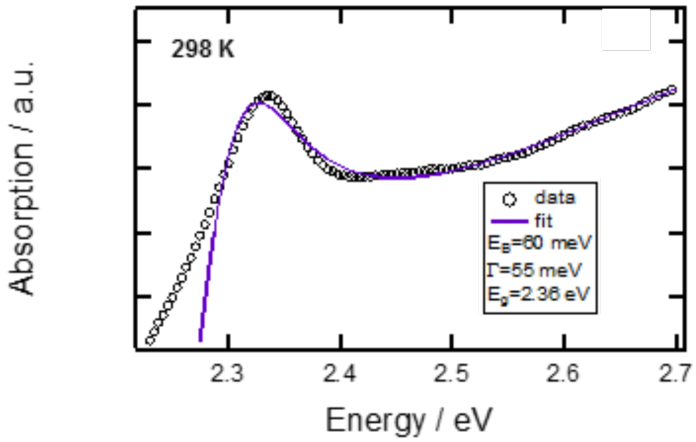

Fig. 4.20: Absorption spectrum of the perovskite nanoplatelets at 298 K with a fit after the Elliott model [303]

At 17 K, two bands are found at 2.2 and 2.6 eV. Additionally for the excitation dependent Pl measurements a new band at around 2.21 eV is revealed on the higher side of the 2.2 eV band. These bands can be explained with the presence of defects [52, 305] and excitonic emission [306, 207] of the $MaPbBr_3$ structure. Even though the other measurements indicate little impurities of the $PbBr_2$ the band at 2.6 eV most likely originates from this impurity. These findings support the further findings of quasi-spherical $PbBr_2$ nanoparticles. By increasing the temperature, the discussed bands are blue-shifted and broadened with a loss of intensity. With that, the excitonic band became stronger than the defect emission above 50 K. With a further increase in temperature, the defect transition drastically decreases and vanishes at around 75 K. This implies, at higher temperatures, only excitonic transitions are responsible for the PL signal of the perovskite. Figure 4.22 shows the peak position at the maximum of the Pl signal as a function of temperature. Here a significant peak shift is observable at the phase transitions.

The Pl signal shows an abrupt change near the orthorhombic/tetragonal phase transition, which is known in the literature for $MaPbBr_3$ bulk single crystals.[52, 305] In contrast to the observation for the bulk, single crystal, the perovskite nanoplatelets exhibited a featureless gradual behaviour of the PL-transition at the phase transition orthorhombic $\rightarrow$ tetragonal. The shift of the Pl_{max} with temperature is attributed to the variation of the band gap in the orthorhombic perovskite phase.[52, 305, 207] The origin for this

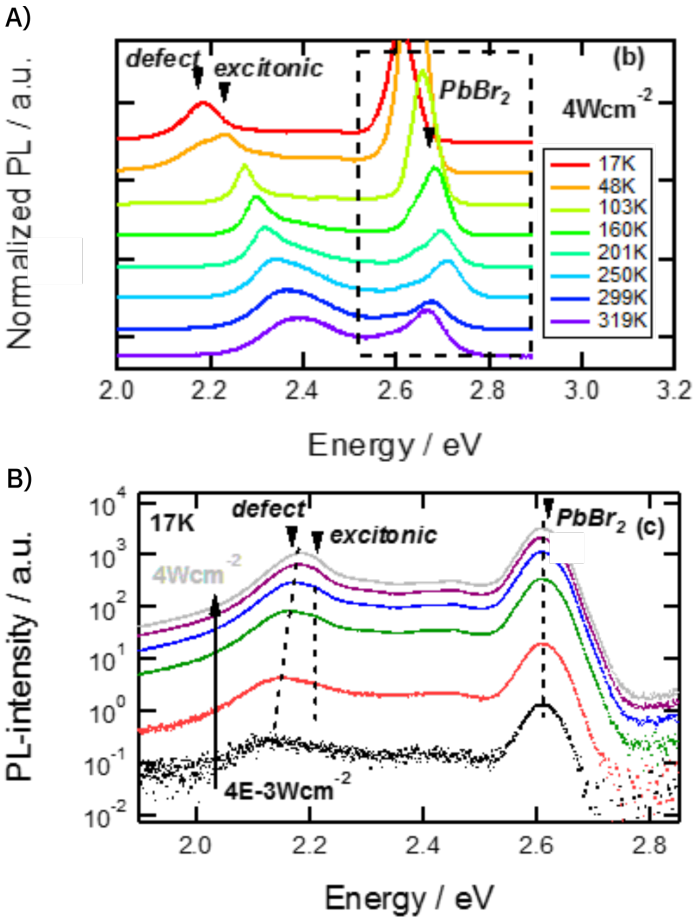

Fig. 4.21: A) temperature dependend PL (17-319 K) B) excidation dependent Pl data at 17 K

behaviour can be found in the thermal lattice expansion and the electron-phonon coupling [207] and can be described with:

$$E_{BG} = E_{BG}^{0} + \frac{\partial E_{BG}}{\partial V}\frac{\partial V}{\partial T}T + A\left(\frac{2}{\exp\left(\frac{E_{ph}}{k_B T}\right) - 1} + 1\right) \tag{4.1}$$

Here E_{BG}^{0} is the band gap at 0 K, $\frac{\partial E_{BG}}{\partial V}$ is the band gap expansions coefficient, $\frac{\partial V}{\partial T}$ Is the thermal expansion coefficient, A is the strength of the electron-phonon coupling, E_{ph} is the average phonon energy, k_B is the Boltzmann constant and T the crystal lattice temperature. For the band gap at 0 K, $E_{BG}^{0} = 2.5eV$ and $A = -0.3eV$ was found for single crystals in literature.[207] The least-square fit in Figure 4.22 results in $\frac{\partial E_{BG}}{\partial V}\frac{\partial V}{\partial T} = 8E^{-4}eV/K$ and $E_{ph} = 50meV$. These results agree well with the values for single crys-

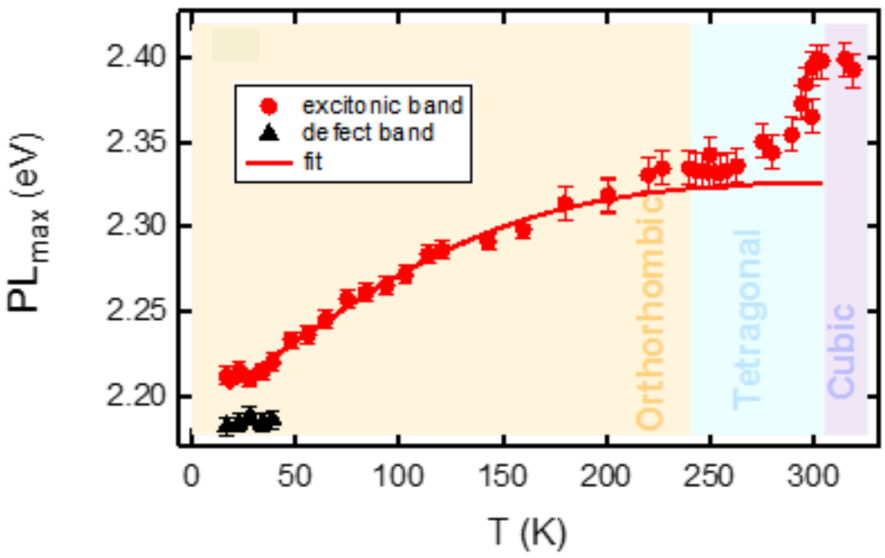

Fig. 4.22: Pl max positions of Figure 4.21 vs temperature of the perovskite nanoplatelets

tals found in literature $\frac{\partial E_{BG}}{\partial V}\frac{\partial V}{\partial T} = 6E^{-4}eV/K$ and $E_{ph} = 47meV$.[207] The transition orthorhombic $\rightarrow$ tetragonal is indicated by an increase of 10 meV for the excitonic transition. For the single crystals, a shift of about 20 meV was observed near the phase transition (150-170 K).[52, 305, 207] For the nanoplatelets in Figure 4.22 another abrupt blue shift of about 50 meV is observable. For this shift, the phase transition tetragonal $\rightarrow$ cubic can be discussed, which is supporting the findings of the XRD and DSC measurements. The room temperature emission agrees well with the Pl band centred around 519 nm (2.38 eV) found in literature.[118] This indicates no quantum confinement in the here analysed samples. This result is expected since the excitonic Bohr radius for $MaPbBr_3$ is at 1.36 nm, which is excited by the tree stacked layers with an expansion of 1.7 nm.[118]

A shift of around 8 meV to higher energies is observable in comparison to the literature value of 2.31 eV for the single crystal $MaPbBr_3$ perovskite.[207] This can be explained by the inner lattice compression of the nanoplatelets, also observed in the XRD-pattern. The lattice compression correlated change of the band gap for $MaPbBr_3$ microcrystals is described in literature.[78] A change for the band gap is usually expected since the binding length of the metal centre and the halide is decreasing. However, the shift of the band gap described in the literature is not expected linear, but with a minimum at around 1 GPa, after which an increase in band gap is observable. This is a

unique behaviour for semiconducting materials and until now only observed for $MaPbBr_3$ micro crystals.[78] An amorphisation of the crystal structure explains this observation. By this, an determination of the inner pressure of the nanoplatelets by the band gap is challenging, and only an estimation can be done. For the microcrystals the band gap of 2.38 eV is reached at a pressure of 1.8 GPa.[78] At this point, a $MaPbBr_3$ microcrystals, described in the literature [78], undergoes a phase transition, as observed for the nanoparticles, this is not the case. However, this pressure might explain the band gap shift of around 8 meV. A different approach for the explanation of the Pl shift is expected be the in literature related to the tilting of the outer perovskite layer.[300] This might additionally explain the shift of the band gap.

To conclude the results, the emission spectroscopy agrees well with the findings in literature for thin films. This gives another proof, that the perovskite structure is present. The Pl spectra are showing impurities of lead bromide, which were not directly detected by the other used methods, but described in literature [118]. The excitation dependent measurement shows a contribution of the defect and excitonic emissions. In the temperature-dependent measurements, the excitonic bands increase while the defect emissions vanish. This leads to the conclusion that the excitonic transitions are responsible for the Pl signal at temperatures above 75 K. The temperature-dependent measurements further reveal abrupt changes in the Pl position for the phase transitions. These are comparable to the previous detected phases transitions. For the phase transition orthorhombic $\rightarrow$ tetragonal, a fit was carried out to investigate the effect of the lattice expansion on the band gap. The obtained values resemble well the findings for the singles crystals found in literature. A small change in energy for the band gap is observable, which might be explainable with a higher lattice compression of the nanoparticles.[78] Additional no quantum confinement is observable. This fits well to the excitonic Bohr radius of about 1.36 nm.[118]

4.3 Discussion

The literature [117, 279, 118] nanoplatelets described could be reproduced. By adaptations of the synthesis protocol, the amount of quasi-spherical lead(II) bromide nanoparticles could be reduced.
This was possible by "quenching" the reaction and suppressing the Ostwald ripening of lead(II)bromide nanoparticles. A different possibility for the formation of the quasi-spherical $PbBr_2$ nanoparticles could be a defect formation by the incorporation of the ligands in the perovskite lattice. These defects might lead to a destabilisation of the perovskite structure and further a local decomposition in the nanoplatelet. As a result, nucleation and formation of $PbBr_2$ can occur. The last-mentioned pathway gets supported by the observation of the $PbBr_2$ nanoparticle formation as a result of the TEM induced beam damage by Sichert et al.[118].
Both possible pathways of the formation of quasi-spherical $PbBr_2$ nanoparticles seem to be temperature-dependent and by a "quenching" of the reaction and a low-temperature purification method suppressed. As an outcome, the here synthesised nanoplatelets are showing less quasi-spherical $PbBr_2$ nanoparticles as an impurity, than the comparable nanoplatelets in literature.[117, 279]
The TEM images show 200-230 nm nanoplatelets with less to zero quasi-spherical $PbBr_2$ nanoparticles than that described in literature.[279, 118] Furthermore, perpendicular to the TEM-grid standing nanostructures are observable. They reveal an insight into the layered nanoplatelets structure. With that, a thickness of 1.7 nm for the surfactant layer and a centre to centre distance of 3.49 nm, which results in a 1.8 nm layer for the perovskite are visible. These findings could also be observed in the SAXS measurement. A tilting of the surfactant or an alkyl chain packing of the ligands could not be investigated. However, a tilting of the surfactant is suggested in the literature for thinner perovskite layers.[285, 300] This might differ because of the interlayer of the perovskite, which might add to the stabilisation of the outer layer of the perovskite.
For the SAXS measurement, no free, quasi-spherical $PbBr_2$ could be found. This indicates, that the quasi-spherical $PbBr_2$ nanoparticles, if present, are incorporated in the perovskite crystal lattice.
Furthermore, a 0.1 mg/mL dispersion in toluene of the nanoplatelets are

arranged to a stack of 9-12 layers. A temperature-dependent change of the structure could not be observed. Nevertheless, a spacial change of the surfactant due to a phase transition is described in the literature for a similar system.[285] However, the system here investigated varies from the literature system by more layers of perovskite. Furthermore, the phase transition orthorhombic→tetragonal might reveal a change in spacing, but due to the limitation of the sample environment of the SAXS, and investigation of this phase transition could not be provided.

The TGA measurements indicate a decomposition temperature of 363 K. A further decomposition could be discussed with the findings in literature [279], but could not be confirmed. The findings here do not resemble the findings in literature.[279] This might be explainable by the fact, that the literature TGA measurement was carried out with a dispersion, while here just the nanoplatelets were investigated. Additionally in the literature [279] a significant higher concentration of quasi-spherical $PbBr_2$ nanoparticles inside the $MaPbBr_3$ layer was shown. Due to the internal defects caused by the $PbBr_2$ nanoparticles, this can lead to different observations concerning the overall stability of the perovskite nanoplatelets.

The DSC-measurement resembles the measurement of the bulk perovskite. This gets obvious by even observing the incommensurable phase. The measurement further reveals a drastic shift in the possible phase transition towards higher temperatures. In this process the phase transitions are changed for 97, 100 and 64 K toward higher temperatures in comparison to the bulk material.[283] However, the phase transitions of the nanoplatelets resemble the phase transitions of the bulk material in shape and position. This behaviour is on first sight contrary concerning the behaviour of nanoparticles, which usually show a melting-point depression.[307, 162] Additionally the transition energies for every phase transition of the nanoplatelets is significantly higher than for the bulk material. The transition energies for the pure surfactant is ten-fold higher than the one of the bulk perovskites. This leads to the consideration that the perovskite surface bonded surfactant has a significant influence on the phase transitions of the nanoplatelets.[22]

The surfactant seems to stabilise the phase of the perovskite. With that, the phase transition of the perovskite gets suppressed for around 100 K, and the phase transition of the surfactant gets promoted by 10 or 20 K. This can be explained by the different energies needed for the phase transition of

the different materials. For the phase transition of the perovskite with the surfactant, more energy is needed, since the alkyl chains of the surfactant need to be taken into account. The energy barrier for the phase transition of the perovskite, therefore, becomes increased. This results in a shift of the phase transition temperatures towards higher temperatures. If the energy is surpassed, a possible conformation change of the surfactant might be possible. This is observed for the N-nonylammonium surfactant incorporated into a single layer of PbI_2Br_2 by infrared and raman spectroscopy of Abid et al.[285]

Furthermore, the crystal structure was investigated by XRD. The cubic phase could be assigned in the resulting XRD pattern. The background of the lead bromide particles could drastically be reduced by the different synthesis protocol, mentioned above. If the focus is only on the in the XRD pattern described in the literature[117, 279], the signals of the cubic perovskite phase are as narrow as in the here presented XRD pattern. This indicates that the perovskite nanoplatelets are not limited by crystal lattice on which reflection can occur. (See subsection 3.2.2). The evidence indicated, that the broad XRD signals shown in the literature [117, 279] contains high amounts of a different, nanomaterial with a small size. This would fit the quasi-spherical $PbBr_2$ nanoparticles described by *Sichert* et al. In the literature.[118] Unfortunately no XRD pattern of pure $PbBr_2$ quasi-spherical nanoparticles can be provided or found in the literature. However, by comparing the XRD pattern by Gonzalez-Carrero et al.[277] the here discovered broad signals at around 20°,30° and 45° (background)), are agreeing with the broad signals of the described possible reflections of the $PbBr_2$.

No further precursor impurities e.g. methylammonium bromide are observable in the XRD pattern.

Nevertheless, additional signals originates from the N-octylammonium bromide is observable. A comparison could assign these signals with the pure N-octylammonium bromide. However, it is mentioned, that the pure surfactant will probably not form a bilayer orientation like found in the perovskite structure here. For this reason, the XRD pattern of the perovskite with a focus on the surfactant will differ from the pure surfactant.

The signals of the perovskite structure are shifted towards lower angles and reveal a smaller unit cell, than the structure found in literature.[283] This could be explained by the surface energy induced stronger binding of the

N-octylammonium surfactant, which leads to a compression of the unit cell. This can be compared to a pressure dependent XRD-measurement of $MaPbBr_3$ micro crystals.[78]
The temperature-dependent XRD measurements reveal a change in peak position comparable with the DSC determined phase transition temperatures. Because of the similarity of the crystal structures, the differences in XRD-pattern are relatively small. In addition to that the nanoplatelets are revealing a relatively small signal. Furthermore, the unknown phase of the surfactant makes it impossible to refine the structures and give a detailed insight into the phase transition. However, a less sophisticated method by observing single peaks show the phase transition. These can be compared to the findings for the bulk perovskite of Poglitsch et al.[283] Further, more a linear expansion of the perovskite unit cell is detectable by the pseudocubic analysis. This shows that the general perovskite crystal structure stays intact and no decomposition is occurring.
The optical properties were investigated by absorption spectroscopy and temperature-dependent photoluminescence. With that, the band gap and the exciton binding energy could be fitted with the Elliot model.[303] These findings could be compared to $MaPbBr_3$ thin films. Furthermore, the phase transitions are observable in the temperature-dependent PL measurements. Here especially the low-temperature behaviour is investigated in detail. With the least-square fit [207] of the measured data insights into the thermal behaviour of the band gap are revealed. These findings are comparable to the findings for single crystals of $MaPbBr_3$. This supports the evidence of the presence of the perovskite as material and the detection of phase transitions. Additionally the band gap is dependent on the crystal lattice expansion.[78] This is also represented in the shift of 8 meV towards higher energies, which is confirmed with the pressure experiments of $MaPbBr_3$ micro crystals.[78] The lattice compression pressure of the perovskite could not be determined because the $MaPbBr_3$ microcrystals are undergoing an amorphisation during the measurement. For the nanoplatelets, this seems to be unlikely because of the stabilising surfactant is supporting the perovskite structure. Moreover, further sharp XRD peaks are observable in the measurement. A different explanation for this observation can be found in the literature for a single layer of perovskite.[300] The authors were investigating single layers of perovskite and also observed a shift in the Pl maximum with the origin in a

tilting of the perovskite octahedral.[300] Quantum confinement could not be observed for the 1.7 nm layers. This could be explained with the smaller excitonic Bohr radius of 1.36 nm of the $MaPbBr_3$.[118]

4.4 Conclusion & Outlook

4.4.1 Conclusion

The in literature [117, 118, 279] described nanoplatelets could be reproduced. In addition a slight change in the synthesis protocol was made. Cooling the system after injecting the precipitation agent (acetone) solution, lead to less quasi-spherical $PbBr_2$ nanoparticles. These quasi-spherical $PbBr_2$ nanoparticles were previously described as the resulting perovskite quantum dots[117, 279], but an analysis of Sichert et al. lead to the hypothesis of an impurity during the synthesis and additionally during the TEM measurement, caused by beam damage.[118] As a result, the TEM images show less $PbBr_2$ particles and furthermore the XRD pattern is not dominated by broad signals. For the TEM images, 200-230 nm nanoplatelets with a thickness of 1.7 nm and a centre to centre distance of 3.49 nm could be found. These findings are very comparable to the SAXS data. Additionally the SAXS data revealed a stacking of 9-12 layers in a 0.1mg/mL dispersion. In the temperature range of the SAXS measured, a temperature-dependent structural change of the nanostructure could not be observed.
The thermal behaviour was further investigated by thermogravimetric analysis and differential scanning calorimetry. The thermogravimetric measurement revealed a decomposition temperature of 363 K. The decomposition temperature was of main interest, even though more decomposition steps are observable, an analysis was done. A comparison to the literature was not directly possible since found in the literature was investigating the decomposition of the particles in dispersion.[279] In this thesis, the pure perovskite nanoplatelets without dispersant were investigated.
The thermal, reversible behaviour was further investigated by a DSC measurement. This measurement showed similar behaviour for the phase transitions in comparison to the bulk material.

Nevertheless, the phase transitions of the nanoplatelets are surprisingly shifted towards higher temperatures in comparison to the bulk material. Furthermore, the phase transitions are expanded over an enlarged temperature range. This could be explained by the surfactant, which is incorporated into the perovskite structure and is interacting with surrounding surfactants. So the phase transitions are suppressed and shifted towards higher temperatures.

The phase transitions were further investigated by temperature-dependent XRD measurements. Firstly, the cubic phase at 300 K could be assigned. Besides the assigned signals of the cubic perovskite phase, further signals are observable. These are assigned to the used surfactant N-octylammonium. Asides the slight background shift, with a possible origin in the quasi-spherical $PbBr_2$ nanoparticles, no further signals were observed. An additional observation is the shift of the XRD peaks towards higher angles, which is indicating a smaller unit cell, than the one described in literature. This can be explained by the higher surface energy of the nanoplatelets and the interaction of the surfactant, which leads to a lattice compression of the perovskite structure. The temperature-dependent XRD-measurements shows a change of the cubic assigned signals. Because of the unknown phase of the surfactant and further the unknown temperature-dependent phase change, a refinement method was not possible.

For this reason, the peak position and a comparison to the known phases shows a phase transition as expected for the bulk material. During the phase transitions, a non-linear peak shift of the signal is indicating a phase transition. To support this analysis, the pseudocubic analysis for the perovskite structure is revealing a linear unit cell expansion over the measured temperature range (excluding the phase transitions). This behaviour is expected.

Further investigations of the $MaPbBr_3$ nanoplatelets where conducted with optical measurements. The room temperature measurements, therefore, agree well with the findings of thin layers and single crystals in literature. In addition to the perovskite signal, also $PbBr_2$ impurities are found. The temperature-dependent and excitation dependent measurement reveals defect and excitonic bands. These excitonic bands dominate the Pl spectra starting at temperatures above 75 K. Furthermore, sudden changes in the Pl position by increasing the temperature are observed. These can be assigned to the phase transition, investigated with earlier measurement methods. No

additional phase transitions at lower temperatures are observed. Furthermore, the expansion of the lattices were investigated and could be assigned to the findings in literature. Additionally to these findings, a shift of 8 meV in the band gap was observable. This shift can be explained with the lattice compression inside the nanoplatelets, observed also in the XRD measurements. This behaviour is further discussed in the literature for microcrystals, which undergoes an amorphisation at around 1 GPa.[78] In addition to that assumption in the literature it is described, that the surfactant will induce a tilting of the perovskite octahedral [300], which further will lead to a shift of the Pl peak position.
A quantum confinement for the 1.7 nm nanoplatelets could not be found. This aggress well with the findings in literature and further a calculated excitonic Bohr radius of 1.36 nm for $MaPbBr_3$.[118]
As a consequence, this material is showing a phase transition close to room temperature. The usage as, e.g. optical detector might be phase-dependent. This should be taken into account.

4.4.2 Outlook

The here investigated system shows potential for further investigation. Despite the challenges of the nanomaterial, a temperature investigation could be done, which delivers insight in the unusual behaviour of the here observed perovskite nanoplatelets. Nevertheless, further temperature-dependent measurements of, e.g. the surfactant N-octylammonium bromide could be done as a first step. With that, a refinement of the crystal structure could be performed and more information of the behaviour could be obtained. Furthermore, a temperature-dependent Raman or infrared spectra might reveal a conformational change in the surfactant structure as shown for a similar structure by Abid et al.[285]. A rheology measurement of the system could also be suitable to obtain an insight into the interlayer forces. These measurements might provide access to a better understanding of the system and lead to further possibilities in applying different surfactants.
The nanoplatelets are not stable without the surfactant, so a pure, perovskite nanoplatelet without surfactant, cannot be investigated. Furthermore, the surfactant is showing a stabilising effect on the perovskite structure and

their crystal phases. For this reason, further investigation with a different surfactant is a field of interest. Therefore shorter surfactant or further functionalized surfactant, e.g. conducting surfactants could be investigated. With shorter surfactants, the perovskite structure could be adjusted to a suitable phase since a potential stabilising effect seems chain length-dependent.[297] Shorter chain lengths further imply a higher interlayer electron conductivity, which results in a higher overall conductivity and a higher efficiency of the optical and electronic device.

Further functionalization of the surfactant might lead to direct connection to a selective electrode for light-emitting, light-detecting or solar cell devices. The incorporated head group of the surfactant supports the extraction of holes or electrons towards the selective electrode. In addition to that different morphologies could be achieved by differed surfactant structures, so self-assembly and better coverage of the nanoplatelets results in an improved layer.

For the inorganic part, the perovskite structure with the stoichiometry $MaPbBr_3$ could be replaced for different perovskites. The surfactant shows a stabilising effect on the perovskite structure. With that, possible other perovskite structures might form due to the support of the surfactant, which otherwise would not be present in a bulk material. One of these examples and in the literature already published is the $CsPbI_3$ perovskite.[308] Furthermore, structures are conceivable, even lead-free variants of the perovskite structure. With that, the system is showing exciting possibilities for a more stable and higher efficient device.

5

Enhancing the charge mobility and stability of $CsPbI_3$ nanocrystals

> *If you do too much people get dependent on you. And if you do nothing, they lose hopewhen you do things right, people wont be sure youve done anything at all.*
>
> **— Matt Groening**
> American cartoonist

This chapter focuses on the caesium lead triiodide ($CsPbI_3$) nanocrystals. In comparison to the hybrid organic perovskite like methylammonium lead triiodide, $CsPbI_3$ is fully inorganic. For this reason, no volatile organic components are present, and higher stability is proposed.[309] For solar cell application, the most appropriate phase is the cubic α- phase with a band gap of $E_{Bg} = 1.73eV$.[310] Unfortunately only yellow, non-perovskite, orthorhombic δ-phase is thermodynamically preferred at room temperature.[114, 311] The cubic α-phase desired for solar cell applicationes emerges at temperatures above 310°C.[114, 310, 312] A reason for that behaviour could be the small size of the Cs ion, which leads to the low Goldschmidt factor of 0.8 for $CsPbI_3$.[75, 313]

Protesescu et al.[23] showed a hot injection synthesis for $CsPbI_3$ nanocrystals. These nanocrystals show a stable room temperature $CsPbI_3$ phase with a size-dependent band gap of around $E_{Bg} = 1.7eV$, which are for this reason an interesting material for solar cell applications. The phase stabilisation of these nanocrystals can be explained by the high surface energy of the nanocrystals. A general trend is observed concerning the reduced size of material and the stability of a certain phase. This empirically found trend

shows that materials tend to convert to a more symmetrical crystal structure by the reduction of dimensions.[314, 315] Additionally the used ligand also adds to the stabilization of the quantum dots.[316, 317]
The quantum dot stabilising and for the synthesis essential, ligand leads to a problem of an insulating layer in between the arranged nanocrystals.
As a consequence, the charge carrier mobility is limited. Therefore Sanehira et al.[197] managed to exchange these ligands resulting in a $CsPbI_3$ quantum dot solar cell with an efficiency of 13,5%.
This chapter is divided into three parts. The first part, investigates the properties and the layer formation of the $CsPbI_3$ nanocrystals. For this purpose transmission electron microscopy, X-ray diffraction and X-ray reflectometry are used to determine the crystal structure, the size and the orientation in a layer.
Furthermore, in this chapter, the optical properties are investigated by spectroscopic methods like absorption spectroscopy, photoluminescence, time-resolved photoluminescence and optical pump, terahertz probe spectroscopy.
In the second part, the investigation is focused on the ligand exchange. Here the goal is set on an increase of the charge mobility in the nanocrystal layer. For this purpose, the same analytical spectroscopy methods are used to investigate the treated, and none treated nanocrystals.
The third part focusses on the enhancement of the stability of the $CsPbI_3$ nanocrystals by incorporating potassium in the system. The incorporation of potassium is investigated by using X-ray diffraction and spectroscopic methods.

5.1 Synthesis

The general synthesis for the $CsPbI_3$ is the hot injection synthesis. The actual quantum dot synthesis takes around 25 seconds, but a precursor had to be synthesised in advanced. For this reason, this method can be divided into several sections. The process will be described in the following subsections for each step.

5.1.1 Precursor synthesis of caesium oleate

The synthesis was performed as found in literature.[23] For the synthesis of caesium oleate, the precursor caesium hydrogen carbonate (Cs_2CO_3) and double the amount of oleic acid in access of 10% were given in a two neck round bottom flask equipped with a stirring bar and a sleeve stopper septa. The high boiling, non coordinating solvent 1-octadecene was added. Then the reaction temperature of the reaction slurry was set to 120°C, and the reaction was kept under vacuum. The reaction was complete when no gas release was observable, and a clear solution was formed. The reaction is considered as quantitative, and no further purification was done. This solution is saturated at room temperature. So before every synthesis, the reaction flask was heated until all Cs-Oleate was dissolved.
The general reaction for synthesizing caesium oleate is an equilibrium reaction. As shown in Figure 5.1 A, the reaction under normal conditions will never completely react to the products.[174] For this reason, the reaction was carried out under vacuum and at 120°C. With that, the equilibrium is shifted towards the desired product. The formed carbon dioxide and water are extracted from the reaction forcing the reaction equilibrium to the side of the product. This is shown in Figure 5.1 B. It should be mentioned that, under ambient air, the Cs-Oleate reacts with CO_2 to form the precursors.

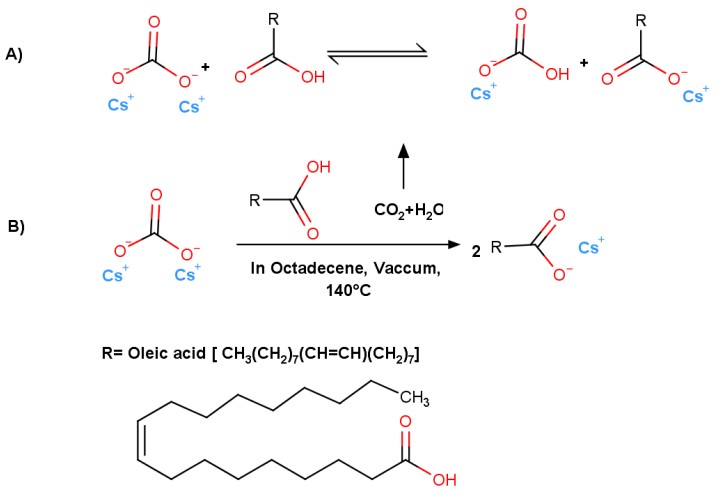

Fig. 5.1: A) Equilibrium reaction of Caesium carbonate with an organic acid
B) Used reaction with the elimination of water and CO_2 during the reaction and shifting the equilibrium to the side of the product. Oleic acid as a molecule is drawn

5.1.2 Precourser synthesis of the lead complex

The synthesis was performed like described in literature.[23, 316] In a three-neck round bottom flask, equipped with a sleeve stopper septa, a thermocouple, a reflux condenser and a stirring bar, placed in a heating mantle, lead(II)iodide (PbI_2) and 1-octadecen were evacuated in a vacuum to remove the impurities (i.e. water, short-chain alkanes etc.). The reaction slurry was heated to around 60°C. During the time the slurry was heated, equal amounts of oleic acid and oleylamine were mixed in a beaker with a stirring bar and heated to 60°C.
As no gas release in the lead(II)iodine slurry was observed, the oleic acid/oleylamine mixture was added to the round bottom flask. The reaction mixture was kept under vacuum and heated at 120°C. After around 20 minutes, the slurry cleared up to a clear, yellow solution. The following reaction was observed.See Equation 5.1.

$$\mathrm{PbI_2 + HOOCR + X\,RNH_2 \longrightarrow PbI_{2-x}\,(OOCR)_x{}^{+}x\,RNHN_3I} \qquad (5.1)$$

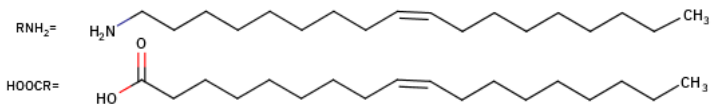

Fig. 5.2: Oleic acid and oleylamine

Lead(II)iodide as an inorganic salt, is a polar substance and not soluble in the reaction solvent 1-octadecen. So a metal complex needs to be formed. For this purpose, oleic acid as a ligand is needed. The oleylamine, which becomes later the task of surfactant, is present and already forming a weak bond to the halide, and is further stabilizing the complex. This metal complex has thermal stability until around 190°C.[23] No further investigations to this complex are described in the literature. The effect of the amino ligand, therefore, cannot be discussed but seems to affect the stability of the lead complex.

5.1.3 Hot injection and purification

The precursor solutions were both heated and well stirred, with the attention, that no precipitation was observable. The lead(II)iodide ligand solution was heated to the desired temperature. In this case to 170°C (size target around 8 nm [316]). After a time of temperature stabilization (around 10 minutes), the Cs-Oleate solution was injected as fast as possible into the lead(II)iodide ligand solution, and instantly a colour change to a dark red was observed. After around 20 seconds [318] the reaction mixture was cooled down in a water bath. The temperature was kept above 70°C to prevent the long-chained byproducts from solidifying. The simplified ionic metathesis reaction is shown in Equation 5.2.[23]

$$2Cs(OOCR) + 3PbI_2 \rightarrow 2CsPbI_3 + Pb(OOCR)_2 \tag{5.2}$$

For simplifying the reaction, the lead(II) iodide stabilizing ligand oleic acid and the oleylamine is not shown. The alkyl chains of the oleic acid and the oleylamine are represented with R. The product $CsPbI_3$ is stabilized with the oleylamine as surfactant/ligand which is not shown in this reaction.
During the reaction, the oleic acid is exchanged against oleylamine, which is assumed to incorporate into the outer perovskite crystal structure. The formed $CsPbI_3$ nanocrystals are caped with oleylamine as a ligand/surfactant. The excess oleic acid forms a complex with not reacted lead.[23]
The mixture was given in a three-fold excess of methyl acetate, to purify the reaction mixture. With that, the nanocrystals are precipitate. Immediately the product was centrifuged at 8000 rpm for 10 minutes. The methyl acetate does not destabilize the $CsPbI_3$ nanocrystals like other organic solvents. A too high concentration of these organic solvents removes the surface ligands and further destabilizes the quantum dots.[316]
After that, the precipitate was separated from the solvent and was redispersed in n-heptane. The centrifugation process was repeated at 8000 rpm for a further 10 minutes. After the second redispersion in n-pentane, the product was filtered through a 0.25 μm syringe filter to remove impurities. The red dispersion was stored in a refrigerator for 48 h, and the dispersion was separated from the reddish/brown precipitation.[23]

5.2 Investigation of the nanocrystals

As a foundation of this chapter, the $CsPbI_3$ quantum dots with oleylamine as ligand are analysed. For this purpose, the shape, size, phase and arrangement on a substrate is analysed. Furthermore, the spectroscopic properties are investigated to investigate the results of the treatment in the second part of the chapter.

5.2.1 Transmission electron microscopy

TEM images were taken and analysed to investigate the nanocrystals. First conclusions about the size, shape and a possible phase could be made. The TEM-image in Figure 5.3 shows around 8 nm squared structures divided by light gaps with a distance of around 2.5 nm.

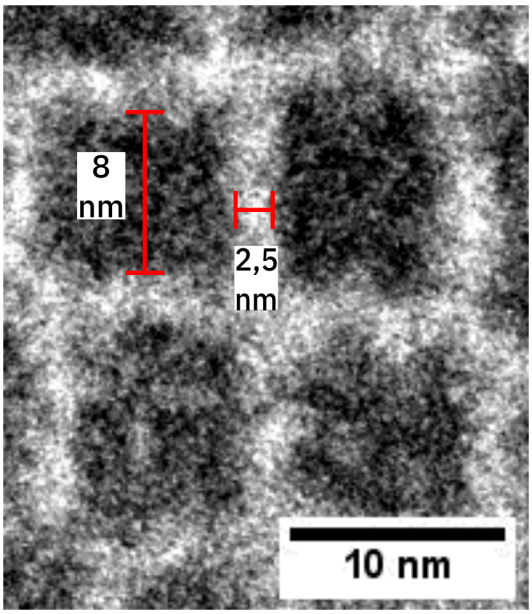

Fig. 5.3: $CsPbI_3$ quantum dots (around 8 nm) arranged in a surrounding of the ligand oleylamine (around 2,5 nm)[1]

If the desired perovskite is formed, it would have high contrast in comparison with the surrounded, organic ligand oleylamine. The perovskite consists of the elements Cs, Pb, I, All elements having a high atomic number with high electron density. The high electron density leads to a dark contrast originating

from the high electron scattering and resulting in a low transmission rate of the electrons. The organic ligand consists of C, H and N, and appear light in the TEM-image. These findings here are comparable to the findings in literature.[23]
As one can already surmise, the quantum dots are surrounded by other quantum dots. In this case, they are forming a self-assembled structure over an extended area (see Figure 5.4).

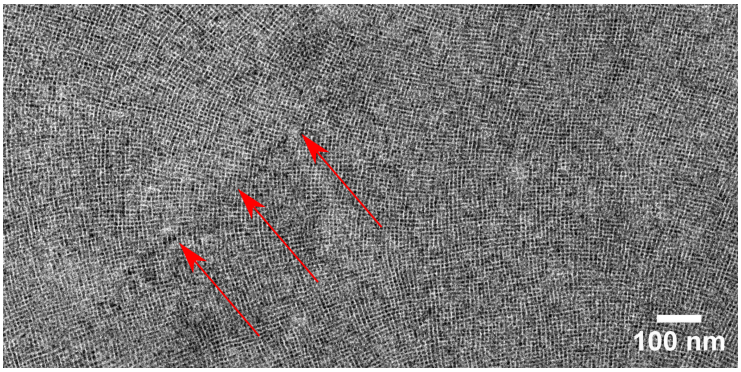

Fig. 5.4: Overview of self-assembled $CsPbI_3$ nanocrystals with a disorientation marked with arrows

Figure 5.4 shows an overview image of the arranged nanocrystals. Visible is also disorientation marked with red arrows. This might result from drying-effects on the TEM-Grid. In addition, an overview image of the sample is given in Figure 5.5

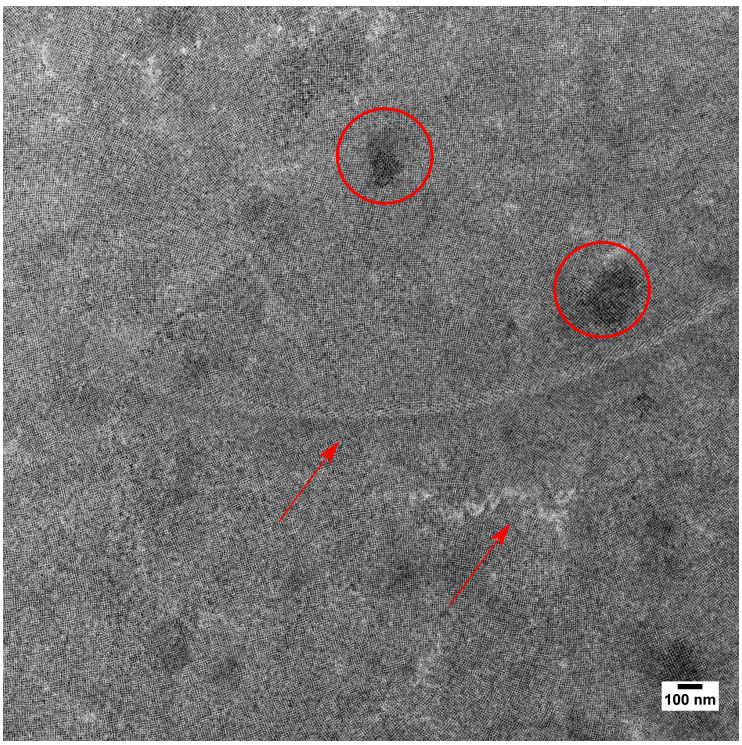

Fig. 5.5: Overview TEM image with red arrows showing drying effects and dark spots showing stacking of several layers of $CsPbI_3$ nanocrystals (red circle)

The self-assembly of the nanocrystals is extended over the whole measured area. Within this image, inhomogeneities of the arranged $CsPbI_3$ nanocrystals are observable (marked with red arrows (in Figure 5.5). Additionally dark spots are observable (marked with red circles in Figure 5.5). The inhomogeneities can be explained by drying-effects of the sample on the TEM-Grid. These effects lead to the observable miss arrangements and defects in the self-assembled structure. The dark spots are likely to be a stack of more than a monolayer on the TEM-Grid. To estimate the particle size and the distance in between the gaps, 1000 quantum dots and additional 1000 gaps in between the quantum dots were measured. The results are shown in Figure 5.6

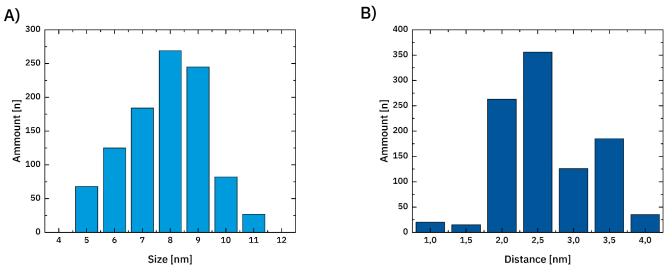

Fig. 5.6: A) Counted size distribution for the $CsPbI_3$quantum dots (n=1000) B) Counted length distribution of the gap in between the $CsPbI_3$ quantum dots

The size distribution shown in Figure 5.6 A of the $CsPbI_3$ nanocrystals is in a range of 5-11 nm. The mean distribution is showing two dominant sizes of 8 and 9 nm. The gap distance distribution is shown in Figure 5.6 B. Here, the distribution is in a region of 1 to 4 nm. As for the quantum dot size, here also two main distances are observable with 2 and 2.5 nm.

As expected from the hot injection method, narrow size distribution is acquired. The average size is around 7.8 nm. Additionally to that it seems that two main sizes are observable. This observation might be explainable with a different shape, then the expected square (in 3D, cubic) shape. The gap between the nanoparticles is around 2 - 2.5 nm wide, with also two main distributions. These findings are adding up to the explanation of the different shape. Additionally to this finding, the gap in between the quantum dots nearly resembles the size of oleylamine. The alkyl chain length of 2,04 nm is found in literature.[319, 320] This fits well to the assumption that the stretched alkyl chain of the oleylamine is forming a nearly fully incorporated alkyl chain layer.

A fast Fourier transformation (FFT) of the whole image Figure 5.5 was carried out. Additionally an integration over the area of the FFT was carried out.(see Figure 5.7)

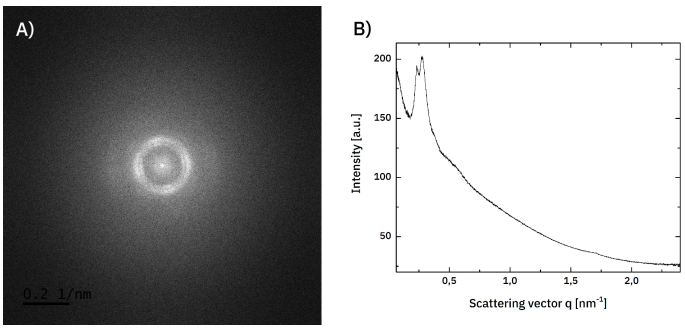

Fig. 5.7: A) Resulting FFT of the overview image B) Area integration over the FFT

The FFT in Figure 5.7 A shows two circles with a thickening on four sides and a wider circle surrounding the two inner circles. The area integral Figure 5.7 B is showing a double signal at 0.23 and 0.27 nm^{-1}. The double circle of the FFT fits well to the observation made at the particle and gap distance distribution.In all three analysis made above two main distributions are observable. From the area integral the centre-to-centre distance could be calculated with $d_1 = 13.5$nm and $d_2 = 11.2$nm. These values are slightly off the values found by counting the particles. The above-described defects in the self-assembled structure could explain this observation, which leads to a higher centre to centre distance than calculated. In addition to this, the resolution of the image is fairly low. With that, an uncertainty at the edges of the particles leads to an additional error. The two distances between the particles can be explained by assuming a rectangular shape (a 3D, cuboid structure) of the particles, rather then a square shape(for a 3D, cubic model). The four thicker parts of the FFT indicates a rectangular shape of the particles, which is smeared out because of the defects in the self-assembled structure.

To conclude, the TEM images are compared with the findings in literature.[23, 197, 316] The size of the here synthesized nanocrystals, shows two main distributions of 8 and 9 nm. The distance of the gaps is also distributed at two separate distributions of 2 and 2.5 nm. The FFT is supporting the finding by showing two separate circles. The area integration of the FFT results in a centre to centre distance of $d_1 = 13.5$ nm and $d_2 = 11.2$ nm. These values are slightly off in comparison to the measured values. The reason could be found in the defects in the self-assembly and the low resolution of the image. The explanation of the two found sizes can be explained by assuming non cubic nanoparticles, rather then rectangular or in 3D terms a cuboid. The difference in shape might be explainable with a different phase than the in

the literature discussed α-cubic crystal structure.[197] For investigating the crystal structure, high-resolution TEM-Images cannot be provided. Therefore further investigations are needed to support the here found results.

5.2.2 X-ray diffraction and phase

The findings in the previous section are indicating a different phase, than the α $CsPbI_3$ perovskite structure, suggested in literature.[197] The discussion about the phase is extended in literature.[23, 321, 322, 323] For the red $CsPbI_3$ nanocrystals the non perovskite δ-phase can be excluded because of the yellow appearance.[77] The different phases involved in the discussion are shown in Figure 5.8

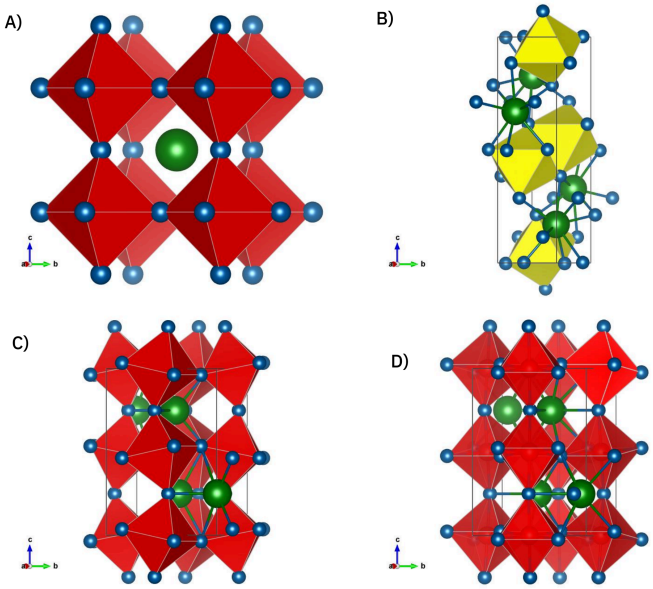

Fig. 5.8: A) α-cubic phase B) Non perovskite δ-Phase C) γ-phase (orthorhombic) D) γ-phase (nanotwins)

Besides the α $CsPbI_3$ crystal structure, also more disordered structures like the γ $CsPbI_3$ phase are described.[114] In the literature the $CsPbI_3$ nanocrystals are often described as a cubic α perovskite structure.[23, 316] Furthermore, the orthorombic γ perovskite structure might also be present.[322] But due to the reduction in size, the XRD pattern results in broad signals with a large amount of diffuse scattering. Additionally the difference in the XRD pattern of the possible crystal structures is quite narrow.[119] This exacerbated the

analysis of the nanocrystal crystal structure. A LeBaile fit of the cubic α $CsPbI_3$ phase is shown in Figure 5.9 A additionally the same measurement with the nanotwin [119] fit is shown in Figure 5.9 B.

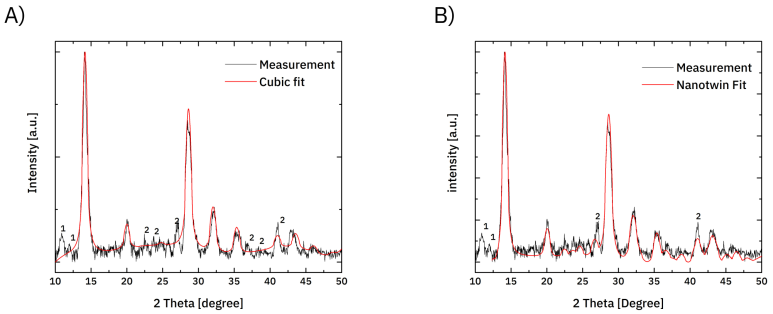

Fig. 5.9: GIXRD-Measurement with the cubic LeBaile fit in A) and the same measurement with the nanotwin LeBaile fit in B

As expected, the XRD of the nanocrystals results in broad signals. The pattern resembles the findings in literature [23] even though the intensity of the first signal at 10° 2θ is significantly higher than in the literature. This might come from the here used GIXRD technique on a thin film, which varies from that in the literature [23] used powder diffraction, spinning method. The LeBail fit of the cubic phase does not include the signals between 20 and 25° 2θ and between 35 and 40° 2θ marked with 2 in Figure 5.9. For that reason, the cubic phase is not suitable for the nanoparticles. These observations are also fitting to the TEM-image observation of a non-cubic structure but more cuboid structure.

In comparison to that, Bertolotti et al.[119] suggested a modified γ-phase the so-called nanotwin structure. The space group for the nanotwin structure is $Pbnm$ with lattice parameters of a=8.61 Å b=8.84 Å c= 12.52 Å.[119] The LeBail fit is shown in Figure 5.9 B. This fit is more suitable for the system, even though the first two peaks cannot be assigned.

As an explanation for the confusion in the literature, the high dynamics inside the $CsPbI_3$ perovskite structure can be used.[324, 325] Therefore the perovskite structure appears cubic but fluctuates to non-cubic structures. Bertolotti et al.[119] suggest that the high fluctuation leads to orthorhombic subdomains hinged through the 2D or 3D network by the formation of twin boundaries through the whole nanocrystals. These findings are based on a Debye scattering equation/atomic pair distribution function approach, explained else-where.[119, 326] The findings of the different nanocrystals

shapes in the TEM-image supports the observation of Bertolotti et al.[119] the γ-phase perovskite phase would result in cuboid-shaped nanocrystals. In addition to the here fitted signals of the nanotwin phase, two marked signals at around 27° and 42° seems not to fit by their intensities. This can be explained by adding the caesium rich, Cs_4PbI_6 phase.[327] (see Figure 5.10)

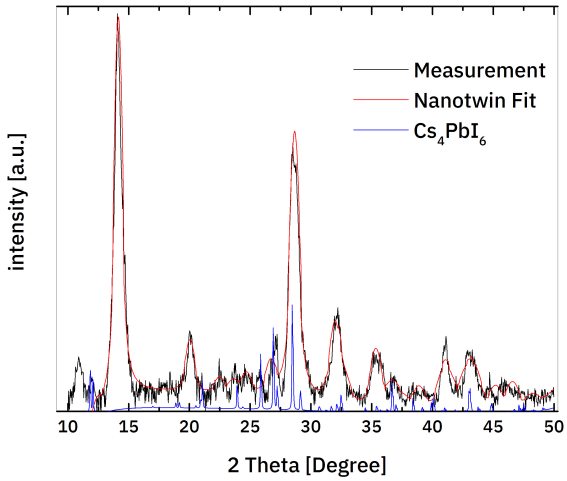

Fig. 5.10: XRD pattern of the $CsPbI_3$ quantum dots with the nanotwin fit and additional peaks of the caesium rich Cs_4PbI_6 perovskite

Additionally at lower angles, the XRD-Pattern is showing signals, which cannot be assigned. For the lattice parameters of the fit, the results are given with a=8,693 Å b=8,822 Å c= 12,452 Å. The variations of these values can be explained with the different size of the nanocrystals used here. In the literature [119], 10 nm nanocrystals were used, while in this thesis, 8 nm nanocrystals are investigated. Therefore the surface/volume ratio is higher for the here investigated quantum dots. Furthermore, the surface of the quantum dot with its incorporated ligand (oleylamine) might occur with a different unit cell expansion. This leads to a variation in the lattice parameter values. From the broader signals of the nanocrystals, the size of these could be calculated using the Scherrer equation. As a result, a size of 7.9 nm was determined, which fits well to the results of the TEM-images.

To conclude, the findings of the different, nanotwin crystal phase adds up to the findings in the here investigated TEM-Images (subsection 5.2.1). In

a cubic system, a square shape would be assumed. This is not the case, the findings here extracted of the TEM-Images, are suggesting a different phase, which fits well to the findings of Bertolotti et al.[119] The slightly off results of the LeBaile fit can be explained by the different size of the here used nanocrystals with a higher surface to volume ratio.In addition to that some peaks lead to the suggestion of a present Cs rich crystal structure. Nevertheless, the nanotwin crystal structure is applied for further investigations in this thesis. Furthermore, by calculating the size of the nanocrystals with the Scherrer equation, 7.9 nm could be acquired. This fits very well to the findings of the TEM-image investigation.

5.2.3 X-ray and neutron reflectivity

For a further investigation regarding the self-assembly of the $CsPbI_3$ nanocrystal, X-ray reflectivity (XRR) measurements were conducted. These give insights into the arrangement of the nano cuboids in the Z-axis (orthogonal to the substrate). A silicon wafer with a size of 5*5 cm was used. The X-direction has 5 cm and the Y-direction has 3.5 cm, with an area of 17.5 cm^2 shown in Figure 5.11A. The resulting XRR-pattern is shown in Figure 5.11 B.

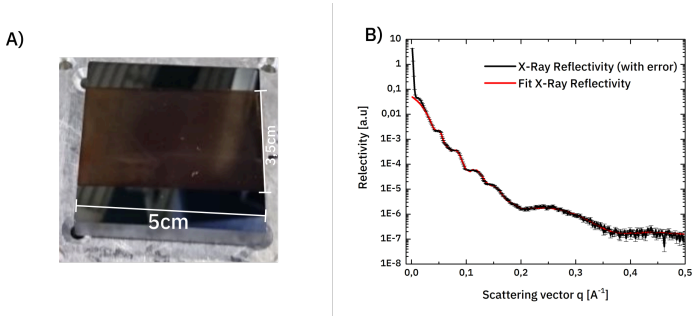

Fig. 5.11: A) Resulting XRR measument with corresponding fit B) Sample with the observed size

A decay in Figure 5.11 B with narrow fringes towards lower q are visible. In higher q-ranges, the fringes get broader. Previous to analysing the data, the scattering length density for pure $CsPbI_3$ and the ligand oleylamine were calculated by the composition and the density. (See Table 5.1)

Tab. 5.1: Scattering length density of $CsPbI_3$ and oleylamine

Substance	Composition	Density [$\frac{g}{cm^3}$]	X-Ray-SLD [$\frac{10^{-6}}{2}$]	Neutron SLD
$CsPbI_3$	$CsPbI_3$	5.05 [114]	34.120	1.276
Oleylamine	$C_8H_{19}N$	0.813 [328]	7.598	-0.31
Air/Vaccum	-	-	0.0	0.0

The scattering length density is calculated by using the density of the substance. The density of the perovskite nanocrystals is not accessible here. So the density for a solid, bulk phase was taken, found in literature.[114]
To limit the fitting algorithm the total layer thickness of the perovskite nano cuboids need to be estimated. The softness of the layer made it impossible to estimate the thickness of the layer with a mechanical method (profilometer). Estimating the thickness of the sample by scanning electron microscope was also not successful because of a high charging of the layer. So a scanning laser microscope [329] was used to determine the thickness of the sample layer. This measurement is shown in Figure 5.12.

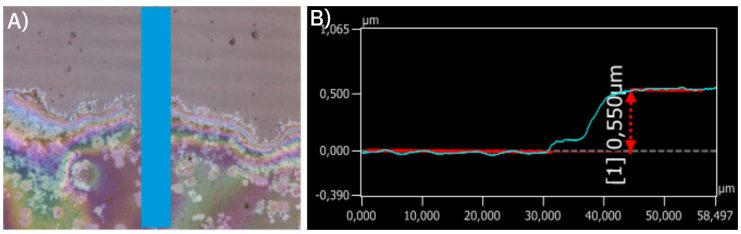

Fig. 5.12: A) Laser microscope measurement B) profile of the thickness

The laser scanning microscope gave an average thickness of 550 nm at the edge. This value was used for limiting the fit of the XRR profile. For this purpose the fit was performed by the Igor plugin Motofit [2].[251] The resulting XRR profile is shown in Figure 5.13.

[2]The fit of the 240 parameters was carried out by Arne Ronneburg

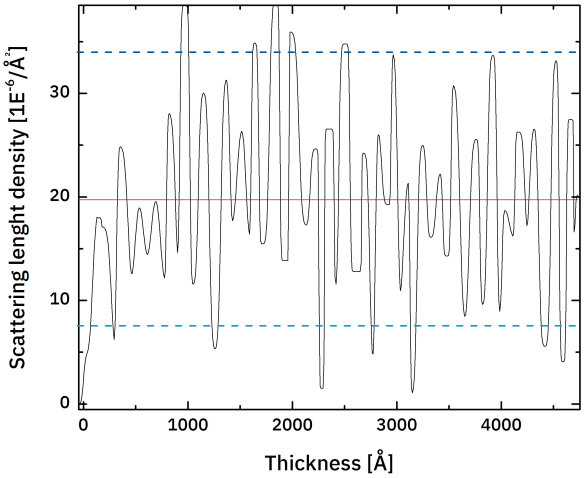

Fig. 5.13: Scattering length density of the measured $CsPbI_3$ nano cuboids

The results of the thickness measurement with the laser microscope and the XRR varies. The first approach to explain this variation is the difference in the measurement method. While the laser microscope is measuring a single line, the XRR is integrating over the whole sample. Nevertheless, the variation is too significant for this explanation. It is more likely, that the variation results from the high X-ray absorption of the heavy elements Cs, I and Pb. On top at around 34.12 $\frac{10^{-6}}{2}$ is the perovskite SLD marked (in Figure 5.13). The full SLD is not always reached. This could be explained with drying-effects like seen in the TEM-images. Air/vacuum in the vacancies of the self-assembled cubes would interfere with the SLD of the perovskite. The reason is in the definition of the SLD of a multi atom system, which is described as.[198]

$$SLD_{1,2} = \frac{V_1 \cdot SLD_1 + V_2 \cdot SLD_2}{V_1 + V_2} \tag{5.3}$$

In Equation 5.3, the SLD of two atoms is given as an example. Here V is described as the volume of atom 1 and 2 and the SLD of atom 1 and 2. As a result, the assumption of a stacked-layer in three dimensions can be made, with minor vacancies due to drying-effects. Additionally the density of the $CsPbI_3$ in the nano cuboids is here not accessible and by considering the higher inner pressure of the system (see Phase transition and Nanoparticles on the example of melting point depression subsection 2.3.3), the density

might be higher, which leads to a higher SLD.
For the ligand oleylamine, with an estimated SLD of 7.59 10^{-6}/Å^2 larger and smaller SLD are observed. The SLD smaller than the SLD of the oleylamine might be explainable with trapped air or vacuum in the layer. The free-moving alkyl chains of the ligand, probably do not always align perfectly. So internally defects can be expected. In general, the SLD surpasses the expected SLD of the oleylamine. The calculation of the SLD could explain this observation. The SLD of a multi atom system is calculated based on the density of the molecule. The density of the unordered liquid was used. However, because self-assembly is observed, the ligand might assemble in a layered structure and therefore, the density increases. With that, the total SLD might also increase. Even though the resulting high fluctuation of the SLD seems to imply a high unordered system on first sight. The self-assembly in the system for an expanded sample size is high, with only minor vacancies. A possible error, which needs to be taken into account could be the X-Ray absorption of the heavy elements Cs, Pb, and I. This could be solved by measuring with a complementary method with a non-absorbing beam. This was done here with neutron reflectometry.
For neutrons, the SLD is changing, to different values (Table 5.1). The same sample was used, but due to limitation factors like a significantly lower flux ($\Phi_{neutrons} = 1 \cdot E^5$ versus $\Phi_{X-rays} = 1 \cdot E^8$) and limited time at the beamline, the same amount of points could not be measured.
Nevertheless, the measurement should be comparable to the X-ray measurement. The results of the XRR measurements were applied to fit the neutron reflection data. The fit is not fitting the measured curve like in the XRR data. The resulting SLD as a function of thickness changes in comparison to the XRR data. Besides the expected change in SLD and a lower contrast as with the XRR data, also the variation in SLD seems to be higher. The reduced and corrected data collected at V6 are shown with a fit and the resulting SLD as a function of the thickness is shown in Figure 5.14. [3]

[3] the data reduction and the correction of the neutron reflectivity data were carried out by the beamline scientist Dr.Luca Silvi, and Arne Ronneburg performed the fitting of the data with the known values of the XRR fit

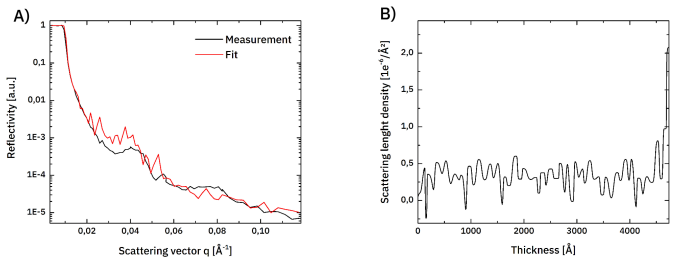

Fig. 5.14: A) Neutron reflectometrie data with fit B) resulting SLD

The method was used to observe changes in the system with a complementary method. The unsatisfying convergence of the fit from the XRR measurement applied to the NR data can be explained with the high X-ray absorption of the X-rays. The XRR fit seems to be defective. However, the relative constant fluctuation of the samples is showing an evenly distributed self-assembled structure over the whole substrate. Small vacancies lead to variations of the SLD over the whole sample. The method is suitable for analysing and comparing differences quantitatively.

To conclude the layer formation of $CsPbI_3$ was investigated by XRR measurement. A high degree of self-assembly could be determined. Despite the high degree of self-assembly, a certain amount of defects could be observed. This can be seen as typical for a nano arrangement in this size of the expansion. Nevertheless, the high X-ray absorptivity of the $CsPbI_3$ leads to high uncertainty of the found values. Therefore neutron reflectometry was used. These measurements adds to the conclusion that the high X-ray absorptivity leads to a high error in the XRR measurement.

5.2.4 Optical Properties

In this subsection, the optical properties of the pure $CsPbI_3$ shall be discussed. For this purpose, the dispersion of the $CsPbI_3$ Nanocrystal was analysed first. The layered structure was analysed, later.

For estimating the band gap of the sample, absorption and photoluminescence (Pl) measurements[4] were conducted. Additionally a photo of the sample during the Pl-measurement is shown to present the high absorptivity

[4]Dr. Sergiu Levcenco performed the PL measurement

and emission of the 0.1 mg/mL $CsPbI_3$ nano cuboids in octane dispersion.Figure 5.15

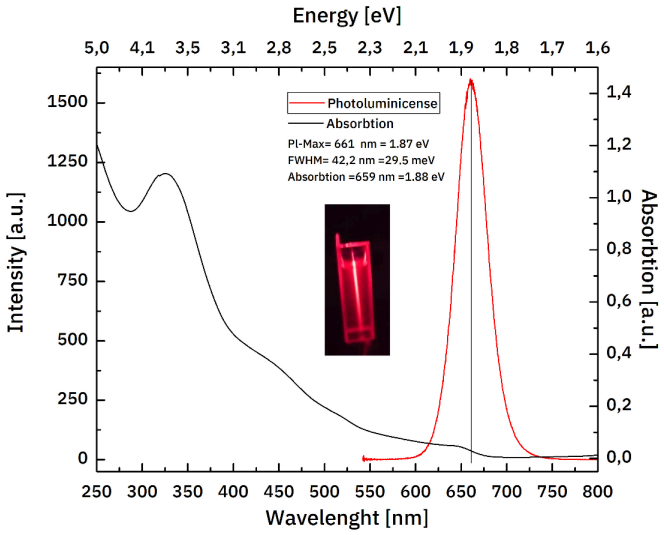

Fig. 5.15: A) Absorption and emission spectra of a 0,1mg/1mL dispersion of $CsPbI_3$ nanocrystals in octane as dispersion with photo of the emission B) Normalized absorption spectra of the $CsPbI_3$ nanocrystal in comparison to pure oleylamine

The absorption onset is extracted by the first derivation of the absorption spectra. With that a onset of $\lambda_{\text{onset}} = 660$ nm = 1.877 eV is found. This is an as expected shift with the cause being quantum confinement. Due to the low concentration in the dispersion, the excitonic feature is only signified. Towards lower wavelengths at around $\lambda = 441$ nm or 2.81 eV and $\lambda =$ 328 nm or 3.78 eV two bands are observable. The origin of both bands remains unclear. An explanation could be a higher excitation caused by the ligand oleylamine. This is described for CdS and CdSe nanoparticles.[330] Another explanation for the observed unclear bands might be the presence of the caesium rich phase Cs_4PbI_6.[331] However, these bands are also shifted towards higher energies in comparison to the observed absorption spectra. Furthermore, investigations could not be done in this thesis. Therefore only the described explanations are given.
The emission is as expected red-shifted to $\lambda_{em} = 661$ nm = 1.875 eV with a FWHM= 42 nm = 29.8 meV. This is comparable to the findings in literature.[23]

Further, time-resolved photoluminescence measurements[5] were carried out and are shown in.Figure 5.16

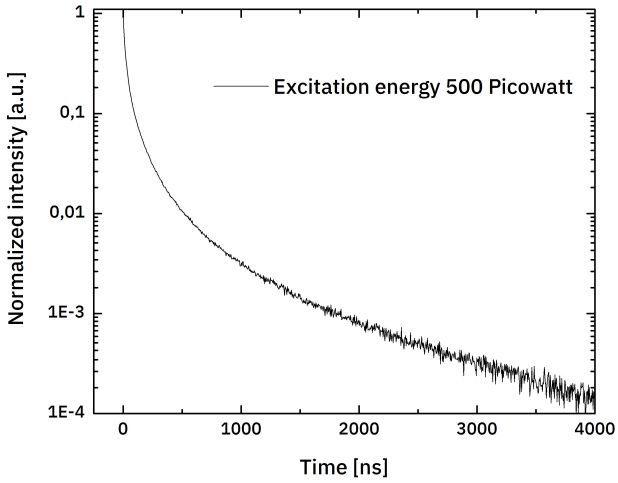

Fig. 5.16: Normalized time resolved photoluminescence measurement with an excitation energy of 500 pico watt]

The quantum yield in dispersion found in literature [316] is stated with a value of around 55%. Therefore it can be assumed that the majority of the observed emission is radiative.
In comparison to a vapour-deposited $CsPbI_3$ film (tens of microseconds) [332], the lifetime of the here measured sample is significantly smaller. The decay is divided into two separate decays. The first is a rapid decay during the first hundred nanoseconds. After around 100 ns, 99% of charge carriers are radiatively recombined. After this decay, a longer decay process can be interpreted. Unfortunately, this decay could not be fitted.(see Appendix) An explanation, therefore, could be found in the unknown and until this point unusual processes inside the perovskite quantum dots.[316]
The high quantum yield can be explained with the high charge carrier density, which could be explained by the small size of around 8 nm of the nanocrystal. If a photon excites an electron the charge carrier density is at around $10^{18} \cdot cm^{-3}$ which is comparably high (for evaporated $CsPbI_3$ $10^{15} \cdot cm^{-3}$ [332]). The high density of insulating ligand hinders the transport of charge carriers. Additionally the transfer of a charge carrier from one quantum dot to another quantum dot is unlikely due to the low concentration inside the

[5]Dr.Sergiu Levcenco performed the TRPL measurement

dispersion. So the majority of the recombination is occurring on a limited volume inside the quantum dot. This explains the fast radiative decay at the beginning. Moreover, the significantly smaller lifetime in comparison to a vapour-deposited $CsPbI_3$ film.
Assumptions can discuss the longer decay of around 1 %. First the quantum dot is not only consisting out of the volume phase. The surface is also adding a significantly proportion of the nanostructure, which differs of the volume phase. This is discussed above in subsection 5.2.2 for the quantum dot. The phase of the outer layer, therefore, is dominated by the ammonium group of the oleylammonium heat group.[333] This leads to a size reduction of the unit cell [317] which influences the band gap.[334] An illustration of the quantum dot is given in Figure 5.17

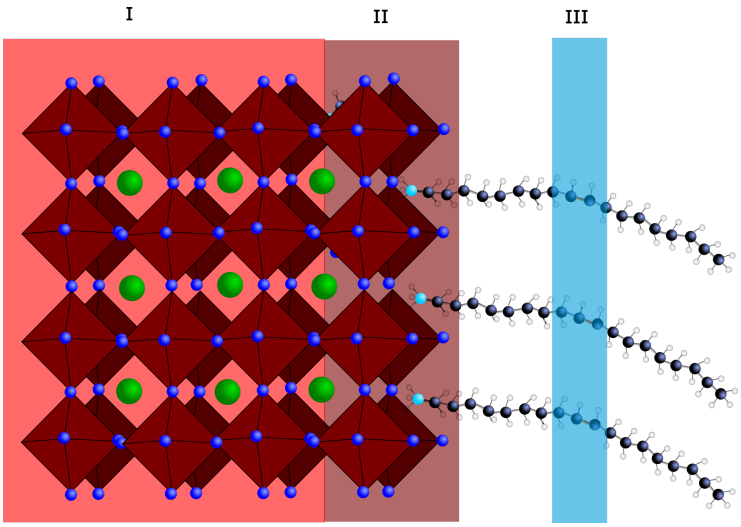

Fig. 5.17: Model of the surface of a quantum dot. I) volume part II) surface III) double bond

In Figure 5.17, a section of a quantum dot is given. Here the bulk of the quantum dot (I), the surface (II) with the oleylammonium (III) is shown. One possibility is the transfer of the charge carrier to the surface layer of the quantum dot caused by the different band alignments. Possible surface recombination might also be present there, but shall not be further discussed. Another possibility is a charge transfer to the double bond of the oleylammonium. The double bond has in comparison to the perovskite insulating effects with a band gap energy of E_{Bg} 6eV. Tunnelling to the double bond is unlikely. A transfer from one to another quantum dot is, as discussed above, unlikely. The longer decay of the nanoparticles cannot be evidence-based explained

at this point. An exponential fit or a different fit could not be applied. The $CsPbI_3$nano cuboid system seems to complex, for a "simple" analysis.

Besides the dispersion, a layer of the quantum dots was investigated. Therefore the dispersion was spin-coated on glass. A measured PL-spectra of the layer in comparison to the dispersion is shown in Figure 5.18

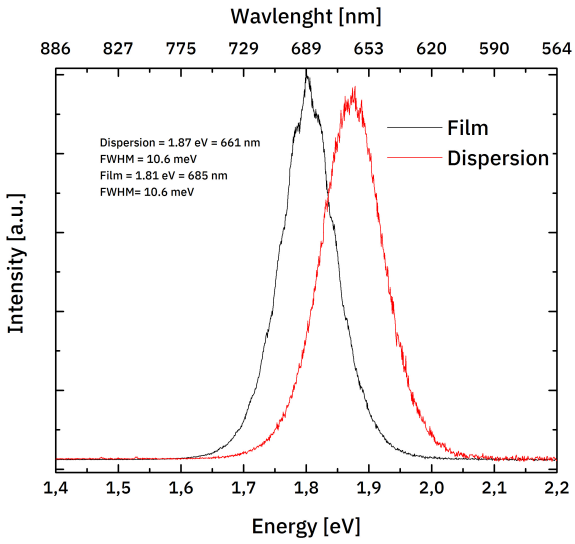

Fig. 5.18: Pl measurement in comparing a normalized $CsPbI_3$ layer and a normalized $CsPbI_3$ dispersion spectra

The Pl max of the layer is shifted towards lower energies, while the FWHM is not changing. The shift towards lower energies can be explained by the formation of a quantum well, moreover, a possible quenching inside the layer.[63] Further, a change of the density of states might occur, since the quantum dots are here close together.[63] The constant FWHM is indicating no further change in the distribution of the nanoparticles.
The quantum efficiency of the layered quantum dots is Pl_{EQE}= 5.6% a ten-fold lower than that reported in the literature.[316] The reason could be found in the different sample configuration. While the literature was investigating the quantum dots in dispersion, here we observed the quantum efficiency in a layer. This leads to a lower intensity caused by the formation of a quantum well [63] Additionally TRPL measurements with an excitation energy of 500 pico watts were conducted and are shown in Figure 5.19

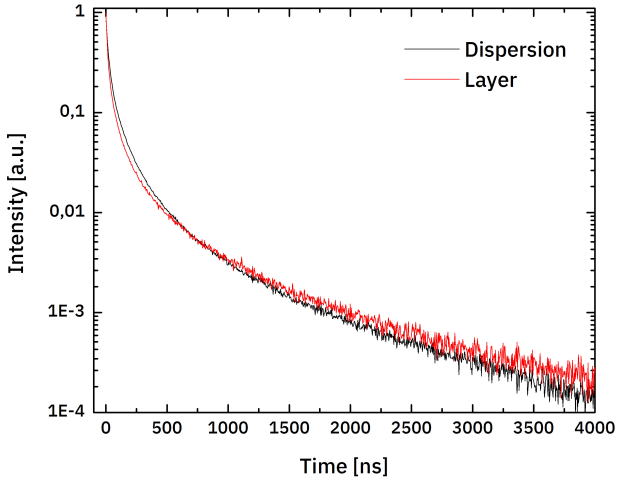

Fig. 5.19: Normalized TRPL measurement of the dispersion and a layer of $CsPbI_3$ quantum dots

Here the differences are minor but observable. The first decay of the layer is faster in comparison to the dispersion. The second decay, on the other hand, is slower. This gets distinct at around 700 ns, at which time the layer decay is crossing the dispersion decay. As seen in the dispersion, the majority (99,99%) of the charge carriers recombine inside the quantum dot. A few charge carriers surpass the ligand by tunnelling. For this reason, it is to mention that the tunnelling distance for an electron of 2 nm is unlikely. This could explain the few charge carriers which surpass the insulating ligand. Another possibility, which increases the likely hood of the tunnelling might be the double bond found in the oleylamine ligand. With that, the double bound might serve as an aid for the charge carrier transport. In the next quantum dot, they can recombine. The second recombination process cannot be determined here. A model for the ongoing process is illustrated at Figure 5.20

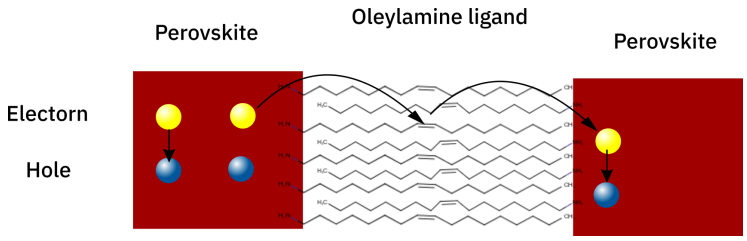

Fig. 5.20: Model drawing of the recombination process inside a $CsPbI_3$ quantum dot layer

The confined conductivity furthermore is represented in the optical pump terahertz probe measurement [6]. The measurement of the quantum dots is compared with a polycrystalline $CsPbI_3$ film [7] shown in Figure 5.21

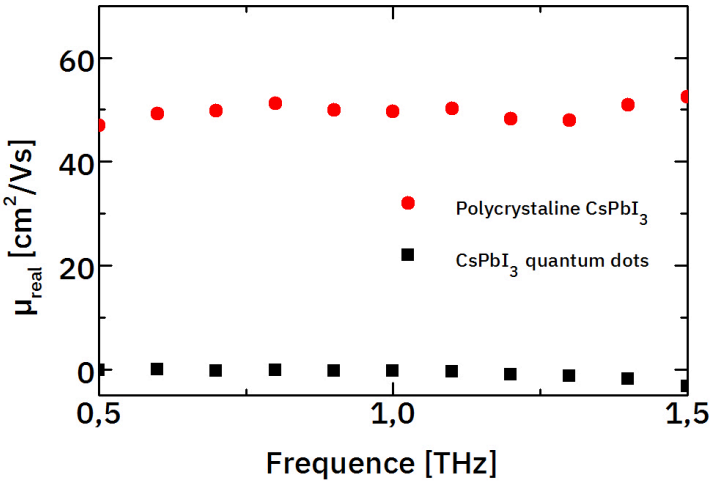

Fig. 5.21: Tera Hertz spectrum of polycrystaline $CsPbI_3$ and a ligand caped quantum dot assembly

The spectra are showing the differences in charge carrier conductivity in between the polycrystalline film and the $CsPbI_3$ quantum dots. Within this measurement the significantly higher conductivity in the polycrystalline film (μ =48 $cm^2/V \cdot s$) is revealed in contrast to the quantum dots (μ=0.2 $cm^2/V \cdot s$)). This adds to the explanation of the insulation ligand and the good intra dot conductivity but bad inter dot conductivity. The ligand is hindering the good conductivity inside the quantum dot assembly.

[6]The measurement was performed and analysed by Hannes Hempel
[7]The polycrystalline $CsPbI_3$ film was produced by Pascal Becker by physical vapour deposition

The optical properties of the samples are comparable to the findings in literature.[23, 316] Furthermore, the time-dependent photoluminescence measurements are discussed. By a layer formation of the quantum dot dispersion, the Pl position is shifted towards lower energies, which can be explained with a formation of a quantum well.[63] Also, the quantum efficiency is decreasing. The reason, therefore, is again the formation of quantum well and a quenching of the Pl intensity.[63]
The TRPL measurement reveals two differential decays. The first decay represents the majority of the charge carriers and can be explained with the inter quantum dot recombination. The second decay is significantly longer. An evident based explanation could not be found since a fitting of the measured data was not possible. The same can be applied here to the layer. Furthermore, investigations in this direction could not be given. As of the last method in this subsection, the OPTP measurement reveals the low conductivity of the perovskite quantum dots in comparison to a PVD- $CsPbI_3$ film.

5.3 Ligand exchange for a higher charge mobility

As seen in the previous section, the main recombinations are occurring inside the quantum dot nanocrystals. An inter dot transportation is unlikely, which results in a poor extraction of electrons and with that poor solar cells[335]. For this reason, the group of Swarnkar et al.[197] performed a ligand exchange, which shall be the foundation of further investigation in this thesis. In this section first, the exchange method is described and analysed, and further other exchanged methods are performed to increase the interdot charge carrier transport.

5.3.1 Ligand exchange procedure

The ligand exchange procedure was performed after the method described in the literature.[197]. Methyl acetate was used to remove the oleylamine

ligand.[316] This was done by preparing a spin-coated layer of $CsPbI_3$ on glass and dipping the substrate with the sample film into methyl acetate. Subsequently, the sample was dipped into a solution of different salts (lead(II)nitrate ($Pb(NO_3)_2$) and/or Formamidinium iodide (FaI)). After drying, the spin-coating was repeated, and another cycle of ligand exchanges was done. The process is illustrated in Figure 5.22

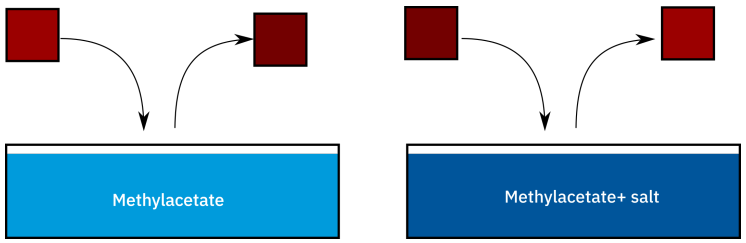

Fig. 5.22: Illustration of the ligand exchange process

During the ligand exchange process, the perovskite structure is known to stay stable. The stability is explained with the high surface energy of the quantum dots.[197, 316] Therefore the next step of implementing a new ligand becomes possible. For the following discussions, two different exchange procedures were used. The first one was the removal of the oleylamine and exchanging the ligand against formamidinium iodide (FAI) by dipping the sample in a with FAI saturated solution of methyl acetate. The second was in the same procedure, but additional with a washing process with a saturated solution of lead(II)nitrate in methyl acetate was used.

5.3.2 Transmission electron microscope analysis

This section will investigate the treated samples by TEM measurements. The challenge here was to prepare the sample on a TEM-Grid. Spin coating delivered to thick layers for the TEM analysis, so transmission of electrons was not possible. With a single layer of nano cuboids, most washing attempts result in a blank TEM-Grid. One TEM-Grid of the FaI treated sample allowed investigating the samples further. To compare the result first of all to a already shown TEM image from subsection 5.2.1 showing the $CsPbI_3$ nano cubois is presented in Figure 5.23

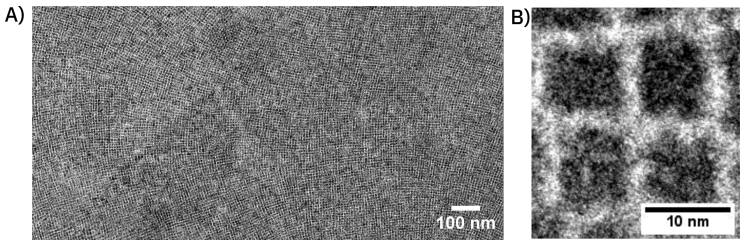

Fig. 5.23: A) Overview of the Self assembled $CsPbI_3$ nano cuboids B) Zoom on 4 $CsPbI_3$ nano cuboids

This shows the broad expansion of the self-assembled $CsPbI_3$ nanocrystals. In addition to that, a clear separation of the single nanocrystals is observable. In comparison to that the with FaI solution washed sample is shown in Figure 5.24

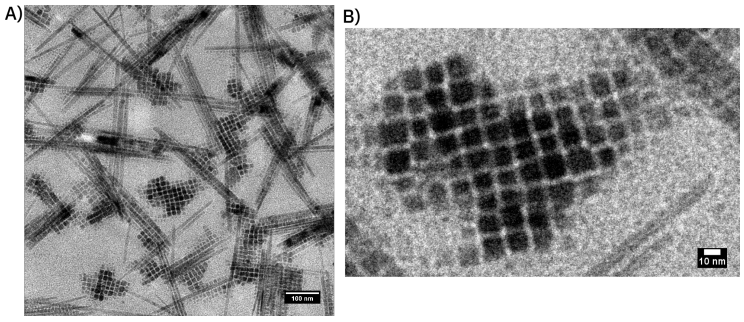

Fig. 5.24: A) Overview image of the FaI washed sample B) magnification of a array of FaI treated quantum dots

Figure 5.24 A is showing an overview of the nano cuboids film washed with FaI solution. Here nano cuboids in arrays are observable distributed over the grid. Furthermore, large needle-like structures are observable. These could be discussed as formamidinium iodide crystals.Figure 5.24 B is showing a magnification of the overview image. Here the nano cuboid structure can be seen.

In comparison to the image of the pure nano cuboids, the gap between the nano cuboids is lower in contrast. This could indicate the formation of a connecting structure between the nanocrystals. The size of 100 nano cuboids was measured and is shown in Figure 5.25. The distances between the structures could not be measured because of the uncertainty of the gap size.

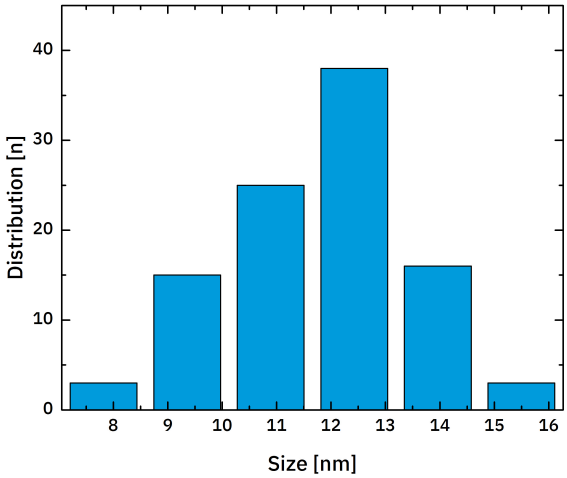

Fig. 5.25: Size distribution of FaI solution treated $CsPbI_3$ nano cuboids

The distribution of 100 nano cuboids results in a slightly shifted size. Instead of 8 nm measured for the pure, untreated nanocuboids, 12.5 nm seems to be the average size for the treated nano cuboids. An FFT measurement could not be performed, since the amount of quantum dots were to little. In addition the contrast of the quantum dots in comparison to the gap was too low. Unfortunately, no images of the treatment with FAI and $Pb(NO_3)_2$ could be collected because of the challenge, as mentioned earlier.

As a conclusion of the TEM investigation, the arrangement of the FaI treated samples seems to be changed. Additionally to the nano cuboids, needle-like structures are occurring, which could be assumed to be formamidinium iodide. The gap in between the nano cuboids are showing a lower contrast in comparison to the pure nano cuboids. Additionally the FaI treated samples are enlarged in size. Both results lead to the conclusion that in between the nanostructures, a connection is implemented. A further investigation by X-ray diffraction might deliver more data concerning the hypothesis.

5.3.3 X-Ray Diffraction analysis of the treated samples

In this section, the treated samples are investigated by X-ray diffraction. The focus here is on a potential change in the quantum dot structure and size and

furthermore on the previously in the TEM analysis discovered size increase by the treatment with formamidinium iodide.
As discussed in *X-ray diffraction and phase*(subsection 5.2.2) the phase of the $CsPbI_3$ was investigated by the nanotwin phase described in literature.[119]. The LeBail fit extracted unit cell sizes of each treated sample are shown in Figure 5.26. Furthermore, the unit cell size of formamidinium lead triiodide ($FaPbI_3$) is shown, so a possible formation of the $FaPbI_3$ between the $CsPbI_3$ quantum dots can be investigated.

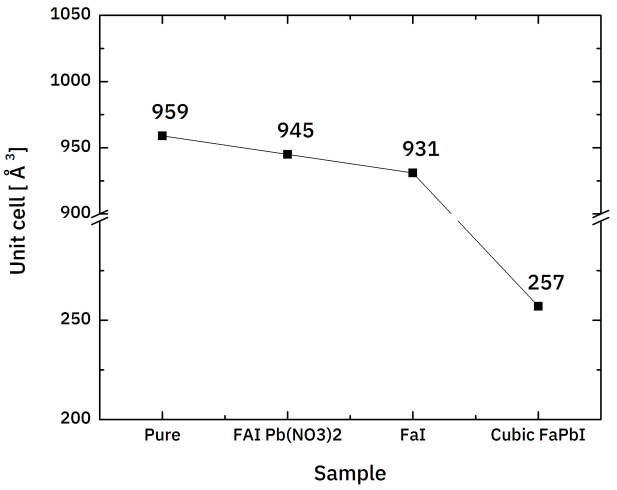

Fig. 5.26: Extracted Unitcell sizes for the $CsPbI_3$ samples with a reference of the $FaPbI_3$ cubic crystal structure [336] (pattern in Appendix)

In Figure 5.26 a clear decay towards the formamidinium lead iodide ($FaPbI_3$) unit cell is to observed. It is known from the literature, that $CsPbI_3$ is forming an alloy with $FaPbI_3$.[75] The concentration of $FaPbI_3$ in comparison to $CsPbI_3$ is assumed to be significantly lower. A direct comparison to the literature is therefore not possible. However, the clear declining trend in the unit cell size is showing possible intercalation of the $FaPbI_3$. The cubic $FaPbI_3$ phase [336] seems to be the most suitable. The trend is further indicating that an incorporation of the formamidinium iodide in the $CsPbI_3$ quantum dots by the addition of lead(II)nitrate is reduced. An explanation for this might be the passivation of the surface with nitrate ions.[337] Unfortunately, the signals of the $FaPbI_3$ in the XRD pattern are overlayed by the broad signals of the $CsPbI_3$ nanocrystals. The peak broadening was further investigated.

From this, the nanocrystal sizes were calculated by the Scherrer equation. The results are shown in Table 5.2

Tab. 5.2: Calculated sizes with Scherrer equation for the different treatments

Sample	Size in nm
Pure	8
FaI+ $Pb(NO_3$	8.5
FaI	13

The results from the Scherrer equation are showing an increase in nanocrystal size. Therewith the increase of size for the treatment with formamidinium iodide is the most remarkable. With 13 nm the quantum confinement should not be present.[23]

To conclude this section, even if the challenging character of the quantum dots are hindering a complete analysis of the system, some information could be extracted. The formamidinium iodide seems to influence the unit cell size. This suggests a formation of a $CsPbI_3$ alloy with the $FaPbI_3$. (An illustration is given in Figure 5.27) In literature it is known, that a formamindium lead iodide/caesium lead iodide alloy is forming.[75] Additionally to that, the described alloy in literature seems to have increased phase stability. It is essential to mention that the same concentrations as here observed are not described in the literature for the $FaPbI_3$/$CsPbI_3$ alloy. The sample with the additional treatment of FaI+$Pb(NO_3)_2$ shows less effect on the unit cell size. The determined crystal sizes with the Scherrer equation are supporting these conclusions. Here the same trend is observable. The size change only occurs with the formation of an alloy. As an illustration of the exchange process is given in Figure 5.27.

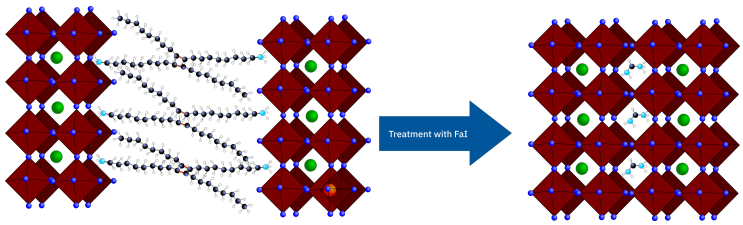

Fig. 5.27: Idealized illustration of the treatment with FaI and formation of a $FaPbI_3$/CsPbI alloy

5.3.4 Optical Properties

In this section, the optical properties of the different treatments shall be discussed and compared. Therefore first, the band gap onset and the photoluminescence data are evaluated, and later the charge carrier mobility shall be investigated by the OPTP method.

Absorption spectroscopy The band gap of each sample is estimated by the first derivation of the absorption onset. The resulting band gap onsets of the different treatments are presented in Figure 5.28. Supplementary the band gap of the bulk $CsPbI_3$ [332] and bulk $FaPbI_3$ [338] are given.

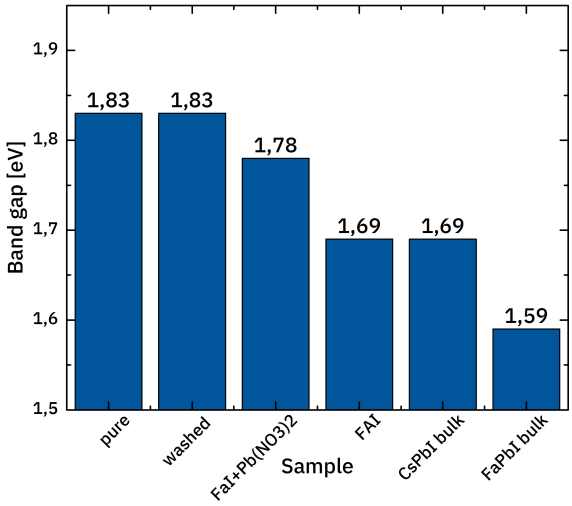

Fig. 5.28: Estimated band gap of the different treatments including a pure washed sample, the band gap of the bulk $CsPbI_3$[332] and bulk $FaPbI_3$[338] (spectra in Appendix)

The pure, untreated $CsPbI_3$ nanocrystal film is showing a band gap onset of 1.83 eV. The washing process with methyl acetate is not changing the band structure. So the removed ligand of the $CsPbI_3$ nanocrystal seems not to influence the optical properties of the material.
For the treatment with formamidinium iodide and lead(ii)nitrate, the band gap narrows to a value of 1.78 eV. This value is lower than expected concerning the calculated size by XRD data. A reason, therefore, could be the integration of formamidinium iodide in $CsPbI_3$ structure and further surface

passivation with nitrate ions[337]. The treatment with just formamidinium iodide leads to a comparable band gap as observed for the pure, bulk $CsPbI_3$ [332]. This observation fits well with the expectation of the lost of quantum confinement because the particles exceed the 12 nm size of the excitonic Bohr radius.[23].

Photoluminicense spectroscopy The emission spectra of the samples were investigated by photoluminescence measurement. The maximum emission peak of each sample and the full width at half maximum (FWHM) is shown in Figure 5.29

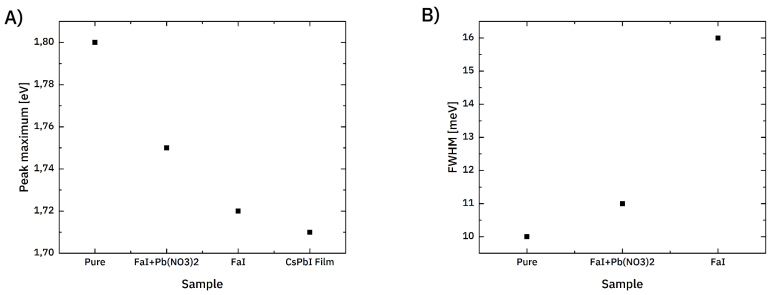

Fig. 5.29: A) Pl signal maximum of the different treated samples compared to the bulk $CsPbI_3$ [332] B) The FWHM of the different treated samples(Spectra in Appendix)

At first sight, a decrease in the Pl maximum towards lower energies is observed in Figure 5.29 A. This can be combined with the results of the absorption spectroscopy. Furthermore, more the increase in the FWHM indicates a broader distribution of quantum dots. These findings fit further to the above-discussed data, especially to the size increase of the formamidinium iodide treated samples. Furthermore, the quantum yield of the samples was measured (see Table 5.3)

Tab. 5.3: Quantum yield of the different treated samples

Sample	Pl max [eV]	EQE Pl [%]
$CsPbI_3$ pure	1.81	5.583
FaI+ $Pb(NO_3)_2$	1.74	0.033
FaI treated	1.70	0.014

The quantum yield supports the findings of the shifted Pl_{max} signals. These could be explained with the analysis of the whole sample and also includes possible defects in the structure.
The external quantum efficiency is decreasing drastically. An explanation could be an increased charge mobility in the system, so an inter quantum dot recombination is less likely. This effect would be wanted for a solar cell application. OPTP further measured the charge carrier mobility. The resulting conductivities are shown in Figure 5.30

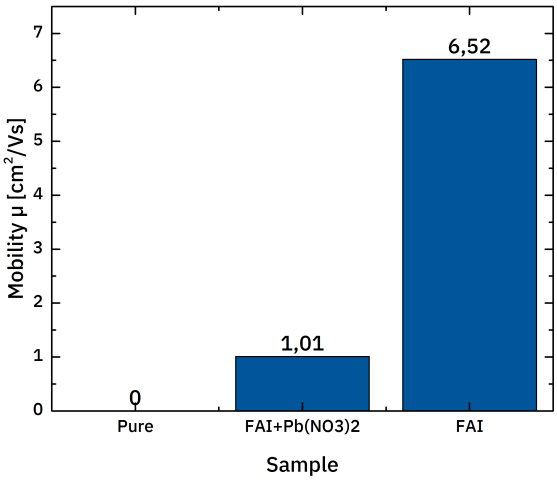

Fig. 5.30: Optical pump terahertz probe measurement of the different treatments (spectra in Appendix)

Here an increase in charge carriers mobility is observable. The charge carriers mobility increases from $\approx 0\ cm^2/V \cdot s$ for the pure untreated $CsPbI_3$ nanocrystal film to μ= 1.01 $cm^2/V \cdot s$ for the treatment with FaI and $Pb(NO_3)_2$ and further to μ= 6.52 $cm^2/V \cdot s$ for the treatment with the FaI solution. These results are also comparable to the findings in literature.[197] However, the values of the OPTP measurements here are significantly increased, especially for the treatment with FaI. An explanation could be the here used FaI was synthesised and several times purified. The NMR spectrum is not showing any precursor impurities like i.e. acetate.(see Appendix)
The precursor, i.e. acetate, might react with the surface of the quantum dots and change the surface, so charge conduction becomes hindered. Furthermore, in the literature [197] no spectrum of the OPTP measurement is provided, so a full comparison is not possible.

Efforts were conducted to build a solar cell device. The approach of a PEDOT:PSS based devices failed, since the dispersant of the nanocrystals octane, was dissolving the PEDOT:PSS and always lead to short circuits in the device. Nevertheless, the ten-fold higher charge carrier conductivity lead to further investigations.

Time resolved photoluminescence For investigating the charge carrier dynamics further, time-resolved photoluminescence measurements were conducted and compared. The measurements are shown in Figure 5.31.

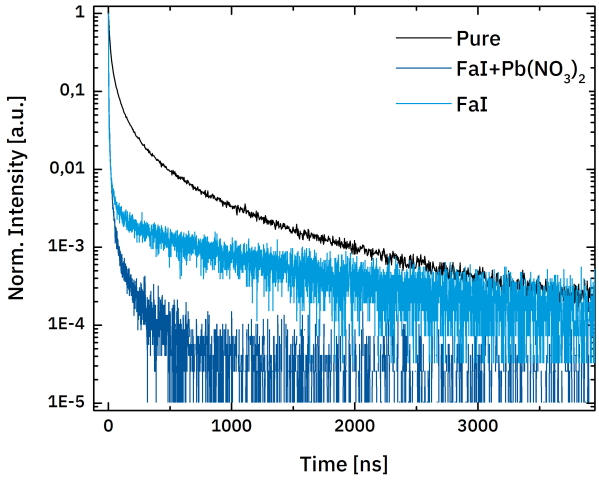

Fig. 5.31: Comparison of the TRPL measurements of the $CsPbI_3$ nanocrystals and their treatments

In Figure 5.31, the normalised decays of the differently treated samples are shown. Each of the resulting decays can be divided into two separate decays. The first decay is, therefore, of short duration. The second decay is significantly longer. This observation is comparable with the untreated sample, discussed earlier. Differences in treatments are visible in the measurement. The first decay is decreasing with different treatments, and the second stay comparable but shifted in respect to the first decay. As for the above mentioned pure $CsPbI_3$ nano cuboids, fitting of the decays was here also not possible, so only a quantitative analysis can be given.
As discussed for the pure sample in subsection 5.2.4, a shorter first decay indicates an even higher recombination rate for the first process and an

expanded for the second. The FaI and $Pb(NO_3)_2$ treated sample shows the fastest decay. Nearly 99.999% of the generated charge carriers are recombining during the first 200 ns. The second decay could not be completely followed to the whole, because the signal vanishes in to the noise.
For the treatment with FaI, the first decay is also faster than the decay of the pure sample. The second decay could be followed until the end of the measurement time.
As mentioned, a fit of the decays was not possible. Additionally the processes inside the quantum dots are unknown and unusual.[316] Therefore a qualitative instigation with, i.e. a fit could not be done in this thesis. Nevertheless, the decays could be interpreted. As for the pure sample, the first decay of both treatments is very fast. This implies that the recombination rate inside the quantum dot seems to be high. For the FaI and $Pb(NO_3)_2$ treatment even higher, that 99.999% of the charge carriers are recombined in around 200 ns. For the FaI treatment, a similar, but not as drastic image is given. An explanation might be a more significant amount of defects on the surface of the quantum dots originating in the removal and addition of ligands or other salts. This might lead to faster recombination inside the quantum dots.
The second longer decay shows a longer lifetime for the FaI-treated samples than for the pure samples. This is also observed in literature.[197] These findings are fitting to the findings of the OPTP measurements and indicate an inter quantum dot transport and recombination.
Furthermore, measurements also indicate a merging of the quantum dots. A size-dependent longer lifetime is excluded. A difference in 8 nm quantum dots and 12 nm nanocrystals, would not sufficiently explain an increase of the six-fold in charge carrier mobility. One different approach to this behaviour could be the photo-induced anion exchange [339] and phase transition[340] of the $CsPbI_3$ nano cuboids. This could have lead to a phase transition or a decomposition which was not observed after the OPTP measurement.

To conclude the optical investigation part, the optical properties of the samples with different treatments are changing. These findings could be compared to the literature findings. The here provided optical measurements, are fitting well to the other measurements done in this thesis. Therefore especially the size increase of the particles are visible by an FWHM broadening of the PL signal. This indicates that an increase in size distribution is

present. A merging of the particles caused by the absence of the ligand and access of formamidinium iodide could explain this observation. With that, a further Ostwald ripening is likely which is described in literature.[341] The OPTP measurement reveals a ten times higher charge carrier mobility then described in literature [197]. This could be explained by the here used synthesised and purified formamidinium iodide. The NMR-spectra showed the absence of the precursor formamidinium acetate. A possible presence of acetate is leading to surface passivation.[316] This would hinder the conduction of the charge carriers. The process described in literature [316, 197] was using a commercially available formamidinium iodide. The commercial synthesis is unknown and it was not possible to investigate the purity of the commercially available substance. A full comparison to the literature was not possible because no OPTO spectra were provided. The TRPL data adds up to the findings. A different ligand might increase the charge carrier mobility to reach higher conductivities. Unfortunately, due to the unknown processes inside the perovskite nanocrystals [316] a fitting of the decays and further investigations were not possible. For a further improvement of the charge carrier dynamic inside the quantum well, further ligands could be investigated.

5.4 Further $CsPbI_3$ nanocrystal treatments

In this part, the exchange of different ligands shall be discussed. For this purpose, three main methods were followed. The first attempt was to synthesise the nanocrystals with shorter ligands. With that, an exchange of the ligands and a possible decomposition of the perovskite structure or a phase transition could be avoided.
The second attempt was to remove the ligand with a thermal annealing process.
The third attempt was an exchange of the ligands against a di-ammonium functionalized ligand. Additionally to that the attempt was to exchange the ligand against a di-amino functionalized ligand with a possible electron conductivity. The results will be presented in the following sections.

5.4.1 Synthesis of $CsPbI_3$ nano structures with shorter ligands

The ligand capped $CsPbI_3$ quantum dot is known to have significantly higher phase stability in comparison to the layer.[316] The ligand exchange method may lead to a vulnerability of the system, therefore the attempt in this section was to eliminate the ligand exchange by direct synthesis of the $CsPbI_3$ nanocrystals with a shorter alkyl ligand chain. .

Synthesis The same hot injection synthesis method as described in section 5.1 was used. However, instead of using oleylamine the ligand was changed to the C_8 n-octylamine or N,N-dioctylamine (shown in Figure 5.32).

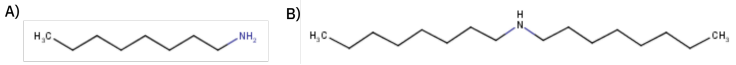

Fig. 5.32: Chemical structure of A) N-octylamine B) N,N-Dioctylamine

$CsPbI_3$ synthesis with N-octylamine as ligand Before reaching the injection temperature of 170°C, the formed lead(II)iodide oleic acid complex decomposed. The decomposition was noticeable by a colour change from yellow to orange and a visible precipitation of the precursor. This is known for oleyleamine for temperatures above 180°C.[23] The observation was ignored, and the synthesis protocol was continued, leading to an expected yellow precipitate and no dark dispersion like in the case of the oleylamine. The resulting product was not further investigated since the colour already indicated a failed reaction to the δ-phase or the precursors.[23] A possible cause for this behaviour can the compatibly low boiling point of N-octylamine (179°C [342]). Before reaching this temperature, evaporation might already occur, which leads to destabilisation and decomposition of the formed complex. No further information for the complex could be found in the literature, so this explanation could only be based on assumptions.

$CsPbI_3$ synthesis with N,N-dioctylamine as ligand A ligand with a higher boiling point and the same chain lengths is the N,N-dioctylamine. The

stronger basic character because of the secondary amine of the N,N-dioctylamine might further contribute to enhanced stability of the complex. The lead(II)iodide oleic acid complex surpasses the aimed temperature of 170°C, and by the injection a black precipitate was observable. On the first side, this indicates a successful reaction.
Furthermore, an investigation was carried out by transmission electron microscope.(See Figure 5.33)

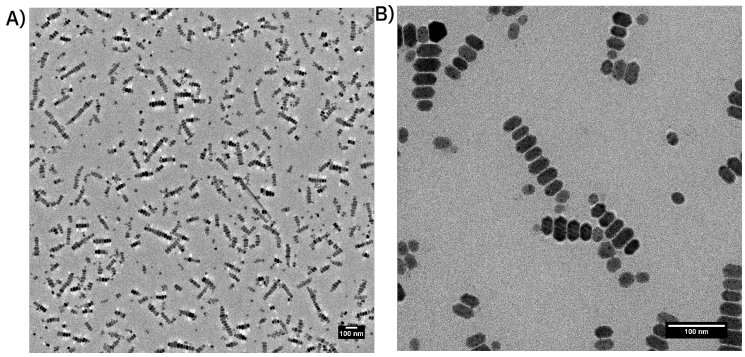

Fig. 5.33: A) Overview TEM-Image of the N,N-dioctylamine sample B) Magnification of the TEM-Image

In Figure 5.33 A distributed hexagon structures are observable. The hexagonal structure is stretched in one direction. The sizes of the particles varies from 25 to up to 60 nm in the longitudinal direction and 15 to 25 nm in the transversal direction. Furthermore, the hexagonal structures are arranged in rows. These rows consist of 5-20 hexagons. The relatively high transmission of electrons, observable by the grey contrast, suggest a limited size expansion in the z-direction. The hexagons are showing so-called "halos" (white shadows originating in the scattering of electrons on high crystalline samples), which indicate a high crystallinity. These halos are always visible with black hexagonal structures. This further leads to the conclusion of a high crystalline material with additional high electron scattering.
In addition different contrasts are indicating different crystal orientations. In Figure 5.33 B a magnification of the hexagonal structures is shown. Here a light gap in between the nanostructures is observable. The gap in between the particles is around 2 to 2.5 nm as big as the gap in between the $CsPbI_3$ quantum dots with oleylamine as a ligand.
The high contrast indicates the presence of heavy atoms, so a possible formation of a perovskite structure can be assumed. In addition to this assumption is the observation of the halos and the contrast differences. The usage of a

different ligand with a shorter chain length and a different overall molecule geometry can explain the different shape and size .[343] The comparable gap to the above discussed $CsPbI_3$ nano cuboids could be explained by a formation of a bilayer of the N,N-dioctylamine, which is observed for two chained ligands.[343]
Further GIXRD measurements were conducted to investigate the crystal structure. The obtained pattern is presented in Figure 5.34

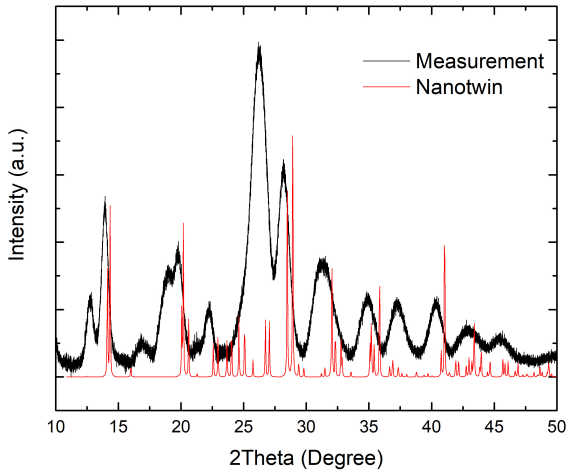

Fig. 5.34: XRD pattern of the $CsPbI_3$ nanoparticles with N,N-dioctylamine as a ligand, showing also the nanotwin phase

The XRD pattern shows broad signals over the whole measured area. The nanotwin structure could be assigned (red signals) to the measurement, but a second unknown phase is present. Noticeable is the signal at around $2\theta =$ 14° and 28°, which are narrower in comparison to the other, assigned signals. This suggests an unidentified, unknown phase. Every known perovskite structure and every precursor were compared, without a sufficient fitting of the signals. For this reason, the unknown phase remains unclear. A LeBail fit was for this reason not possible.
To investigate the charge carrier mobility of this sample, OPTP was measured and is shown with the pure, untreated sample, and the FAI treated sample in Figure 5.35

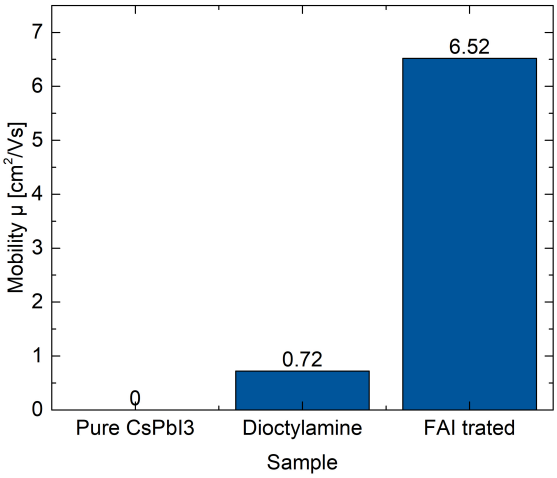

Fig. 5.35: Charge carrier mobility measured with OPTP a comparison of the untreated, the N,N-dioctylamine synthesized and the FaI treated sample (Spectra in the appendix)

The charge carrier mobility with μ=0.72 $\frac{cm^2}{V \cdot s}$ a slight increase is observed. This is most likely the result of the increased size of the particles. The distance of 2.5 nm in between the particles and the potential double layer of ligands, makes a transfer to other particles not likely. No further investigations were conducted on this sample.

To conclude, the synthesis route with N,N-dioctylamine as a ligand leads to a successful synthesis of nanostructures. The TEM-analysis reveals hexagonal nanoplatelets with an expansion of 25 to up to 60 nm in the longitudinal direction and 15-20 nm in the transversal direction. These structures are arranged in rows and are divided by 2-2.5 nm gaps. These gaps are likely to originate in the ligand, which is likely to form a double layer. The XRD measurement reveals the possibility of the nanotwin phase, but an additional unknown phase is also occurring. The unknown phase could not be assigned to this thesis.
The OPTP measurement leads to a slightly increased conductivity, which originates in the expanded size of the nanostructures. Transport from one to the next particle is unlikely. No further investigations were conducted with this material.

5.4.2 Thermal annealing of the $CsPbI_3$ cuboids

Another method for changing the properties of the spin-coated nanocrystal film is the post-synthesis thermal annealing process. The strategy here is to remove the ligands from the perovskite and merge the particles together. This procedure is reported for other quantum dots.[344, 345, 346] Furthermore, first attempts were made for the $CsPbI_3$ quantum dots, with the result of the decomposition of the sample.[316]

Preparation The $CsPbI_3$ nanocrystals were synthesized by the hot injection method as described above (see section 5.1). A red nanocrystal film was spin-coated on glass. The coated film was heated to 150°C for around 1 minute under a nitrogen atmosphere. During the heating, a colour change to brown was observed.

Transmission electron microscopy analysis For investigating the sample with TEM [8], the dispersion of $CsPbI_3$ nanoparticles were drop-casted on a TEM grid and heated at 150°C under nitrogen atmosphere. This resulting in the following images Figure 5.36.

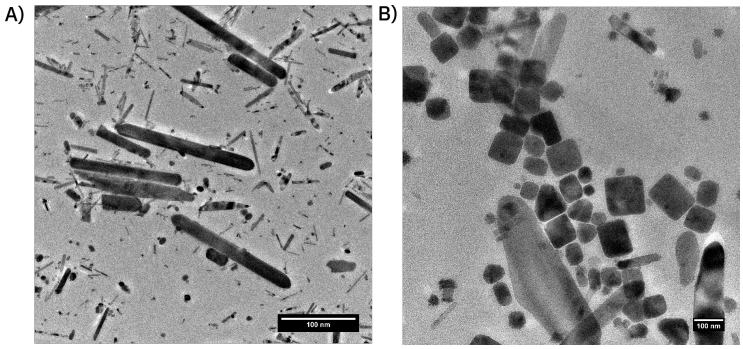

Fig. 5.36: TEM-Images of the post synthesis thermal annealed $CsPbI_3$ quantum dots

The TEM-image Figure 5.36 A shows rod-like structures with different sizes. These rods have longitudinal sizes of 15 to 190 nm in lenght distribution. The expansion in the transversal direction is 2 to up to 20 nm.
In Figure 5.36 B also other sizes and shapes are found. The sharp cuboid shape of the nanocrystals vanishes. The contrast of the different particles

[8] Daniel Besold performed the TEM measurement

varies, indicating different thicknesses of the layers. All evidence is indicating a merging of the phases and further an uncontrolled growth of the particles. A possibility of different crystal phases like described in the literature for thermal annealing above 200°C is likely.[316]

Grazing incidence X-ray diffraction analysis A further investigation of the resulting product was done by X-ray diffraction. An XRD pattern of a post-synthesis, thermally annealed sample is given in Figure 5.37

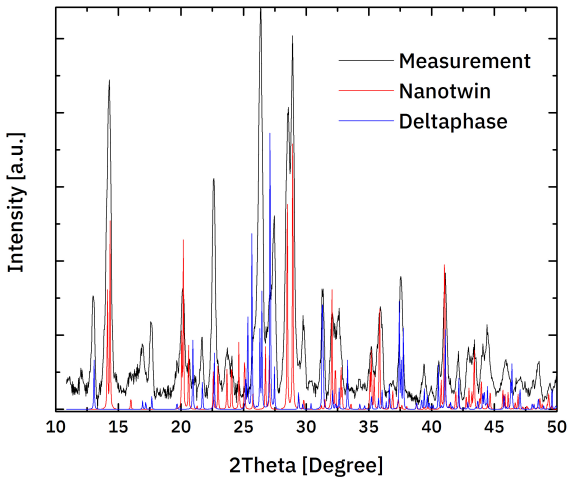

Fig. 5.37: XRD of the post synthesis, thermal annealed $CsPbI_3$ nanocrystals

The signals are narrower than for the pure, unannealed $CsPbI_3$ nanocrystals. Additional signals are present. The narrower XRD-Peaks are indicating in size expanded crystals. This is comparable to the findings of the TEM investigation. The nanotwin phase could be assigned. Unfortunately, other peaks are present. These could be assigned to the non-perovskite δ-phase. A destabilisation of the $CsPbI_3$ quantum dots without the ligand is likely.[316] This could also be seen by lower temperatures than 200°C. A possible transformation to the δ-Phase is already described in the literature for higher temperatures.[316]
Additional signals could not be assigned to the mentioned phases and not to precursor signals. The origin remains unclear. No further investigations were conducted for this treatment method.

The post-synthesis thermal annealing process seems not to be a sufficient method for merging the perovskite quantum dots. The thermal annealing of around 150°C is already leading to a decomposition of the perovskite by forming the non-perovskite δ-phase and other phases. This agrees with the findings in literature for higher temperatures.[316]

5.4.3 Different ligand by exchange

Besides the ligands as mentioned earlier, also other ligands as exchange ligands were investigated. The focus here was an easy and direct exchange method with an excess of the ligand in the solvent. As a ligand for the exchange, task-specific ligands were investigated. The task of these ligands was to connect the nano cuboids, lower the distances in between nano cuboids and additionally an electric conductivity by implementing, e.g, a ring system. For these purposes, two molecules (1,6-Hexanediamine and 1,4-benzenedimethanamine) were chosen with a similar molecular size expansion. These shall be discussed in the following and are show in Figure 5.38

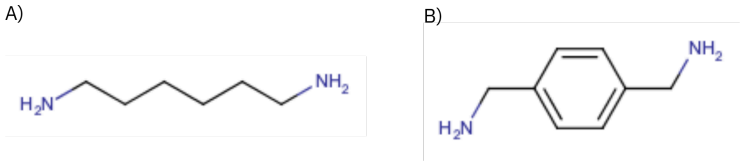

Fig. 5.38: A)1,6-Hexanediamine B)1,4-benzenedimethanamine

5.4.4 Ligand exchange to 1,6-hexanediamine

The 1,6-Hexanediamine was used as received and the product was dissolved in methyl acetate. During ligand exchange by dipping the spin-coated layer $CsPbI_3$ in the saturated solution, the layer turned immediately yellow. This was assumed to be the non-perovskite $CsPbI_3$ δ phase. No further investigation was conducted at this point. A possible explanation for this behaviour might be the formation of a poly iodide with iodine of the $CsPbI_3$. The 1,6-Hexanediamine is known to form poly iodine.[347] This might lead to a decomposition of the $CsPbI_3$ Quantum dots. Furthermore, investigations were not done at this point.

5.4.5 Ligand exchange to 1,4-benzenedimethanamine

The 1,4-Benzenedimethanamine was used as received and the product was dissolved in methyl acetate. The ligand exchange was performed like discussed in the abovesubsection 5.4.3. As a result, a red layer was obtained. This layer decomposed under nitrogen protection after around 1 hour. The experiment was repeated, and the same result was obtained. A second dipping of the sample lead to even faster decomposition. No further experiments were conducted because the resulting product was too unstable to investigate. As a reason for the fast decomposition might be the possibility of a poly iodine formation, as seen for the 1,6-Hexanediamine [347]. This process seems to be hindered by the steric expanded ring system in comparison to the alkyl chain of the 1,6-Hexanediamine

Both ligands were decomposing the $CsPbI_3$ structure by forming a yellow layer. Furthermore, investigations were not conducted. An enhanced stability of the $CsPbI_3$ phase might lead to a better result since several dippings of the sample might be possible, and improved coverage of the overall quantum dot surface could be reached.

5.5 Incorporation of potassium into the $CsPbI_3$ quantum dots

Even though the phase of the $CsPbI_3$ nanocrystals is stable for some time[316], a phase transition to the non-perovskite δ-phase is occurring, and with that, the optical properties of the sample are changing. Especially with the influence of light this process is observed.[339, 340]
In general, an increase of stability of the quantum dots is desired. This further could support a better manipulation of the surface and therefore increase the possibilities for a ligand exchange with the goal of higher charge mobility inside a quantum dot layer. First attempts in the direction of enhanced stability were done with a film of $CsPbI_2Br$ by Nam et al.[348] The group exchanged the caesium ion A of the ABX_3 structure against a potassium ion in a spin-coated film. In the publication [348] 1, 2.5, 5, 7.5, 10 and 20 w %

of potassium were incorporated into the perovskite.
The $KPbI_3$ crystal phase is not described in the literature and also is not stable with a Goldschmidt factor of 0.747.
For this reason, Vegard's law [349]could not be applied for the investigation. Nevertheless, the incorporation of potassium into the CsPbX lattice seems to be possible and leads to a size reduction of the unit cell and further to a stabilisation of the perovskite.[348] In this thesis, the potassium was interoperated during the hot injection synthesis.

5.5.1 Synthesis

For the synthesis of the potassium doped $CsPbI_3$ nano cuboids the synthesis method as described in Synthesis (section 5.1) with different contents of potassium (1, 2.5, 5, 7.5, 10 and 20 mol%) in the above described cs-oleate precursor solution was used. For this purpose, the caesium oleate was produced like described in subsection 5.1.1. The same procedure was conducted for the potassium oleate. Both precursors were combined in the prescribed ratios in a separated flask. Afterwards, the described Hotinjection synthesis was conducted(section 5.1).
All reactions led to a red precipitate during the injection of the Cs/K oleate, which indicates a successful synthesis. The degradation of the samples was observed and is represented in Table 5.4.

Tab. 5.4: Stability observation of the potassium incorporated $CsPbI_3$

Content of K in %	Decomposition of the sample
0	1 month
1	1 day
2.5	2 days
5	1 month
7.5	3 month
10	2 weeks
20	3 weeks

The observation was done by assuming a decomposition by a yellow precipitate in the solution (stored in a refrigerator at 2°C). In comparison to the drop cast samples in the glove box under nitrogen, protection was observed.

Both underwent the above-described decomposition. Here the 7.5 mol% potassium sample has the highest stability. This is comparable to the findings in the literature for layered structures.[348] The explanation is given in a compression of the unit cell of the α-$CsPbI_3$.
The reproducibility of the synthesis was not given. After the first synthesis cycle of the first seven samples, several attempts were made to reproduce the results described here without the incorporation of potassium in the $CsPbI_3$ nanostructure. An explanation can be found by the usage of volatile sulphur components (i.e. H_2S) inside the used glovebox, in which the used precursors were stored. The volatile H_2S is reacting with lead halide salts.
Furthermore, it is known that potassium carbonate can absorb H_2S.[350] This might influence the nanocrystal synthesis, even in traces. No literature for this observation could be found. However, it is known that trace amounts of impurities can influence nanoparticle synthesis. This is shown for the far more investigated and reliable gold nanoparticle synthesis.[351]
The samples were further investigated as long as they were stable for an investigation.

5.5.2 Transmission electron microscope analysis

The resulting products were investigated by a transmission electron microscope. For this purpose, the sample containing 1 and 2.5 mol% potassium was already decomposed, so for these samples, no TEM-Images can be provided. Furthermore, investigations were conducted with samples of 5, 7.5, 10 and 20 mol % potassium. The results of the TEM-measurements [9] are shown in Figure 5.39

[9] Daniel Besold measured the TEM-Images

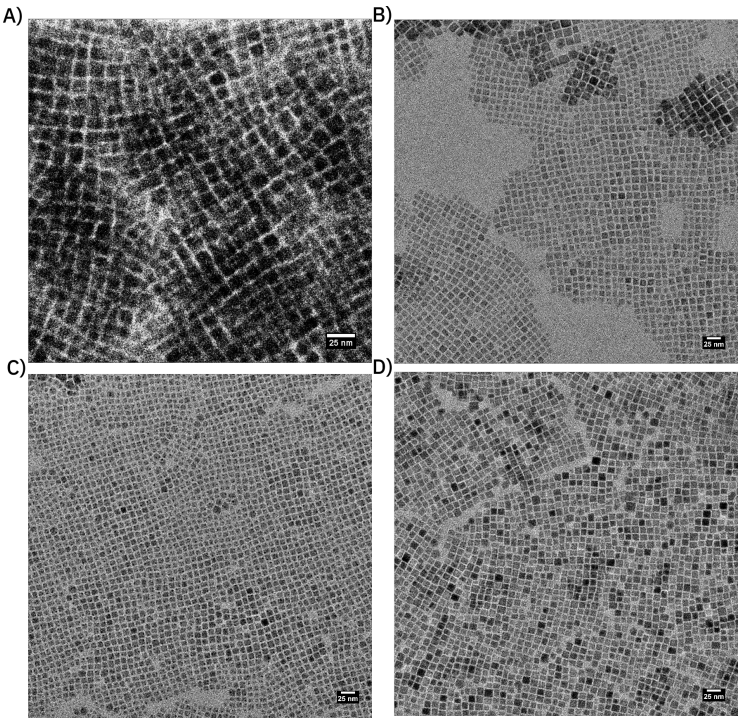

Fig. 5.39: A) TEM-Image of the sample 5 mol% K, B) TEM-Image of the sample 7.5 mol% K, C) TEM-Image of the sample 10 mol% K, D) TEM-Image of the sample 20 mol% K

All TEM images show the nano cuboids comparable with the synthesis of the $CsPbI_3$. Figure 5.39 A is showing a thick layer of the nano cuboids and differs therefore from the other sample. The differences in the size of the particles can be explained with the slightly different conditions of injection during the hot injection process and can here be neglected. The TEM-images are showing the successful synthesis of nano cuboids, but no further information about the potassium content. Therefore different analyses need to be conducted.

5.5.3 X-Ray fluorescence

For the investigation of the potassium content in layers, X-Ray fluorescence (XRF) was used. Here the 1 and 2.5 mol % sample were decomposed and not measured. The potassium content in each sample is shown in Table 5.5.

XRF is a semi-quantitative method. A pure reference sample with the same composition should be used to compare the results. A reference sample was not available, so just semi-quantitative analysis was possible. However,

Tab. 5.5: XRF measurement of the samples

Sample	K in %
$CsPbI_3$ 5% K	4.70
$CsPbI_3$ 7.5% K	6.57
$CsPbI_3$ 10% K	9.08
$CsPbI_3$ 20% K	22.58

the resulting data fit well to the used mol% of potassium. The potassium, therefore, seems to be interoperated into the sample or on the surface. The purification process described in section 5.1 is removing the access potassium oleate so that an outer potassium layer can be excluded. GIXRD was used for a further investigation of the crystal structure.

5.5.4 Grazing incident XRD measurements

The GIXRD measurements were investigated on drop casted samples. The thickness of the film might vary. In Figure 5.40 as an example the background corrected GIXRD pattern of the $CsPbI_3$ quantum dots with 7.5 mol% potassium and the resulting LeBail fit with the initial condition found in literature [119] is shown in Figure 5.40

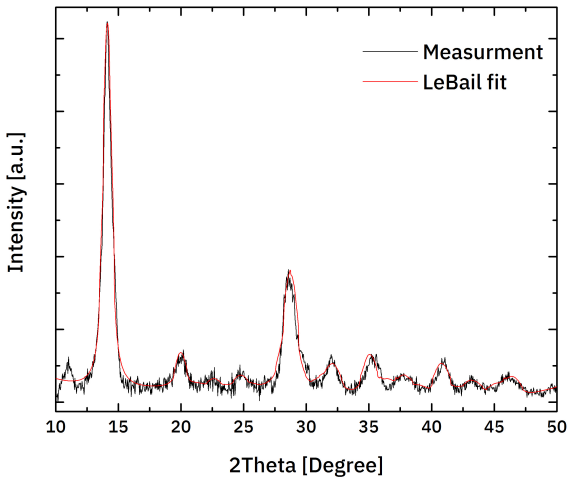

Fig. 5.40: GIXRD measurement and LeBail fit of the 7.5 mol% sample

Every signal could be assigned with the Lebail fit to the nanotwin structure [119] except for the first signal between θ=10 and 11.5°. These regions were always excluded LeBail fits. All XRD-patterns were fitted, and the resulting unit cell size are shown in Figure 5.41

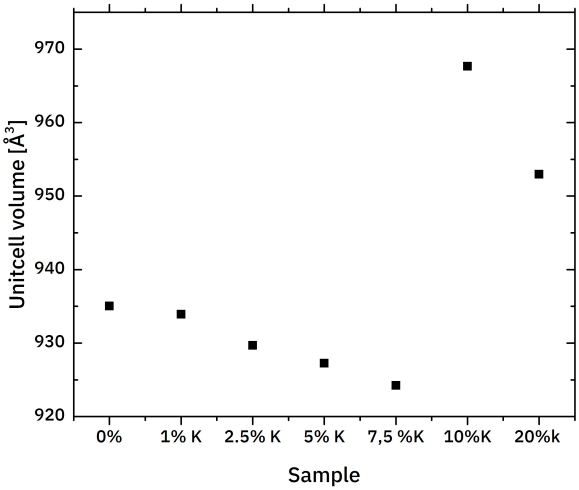

Fig. 5.41: Unitcell size of the potassium doped $CsPbI_3$ nano cuboids (All pattern are in the Appendix)

In Figure 5.41 a unit cell contraction until the 7.5 mol% sample is observable. The 10 and 20 mol% samples are not following this trend. This behaviour is also reported for the $CsPbI_2Br$ in literature.[348] The phase stability of the perovskites is dictated by the volumetric ratio between the A-side ion and the PbX_6 octahedral.[75] By the incorporation of potassium in the perovskite structure, a shrinking of the PbX_6 octahedral volume is observed.[348] This could indicate a stronger connection to the PbX_6 octahedral, and therefore, an enhancement of the perovskite structure is observed.[348] An explanation for the low stability of the 1 and 2.5 mol% sample could not be given with this assumption. An explanation attempt could be a destabilisation of the phase at lower percentages of incorporation potassium. The unit cell expansion of the 10 and 20 mol% is observed. This could be explained with the formation of a new phase in the solid solution. Detection of a new phase was not possible, because of the challenging character of the nanoparticles, with their broad XRD signals. In addition to that the reproducibility of this material was not possible, and further investigations were hindered.

5.5.5 Photoluminescence measurements

For analysing the optical properties of the samples, photoluminescence was measured on the drop cast samples. From the previous discussed GIXRD measurements, the non decomposed samples with a potassium content of 0, 2.5, 5 and 7.5 mol% potassium should be discussed first. These are presented in Figure 5.42

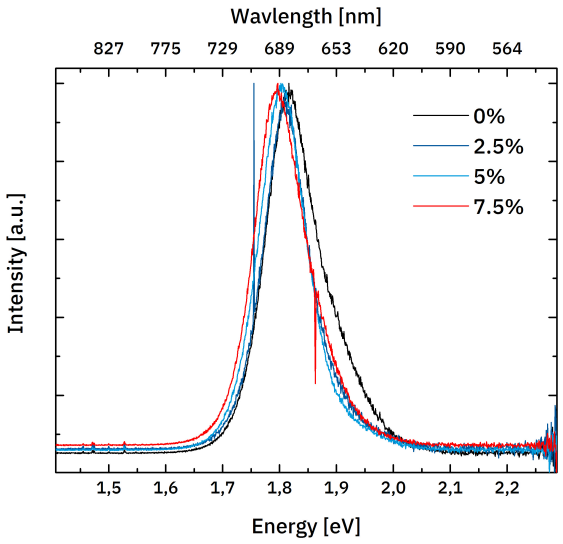

Fig. 5.42: Normalized PL spectra of the samples with 0, 2.5, 5 and 7,5 mol% potassium incorporated into the $CsPbI_3$ nano cuboids

The resulting normalised Pl-spectra of the 0-7.5 mol% samples are showing an expected constant shift towards lower energies. This fits well to the observation of the unit cell contraction and the findings in literature for $CsPbI_2Br$.[348] The difference FWHM is explainable with the small variation in the size distribution of each hot injection process. To compare these results the 10 and 20 mol% samples are included in Table 5.6

Tab. 5.6: Photoluminicense maximum and FWHM of the potassium doped samples

Potassium content in mol%	Peak maximum in eV	FWHM in meV
0	1.82	12
2.5	1:81	10.5
5	1:805	10.5
7.5	1:8	10,5
10	1.805	11,5
20	1,81	13

Here for the 10 and 20 mol% sample, a slight shift towards higher energies is observable. Additionally the FWHM is increasing. In Figure 5.43 the PL spectrum with 20 w% potassium is compared with the Pl spectrum of 7.5 mol%.

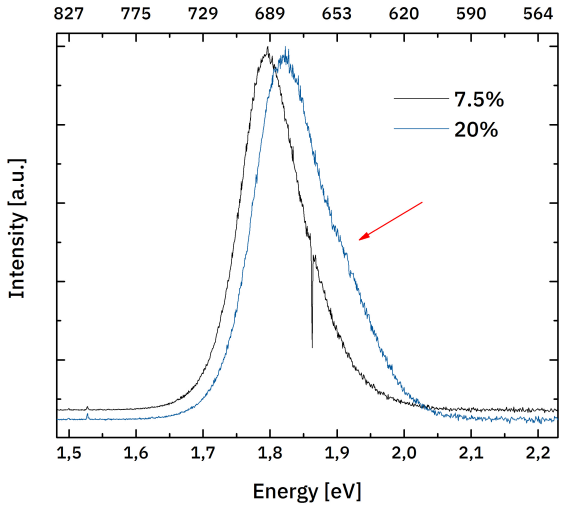

Fig. 5.43: Normalized Pl Spectrum of $CsPbI_3$ nano cuboids with 7.5 and 20 mol% of potassium

In Figure 5.43, a formation of a shoulder is observable. This can indicate a formation of a different phase which might also explain the expansion of the unit cell see subsection 5.5.4. Additionally to that the shift towards higher energies can also support this thesis. Because of the non-reproducibility of the synthesis and the decomposition of the samples, no further investigations were conducted.

To conclude the synthesis with the aim of incorporation potassium inside the $CsPbI_3$ structure, was successful. Reproducibility of the samples was not

possible. A reason, therefore, could be the impurities (H_2S) of the precursors. For the remaining samples, the observation of a phase transition was made. Therefore the highest stability was given by the 7.5 w% sample. Further measurements were carried out with the remaining samples. The TEM- images are showing a comparable size and shape with the 0% sample. The conducted XRF measurements were supporting the presence of potassium at or in the quantum dots. The findings were fitting well to the used w% of potassium at each sample. The LeBail refinement of the GIXRD measurements were indicating a size change in the unit cell. This is comparable to the findings in literature for a layered system.[348] Here the authors are suggesting a better stabilisation of the phase, originating in the influence of the A ion onto the PbX_6 octahedral.
For the samples with 10 and 20 w% potassium an expansion of the unit cell was observed. This can be explained with a possible formation of a new phase. The Pl-measurements are supporting these findings.

5.6 Discussion

The in literature [23, 316] described $CsPbI_3$ nanocrystals could be reproduced. The hot injection delivers a red dispersion of nanocrystals.

Size, shape and crystal phase of the $CsPbI_3$ nanocrystals Transmissions electron microscope analyses reveals on first sight, squares with high contrast and a surrounding light contrast. The high contrast squares could be assigned to the $CsPbI_3$ perovskite, while the surrounding gap is assigned as the organic ligand oleylamine. Furthermore, the size of around 8 nm for the injection temperature of 170° C could be reproduced [23] and found in the following measurements. The quantum dots are self-assembled in a large area. These findings are comparable to the findings in literature.[23, 316] Additionally to that, two main distributions of size and gaps are visible. This gets supported by the FFT of an overview image. An area integral shows two distinct signals of the FFT. The size difference of the FFT in comparison with the counted particle size can be explained with defects in the self-assembled structure and the limited resolution of the TEM-Image. A different shape than in the literature described cube-like structure can explain the two different size distributions.[23] This adds up to an ongoing conflicting discussion in the community about the actual crystal structure [23, 321, 322, 323] which could be solved by Bertolotti et al.[119].
Instead of describing the crystal structure of the $CsPbI_3$ nanocrystals, the crystal structure is determined by a Debye scattering equation/atomic pair distribution function approach.[119] This method reveals a so-called nanotwin structure. The origin of this structure is found in the high dynamics inside the nanocrystal, which leads to a twinning inside the γ (orthorhombic)- perovskite crystal phase. The misinterpretation of the high-resolution TEM images and the XRD pattern found in literature might be explainable with the high dynamics inside the perovskite structure.[324] These findings are fitting well to the observations made in the TEM-images with the FFT analysis. Instead of the cubic shape, the resulting shape should be described as a cuboid structure.
An additional proof for this observation is the LeBail fit of the GIXRD measurements, which reveals a bad fit for the cubic crystal structure. The nanotwin

structure is therefore superior for the investigation of the crystal structure and shall be further used in this thesis as standard for analysing further $CsPbI_3$ nanocrystals. The lattice parameters of the here synthesized nano cuboids are vary from the results found in literature.[324] The origin for this could be the smaller size of the here investigated nanocrystals and with that a higher surface to volume ration. This is resulting in a higher internal pressure on the lattice, which lead to a smaller unit cell. Additionally to the fit, further signals are observable, which could be assigned to the Cs-rich perovskite.[327]

X-ray Reflectivity of the $CsPbI_3$ nanocrystals layers X-ray reflectivity was measured to analyse the self-assembly of the nanocrystals in a layer on a substrate. With that an investigation of the whole sample (17.5 cm^2) in z-axis was possible. These results show a decay with fringes on top. For a further investigation, the layer thickness was determined by a laser microscope measurement with a resulting thickness of d_{layer}=550 nm. The estimated thickness and the X-ray reflectivity data were further analysed with a Parratt algorithm[250]. As a result, a lower total thickness of the sample was found d_{layer}= 470 nm. The lower thickness measured in XRR could be explained by the high X-ray absorptivity of the heavy atoms Cs, Pb and I.
Also, a high fluctuation in the scattering length density was observed. For the investigated sample, this is expected, with the high SLD for the perovskite and the low SLD for the organic ligand. Consequently an alternating layer structure can be assumed. These observations fit well to the observation made in the TEM-Image for a 2D structure. Moreover, this supports the idea of an arrangement in a 3D layered structure with alternating ligand, perovskite cuboids.
Nevertheless, the calculated and resulting scattering length density varies. This could be on one side explained with defects in the self-assembled structure. Moreover, incorporation of air or vacuum in the sample, which leads to a lower SLD than that expected. A reason, therefore, can be found by taking drying-effects into account, which are also observed in the TEM-Images. Furthermore, also higher SLD than that calculated are observable, which could be explained with a shift in the layer structure caused by the mentioned defects. This leads to a higher SLD value. The reason, therefore, is the additive calculation of the SLD on the technical side.[198]

The defects in the sample are possibly shifting parts of the perovskite cuboids into the voids of the defects. Therefore the SLD of the ligands are shifted towards higher SLDs.
Neutron reflectivity (NR) as a complementary method for the XRR was used for a further investigation of the layered structure. For this purpose, the same sample as for the XRR measurement with the same resulting fit parameter from the XRR measurement was applied to the NR measurement. The fit of the NR-data does not converge well. The explanation here is probably the assumed high X-ray absorption of heavy elements, which leads to errors in the measurement. From the resulting SLD, an alternation is visible. This adds up to the conclusion of a regular stacked orientation of the nano cuboids inside the perovskite layer. It is evident that the SLD is smaller for the NR measurement, than for the XRR measurement, this is expected and revealed at the calculated SLD for the different layers. More pieces of information are not to obtain originating in the error of the high X-ray absorption.
Nevertheless, the results are showing a high ordered structure in Z-direction in an expanded area of 17.5 cm^2.

Spectroscopic investigation of the $CsPbI_3$ dispersion Further, investigations were conducted with spectroscopic methods like photoluminescence, absorption, and time-resolved photoluminescence measurements. Within the absorption and photoluminescence measurements, quantum confinement was observed, which fits the findings in literature.[316] The absorption spectra are showing bands in higher energies (lower wavelengths). The absorption onset is estimated by the first derivation of the absorption spectra with an onset of $\lambda_{\text{onset}} = 660\text{nm} = 1.877\text{eV}$. This shift towards higher energy is expected, and the cause can be found at the quantum confinement.[316] Due to the low concentration in the dispersion, the excitonic feature is only signified. Towards lower wavelengths at around $\lambda = 441\text{nm} = 2.81\text{eV}$ and $\lambda = 328\text{nm} = 3.78\text{eV}$ two bands are observable. The origin of both bands are unclear. An explanation could be a higher excitation caused by the ligand oleylamine. This is described for CdS and CdSe nanoparticles.[330] An other explanation for the observed unclear bands might be the presence of the caesium rich phase Cs_4PbI_6.[331, 352] However, these bands are also shifted towards higher energies in comparison to the observed absorption spectra. Furthermore, investigations could not be done in this thesis. Therefore only

the described explanations are given.
The photoluminicense emission is as expected red-shifted to $\lambda_{\text{em}} = 661\text{nm} = 1.875\text{eV}$ with a FWHM = 42 nm = 29.8 meV. This is comparable to the findings in literature.[23]
Further, investigations were conducted with the time-resolved photoluminescence. As a first step, the high quantum yield of the dispersion was in focus. This is with values up to 55% [316] considerably high. The high quantum yield can be explained with the high charge carrier density in the nanocrystals. In comparison to an excitation of $10^{15} \cdot cm^{-3}$ [332] for a thin film of $CsPbI_3$ the quantum dots with sizes of around 8 nm have a way higher charge carrier density of around $10^{18} \cdot cm^{-3}$. This observation is explainable with the size of the observed object. It can further be assumed that the majority of charge carriers are recombining in a radiative manner.
In comparison to a $CsPbI_3$ film, with lifetimes of around tens of microseconds [332] the lifetime of the nanoparticle dispersion is significantly smaller. The decay as such is decided into two decays. The first one is a rapid decay in around 100 ns. After that decay, around 99% of charge carriers are already recombined. After that a longer decay is observed, which is vanishing into the noise.
The fast first decay can be explained by a rapid inter quantum dot recombination. The likelihood of recombination inside a quantum dot of 8 nm is very high. Hopping to a different quantum dot is impossible. Furthermore, the quantum dots are surrounded by insulating ligands.
For the longer decay, several pathways are discussable. As a first pathway the charge carriers could go to the surface of the quantum dot, which potentially resembles a different phase [317, 333] with a different band gap [334]. Furthermore, at this point, surface recombination might be present. Additionally to these pathways, the ligand oleylammonium has in its ninth position a double bond. Possible tunnelling surpassing the insulating CH_2 groups and the energy gap of up to $E_{\text{Bg}}\ 6eV$ is discussable but unlikely. An evidence-based explanation could not be given at this point. Further, the fitting of the TRPL decay was not possible, because of the underlying processes inside the quantum dot are not understood. Exponential fits were not converging. This becomes obvious by the comparison to different quantum dots made in literature.[197]

Investigation of the treated $CsPbI_3$ quantum dot layer The dispersion was spin-coated on glass and further investigated by TEM, XRD, Absorption, Pl, TRPL and OPTP. For the spin-coated, untreated $CsPbI_3$ quantum dot sample, the band gap is shifting, and the quantum yield is decreasing. A quenching process can explain this, which is described in literature.[63] The lifetime of the spin-coated sample has an even faster first decay in comparison to the dispersed sample. The decay is in the latter at around 200 ns surpasses the decay of the dispersed sample slightly. This can be explained with the higher likelihood of charge carrier mobility towards other quantum dots. Unfortunately, due to the complexity of the mechanism inside the quantum dot, the charge carrier dynamics are not fully understood, and a different behaviour than for other quantum dots is observed.[316] With that neither an exponential nor other fits were successful. A modelling of a TRPL-fit for the here measured samples was, as part of this thesis, not possible.
The optical pulse terahertz probe analysis reveals mobilities towards μ=0 $cm^2/V \cdot s$. This is significantly lower than for a PVD fabricated $CsPbI_3$ layer with μ=48 $cm^2/V \cdot s$. This fits the observations of the hindered charge mobility inside the quantum dot layer, possibly caused by the insulating ligand. Moreover, the results further fit the data found in the literature.[197]
The XRD measurement of the different treatments reveal as discussed earlier the nanotwin phase.[119] This indicates that no decomposition of the samples had occurred.
As a next step, the oleylamine ligand should be removed from the surface of the quantum dot. This is done by washing the sample with methyl acetate, described in literature.[23, 197] The here performed OPTP measurement shows no improvement in charge carrier mobility by just washing the sample. Furthermore, the absorption measurement of the methyl acetate washed sample shows no change in the band gap, with that a degradation is (at least for the time of measurement) unlikely.
As a foundation, the suggestion of Sanehira et al.[197] was followed, and the ligand was exchanged against formamidinium iodide and formamidinium iodide and lead(II)nitrate. The TEM images show a merging of the quantum dots for the formamidinium iodide sample. On first sight, this is suggesting the formation of a formamidinium lead triiodide/caesium lead triiodide alloy, which is for higher concentrations observed in literature.[75] A TEM-measurement for the lead(II)nitrate and formamidinium iodide treated sam-

ple was not successful. The washing process annihilated the monolayer.
Further, GIXRD measurements of the differently treated samples were conducted. The resulting measurements were refined by a LeBail fit with the initial data of the nanotwin structure, found in literature[119]. The resulting unit cells were compared with the cubic formamidinium lead triiodide. A decay of the unit cell size from the pure, untreated sample, to the lead(II)nitrate and formamidinium iodide and to the formamidinium iodide is observable. This finding suggested the incorporation of the formamidinium iodide into the $CsPbI_3$ structure. It further seems that the incorporation of the formamidinium is hindered in the sample, which is additionally treated with lead(II)nitrate. The reason, therefore, could be found in the passivation properties of the lead(II)nitrate on the surface of the $CsPbI_3$ quantum dots [316, 337]
The XRD measurements could not make a difference between the surface and bulk incorporation, but the TEM image is suggesting a connection or merging of the formamidinium treated quantum dots. So a connection of the quantum dots by the formation of an interlayer of formamidinium lead iodide is possible. This is also suggested in the literature.[353] However, other than described in the literature for this sample, the quantum confinement vanishes. This adds up to the idea of the merging of the quantum dots. The charge carrier mobility with μ=6.52 $\frac{cm^2}{Vs}$ is ten-fold higher than that reported in literature.[353] This could be explained by a better connection of the quantum dot with formamidinium lead iodide. The here used formamidinium iodide was synthesised and purified, so no precursor was observed in the NMR-measurement. One possible precursor for the synthesis of formamidinium iodide is formamidinium acetate. Furthermore, acetate ions are known to passivate the surface of the quantum dots.[316] This would lead to a hindered merging of the quantum dots as observed for the lead(II)nitrate and a lower charge carrier mobility.
The quantum yield of the sample decreases dramatically. This could be interpreted as higher charge mobility and less confined recombination. The TRPL measurement of this sample is revealing a two decay mechanism, similar to the measurement of the untreated sample. The decay here differs from the untreated sample by a faster first decay with recombination of around 99.99% of charge carriers after 50 ns for the formamidinium iodide treated sample. The fast decay is followed by a longer decay, which lasts comparably

longer than the one of the untreated sample.
The OPTP measurement adds up with the previously discussed observations of the lead(II)nitrate treated samples. A charge carrier mobility of μ=1.01 $\frac{cm^2}{Vs}$ higher than the pure sample, but dramatically lower than the one of the formamidinium iodide treated sample. This further implements a worse merging of the quantum dots, due to the surface passivation with lead(II)nitrate.[316, 337]
The TRPL measurement is showing an even faster decay of the first decay than the formamidinium treated sample. The explanation for this could also be the passivation of the surface layer of the perovskite, and with that a faster recombination is likely.
Efforts were conducted to build a working solar cell of the material, but the approached failed because the nonpolar dispersant octane was dissolving the selective contact layer.

Further, Ligand exchange Other treatments for increasing the charge mobility were investigated. For this purpose, three distinct methods were used. Direct synthesis with two shorter ligands were carried out, to prevent the sensitive perovskite from degrading during the washing process. The synthesis with the ligand N-octylamine was not successful. A decomposition of the lead(II)iodide-oleic acid/N-octylamine complex was observed at around 150°C. The further conducted experiment failed, and no dark precipitation was obtained. An explanation, therefore, could be the low boiling point of the sample and furthermore, instability of the formed complex. Unfortunately, no investigation on the ligand could be found in the literature. So an adjustment of the synthesis was not possible.
A different ligand N,N-dioctylamine was used with a higher boiling point, with an increased basic character origin in the presence of the secondary amine. Nevertheless, the different basicity of the ligand seems not to hinder the reaction of the ligand formation, and it is assumed, that the lead complex has an increased stability, which led to a successful synthesis and a black precipitate was collected.
The TEM reveals hexagon structures, which aligns in rows. Here the size is more expanded than the $CsPbI_3$ nano cuboids. Additional the size distribution is increased in comparison to the $CsPbI_3$ quantum dots with oleylamin as a ligand. This can be explained with the usage of the different ligand.

The shorter chain lengths lead to expanded particles.[343] The two-chained ligand further forms different micelles because of the different packing parameter.[168, 354] Therefore the shape varies from the nano cuboid with oleylamine as a ligand, published in literature.[23]
The purpose of narrowing the ligand gap in between the nanocrystals could not be achieved. In the TEM-Images, a distance of around 2,5 nm is still visible. This implies the formation of a double layer. For two chained ligands, this is already reported for different systems with a double alkyl chain ligand.[355, 356, 357] The alkyl chain packing with alternating alkyl chains, therefore, is not present, and a formation of a double layer is, as observed, likely.
Furthermore, the crystal structure was investigated by GIXRD. Here a pattern with broad signals is observed. Some of these signals could be assigned to the nanotwin phase, but additional more signals are present. These signals appeared with a different broadness, which indicates a different phase. This phase was compared to all known perovskite and non-perovskite phases and additionally to all precursor phases. An assignment to the observed signals was not successful. For this reason, a LeBail fit was not conducted. The broadness of the signals further made it impossible to assign the phase.
The OPTP measurement reveals a higher charge carrier mobility than for the 8 nm $CsPbI_3$ quantum dots capped with oleylamin as a ligand. The higher charge carrier mobility is therefore explainable with an expanded size of the nanoparticle size. An inter nanoparticle transport is suppressed by the formed double layer of the ligand. No further investigations were conducted with this ligand.
A more straightforward method for removing the ligands from the perovskite and possible merging the quantum dots is the post-synthesis thermal annealing method. This had shown for other quantum dots to be successful.[344, 345, 346] Also, the perovskite quantum dots were thermally annealed in literature but at temperatures above 200° C, with the result of a phase transition towards the δ-phase, which indicates the decomposition of the perovskite quantum dots.[316] The thermal annealing was carried out at 150°C under nitrogen protection, to prevent the degradation of the perovskite. As a result, in the TEM-images, a variety of shapes and sizes are observable. The majority of these structures seems to be rod-like structures. Furthermore, at some particles, separations into smaller segments are observable. This leads to the

conclusion that an uncontrolled merging of the particles had occurred.
The X-ray diffraction pattern further reveals narrower signals. This would add up to the conclusion of the merging of the quantum dots, which then form enlarged structures.
Further, more signals are observable. These additional signals could be assigned to different perovskite and non-perovskite phases. Hence a decomposition or a phase transition of the perovskite quantum dots had been occurring. This fits partly to the observations of the literature.[316] Since this leads to a further decomposition of the material and unwanted optical and electronical properties, no further investigations were not performed at this point.
Besides the exchange methods mentioned above, also other ligands were used for an exchange with the procedure described in literature.[316] Therefore bi factionalised amine ligands were chosen. The idea was to connect the nanocrystals and archive by implementing a ring system in the organic structure charge mobility in the ligand.
As a first ligand 1,6-hexanediamine was used. This lead to an instant decomposition of the sample. A reason, could the formation of a stable poly iodide compound .[347]This leads to an instant decomposition of the ligand-free, unprotected sample by the formation of first iodides and in the latter poly iodides, which leads to a further decomposition by a possible redox reaction with the perovskite.
As a second ligand 1,4-benzenedimethaneamine was used. With its ring system, a possible increase in charge mobility in the quantum dot layer might be possible.
Furthermore, the π-system of the benzene ring might add to a stabilization of the self-assembled structure by π-stacking.
Nevertheless, also for this ligand, a fast decomposition was observable. Even if the sample was stable for around one hour, a fast decomposition occurred after that time. A reason could also be a formation of iodine or polyiodides[347], by a decomposition of the sample. Several attempts led to the same results and made an investigation of the sample impossible. No further investigations were made.

Potassium incorporation into the $CsPbI_3$ Quantum dots The last part of this chapter is devoted to the effort in increasing the stability of the perovskite

nanocuboids. For this purpose, the suggestion of *Nam et al.,Nam2017* was taken, to incorporate potassium into the $CsPbI_3$ structure, for reducing the unit cell expansion. This is described for $CsPbI_2Br$ [348] because of the difficulty of stabilizing the $CsPbI_3$ structure at room temperature.[348, 358, 359]

The the synthesis was carried out as described for the hot injection synthesis in literature [23] with the addition of 0, 1, 2.5, 5, 7.5, 10 and 20 mol% of potassium-oleate to the cs-oleate. All reaction delivered a product like observed for the base line $CsPbI_3$ quantum dots with 0 mol% potassium described in literature [23]. Unfortunately, the reproducibility of the potassium doped samples was not possible. The reaction was carried out several times following the same protocol under the same conditions, delivering no incorporation of potassium into the $CsPbI_3$ structure.

Noticeably is the usage of hydrogen sulfide in the glovebox, in which the storage of the here used chemicals was placed. Moreover, the possibility of a reaction of the lead(II)iodide with sulphur or potassium carbonate.[350] Inasmuch as even traces of impurities are influencing the nanoparticle synthesis [351] this could be an explanation for the non-reproducibility of the potassium incorporated $CsPbI_3$ quantum dots.

Additionally observations of the decomposing time were qualitatively done. Within that, the sample differs in decomposition time. The 1 and 2.5 mol% samples degraded during days. The highest stability was found for the 7.5 mol% sample, which degraded after around three months. This is comparable with the findings in literature for the incorporation of 7.5 mol% potassium in the $CsPbI_3$ structure, leading to the highest stability.[348] The control sample with 0 mol% potassium was in contrast, already degrading after around one month. As an explanation for the fast degrading of the small mol% samples could be, that for the stabilisation, a certain threshold needs to be present. If this is not the case, degradation is likely. The 7.5 mol% sample show here the highest stability of the samples. This sample seems to compensate for the small Goldschmidt factor of the pure $CsPbI_3$ towards a structure with higher stability. Higher concentrations will lead to an earlier degradation of the sample.

Furthermore, the XRF is showing well-fitting concentrations of potassium in or on the samples of 5, 7.5, 10 and 20 mol%. Even though XRF is not a qualitative method, the results are fitting very well with the used potassium

amount in the synthesis. Impurities can be excluded since the purification method would remove all excess precursor. This assumption gets supported by the GIXRD measurements. Every pattern was fitted with a LeBail refinement with the nanotwin phase [119], and the unit cell size was extracted. Here a decrease in unit cell size was observed until the 7.5 mol% sample, which is also described in literature.[348] Higher concentration leads to an expansion of the unit cell. This might be explainable with a formation of a different phase in a solid solution and further a destabilisation of the perovskite phase.
The $KPbI_3$ is not forming a stable perovskite structure. Thus an extrapolation of the potassium content inside the $CsPbI_3$ with, i.e. Vegard's law [349], was not possible.
Further, investigations are needed to explain these observations, but were not possible because of the non-reproducibility of the samples.
The conducted PL- experiments support the findings of the GIXRD measurements. The unit cell and with that, a shift of the Pl signal is shifting. The FWHM stays constant for the samples up to 7.5 mol%, Indicating an equal size distribution, further no additional phase seems to be present.
For higher concentrations, an increase of the FWHM is detectable, which might indicate a different phase inside the crystals. This idea gets further supported by the observation of a shoulder formation of the Pl peak for the 20 mol% sample.
The results are suggesting the incorporation of the potassium and with that a stabilisation of the $CsPbI_3$ quantum dots. Other groups [360] are suggesting for a post-synthesis treatment a non-incorporation of the potassium, but the passivation of the surface. Because of the lack of reproducibility concerning the synthesis, no further investigation could be done.

5.7 Conclusion & Outlook

5.7.1 Conclusion

$CsPbI_3$ nano cuboids The in literature described synthesis could be reproduced.[23, 316] The TEM-images are showing on first side squarish structures which are assigned as the $CsPbI_3$ quantum dots. These quantum dots are self-assembled over an expanded area. Furthermore, the quantum dots are divided by gaps, which is assigned to the ligand.
By a closer investigation, two distinct sizes of the quantum dots are observed. The FFT of the measurement and the area integration supports this observation. This leads to the conclusion that the square structure might be better discussed as a rectangular structure. The explanation for this observation could be found in the crystal structure. The often described cubic α-phase [316, 197, 23] seems not be present. The group of *Guagliardi* describes a nanotwin, orthorhombic structure.[119] These results are fitting well with the measured GIXRD pattern and with the observed shape in the TEM-images.
X-ray reflectometry was used for investigating the layered $CsPbI_3$ quantum dot structure. As a result, an alternating layered structure of ligand and quantum dot could be found. The SLD does not always fit the calculated values. Defects in the layered structure by the incorporation of air or vacuum can explain this. Furthermore, stacking mistakes might also be involved. The total thickness of the layer was not fitting to the results of the estimated layer thickness. As a complementary method neutron reflectivity was used, and the used fit of the X-ray reflectivity data were applied to the neutron reflectivity measurement. As a result, the fit was not converging, which leads to the conclusion that the high X-ray absorptivity of the heavy elements is interfering with the obtained results.
Nevertheless, these methods reveal a highly ordered structure of a 17.5 cm^2 area.
Furthermore, the optical properties were investigated. The data are fitting the results of the literature.[23, 316] A spin-coated sample of the quantum dots was further investigated by optical pump terahertz probe method. As a result, a charge carrier mobility towards μ=0$\frac{cm^2}{Vs}$ was observed. The time-resolved photoluminescence revealed a two ways divided decay. Unfortunately, a fit

of the observed decay mechanism was not possible. It is suggested, that the decay mechanism in $CsPbI_3$ quantum dots is not comparable with other, known quantum dots.[316] Thus a quantitative discussion could be made. The first fast decay is most likely an inter quantum dot recombination. This gets supported by the high quantum yield of the particles. The limited size of the quantum dots is responsible for the fast recombination inside the quantum dots. The second longer decay is challenging to explain. The charge carriers might diffuse in the assumed different ligand layer on the surface of the quantum dot. A charge carrier transport to the double bond of the ligand is unlikely. Furthermore, tunnelling of the charge carriers to other quantum dots could occur. These models could explain the longer decay.

Ligand exchange of the $CsPbI_3$ quantum dots The ligand of the quantum dots as insulating material are suppressing the charge carrier mobility in between the quantum dots. The Luther group [197] suggested a washing method for ligand exchange for increasing the charge carrier mobility. For this purpose, one exchange is done by a solution of $Pb(NO_3)_2$ and Formamidinium iodide, and the second one is an exchange in formamidinium iodide (FaI) solution. This was here repeated for the formation of a foundation.
As a result, a ten times higher charge carrier mobility of μ= 6.52 $cm^2/V \cdot s$ by OPTP was measured for the FaI-solution treated sample, than published in literature.[197] An explanation for this observation could be the here used formamidinium iodide with a potential higher purity. In literature, it is described, that the acetate ion as a potential precursor of the formamidinium iodide synthesis, has a passivating effect on the quantum dots.[316] Unfortunately, a spectrum of the in literature published data of the OPTP measurement was not found, so a direct comparison is not possible. Because of the nonpolar solvent octane, which dissolved the PEDOT:PSS, a solar cell could not be produced.
Furthermore, the samples were investigated by GIXRD measurement. This reveals a change of the unit cell size towards smaller sizes. This indicates the incorporation of formamidinium into the $CsPbI_3$ lattice, which further explains the higher conductivity. This gets further supported by an increase in the size of the FaI treated samples. The optical analysis reveals further a loss of the quantum confinement, which supports this idea. For the lead(II)nitrate

treated samples, the same observation was made, but not as strong as for the just FaI treated samples. The explanation for this could be the passivation of the perovskite quantum dot by lead(II)nitrate on the surface.
To further improve the charge carrier mobility inside the quantum dots, additional ligand exchange methods were conducted. As a first attempt, a direct synthesis with shorter ligands was investigated. For this purpose, N-octylamine and N, N-dioctylamin as ligand were chosen and the same in the literature described synthesis route [23, 316]was conducted. During the synthesis, the lead(II)iodine/oleic acid and N-octylamine complex decomposed at a temperature around 150°C. An injection of the Cs-Oleate did not lead to a successful reaction. No further investigations were performed.
The N, N-dioctylamine with its higher boiling point and more basic properties and with that a higher binding affinity towards the lead complex, showed higher stability of the lead(II)iodide/oleic acid and N,N-dioctylamine ligand. A synthesis with this ligand was successful, and further investigations were conducted. The TEM-Images revealed hexagonal structures which vary in size. Furthermore, high crystallinity of these particles was observed by observing halos. Different grey scales further suggested a different orientation of the particles towards the incoming beam. The GIXRD revealed broad signals, which could be in part assigned to the nanotwin phase. Additional further signals are present, which could not be assigned to any perovskite, non-perovskite or precursor phase. The origin of this phase might be the incorporated ligand in the outer layer of the particle, which is unknown.
The OPTP measurement reveals a charge carrier mobility of μ=0.72 $cm^2/V \cdot s$ is slightly increased in comparison to the oleylamin caped ligand. The expanded particles can explain this observation. An inter particle transport of the charge carriers is unlikely due to the 2.5 nm thick insulating layer.
For this reason, no further investigations were performed at this point.
As a next method, post-synthesis thermal annealing of a $CsPbI_3$ quantum dot layer was conducted. This is reported for higher temperatures <200° C which is leading to an instant phase transition to the non-perovskite δ-phase.[316] For this reason, the thermal annealing was performed at ≈ 150° C. On first sight, no decomposition towards the yellow δ-phase was observed. The TEM images reveal particles with uneven sizes and shapes with a majority of rod-like shapes.
Furthermore, some of these structures are divided into smaller cuboid struc-

tures, which indicates a merging of the particles. The GIXRD measurement reveals narrower and additional signals in comparison to the oleylamine caped $CsPbI_3$ quantum dots. This suggests, on the one hand, the merging of the particles. However, on the other hand, a decomposition of the particles towards a different phase or the precursors. With that, no further investigations were conducted. As of the last method, the ligands were exchanged for task-specific ligands. For this purpose, two ligands with two amino groups were chosen. The task of these ligands was to connect the quantum dots and add an electron conductivity by, i.e. a ring system to the system. As ligands 1,6-hexanediamine and 1,4-benzenedimethanamine were chosen. During the ligand exchange with 1,6-hexanediamine, an instant decomposition of the sample was observed. A possible explanation could be the formation of an iodide and poly iodide, observed for this structure.[347] This would lead to a decomposition of the perovskite structure. The 1,4-benzenedimethanamine was stable for around one hour but soon decomposed after that time. The slightly higher stability could be explained with the steric hindered, caused by the ring structure of the reaction. Thus the decomposition of the perovskite phase, a further investigation was not possible.

Potassium incorporation in the $CsPbI_3$ lattice for enhancing the perovskite phase stability An enhancement of the stability was observed by the incorporation of potassium in the crystal lattice of $CsPbI_2Br$ layers in literature.[348] It is suggested, that the incorporation leads to a narrowing of the unit cell size following the stabilisation of the perovskite structure.[348]
Here the hot injection synthesis as described in literature [23] was conducted with the difference in 0, 1, 2.5, 5, 7.5, 10 and 20 mol% potassium oleate added to the caesium oleate. These syntheses lead to red precipitation, which indicates a successful synthesis of quantum dots. The following measurements are suggesting the incorporation of the potassium inside the $CsPbI_3$ lattice. An increase in stability towards the 7.5 mol% sample was observable. This is comparable to the literature.[348] The incorporation of the potassium was investigated by XRF, which fits the aimed values surprisingly well, even if no reference material was present.
The XRD pattern was refined with a LeBaile fit of the nanotwin [119] phase, and the unit cell size was estimated and compared. This revealed a decrease

in the unit cell and with that an increase in stabilisation towards the 7.5 mol% sample. Higher amounts of potassium inside the $CsPbI_3$ lead to faster decomposition. Unfortunately, the formation of $KPbI_3$ is not observed. Thus an estimation of the potassium content by Vegard's law was not possible.[349] These findings are also observable by the Pl- measurements of the samples. Furthermore, more a second phase is occurring at 20 mol% of potassium noticeable by a shoulder in the Pl spectra.
Nevertheless, after the first seven successful syntheses, this reaction was not reproducible. Even after several attempts, no potassium was incorporated into the $CsPbI_3$ lattice. An explanation for this observation could not be given here. A possibility is a negative influence of the hydrogen sulphide used inside the glovebox, which might react with the precursor and further lead to the unsuccessful incorporation of the potassium inside the $CsPbI_3$ lattice. The last-mentioned challenge leads further to a non-plain analysis of all the samples because the 1 mol% and 2.5 mol% sample decomposed after around two days.

5.7.2 Outlook

The $CsPbI_3$ quantum dots show high potential for quantum dot solar cell applications.[197, 316] This is achieved if the insulating ligand, oleylamine is replaced by, e.g. formamidinium iodide, which might form $FaPbI_3$ in between the quantum dots.[197] Nevertheless, the here showed increase of the charge mobility of μ= 6.52 $cm^2/V \cdot s$ leads to a possibly higher solar cell efficiency than found in literature [197], with a different solar cell design. The ligand of the $CsPbI_3$ quantum dots gave a stabilizing but insulating effect on the layered structure. For this reason, further investigation could be conducted towards stabilizing and conducting ligands. As an example, the ligand could be an amino derivate of a polyunsaturated fatty acid. The fatty acid docosapentaenoic acid, with its conducting π-system seems a promising electron conductor, which is further discussed as an electron conductor in the brain.[361, 362, 363] As a ligand for the perovskite synthesis docosahexaenoic-amine might be a candidate for a reliable synthesis and a charge carrier conductivity inside the solar cell.
The incorporation of potassium seems to increase the stability of the $CsPbI_3$

structure, by a post-synthesis method this is already shown in literature.[360] A direct synthesis would eliminate a further step, but the non-reproducibility of the synthesis here makes this unusable for an application.
For this reason, a more reliable synthesis method with pure precursors could be used. This might lead to a further understanding of the influence of dopants in $CsPbI_3$ quantum dots. First steps in this direction are already made with incorporating manganese in the crystal lattice.[364, 365] With that, an overall increase of the stability could be achieved, which further might lead to lead-free, stable perovskite nanocrystals.

Appendix

$CsPbI_3$ nanocrystals & treatments

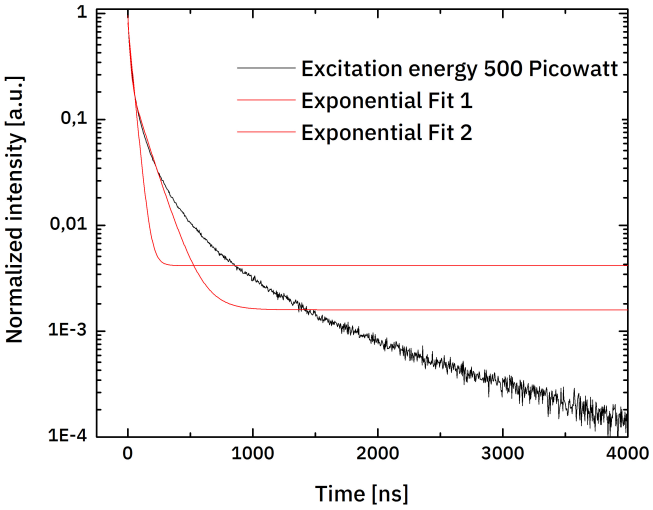

Fig. .44: TRPL decay of the $CsPbI_3$ dispersion with two non correlating exponential fits

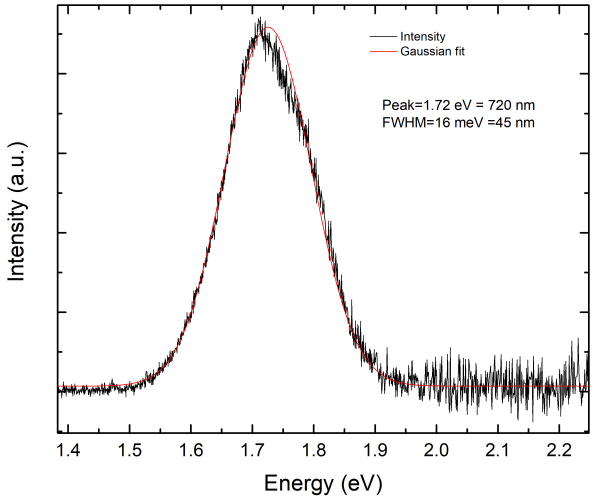

Fig. .45: Emission spectra of the $CsPbI_3$ quantum dot layer treated with FaI with the resulting Gaussian fit

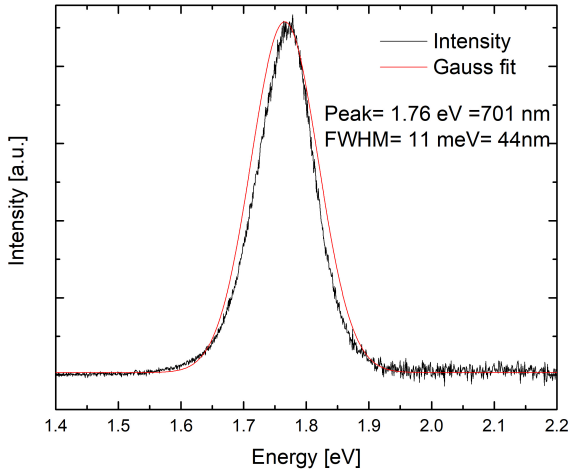

Fig. .46: Emission spectra of the $CsPbI_3$ quantum dot layer treated with FaI and $Pb(NO_3)_2$ with the resulting Gaussian fit

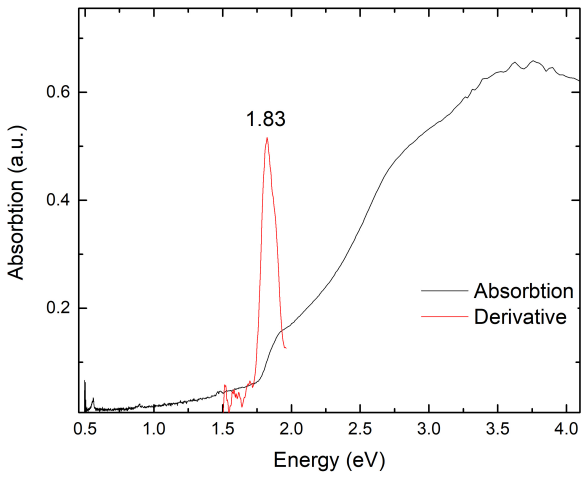

Fig. .47: Absorption spectra of the Pure $CsPbI_3$ quantum dots with the first derivative

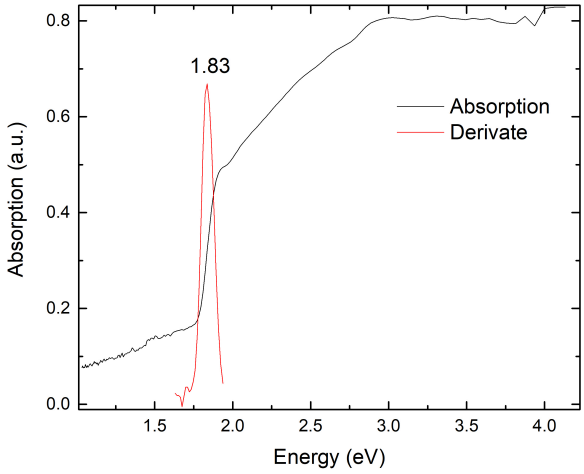

Fig. .48: Absorption spectra of the washed $CsPbI_3$ quantum dots with the first derivative

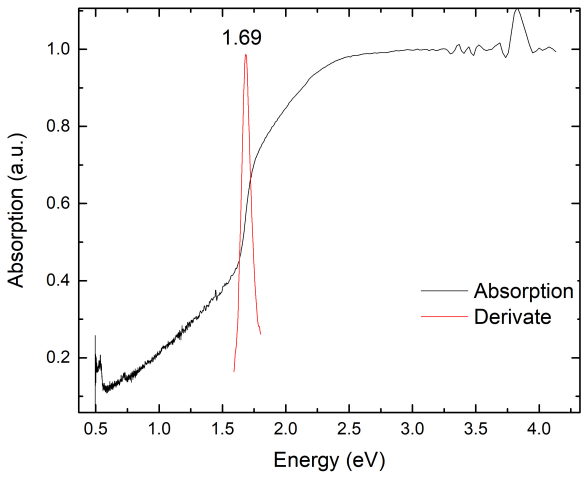

Fig. .49: Absorption spectra of the $CsPbI_3$ quantum dots treated with FAI with the first derivative

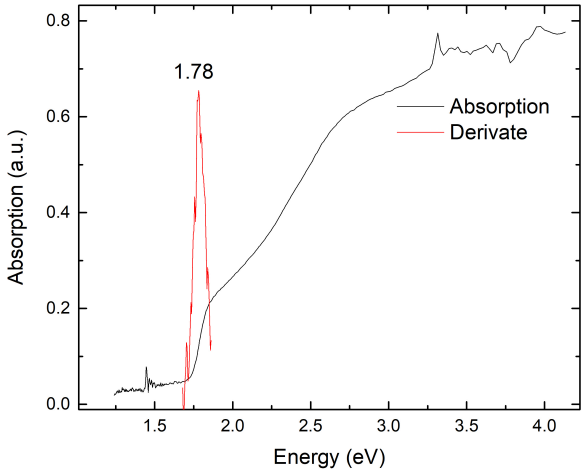

Fig. .50: Absorption spectra of the $CsPbI_3$ quantum dots treated with FaI and $Pb(NO_3)_2$with the first derivative

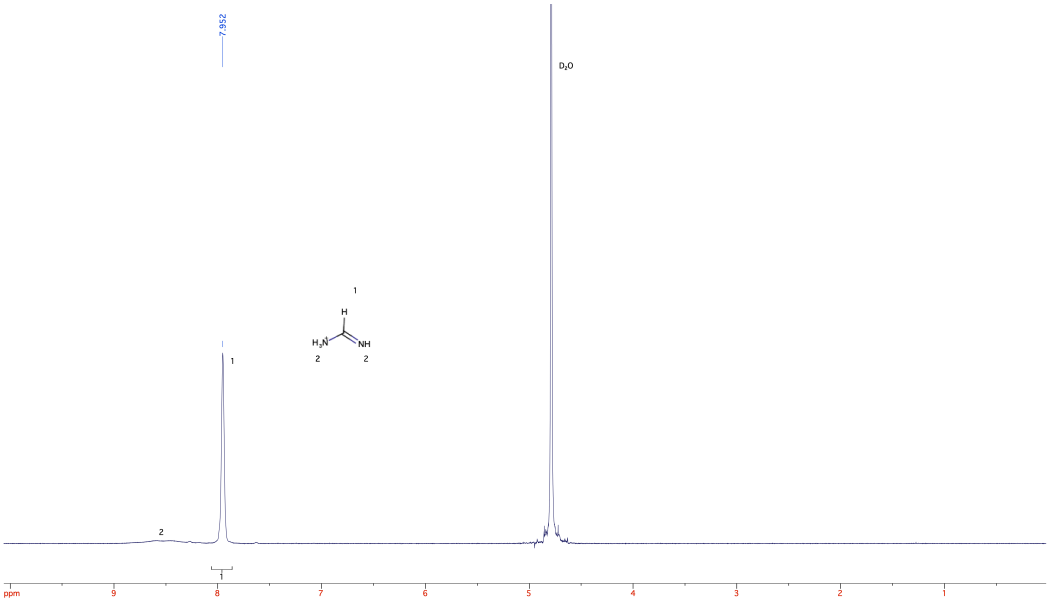

Fig. .51: NMR spectra of the formamidinium iodide product without acetate signals

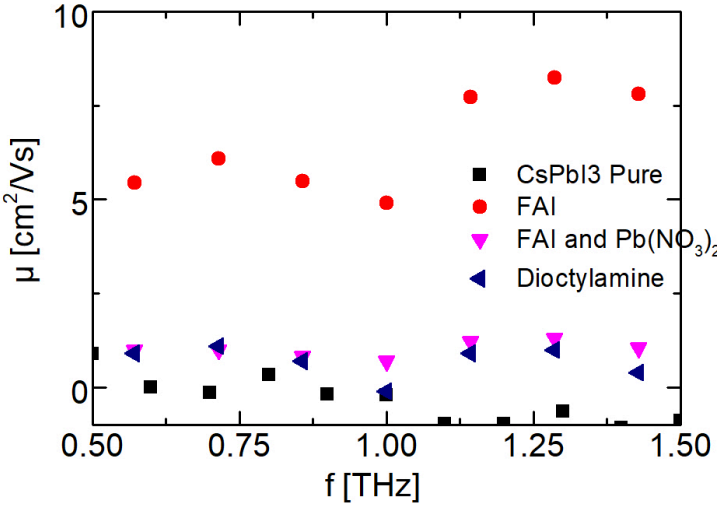

Fig. .52: Terahertz spectra of all investigated samples

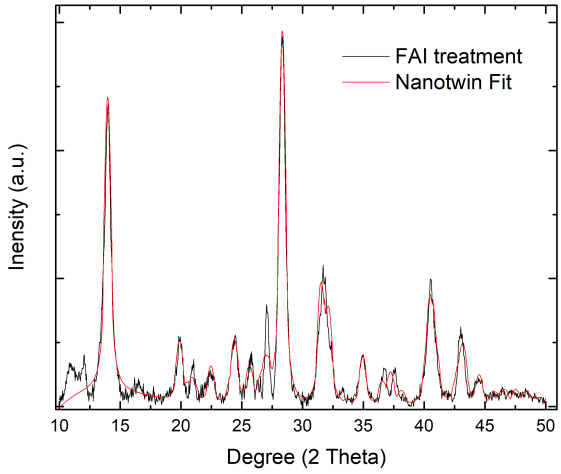

Fig. .53: XRD of the $CsPbI_3$ quantum dots treated with FaI and LeBail fit

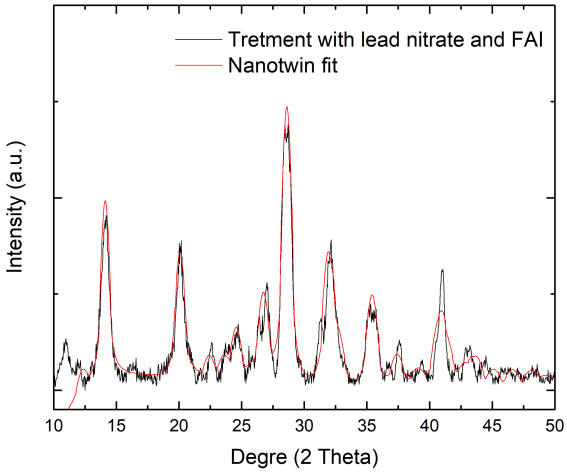

Fig. .54: XRD of the $CsPbI_3$ quantum dots treated with FaI and $Pb(NO_3)_2$ and LeBail fit

$CsPbI_3$ quantum dots incorporated with potassium

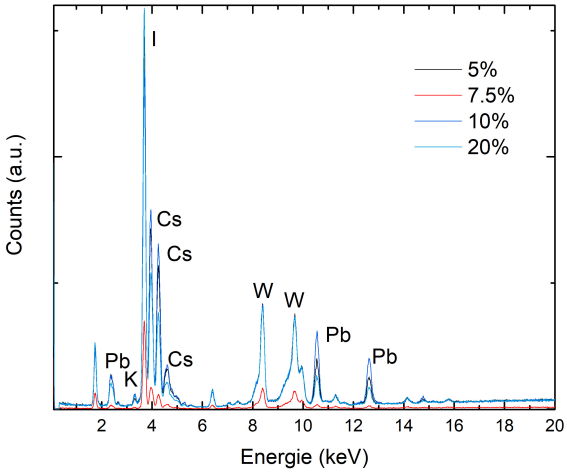

Fig. .55: XRF spectra of 5, 7.5, 10 and 20% K in $CsPbI_3$ Nanoparticles

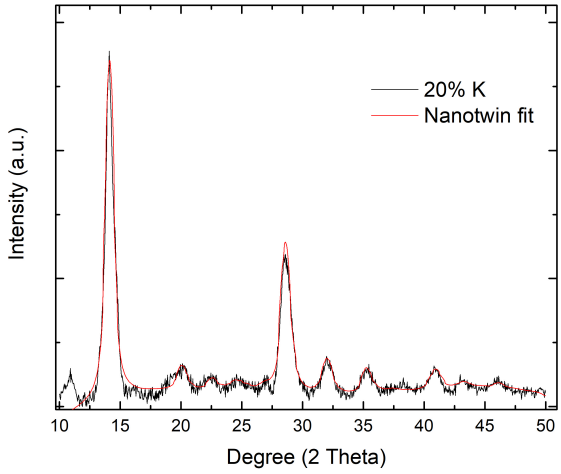

Fig. .56: XRD of the $CsPbI_3$ quantum dots with the incorporation of 1% potassium and the resulting LeBail fit

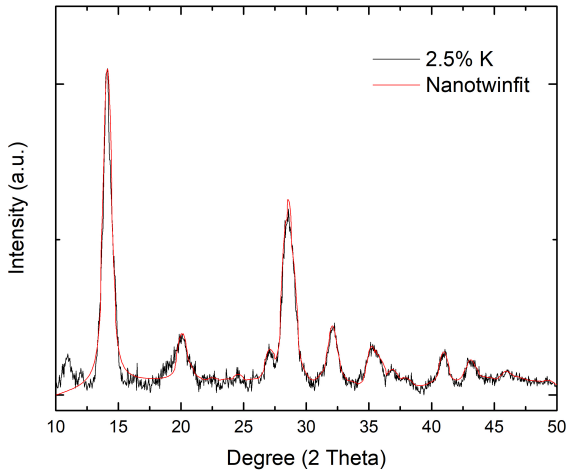

Fig. .57: XRD of the $CsPbI_3$ quantum dots with the incorporation of 2.5% potassium

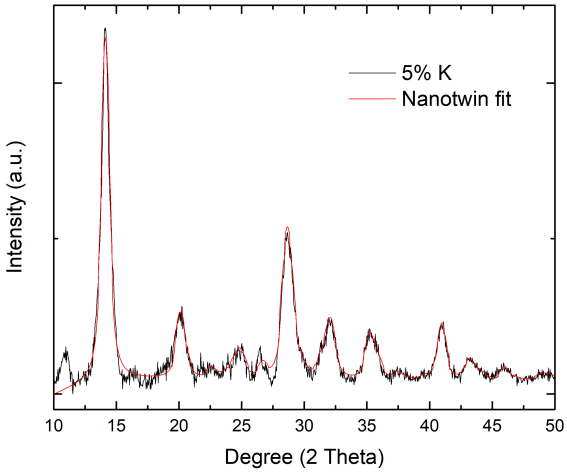

Fig. .58: XRD of the $CsPbI_3$ quantum dots with the incorporation of 5% potassium

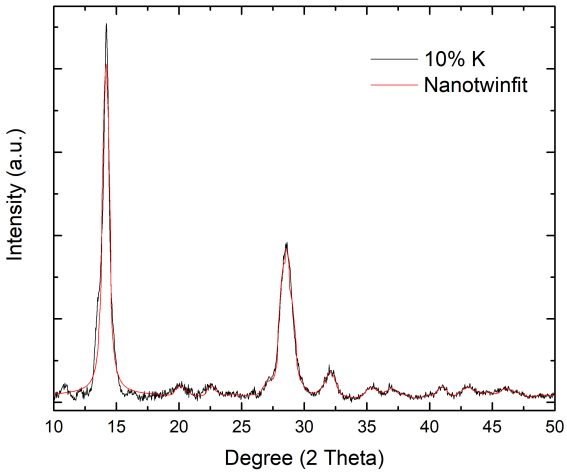

Fig. .59: XRD of the $CsPbI_3$ quantum dots with the incorporation of 10% potassium

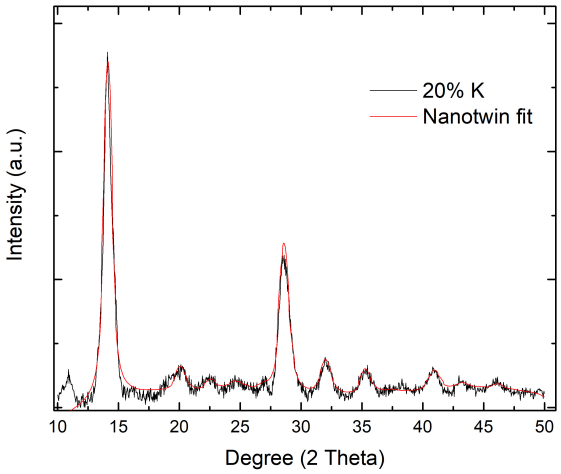

Fig. .60: XRD of the $CsPbI_3$ quantum dots with the incorporation of 20% potassium

Bibliography

[1] Stephen A. Holditch and Russell R. Chianelli. “Factors that will influence oil and gas supply and demand in the 21st Century”. In: *MRS Bulletin* Vol.33.Nr.4 (Apr. 2008), pp. 317–323 (cit. on p. 1).

[2] Nicholas Stern. “The Economics of Climate Change”. In: *American Economic Review* Vol.98.Nr.2 (Apr. 2008), pp. 1–37 (cit. on p. 1).

[3] Amir Shahsavari and Morteza Akbari. “Potential of solar energy in developing countries for reducing energy-related emissions”. In: *Renewable and Sustainable Energy Reviews* Vol.90 (July 2018), pp. 275–291 (cit. on p. 1).

[4] Raphael Neukom, Luis A. Barboza, Michael P. Erb, et al. “Consistent multidecadal variability in global temperature reconstructions and simulations over the Common Era”. In: *Nature Geoscience* Vol.12.Nr.8 (Aug. 2019), pp. 643–649 (cit. on p. 1).

[5] George Tsatsaronis, Tatiana Morosuk, Daniela Koch, and Max Sorgenfrei. “Understanding the thermodynamic inefficiencies in combustion processes”. In: *Energy* Vol.62 (Dec. 2013), pp. 3–11 (cit. on p. 1).

[6] Stephen A. Rackley. “Power Generation Fundamentals”. In: *Carbon Capture and Storage*. Elsevier, 2010, pp. 29–64 (cit. on p. 1).

[7] Ola Eriksson. “Nuclear Power and Resource Efficiency. A Proposal for a Revised Primary Energy Factor”. In: *Sustainability* Vol.9.Nr.6 (June 2017), p. 1063 (cit. on p. 1).

[8] T Kamiya and H Venghaus. *Thin-Film Solar Cells*. Ed. by Yoshihiro Hamakawa. Vol. 13. Springer Series in Photonics. Berlin, Heidelberg: Springer Berlin Heidelberg, 2004 (cit. on pp. 1, 2).

[9] Richard J. Pearson, Armando B. Antoniazzi, and William J. Nuttall. “Tritium supply and use: a key issue for the development of nuclear fusion energy”. In: *Fusion Engineering and Design* Vol.136 (2018), pp. 1140–1148 (cit. on p. 1).

[10]H Wirth. *Recent facts about photovoltaics in Germany*. (https://www.ise.fraunhofer.de/content/dam/ise/en/documents/publications/studies/recent-facts-about-photovoltaics-in-germany.pdf). Freiburg, 2019-06-19 (cit. on p. 1).

[11]Gary A. Chapman. "Solar luminosity". In: *Encyclopedia of Planetary Science*. Dordrecht: Kluwer Academic Publishers, pp. 748–748 (cit. on p. 1).

[12]United Nations Development Programme. *World Energy Assessment. Energy and the challenge of Sustainability*. 2000, p. 506 (cit. on p. 1).

[13]Thomas Dittrich. *Materials Concepts for Solar Cells*. World Scientific (Europe), Apr. 2018 (cit. on pp. 1, 2, 6, 11–13).

[14]Sergio Pizzini. "Towards solar grade silicon: Challenges and benefits for low cost photovoltaics". In: *Solar Energy Materials and Solar Cells* Vol.94.Nr.9 (2010), pp. 1528–1533 (cit. on pp. 1, 2).

[15]Peter Y. Yu and Manuel Cardona. *Fundamentals of Semiconductors*. Graduate Texts in Physics. Berlin, Heidelberg: Springer Berlin Heidelberg, 2010 (cit. on pp. 2, 6–12, 26, 27, 44–47).

[16]S.W. Glunz, R. Preu, and D. Biro. "Crystalline Silicon Solar Cells". In: *Comprehensive Renewable Energy*. Vol. 1. Elsevier, 2012, pp. 353–387 (cit. on p. 2).

[17]Martin A. Green, Ewan D. Dunlop, Dean H. Levi, et al. "Solar cell efficiency tables (version 54)". In: *Progress in Photovoltaics: Research and Applications* Vol.27.Nr.7 (July 2019), pp. 565–575 (cit. on pp. 2, 17).

[18]Niraj N. Lal, Yasmina Dkhissi, Wei Li, et al. "Perovskite Tandem Solar Cells". In: *Advanced Energy Materials* Vol.7.Nr.18 (Sept. 2017), p. 1602761 (cit. on p. 2).

[19]Bekele Hailegnaw, Saar Kirmayer, Eran Edri, Gary Hodes, and David Cahen. "Rain on Methylammonium Lead Iodide Based Perovskites: Possible Environmental Effects of Perovskite Solar Cells". In: *The Journal of Physical Chemistry Letters* Vol.6.Nr.9 (May 2015), pp. 1543–1547 (cit. on pp. 2, 20).

[20]Aurélien M. A. Leguy, Yinghong Hu, Mariano Campoy-Quiles, et al. "Reversible Hydration of $CH_3NH_3PbI_3$ in Films, Single Crystals, and Solar Cells". In: *Chemistry of Materials* Vol.27.Nr.9 (May 2015), pp. 3397–3407 (cit. on pp. 2, 20).

[21] Guangda Niu, Wenzhe Li, Fanqi Meng, et al. “Study on the stability of $CH_3NH_3PbI_3$ films and the effect of post-modification by aluminum oxide in all-solid-state hybrid solar cells”. In: *J. Mater. Chem. A* Vol.2.Nr.3 (2014), pp. 705–710 (cit. on pp. 2, 20).

[22] Sneha A. Kulkarni, Subodh G. Mhaisalkar, Nripan Mathews, and Pablo P. Boix. “Perovskite Nanoparticles: Synthesis, Properties, and Novel Applications in Photovoltaics and LEDs”. In: *Small Methods* Vol.3.Nr.1 (2019), p. 1800231 (cit. on pp. 2, 23, 24, 27, 77, 83, 91, 106).

[23] Loredana Protesescu, Sergii Yakunin, Maryna I. Bodnarchuk, et al. “Nanocrystals of Cesium Lead Halide Perovskites ($CsPbX_3$, X = Cl, Br, and I): Novel Optoelectronic Materials Showing Bright Emission with Wide Color Gamut”. In: *Nano Letters* Vol.15.Nr.6 (June 2015), pp. 3692–3696 (cit. on pp. 2, 10, 19, 21–23, 27, 113, 115–117, 119, 122–124, 131, 137, 142, 144, 149, 165, 168, 169, 172, 174, 176, 178, 179).

[24] Eric T. Hoke, Daniel J. Slotcavage, Emma R. Dohner, et al. “Reversible photo-induced trap formation in mixed-halide hybrid perovskites for photovoltaics”. In: *Chemical Science* Vol.6.Nr.1 (2015), pp. 613–617 (cit. on p. 2).

[25] Jun Pan, Li Na Quan, Yongbiao Zhao, et al. “Highly Efficient Perovskite-Quantum-Dot Light-Emitting Diodes by Surface Engineering”. In: *Advanced Materials* Vol.28.Nr.39 (Oct. 2016), pp. 8718–8725 (cit. on p. 2).

[26] Meng Zhang, Fan Zhang, Yue Wang, et al. “High-Performance Photodiode-Type Photodetectors Based on Polycrystalline Formamidinium Lead Iodide Perovskite Thin Films”. In: *Scientific Reports* Vol.8.Nr.1 (Dec. 2018), p. 11157 (cit. on pp. 2, 17).

[27] Haishan Wu, Weiwei Zhang, Junjie Wu, and Yuwu Chi. “A Visual Solar UV Sensor Based on Paraffin-Perovskite Quantum Dot Composite Film”. In: *ACS Applied Materials & Interfaces* Vol.11.Nr.18 (May 2019), pp. 16713–16719 (cit. on p. 2).

[28] D. R. Baer, J. E. Amonette, M. H. Engelhard, et al. “Characterization challenges for nanomaterials”. In: *Surface and Interface Analysis* Vol.40.Nr.3-4 (Mar. 2008), pp. 529–537 (cit. on p. 2).

[29] Louis De Broglie. *New Perspectives in Physics*. Ed. by Louis De Broglie. New York: New York: Basic Books, 1962, p. 184 (cit. on p. 5).

[30] D. R. Williams. *NASA Goddard Space Flight Center*. (`https://nssdc.gsfc.nasa.gov/planetary/factsheet/sunfact.html`). 28.07.2019 (cit. on p. 6).

[31]Peter V. Foukal. *Solar Astrophysics*. Ed. by Peter V. Foukal. Vol. 55. Nr.9. Weinheim, Germany: Wiley, Feb. 2004, p. 1315 (cit. on p. 6).

[32]A.E. Becquerel. “Memoire sur les effects d’electriques produits sous lt’influence des rayons solaires”. In: *Annalen der Physick und Chemie* Vol.54 (1841), pp. 35–42 (cit. on p. 6).

[33]A. Einstein. “Über einen die Erzeugung und Verwandlung des Lichtes betreffenden heuristischen Gesichtspunkt”. In: *Annalen der Physik* Vol.322.Nr.6 (1905), pp. 132–148 (cit. on p. 6).

[34]C.E. Fritts. “On the Fritts selenium cells and batteries”. In: *Journal of the Franklin Institute* Vol.119.Nr.3 (Mar. 1885), pp. 221–232 (cit. on p. 6).

[35]D. M. Chapin, C. S. Fuller, and G. L. Pearson. “A New Silicon pn Junction Photocell for Converting Solar Radiation into Electrical Power”. In: *Journal of Applied Physics* Vol.25.Nr.5 (May 1954), pp. 676–677 (cit. on p. 6).

[36]Akihiro Kojima, Kenjiro Teshima, Yasuo Shirai, and Tsutomu Miyasaka. “Organometal Halide Perovskites as Visible-Light Sensitizers for Photovoltaic Cells”. In: *Journal of the American Chemical Society* Vol.131.Nr.17 (May 2009), pp. 6050–6051 (cit. on pp. 6, 17, 21).

[37]Hans-Günther Wagemann and Heinz Eschrich. *Photovoltaik*. Wiesbaden: Vieweg+Teubner, 2010 (cit. on pp. 6, 9).

[38]Peter Würfel and Uli Würfel. *Physics of Solar Cells*. 3rd ed. Weinheim, Germany, 2016 (cit. on pp. 6, 7, 10, 11).

[39]Golden. “Reference Solar spectral irradiance: Air Mass Zero”. In: *American Society for testing and materials* NREL (2018) (cit. on p. 7).

[40]Golden. “Reference solar spectral irradiance: Air mass 1.5”. In: *American Society for testing and materials* NREL (2018) (cit. on p. 7).

[41]Leonhard Stiny. *Aktive elektronische Bauelemente*. Wiesbaden: Springer Fachmedien Wiesbaden, 2019 (cit. on p. 7).

[42]Charles Kittel. *Einführung in die Festkörperphysik*. 13th ed. Vol. 13. Berlin, Boston: De Gruyter, 2002 (cit. on pp. 8–10).

[43]Achim Gross, Rudolf Marx. *Festkörperphysik*. 2nd ed. Oldenburg: De Gruyter Oldenburg, 2014, p. 1006 (cit. on pp. 8, 30).

[44]Marius Grundmann. *The Physics of Semiconductors*. Graduate Texts in Physics. Cham: Springer International Publishing, 2016 (cit. on p. 9).

[45]Viktor L. Bon-Bruevi and Sergej G. Kalanikov. *Halbleiterphysik*. Berlin: Deutscher Verlag der Wissenschaften, 1982, p. 646 (cit. on p. 9).

[46]Y.P. Varshni. “Temperature dependence of the energy gap in semiconductors”. In: *Physica* Vol.34.Nr.1 (Jan. 1967), pp. 149–154 (cit. on p. 9).

[47]K. P. O’Donnell and X. Chen. “Temperature dependence of semiconductor band gaps”. In: *Applied Physics Letters* Vol.58.Nr.25 (June 1991), pp. 2924–2926 (cit. on p. 9).

[48]W. Shan, W. Walukiewicz, J. W. Ager, et al. “Pressure dependence of the fundamental band-gap energy of CdSe”. In: *Applied Physics Letters* Vol.84.Nr.1 (Jan. 2004), pp. 67–69 (cit. on p. 9).

[49]Stephen J. Fonash. “Material Properties and Device Physics Basic to Photovoltaics”. In: *Solar Cell Device Physics*. Second Edi. Elsevier, 2010, pp. 9–65 (cit. on p. 10).

[50]Solmaz Torabi, Fatemeh Jahani, Ineke Van Severen, et al. “Strategy for enhancing the dielectric constant of organic semiconductors without sacrificing charge carrier mobility and solubility”. In: *Advanced Functional Materials* Vol.25.Nr.1 (2015), pp. 150–157 (cit. on p. 10).

[51]S.M. Sze and Kwok K. Ng. *Physics of Semiconductor Devices*. Hoboken, NJ, USA: John Wiley & Sons, Inc., Oct. 2006 (cit. on pp. 10, 19).

[52]Jenya Tilchin, Dmitry N. Dirin, Georgy I. Maikov, et al. “Hydrogen-like WannierMott Excitons in Single Crystal of Methylammonium Lead Bromide Perovskite”. In: *ACS Nano* Vol.10.Nr.6 (June 2016), pp. 6363–6371 (cit. on pp. 10, 101, 103).

[53]Uli Wurfel, Andres Cuevas, and Peter Wurfel. “Charge Carrier Separation in Solar Cells”. In: *IEEE Journal of Photovoltaics* Vol.5.Nr.1 (Jan. 2015), pp. 461–469 (cit. on p. 11).

[54]Holger Borchert. *Solar Cells Based on Colloidal Nanocrystals*. Vol. 196. Springer Series in Materials Science. Cham: Springer International Publishing, 2014 (cit. on pp. 11, 26).

[55]Florian Staub, Uwe Rau, and Thomas Kirchartz. “Statistics of the Auger Recombination of Electrons and Holes via Defect Levels in the Band Gap - Application to Lead-Halide Perovskites”. In: *ACS Omega* Vol.3.Nr.7 (2018), pp. 8009–8016 (cit. on p. 13).

[56]Florian Staub, Hannes Hempel, Jan-Christoph Hebig, et al. “Beyond Bulk Lifetimes: Insights into Lead Halide Perovskite Films from Time-Resolved Photoluminescence”. In: *Physical Review Applied* Vol.6.Nr.4 (Oct. 2016), p. 044017 (cit. on pp. 13, 47, 48).

[57]W. Shockley and W. T. Read. “Statistics of the Recombinations of Holes and Electrons”. In: *Physical Review* Vol.87.Nr.5 (Sept. 1952), pp. 835–842 (cit. on p. 13).

[58]H. Q. North. “Properties of welded contact germanium rectifiers”. In: *Journal of Applied Physics* Vol.17.Nr.11 (1946), pp. 912–923 (cit. on p. 13).

[59]Victor I. Klimov. “Multicarrier Interactions in Semiconductor Nanocrystals in Relation to the Phenomena of Auger Recombination and Carrier Multiplication”. In: *Annual Review of Condensed Matter Physics* Vol.5.Nr.1 (2014), pp. 285–316 (cit. on p. 13).

[60]Huaxiang Fu and Alex Zunger. “InP quantum dots: Electronic structure, surface effects, and the redshifted emission”. In: *Physical Review B* Vol.56.Nr.3 (July 1997), pp. 1496–1508 (cit. on p. 13).

[61]William Shockley and Hans J. Queisser. “Detailed Balance Limit of Efficiency of pn Junction Solar Cells”. In: *Journal of Applied Physics* Vol.32.Nr.3 (Mar. 1961), pp. 510–519 (cit. on p. 14).

[62]Thomas Kirchartz and Uwe Rau. “What Makes a Good Solar Cell?” In: *Advanced Energy Materials* Vol.8.Nr.28 (Oct. 2018), p. 1703385 (cit. on p. 14).

[63]Cherie R. Kagan Murray and Christopher B. “Charge transport in strongly coupled quantum dot solids”. In: Vol.10 (2015), pp. 1013–1026 (cit. on pp. 14, 27, 134, 137, 169).

[64]Andreas Klein. “Energy band alignment at interfaces of semiconducting oxides: A review of experimental determination using photoelectron spectroscopy and comparison with theoretical predictions by the electron affinity rule, charge neutrality levels, and the common anion”. In: *Thin Solid Films* Vol.520.Nr.10 (Mar. 2012), pp. 3721–3728 (cit. on p. 14).

[65]Martin A. Green, Anita Ho-Baillie, and Henry J. Snaith. “The emergence of perovskite solar cells”. In: *Nature Photonics* Vol.8.Nr.7 (2014), pp. 506–514 (cit. on pp. 14, 16).

[66]Helen D Megaw. “Crystal structure of double oxides of the perovskite type”. In: *Proceedings of the Physical Society* Vol.58.Nr.3 (1946), pp. 340–340 (cit. on p. 14).

[67]Takeo Oku. “Crystal Structures of $CH_3NH_3PbI_3$ and Related Perovskite Compounds Used for Solar Cells”. In: *Solar Cells - New Approaches and Reviews* (Oct. 2015) (cit. on p. 14).

[68] Wei Li, Zheming Wang, Felix Deschler, et al. “Chemically diverse and multifunctional hybrid organicinorganic perovskites”. In: *Nature Reviews Materials* Vol.2.Nr.3 (2017), p. 16099 (cit. on p. 14).

[69] Aron Walsh. “Principles of Chemical Bonding and Band Gap Engineering in Hybrid Organic-Inorganic Halide Perovskites”. In: *The Journal of Physical Chemistry C* Vol.119.Nr.11 (2015), pp. 5755–5760 (cit. on pp. 15, 18).

[70] Dieter Weber. “$CH_3NH_3PbX_3$, ein Pb(II)-System mit kubischer Perowskitstruktur / $CH_3NH_3PbX_3$, a Pb(II)-System with Cubic Perovskite Structure”. In: *Zeitschrift für Naturforschung B* Vol.33.Nr.12 (Dec. 1978), pp. 1443–1445 (cit. on pp. 15–17).

[71] Pradeep R. Varadwaj, Arpita Varadwaj, Helder M. Marques, and Koichi Yamashita. “Significance of hydrogen bonding and other noncovalent interactions in determining octahedral tilting in the $CH_3NH_3PbI_3$ hybrid organic-inorganic halide perovskite solar cell semiconductor”. In: *Scientific Reports* Vol.9.Nr.1 (Dec. 2019), p. 50 (cit. on p. 15).

[72] Marina R. Filip and Feliciano Giustino. “The geometric blueprint of perovskites”. In: *Proceedings of the National Academy of Sciences* Vol.115.Nr.21 (May 2018), pp. 5397–5402 (cit. on p. 15).

[73] V. M. Goldschmidt. “Krystallbau und chemische Zusammensetzung”. In: *Berichte der deutschen chemischen Gesellschaft (A and B Series)* Vol.60.Nr.5 (Jan. 1927), pp. 1263–1296 (cit. on p. 15).

[74] Chonghea Li, Xionggang Lu, Weizhong Ding, et al. “Formability of ABX_3 (X = F, Cl, Br, I) halide perovskites”. In: *Acta Crystallographica Section B Structural Science* Vol.64.Nr.6 (Dec. 2008), pp. 702–707 (cit. on p. 16).

[75] Zhen Li, Mengjin Yang, Ji-Sang Park, et al. “Stabilizing Perovskite Structures by Tuning Tolerance Factor: Formation of Formamidinium and Cesium Lead Iodide Solid-State Alloys”. In: *Chemistry of Materials* Vol.28.Nr.1 (Jan. 2016), pp. 284–292 (cit. on pp. 16, 21, 113, 141, 142, 161, 169).

[76] I.P. Swainson, R.P. Hammond, C. Soullière, O. Knop, and W. Massa. “Phase transitions in the perovskite methylammonium lead bromide, $CH_3ND_3PbBr_3$”. In: *Journal of Solid State Chemistry* Vol.176.Nr.1 (Nov. 2003), pp. 97–104 (cit. on p. 16).

[77] Subham Dastidar, Christopher J. Hawley, Andrew DeVries Dillon, et al. “Quantitative Phase-Change Thermodynamics and Metastability of Perovskite-Phase Cesium Lead Iodide”. In: *The Journal of Physical Chemistry Letters* Vol.8.Nr.6 (Mar. 2017), pp. 1278–1282 (cit. on pp. 16, 123).

[78] Yonggang Wang, Xujie Lü, Wenge Yang, et al. “Pressure-Induced Phase Transformation, Reversible Amorphization, and Anomalous Visible Light Response in Organolead Bromide Perovskite”. In: *Journal of the American Chemical Society* Vol.137.Nr.34 (Sept. 2015), pp. 11144–11149 (cit. on pp. 16, 91, 103, 104, 108, 111).

[79] E. Lora da Silva, Jonathan M Skelton, Stephen C Parker, and Aron Walsh. “Phase stability and transformations in the halide perovskite $CsSnI_3$”. In: *Physical Review B* Vol.91.Nr.14 (Apr. 2015), p. 144107 (cit. on p. 16).

[80] Sidney E. Creutz, Evan N. Crites, Michael C. De Siena, and Daniel R. Gamelin. “Colloidal Nanocrystals of Lead-Free Double-Perovskite (Elpasolite) Semiconductors: Synthesis and Anion Exchange To Access New Materials”. In: *Nano Letters* Vol.18.Nr.2 (Feb. 2018), pp. 1118–1123 (cit. on p. 16).

[81] Sebastian F. Hoefler, Gregor Trimmel, and Thomas Rath. “Progress on lead-free metal halide perovskites for photovoltaic applications: a review”. In: *Monatshefte für Chemie - Chemical Monthly* Vol.148.Nr.5 (2017), pp. 795–826 (cit. on p. 16).

[82] Hui-Seon Kim, Chang-Ryul Lee, Jeong-Hyeok Im, et al. “Lead Iodide Perovskite Sensitized All-Solid-State Submicron Thin Film Mesoscopic Solar Cell with Efficiency Exceeding 9%”. In: *Scientific Reports* Vol.2.Nr.1 (Dec. 2012), p. 591 (cit. on p. 17).

[83] Baodan Zhao, Sai Bai, Vincent Kim, et al. “High-efficiency perovskitepolymer bulk heterostructure light-emitting diodes”. In: *Nature Photonics* Vol.12.Nr.12 (Dec. 2018), pp. 783–789 (cit. on p. 17).

[84] Alexander D. Jodlowski, Cristina Roldán-Carmona, Giulia Grancini, et al. “Large guanidinium cation mixed with methylammonium in lead iodide perovskites for 19% efficient solar cells”. In: *Nature Energy* 2.Nr.12 (2017), pp. 972–979 (cit. on p. 18).

[85] Giles E. Eperon, Giuseppe M. Paternò, Rebecca J. Sutton, et al. “Inorganic caesium lead iodide perovskite solar cells”. In: *Journal of Materials Chemistry A* Vol.3.Nr.39 (2015), pp. 19688–19695 (cit. on p. 18).

[86] Tomas Leijtens, Rohit Prasanna, Kevin A. Bush, et al. “Tinlead halide perovskites with improved thermal and air stability for efficient all-perovskite tandem solar cells”. In: *Sustainable Energy & Fuels* Vol.2.Nr.11 (2018), pp. 2450–2459 (cit. on p. 18).

[87] Maarten G Goesten and Roald Hoffmann. “Mirrors of Bonding in Metal Halide Perovskites”. In: *Journal of the American Chemical Society* Vol.140.Nr.40 (Oct. 2018), pp. 12996–13010 (cit. on p. 18).

[88] Weiwei Gao, Xiang Gao, Tesfaye A Abtew, et al. “Quasiparticle band gap of organic-inorganic hybrid perovskites: Crystal structure, spin-orbit coupling, and self-energy effects”. In: *Physical Review B* Vol.93.Nr.8 (Feb. 2016), p. 085202 (cit. on p. 18).

[89] Carlos Cardenas-Daw, Thomas Simon, Jacek K Stolarczyk, and Jochen Feldmann. “Migration of Constituent Protons in Hybrid OrganicInorganic Perovskite Triggers Intrinsic Doping”. In: *Journal of the American Chemical Society* Vol.139.Nr.46 (Nov. 2017), pp. 16462–16465 (cit. on p. 18).

[90] Aurelien M. A. Leguy, Jarvist Moore Frost, Andrew P. McMahon, et al. “The dynamics of methylammonium ions in hybrid organicinorganic perovskite solar cells”. In: *Nature Communications* Vol.6.Nr.1 (Dec. 2015), p. 7124 (cit. on pp. 18, 20).

[91] Laura M. Herz. “Charge-Carrier Mobilities in Metal Halide Perovskites: Fundamental Mechanisms and Limits”. In: *ACS Energy Letters* Vol.2.Nr.7 (July 2017), pp. 1539–1548 (cit. on p. 19).

[92] Y. Chen, H. T. Yi, X. Wu, et al. “Extended carrier lifetimes and diffusion in hybrid perovskites revealed by Hall effect and photoconductivity measurements”. In: *Nature Communications* Vol.7.Nr.1 (Nov. 2016), p. 12253 (cit. on p. 19).

[93] Qingfeng Dong, Yanjun Fang, Yuchuan Shao, et al. “Electron-hole diffusion lengths > 175 μm in solution-grown $CH_3NH_3PbI_3$ single crystals”. In: *Science* Vol.347.Nr.6225 (Feb. 2015), pp. 967–970 (cit. on p. 19).

[94] Daniele Meggiolaro, Silvia G. Motti, Edoardo Mosconi, et al. “Iodine chemistry determines the defect tolerance of lead-halide perovskites”. In: *Energy & Environmental Science* Vol.11.Nr.3 (2018), pp. 702–713 (cit. on p. 19).

[95] K. Xerxes Steirer, Philip Schulz, Glenn Teeter, et al. “Defect Tolerance in Methylammonium Lead Triiodide Perovskite”. In: *ACS Energy Letters* Vol.1.Nr.2 (Aug. 2016), pp. 360–366 (cit. on p. 19).

[96] Mojtaba Abdi-Jalebi, Zahra Andaji-Garmaroudi, Stefania Cacovich, et al. “Maximizing and stabilizing luminescence from halide perovskites with potassium passivation”. In: *Nature* Vol.555.Nr.7697 (Mar. 2018), pp. 497–501 (cit. on p. 19).

[97]L. M. Pazos-Outon, M. Szumilo, R. Lamboll, et al. “Photon recycling in lead iodide perovskite solar cells”. In: *Science* Vol.351.Nr.6280 (Mar. 2016), pp. 1430–1433 (cit. on p. 20).

[98]Alexandre Gheno, Yong Huang, Johann Bouclé, et al. “Toward Highly Efficient Inkjet-Printed Perovskite Solar Cells Fully Processed Under Ambient Conditions and at Low Temperature”. In: *Solar RRL* Vol.2.Nr.11 (Nov. 2018), p. 1800191 (cit. on p. 20).

[99]Zongqi Li, Yingzhi Zhao, Xi Wang, et al. “Cost Analysis of Perovskite Tandem Photovoltaics”. In: *Joule* Vol.2.Nr.8 (Aug. 2018), pp. 1559–1572 (cit. on p. 20).

[100]Hui-Seon Kim, Anders Hagfeldt, and Nam-Gyu Park. “Morphological and compositional progress in halide perovskite solar cells”. In: *Chemical Communications* Vol.55.Nr.9 (2019), pp. 1192–1200 (cit. on p. 20).

[101]Luis M. Pazos-Outón, T. Patrick Xiao, and Eli Yablonovitch. “Fundamental Efficiency Limit of Lead Iodide Perovskite Solar Cells”. In: *The Journal of Physical Chemistry Letters* Vol.9.Nr.7 (Apr. 2018), pp. 1703–1711 (cit. on p. 20).

[102]Adam H. Slavney, Te Hu, Aaron M. Lindenberg, and Hemamala I. Karunadasa. “A Bismuth-Halide Double Perovskite with Long Carrier Recombination Lifetime for Photovoltaic Applications”. In: *Journal of the American Chemical Society* Vol.138.Nr.7 (Feb. 2016), pp. 2138–2141 (cit. on p. 20).

[103]Zewen Xiao, Zhaoning Song, and Yanfa Yan. “From Lead Halide Perovskites to Lead-Free Metal Halide Perovskites and Perovskite Derivatives”. In: *Advanced Materials* Vol.1803792 (Jan. 2019), p. 1803792 (cit. on p. 20).

[104]Feliciano Giustino and Henry J. Snaith. “Toward Lead-Free Perovskite Solar Cells”. In: *ACS Energy Letters* Vol.1.Nr.6 (Dec. 2016), pp. 1233–1240 (cit. on p. 20).

[105]Rui Wang, Muhammad Mujahid, Yu Duan, et al. “A Review of Perovskites Solar Cell Stability”. In: *Advanced Functional Materials* Vol.1808843 (Feb. 2019), p. 1808843 (cit. on p. 20).

[106]Andrei Buin, Patrick Pietsch, Jixian Xu, et al. “Materials processing routes to trap-free halide perovskites”. In: *Nano Letters* Vol.14.Nr.11 (2014), pp. 6281–6286 (cit. on p. 20).

[107]Bert Conings, Jeroen Drijkoningen, Nicolas Gauquelin, et al. “Intrinsic Thermal Instability of Methylammonium Lead Trihalide Perovskite”. In: *Advanced Energy Materials* Vol.5.Nr.15 (Aug. 2015), p. 1500477 (cit. on p. 20).

[108] Konrad Domanski, Juan-Pablo Correa-Baena, Nicolas Mine, et al. “Not All That Glitters Is Gold: Metal-Migration-Induced Degradation in Perovskite Solar Cells”. In: *ACS Nano* Vol.10.Nr.6 (June 2016), pp. 6306–6314 (cit. on p. 20).

[109] Felix Lang, Norbert H. Nickel, Jürgen Bundesmann, et al. “Radiation Hardness and Self-Healing of Perovskite Solar Cells”. In: *Advanced Materials* Vol.28.Nr.39 (2016), pp. 8726–8731 (cit. on p. 20).

[110] Davide Raffaele Ceratti, Yevgeny Rakita, Llorenç Cremonesi, et al. “Self-Healing Inside $APbBr_3$ Halide Perovskite Crystals”. In: *Advanced Materials* Vol.30.Nr.10 (Mar. 2018), p. 1706273 (cit. on p. 20).

[111] Federico Bella, Gianmarco Griffini, J.-P. Correa-Baena, et al. “Improving efficiency and stability of perovskite solar cells with photocurable fluoropolymers”. In: *Science* Vol.354.Nr.6309 (Oct. 2016), pp. 203–206 (cit. on p. 21).

[112] Minsu Jung, Tae Joo Shin, Jangwon Seo, Gwisu Kim, and Sang Il Seok. “Structural features and their functions in surfactant-armoured methylammonium lead iodide perovskites for highly efficient and stable solar cells”. In: *Energy & Environmental Science* Vol.11.Nr.8 (2018), pp. 2188–2197 (cit. on p. 21).

[113] K.O. Brinkmann, J. Zhao, N. Pourdavoud, et al. “Suppressed decomposition of organometal halide perovskites by impermeable electron-extraction layers in inverted solar cells”. In: *Nature Communications* Vol.8.Nr.1 (Apr. 2017), p. 13938 (cit. on p. 21).

[114] Rebecca J. Sutton, Marina R. Filip, Amir A. Haghighirad, et al. “Cubic or Orthorhombic? Revealing the Crystal Structure of Metastable Black-Phase $CsPbI_3$ by Theory and Experiment”. In: *ACS Energy Letters* Vol.3.Nr.8 (Aug. 2018), pp. 1787–1794 (cit. on pp. 21, 22, 113, 123, 127).

[115] M. M. Lee, J. Teuscher, T. Miyasaka, T. N. Murakami, and H. J. Snaith. “Efficient Hybrid Solar Cells Based on Meso-Superstructured Organometal Halide Perovskites”. In: *Science* Vol.338.Nr.6107 (Nov. 2012), pp. 643–647 (cit. on p. 21).

[116] Jeong-Hyeok Im, Jingshan Luo, Marius Franckeviius, et al. “Nanowire Perovskite Solar Cell”. In: *Nano Letters* Vol.15.Nr.3 (Mar. 2015), pp. 2120–2126 (cit. on p. 21).

[117] Luciana C Schmidt, Antonio Pertegás, Soranyel González-Carrero, et al. "Nontemplate Synthesis of $CH_3NH_3PbBr_3$ Perovskite Nanoparticles". In: *Journal of the American Chemical Society* Vol.136.Nr.3 (Jan. 2014), pp. 850–853 (cit. on pp. 21, 76–79, 87, 88, 105, 107, 109).

[118] Jasmina a. Sichert, Yu Tong, Niklas Mutz, et al. "Quantum Size Effect in Organometal Halide Perovskite Nanoplatelets". In: *Nano Letters* Vol.15.Nr.10 (Oct. 2015), pp. 6521–6527 (cit. on pp. 21, 77, 79, 81, 103–105, 107, 109, 111).

[119] Federica Bertolotti, Loredana Protesescu, Maksym V. Kovalenko, et al. "Coherent Nanotwins and Dynamic Disorder in Cesium Lead Halide Perovskite Nanocrystals". In: *ACS Nano* Vol.11.Nr.4 (Apr. 2017), pp. 3819–3831 (cit. on pp. 22, 123–126, 141, 160, 161, 165, 169, 170, 175, 176, 179).

[120] Andrew M Smith and Shuming Nie. "Semiconductor Nanocrystals: Structure, Properties, and Band Gap Engineering". In: *Accounts of Chemical Research* Vol.43.Nr.2 (Feb. 2010), pp. 190–200 (cit. on p. 23).

[121] A. P. Alivisatos. "Semiconductor Clusters, Nanocrystals, and Quantum Dots". In: *Science* Vol.271.Nr.5251 (Feb. 1996), pp. 933–937 (cit. on pp. 23, 26–28).

[122] Connor G. Bischak, Craig L. Hetherington, Hao Wu, et al. "Origin of Reversible Photoinduced Phase Separation in Hybrid Perovskites". In: *Nano Letters* Vol.17.Nr.2 (Feb. 2017), pp. 1028–1033 (cit. on p. 23).

[123] Andrés F. Gualdrón-Reyes, Seog Joon Yoon, Eva M. Barea, et al. "Controlling the Phase Segregation in Mixed Halide Perovskites through Nanocrystal Size". In: *ACS Energy Letters* Vol.4.Nr.1 (2019), pp. 54–62 (cit. on p. 23).

[124] Young-Hoon Kim, Christoph Wolf, Young-Tae Kim, et al. "Highly Efficient Light-Emitting Diodes of Colloidal MetalHalide Perovskite Nanocrystals beyond Quantum Size". In: *ACS Nano* Vol.11.Nr.7 (July 2017), pp. 6586–6593 (cit. on p. 23).

[125] Georgian Nedelcu, Loredana Protesescu, Sergii Yakunin, et al. "Fast Anion-Exchange in Highly Luminescent Nanocrystals of Cesium Lead Halide Perovskites ($CsPbX_3$, X = Cl, Br, I)". In: *Nano Letters* Vol.15.Nr.8 (Aug. 2015), pp. 5635–5640 (cit. on p. 23).

[126] Owen D. Miller, Eli Yablonovitch, and Sarah R. Kurtz. "Strong Internal and External Luminescence as Solar Cells Approach the ShockleyQueisser Limit". In: *IEEE Journal of Photovoltaics* Vol.2.Nr.3 (July 2012), pp. 303–311 (cit. on p. 23).

[127] Bayrammurad Saparov and David B. Mitzi. “OrganicInorganic Perovskites: Structural Versatility for Functional Materials Design”. In: *Chemical Reviews* Vol.116.Nr.7 (Apr. 2016), pp. 4558–4596 (cit. on p. 23).

[128] Maogang Gong, Ridwan Sakidja, Ryan Goul, et al. “High-Performance All-Inorganic $CsPbCl_3$ Perovskite Nanocrystal Photodetectors with Superior Stability”. In: *ACS Nano* Vol.13 (Feb. 2019), acsnano.8b07850 (cit. on p. 23).

[129] Ioannis Kanelidis and Tobias Kraus. “The role of ligands in coinage-metal nanoparticles for electronics”. In: *Beilstein Journal of Nanotechnology* Vol.8.Nr.1 (Dec. 2017), pp. 2625–2639 (cit. on pp. 23, 38, 39).

[130] Qi Zhang, Hui Nan, Yangying Zhou, et al. “In situ growth of α-$CsPbI_3$ perovskite nanocrystals on the surface of reduced graphene oxide with enhanced stability and carrier transport quality”. In: *Journal of Materials Chemistry C* Vol.7.Nr.22 (2019), pp. 6795–6804 (cit. on p. 23).

[131] Ibrahim Khan, Khalid Saeed, and Idrees Khan. “Nanoparticles: Properties, applications and toxicities”. In: *Arabian Journal of Chemistry* (May 2017) (cit. on p. 23).

[132] Aslihan Babayigit, Dinh Duy Thanh, Anitha Ethirajan, et al. “Assessing the toxicity of Pb- and Sn-based perovskite solar cells in model organism Danio rerio”. In: *Scientific Reports* Vol.6.Nr.1 (May 2016), p. 18721 (cit. on p. 23).

[133] Laurier L. Schramm. *Nano- and Microtechnology from AZ From Nanosystems to Colloids and Interfaces*. Weinheim: Wiley-VCH Verlag GmbH, 2014 (cit. on pp. 24, 31).

[134] K. Eric Drexler. “Nanotechnology: From Feynman to Funding”. In: *Bulletin of Science, Technology & Society* Vol.24.Nr.1 (Feb. 2004), pp. 21–27 (cit. on pp. 24, 31).

[135] Strelka. “Small Science, Big Future”. In: *Chemical & Engineering News Archive* Vol.91.Nr.36 (Sept. 2013), pp. 38–42 (cit. on pp. 24, 31).

[136] Yuanyuang Li, Hermann J. Schluesener, and Shunqing Xu. “Gold nanoparticle-based biosensors”. In: *Gold Bulletin* Vol.43.Nr.1 (Mar. 2010), pp. 29–41 (cit. on p. 24).

[137] Emil Roduner. “Size matters: why nanomaterials are different”. In: *Chemical Society Reviews* Vol.35.Nr.7 (2006), p. 583 (cit. on pp. 24, 27, 30).

[138] Dörfler Hans-Dieter. *Grenzflächen und kolloid-disperse Systeme*. 3rd ed. Berlin: Springer, 2002, p. 989 (cit. on pp. 25, 31, 32, 38).

[139]Lichen Liu and Avelino Corma. “Metal Catalysts for Heterogeneous Catalysis: From Single Atoms to Nanoclusters and Nanoparticles”. In: *Chemical Reviews* Vol.118.Nr.10 (May 2018), pp. 4981–5079 (cit. on p. 25).

[140]A. Picone, M. Riva, A. Brambilla, et al. “Reactive metaloxide interfaces: A microscopic view”. In: *Surface Science Reports* Vol.71.Nr.1 (Mar. 2016), pp. 32–76 (cit. on p. 25).

[141]Cecilia Noguez. “Surface plasmons on metal nanoparticles: The influence of shape and physical environment”. In: *Journal of Physical Chemistry C* Vol.111.Nr.10 (2007), pp. 3606–3619 (cit. on p. 25).

[142]Lyklema J. *Fundamentals of Interface and Colloid Science: Soft Colloids*. Ed. by J. Lyklema. Vol. 5. London, 2005, pp. 1.1–8.94 (cit. on p. 25).

[143]Khalil Ebrahim Jasim. “Quantum Dots Solar Cells”. In: *Solar Cells - New Approaches and Reviews*. Vol. 1. 11. InTech, Oct. 2015, p. 13 (cit. on pp. 26–28).

[144]Lin Wang Wang and Alex Zunger. “Electronic Structure Pseudopotential Calculations of Large (.apprx.1000 Atoms) Si Quantum Dots”. In: *The Journal of Physical Chemistry* Vol.98.Nr.8 (Feb. 1994), pp. 2158–2165 (cit. on p. 27).

[145]Slavica Brki. *Applicability of Quantum Dots in Biomedical Science*. Vol. 1. InTech, Mar. 2018, p. 13 (cit. on p. 27).

[146]Bahaa E-A Saleh and Malvin Carl Teich. *Grundlagen der Photonik*. Berlin: Wiley-VCH, 2008, p. 1406 (cit. on p. 27).

[147]Debasis Bera, Lei Qian, Teng-Kuan Tseng, and Paul H. Holloway. “Quantum Dots and Their Multimodal Applications: A Review”. In: *Materials* Vol.3.Nr.4 (Mar. 2010), pp. 2260–2345 (cit. on p. 27).

[148]Irina A. Ostapenko, Gerald Hönig, Christian Kindel, et al. “Large internal dipole moment in InGaN/GaN quantum dots”. In: *Applied Physics Letters* Vol.97.Nr.6 (Aug. 2010), p. 063103 (cit. on p. 28).

[149]Heather Goodwin, Tom C. Jellicoe, Nathaniel J.L.K. Davis, and Marcus L. Böhm. “Multiple exciton generation in quantum dot-based solar cells”. In: *Nanophotonics* Vol.7.Nr.1 (Jan. 2018), pp. 111–126 (cit. on p. 28).

[150]U. Banin, M. Bruchez, A. P. Alivisatos, et al. “Evidence for a thermal contribution to emission intermittency in single CdSe/CdS core/shell nanocrystals”. In: *The Journal of Chemical Physics* Vol.110.Nr.2 (Jan. 1999), pp. 1195–1201 (cit. on pp. 28, 29).

[151] Pietro P. Altermatt, Andreas Schenk, Frank Geelhaar, and Gernot Heiser. "Reassessment of the intrinsic carrier density in crystalline silicon in view of band-gap narrowing". In: *Journal of Applied Physics* Vol.93.Nr.3 (Feb. 2003), pp. 1598–1604 (cit. on p. 29).

[152] Celso de Mello Donegá, Peter Liljeroth, and Daniel Vanmaekelbergh. "Physicochemical Evaluation of the Hot-Injection Method, a Synthesis Route for Monodisperse Nanocrystals". In: *Small* Vol.1.Nr.12 (Dec. 2005), pp. 1152–1162 (cit. on pp. 29, 31, 35, 37, 38).

[153] J. B. Clarke, J W Hastie, L. H. E. Kihlborg, R Metselaar, and M M Thackeray. "Definitions of terms relating to phase transitions of the solid state (IUPAC Recommendations 1994)". In: *Pure and Applied Chemistry* Vol.66.Nr.3 (Jan. 1994), pp. 577–594 (cit. on pp. 29, 30).

[154] Gregg Jaeger. "The Ehrenfest Classification of Phase Transitions: Introduction and Evolution". In: *Archive for History of Exact Sciences* Vol.53.Nr.1 (May 1998), pp. 51–81 (cit. on p. 30).

[155] P.R. Couchman and WA. Jesser. "Thermodynamic theory of size dependence". In: *Nature* Vol.269.Nr.269 (1977), pp. 481–483 (cit. on p. 30).

[156] P. Pawlow. "Über die Abhängigkeit des Schmelzpunktes von der Oberflächenenergie eines festen Körpers". In: *Zeitschrift für Physikalische Chemie* Vol.65.Nr.1 (2017), pp. 1–35 (cit. on p. 30).

[157] W.H.Qi M.P.Wang G.Y.Xu Z.Li J.Y.Chen. "Size Effect on the Cohesive Energy and the Lattice Parameter of Nanoparticle". In: *Journal of materials science letters* Vol.21 (2002), pp. 1743–1745 (cit. on p. 30).

[158] J. Sun and S.L. Simon. "The melting behavior of aluminum nanoparticles". In: *Thermochimica Acta* Vol.463.Nr.1-2 (Oct. 2007), pp. 32–40 (cit. on p. 30).

[159] Sanjeev K. Gupta, Mina Talati, and Prafulla K. Jha. "Shape and Size Dependent Melting Point Temperature of Nanoparticles". In: *Materials Science Forum* Vol.570 (Feb. 2008), pp. 132–137 (cit. on p. 30).

[160] Q. Jiang, C.C Yang, and J.C Li. "Melting enthalpy depression of nanocrystals". In: *Materials Letters* Vol.56.Nr.6 (Nov. 2002), pp. 1019–1021 (cit. on p. 30).

[161] Takuya Hoshina, Hirofumi Kakemoto, Takaaki Tsurumi, Satoshi Wada, and Masatomo Yashima. "Size and temperature induced phase transition behaviors of barium titanate nanoparticles". In: *Journal of Applied Physics* Vol.99.Nr.5 (Mar. 2006), p. 054311 (cit. on pp. 30, 31).

[162]Jessy B. Rivest, Lam-Kiu Fong, Prashant K. Jain, Michael F. Toney, and A. Paul Alivisatos. “Size Dependence of a Temperature-Induced SolidSolid Phase Transition in Copper(I) Sulfide”. In: *The Journal of Physical Chemistry Letters* Vol.2.Nr.19 (Oct. 2011), pp. 2402–2406 (cit. on pp. 30, 31, 106).

[163]H. H. Farrell and C. D. Van Siclen. “Binding energy, vapor pressure, and melting point of semiconductor nanoparticles”. In: *Journal of Vacuum Science & Technology B: Microelectronics and Nanometer Structures* Vol.25.Nr.4 (2007), p. 1441 (cit. on p. 31).

[164]K. K. Nanda, S. N. Sahu, and S. N. Behera. “Liquid-drop model for the size-dependent melting of low-dimensional systems”. In: *Physical Review A* Vol.66.Nr.1 (July 2002), p. 013208 (cit. on p. 31).

[165]Hideki Sakai. “Surface-induced melting of small particles”. In: *Surface Science* Vol.351.Nr.1-3 (May 1996), pp. 285–291 (cit. on p. 31).

[166]Shei Sia Su and Isaac Chang. “Review of Production Routes of Nanomaterials”. In: () (cit. on p. 31).

[167]C. B. Murray, D. J. Norris, and M. G. Bawendi. “Synthesis and characterization of nearly monodisperse CdE (E = sulfur, selenium, tellurium) semiconductor nanocrystallites”. In: *Journal of the American Chemical Society* Vol.115.Nr.19 (Sept. 1993), pp. 8706–8715 (cit. on pp. 31, 37).

[168]JN Israelachvili. *Intermolecular and Surface Forces*. Elsevier, 2011, p. 704 (cit. on pp. 31–33, 172).

[169]Tharwat F. Tadros. *An Introduction to Surfactants*. 1st ed. Vol. 1. Berlin, 2014, p. 224 (cit. on p. 32).

[170]Mark Green. “The nature of quantum dot capping ligands”. In: *Journal of Materials Chemistry* Vol.20.Nr.28 (2010), p. 5797 (cit. on p. 32).

[171]Daishun Ling, Michael J. Hackett, and Taeghwan Hyeon. “Surface ligands in synthesis, modification, assembly and biomedical applications of nanoparticles”. In: *Nano Today* Vol.9.Nr.4 (2014), pp. 457–477 (cit. on p. 32).

[172]Ana Dominguez, Aurora Fernandez, Noemi Gonzalez, Emilia Iglesias, and Luis Montenegro. “Determination of Critical Micelle Concentration of Some Surfactants by Three Techniques”. In: *Journal of Chemical Education* Vol.74.Nr.10 (Oct. 1997), p. 1227 (cit. on p. 32).

[173]E.P Melo, M.R Aires-Barros, and J.M.S Cabral. “Reverse micelles and protein biotechnology”. In: *Biotechnology Annual Review*. Vol. 7. 2001, pp. 87–129 (cit. on p. 32).

[174] P. Atkins and J. De Paula. *Physical Chemistry*. 8th. New York: Oxfort University Press, 2006 (cit. on pp. 32, 43, 115).

[175] Terence Cosgrove. *Colloid Science Principles, methods and applications Second Eddition*. Ed. by Terence Cosgrove. 2nd ed. Bristol: Wiley-VCH Verlag GmbH, Apr. 2010, p. 394 (cit. on p. 32).

[176] Younan Xia, Yujie Xiong, Byungkwon Lim, and Sara E. Skrabalak. "Shape-Controlled Synthesis of Metal Nanocrystals: Simple Chemistry Meets Complex Physics?" In: *Angewandte Chemie International Edition* Vol.48.Nr.1 (Jan. 2009), pp. 60–103 (cit. on pp. 33, 38).

[177] Victor K. Lamer and Robert H. Dinegar. "Theory, Production and Mechanism of Formation of Monodispersed Hydrosols". In: *Journal of the American Chemical Society* Vol.72.Nr.11 (1950), pp. 4847–4854 (cit. on pp. 33, 34).

[178] Yuan Huang and Jeanne E. Pemberton. "Synthesis of uniform, spherical sub-100nm silica particles using a conceptual modification of the classic LaMer model". In: *Colloids and Surfaces A: Physicochemical and Engineering Aspects* Vol.360.Nr.1-3 (May 2010), pp. 175–183 (cit. on p. 34).

[179] Alexandr Baronov, Kevin Bufkin, Dan W. Shaw, Brad L. Johnson, and David L. Patrick. "A simple model of burst nucleation". In: *Physical Chemistry Chemical Physics* Vol.17.Nr.32 (2015), pp. 20846–20852 (cit. on pp. 34, 37).

[180] Anthony K. Cheetham (Editor) C. N. R. Rao (Editor), Achim Müller (Editor). *Nanomaterials Chemistry: Recent Developments and New Directions*. Ed. by Anthony K. Cheetham (Editor) C. N. R. Rao (Editor), Achim Müller (Editor). Weinheim: Wiley-VCH Verlag GmbH, 2007, p. 420 (cit. on p. 34).

[181] J. L. Katz. "Homogeneous nucleation theory and experiment: A survey". In: *Pure and Applied Chemistry* Vol.64.Nr.11 (Jan. 1992), pp. 1661–1666 (cit. on p. 34).

[182] Jörg Polte. "Fundamental growth principles of colloidal metal nanoparticles a new perspective". In: *CrystEngComm* Vol.17.Nr.36 (2015), pp. 6809–6830 (cit. on p. 35).

[183] X Y Liu. "Heterogeneous nucleation or homogeneous nucleation?" In: *The Journal of Chemical Physics* Vol.112.Nr.22 (June 2000), pp. 9949–9955 (cit. on p. 36).

[184] Richard P. Sear. "Quantitative studies of crystal nucleation at constant supersaturation: experimental data and models". In: *CrystEngComm* Vol.16.Nr.29 (2014), pp. 6506–6522 (cit. on p. 36).

[185]Ilona S. Smolkova, Natalia E. Kazantseva, Vladimir Babayan, et al. “The Role of Diffusion-Controlled Growth in the Formation of Uniform Iron Oxide Nanoparticles with a Link to Magnetic Hyperthermia”. In: *Crystal Growth and Design* Vol.17.Nr.5 (2017), pp. 2323–2332 (cit. on p. 36).

[186]J. A. Marqusee and John Ross. “Theory of Ostwald ripening: Competitive growth and its dependence on volume fraction”. In: *The Journal of Chemical Physics* Vol.80.Nr.1 (Jan. 1984), pp. 536–543 (cit. on p. 36).

[187]W. Ostwald. “Über die vermeintliche Isomerie des roten und gelben Queck-silberoxyds und die Oberflächenspannung fester Körper”. In: *Zeitschrift für Physikalische Chemie* Vol.34.Nr.1 (1900) (cit. on p. 36).

[188]Helmut Grätz. “Ostwald ripening: New relations between particle growth and particle size distribution”. In: *Scripta Materialia* Vol.37.Nr.1 (1997), pp. 9–16 (cit. on p. 36).

[189]Xiaogang Peng, J. Wickham, and A. P. Alivisatos. “Kinetics of II-VI and III-V Colloidal Semiconductor Nanocrystal Growth: Focusing of Size Distributions”. In: *Journal of the American Chemical Society* Vol.120.Nr.21 (June 1998), pp. 5343–5344 (cit. on p. 36).

[190]Kunio Yata and Takashi Yamaguchi. “Effect of Temperature on Ostwald Ripening of Silver in Glass”. In: *Journal of the American Ceramic Society* Vol.75.Nr.8 (Aug. 1992), pp. 2071–2075 (cit. on p. 36).

[191]Giridhar Madras and Benjamin J. McCoy. “Temperature effects during Ostwald ripening”. In: *The Journal of Chemical Physics* Vol.119.Nr.3 (July 2003), pp. 1683–1693 (cit. on p. 36).

[192]Jongnam Park, Jin Joo, Soon Gu Kwon, Youngjin Jang, and Taeghwan Hyeon. “Synthesis of Monodisperse Spherical Nanocrystals”. In: *Angewandte Chemie International Edition* Vol.46.Nr.25 (June 2007), pp. 4630–4660 (cit. on p. 37).

[193]C. B. Murray, C. R. Kagan, and M. G. Bawendi. “Synthesis and Characterization of Monodisperse Nanocrystals and Close-Packed Nanocrystal Assemblies”. In: *Annual Review of Materials Science* Vol.30.Nr.1 (Aug. 2000), pp. 545–610 (cit. on p. 38).

[194]Articles You, M A Y Be, and Interested In. “Theory of diffusion-controlled reactions on spherical surfaces and its application to reactions on micellar surfaces surfaces and its application to reactions on micellar”. In: Vol.2870 (2018) (cit. on p. 38).

[195] Hsien-Hsueh Lee, Kan-Sen Chou, and Kuo-Cheng Huang. “Inkjet printing of nanosized silver colloids”. In: *Nanotechnology* Vol.16.Nr.10 (Oct. 2005), pp. 2436–2441 (cit. on pp. 38, 39).

[196] Angang Dong, Xingchen Ye, Jun Chen, et al. “A Generalized Ligand-Exchange Strategy Enabling Sequential Surface Functionalization of Colloidal Nanocrystals”. In: *Journal of the American Chemical Society* Vol.133.Nr.4 (Feb. 2011), pp. 998–1006 (cit. on p. 39).

[197] Erin M. Sanehira, Ashley R. Marshall, Jeffrey A. Christians, et al. “Enhanced mobility $CsPbI_3$ quantum dot arrays for record-efficiency, high-voltage photovoltaic cells”. In: *Science Advances* Vol.3.Nr.10 (Oct. 2017), eaao4204 (cit. on pp. 39, 114, 122, 123, 137, 138, 145, 147, 148, 168, 169, 176, 177, 180).

[198] Hans-Joachim Eichler, Matthias Freyberger, Harald Fuchs, et al. *Bergmann-Schäfer, Lehrbuch der Experimentalphysik, Band 3:"Optik"*. Ed. by H. Niedrig. 10th ed. Berlin, New York: Walter de Gruyter, Jan. 2004 (cit. on pp. 41, 42, 51, 53, 60, 61, 128, 166).

[199] J. Michael Hollas. *Modern Spectroscopy*. Ed. by J. Michael Hollas. 4th ed. Chichester: John Wiley & Sons Ltd, 2004 (cit. on p. 42).

[200] M. Dieter Lechner. *Einführung in die Quantenchemie*. Berlin, Heidelberg: Springer Berlin Heidelberg, 2017 (cit. on p. 42).

[201] P. Elterman. “Integrating Cavity Spectroscopy”. In: *Applied Optics* Vol.9.Nr.9 (1970), p. 2140 (cit. on p. 43).

[202] James D. Rancourt. *Optical Thin Films: User Handbook*. Bellingham, Washington: SPIE, Aug. 1996, p. 271 (cit. on pp. 43, 55, 61).

[203] Tichlam Nguyen and Andrew Hind. “The Measurement of Absorption Edge and Band Gap Properties of Novel Nanocomposite Materials”. In: *Varaian, UV at Work* Vol.81 (2001), pp. 1–5 (cit. on p. 44).

[204] J. Pankove. *Optical Processes In Semiconductors*. Vol. 9. Englewood Cliffs, New Jersey: Prentice-Hall, Inc., 1975, pp. 2025–2030 (cit. on p. 45).

[205] Fabian Ruf, Alice Magin, Moritz Schultes, et al. “Excitonic nature of optical transitions in electroabsorption spectra of perovskite solar cells”. In: *Applied Physics Letters* Vol.112.Nr.8 (Feb. 2018), p. 083902 (cit. on p. 45).

[206] P. Lautenschlager, M. Garriga, S. Logothetidis, and M. Cardona. “Interband critical points of GaAs and their temperature dependence”. In: *Physical Review B* Vol.35.Nr.17 (June 1987), pp. 9174–9189 (cit. on p. 46).

[207] Daniel Niesner, Oskar Schuster, Max Wilhelm, et al. “Temperature-dependent optical spectra of single-crystal $CH_3NH_3PbBr_3$ cleaved in ultrahigh vacuum”. In: *Physical Review B* Vol.95.Nr.7 (Feb. 2017), p. 075207 (cit. on pp. 46, 101–103, 108).

[208] Knut Rurack. “Fluorescence Quantum Yields: Methods of Determination and Standards”. In: *Standardization and Quality Assurance in Fluorescence Measurements I*. Berlin, Heidelberg: Springer Berlin Heidelberg, 2012, pp. 101–145 (cit. on pp. 46, 47).

[209] Joseph R. Lakowicz. *Principles of Fluorescence Spectroscopy*. Ed. by Joseph R. Lakowicz. Boston, MA: Springer US, 2006, p. 954 (cit. on p. 46).

[210] Wisnu Ananda. “External quantum efficiency measurement of solar cell”. In: *2017 15th International Conference on Quality in Research (QiR) : International Symposium on Electrical and Computer Engineering*. Vol. 2017-Decem. Nr.1. IEEE, July 2017, pp. 450–456 (cit. on p. 47).

[211] R.K. Ahrenkiel. “Minority carriers in III/V seminconductors: physics and appliations”. In: *Semiconductors and Semimetal Vol. 39* Vol.39 (1993), pp. 40–146 (cit. on p. 48).

[212] R. R. Alfano and S. L. Shapiro. “Emission in the Region 4000 to 7000 Å Via Four-Photon Coupling in Glass”. In: *Physical Review Letters* Vol.24.Nr.11 (Mar. 1970), pp. 584–587 (cit. on p. 48).

[213] Robert R. Alfano. *The Supercontinuum Laser Source*. New York, NY: Springer New York, 2016 (cit. on p. 48).

[214] Richard D. Schaller, Milan Sykora, Sohee Jeong, and Victor I. Klimov. “High-Efficiency Carrier Multiplication and Ultrafast Charge Separation in Semiconductor Nanocrystals Studied via Time-Resolved Photoluminescence ”. In: *The Journal of Physical Chemistry B* Vol.110.Nr.50 (Dec. 2006), pp. 25332–25338 (cit. on p. 48).

[215] M. Cornet, A. Ould Hamouda, J. Degert, E. Abraham, and E. Freysz. “Terahertz-field-induced second harmonic generation through Pockels effect in Zinc Telluride crystal”. In: *2014 39th International Conference on Infrared, Millimeter, and Terahertz waves (IRMMW-THz)* (Sept. 2014), pp. 1–2 (cit. on p. 49).

[216] David M. Slocum, Elizabeth J. Slingerland, Robert H. Giles, and Thomas M. Goyette. “Atmospheric absorption of terahertz radiation and water vapor continuum effects”. In: *Journal of Quantitative Spectroscopy and Radiative Transfer* Vol.127 (Sept. 2013), pp. 49–63 (cit. on p. 49).

[217] Hannes Hempel, Charles J. Hages, Rainer Eichberger, Ingrid Repins, and Thomas Unold. "Minority and Majority Charge Carrier Mobility in $Cu_2ZnSnSe_4$ revealed by Terahertz Spectroscopy". In: *Scientific Reports* Vol.8.Nr.1 (Dec. 2018), p. 14476 (cit. on p. 50).

[218] H. Hempel, T. Unold, and R. Eichberger. "Measurement of charge carrier mobilities in thin films on metal substrates by reflection time resolved terahertz spectroscopy". In: *Optics Express* Vol.25.Nr.15 (July 2017), p. 17227 (cit. on p. 50).

[219] Hannah J Joyce, Callum J Docherty, Qiang Gao, et al. "Electronic properties of GaAs, InAs and InP nanowires studied by terahertz spectroscopy". In: *Nanotechnology* Vol.24.Nr.21 (May 2013), p. 214006 (cit. on p. 50).

[220] T. L. Cocker, D. Baillie, M. Buruma, et al. "Microscopic origin of the Drude-Smith model". In: *Physical Review B* Vol.96.Nr.20 (Nov. 2017), p. 205439 (cit. on p. 50).

[221] N Langhoff R Wedell H Wolff. *Handbook of Practical X-Ray Fluorescence Analysis*. Ed. by Burkhard Beckhoff, Birgit KanngieSSer, Norbert Langhoff, Reiner Wedell, and Helmut Wolff. Berlin, Heidelberg: Springer Berlin Heidelberg, 2006 (cit. on p. 50).

[222] Jens Als-Nielsen and Des McMorrow. *Elements of Modern X-ray Physics*. Hoboken, NJ, USA: John Wiley & Sons, Inc., Mar. 2011 (cit. on pp. 50–53, 57, 62, 63).

[223] Temitope D. Timothy Oyedotun. "X-ray fluorescence (XRF) in the investigation of the composition of earth materials: a review and an overview". In: *Geology, Ecology, and Landscapes* Vol.2.Nr.2 (Apr. 2018), pp. 148–154 (cit. on pp. 50, 52).

[224] Rolf Behling. *Modern Diagnostic X-Ray Sources*. CRC Press, July 2015, pp. 1–386 (cit. on p. 51).

[225] J.A. Bearden. "X-Ray Wavelengths". In: *Reviews of Modern Physics* Vol.39.Nr.1 (Jan. 1967), pp. 78–124 (cit. on pp. 51, 53).

[226] G. Hevesy and H. Lay. "Fluorescent Yield of X-Ray Emission". In: *Nature* Vol.134.Nr.3377 (July 1934), pp. 98–99 (cit. on p. 52).

[227] Terry L. Alford, Leonard C. Feldman, and James W. Mayer. *Fundamentals of Nanoscale Film Analysis*. Ed. by Terry L. Alford, Leonard C. Feldman, and James W. Mayer. 1st ed. Boston, MA: Springer US, 2007 (cit. on p. 52).

[228]Yoshio Waseda, Eiichiro Matsubara, and Kozo Shinoda. *X-Ray Diffraction Crystallography*. Vol. Vol.46. Nr.1. Berlin, Heidelberg: Springer Berlin Heidelberg, 2011, p. 012013 (cit. on pp. 52–58).

[229]Lothar SpieSS, Gerd Teichert, Robert Schwarzer, Herfried Behnken, and Christoph Genzel. *Moderne Röntgenbeugung*. Wiesbaden: Springer Fachmedien Wiesbaden, 2019 (cit. on pp. 53, 56–58, 63).

[230]Gwyn P Williams. "A general review of synchrotron radiation, its uses and special technologies". In: *Vacuum* Vol.32.Nr.6 (Jan. 1982), pp. 333–345 (cit. on p. 53).

[231]Alfred Q R Baron. "High-Resolution Inelastic X-Ray Scattering I: Context, Spectrometers, Samples, and Superconductors". In: *Synchrotron Light Sources and Free-Electron Lasers*. Cham: Springer International Publishing, 2015, pp. 1–68 (cit. on p. 53).

[232]M. Born and V. Fock. "Beweis des Adiabatensatzes". In: *Zeitschrift für Physik* Vol.51.Nr.3-4 (Mar. 1928), pp. 165–180 (cit. on p. 54).

[233]Riemannian Geometry and Geometric Analysis. *X-ray and Neutron Reflectivity*. Ed. by Jean Daillant and Alain Gibaud. Vol. 770. Lecture Notes in Physics. Berlin, Heidelberg: Springer Berlin Heidelberg, 2009 (cit. on pp. 54, 60, 62, 63).

[234]Deepak Dwivedi and Kateina Lepková. "SAXS and SANS Techniques for Surfactant Characterization: Application in Corrosion Science". In: *Application and Characterization of Surfactants*. Vol. 2. InTech, July 2017, p. 64 (cit. on p. 54).

[235]Lauren Boldon, Fallon Laliberte, and Li Liu. "Review of the fundamental theories behind small angle X-ray scattering, molecular dynamics simulations, and relevant integrated application". In: *Nano Reviews* Vol.6.Nr.1 (Jan. 2015), p. 25661 (cit. on pp. 54, 66).

[236]Walter Borchardt-ott and Heidrun Sowa. *Kristallographie*. Springer-Lehrbuch. Berlin, Heidelberg: Springer Berlin Heidelberg, 2009 (cit. on p. 55).

[237]B. R. Pauw. "Everything SAXS: small-angle scattering pattern collection and correction". In: *Journal of Physics: Condensed Matter* Vol.26.Nr.23 (June 2014), p. 239501 (cit. on pp. 56, 64–66).

[238]J. Brentano. "Focussing method of crystal powder analysis by X-rays". In: *Proceedings of the Physical Society of London* Vol.37.Nr.1 (Jan. 1924), pp. 184–193 (cit. on p. 56).

[239] Susan Schorr, Christiane Stephan, Tobias Törndahl, and Roland Mainz. "X-Ray and Neutron Diffraction on Materials for Thin-Film Solar Cells". In: *Advanced Characterization Techniques for Thin Film Solar Cells*. Weinheim, Germany: Wiley-VCH Verlag GmbH & Co. KGaA, Apr. 2011, pp. 347–363 (cit. on p. 57).

[240] D. R. Baer and S. Thevuthasan. *Characterization of Thin Films and Coatings*. Third Edit. Elsevier Ltd., 2010, pp. 749–864 (cit. on p. 57).

[241] Minoru Fujimoto. *The Physics of Structural Phase Transitions*. New York: Springer-Verlag, 2005 (cit. on p. 58).

[242] Armel Le Bail. "Whole powder pattern decomposition methods and applications: A retrospection". In: *Powder Diffraction* Vol.20.Nr.04 (2005), pp. 316–326 (cit. on p. 58).

[243] Hugo M. Rietveld. "The Rietveld Method: A Retrospection". In: *Zeitschrift für Kristallographie* Vol.225.Nr.12 (Dec. 2010), pp. 545–547 (cit. on p. 58).

[244] Alexandra Franz, Daniel M. Többens, Julia Steckhan, and Susan Schorr. "Determination of the miscibility gap in the solid solutions series of methylammonium lead iodide/chloride". In: *Acta Crystallographica Section B Structural Science, Crystal Engineering and Materials* Vol.74.Nr.5 (Oct. 2018), pp. 445–449 (cit. on pp. 59, 88, 97).

[245] A.Gunier. *X-Ray Diffraction In Crystals, Imperfect Crystals, and Amorphous Bodies*. San Francisco and London, 1963 (cit. on p. 59).

[246] Luc Vinet and Alexei Zhedanov. "A missing' family of classical orthogonal polynomials". In: *Journal of Physics A: Mathematical and Theoretical* Vol.44.Nr.8 (Feb. 2011), p. 085201 (cit. on p. 59).

[247] P. Scherrer. *Bestimmung der inneren Struktur und der GröSSe von Kolloidteilchen mittels Röntgenstrahlen*. Vol. 277. Nr.1916. Berlin, Heidelberg: Springer Berlin Heidelberg, 1912, pp. 387–409 (cit. on p. 59).

[248] Miho Yasaka. *Rigaku Journal*. Vol. 26. Nr.2. Tokyo: Rigaku Corporation, 2010, pp. 1–9 (cit. on p. 60).

[249] L. A. Feigin and D. I. Svergun. *Structure Analysis by Small-Angle X-Ray and Neutron Scattering*. Ed. by George W. Taylor. Boston, MA: Springer US, 1987 (cit. on pp. 60, 63, 64).

[250] Lyman G. Parratt. "Surface Studies of Solids by Total Reflection of X-Rays". In: *Physical Review* Vol.95.Nr.2 (July 1954), pp. 359–369 (cit. on pp. 62, 166).

[251]Andrew Nelson. “ Co-refinement of multiple-contrast neutron/X-ray reflectivity data using MOTOFIT ”. In: *Journal of Applied Crystallography* Vol.39.Nr.2 (2006), pp. 273–276 (cit. on pp. 63, 127).

[252]P. S. Pershan. “X-ray or neutron reflectivity: Limitations in the determination of interfacial profiles”. In: *Physical Review E* Vol.50.Nr.3 (Sept. 1994), pp. 2369–2372 (cit. on p. 63).

[253]Knoll G.F. *Radiation Detection and Measurement (Third edition)*. 1999, pp. 1–816 (cit. on p. 64).

[254]Benjamin Chu and Benjamin S. Hsiao. “Small-Angle X-ray Scattering of Polymers”. In: *Chemical Reviews* Vol.101.Nr.6 (June 2001), pp. 1727–1762 (cit. on p. 65).

[255]O.Kratky O.Glatter. *Small Angle X-Ray Scattering*. Ed. by O.Kratky O.Glatter. London ; New York: Academic Press, 1982, p. 515 (cit. on p. 65).

[256]Shinichi Sakurai. “SAXS Evaluation of Size Distribution for Nanoparticles”. In: *X-ray Scattering*. Vol. 1. Nr.5. InTech, Jan. 2017. Chap. 5, p. 13 (cit. on p. 66).

[257]Ingo BreSSler, Joachim Kohlbrecher, and Andreas F. Thünemann. “SASfit : a tool for small-angle scattering data analysis using a library of analytical expressions”. In: *Journal of Applied Crystallography* Vol.48.Nr.5 (Oct. 2015), pp. 1587–1598 (cit. on pp. 66, 99).

[258]G. P. Thomson and A. Reid. “Diffraction of Cathode Rays by a Thin Film”. In: *Nature* Vol.119.Nr.3007 (June 1927), pp. 890–890 (cit. on p. 66).

[259]Ariel Lipson, Stephen G. Lipson, and Henry Lipson. *Optical Physics*. Cambridge: Cambridge University Press, 2010, p. 497 (cit. on p. 67).

[260]Hidetaka Sawada, Naoki Shimura, Fumio Hosokawa, Naoya Shibata, and Yuichi Ikuhara. “Resolving 45-pm-separated Si-Si atomic columns with an aberration-corrected STEM”. In: *Microscopy* Vol.64.Nr.3 (2015), pp. 213–217 (cit. on p. 67).

[261]Laurence Marks. “What Are the Resolution Limits in Electron Microscopes?” In: *Physics* Vol.6 (July 2013), p. 82 (cit. on p. 67).

[262]David B. Williams and C. Barry Carter. *Transmission Electron Microscopy*. Boston, MA: Springer US, 2009 (cit. on pp. 67, 68).

[263]David B. Williams and C. Barry Carter. “The Transmission Electron Microscope”. In: *Transmission Electron Microscopy*. Boston, MA: Springer US, 1996, pp. 3–17 (cit. on p. 67).

[264] Jürgen Thomas and Thomas Gemming. *Analytische Transmissionselektronenmikroskopie*. Vienna: Springer Vienna, 2013 (cit. on p. 67).

[265] Peter j. Goodhew, John Humphreys, and Richard Beanland. *Electron Microscopy and Analysis*. Third. London ; New York: Taylo, 2000, p. 264 (cit. on p. 67).

[266] Zhong Lin Wang. *Elastic and Inelastic Scattering in Electron Diffraction and Imaging*. Boston, MA: Springer US, 1995 (cit. on p. 67).

[267] A. W. Coats and J. P. Redfern. "Thermogravimetric analysis. A review". In: *The Analyst* Vol.88.Nr.1053 (1963), p. 906 (cit. on p. 69).

[268] Takeo Ozawa. "Thermal analysis review and prospect". In: *Thermochimica Acta* Vol.355.Nr.1-2 (July 2000), pp. 35–42 (cit. on p. 69).

[269] G. W. H. Höhne, W. F. Hemminger, and H.-J. Flammersheim. *Differential Scanning Calorimetry*. Vol. 84. Berlin, Heidelberg: Springer Berlin Heidelberg, 2003, pp. 115–141 (cit. on pp. 71–73, 84).

[270] A. Boller, Y. Jin, and B. Wunderlich. "Heat capacity measurement by modulated DSC at constant temperature". In: *Journal of Thermal Analysis* Vol.42.Nr.2-3 (Aug. 1994), pp. 307–330 (cit. on p. 71).

[271] Netzsch. *Functional principle of a heat-flux DSC*. (`https://www.netzsch-thermal-analysis.com/en/landing-pages/principle-of-a-heat-flux-dsc/`). 19.06.2019 (cit. on p. 72).

[272] Seungchan Ryu, Jun Hong Noh, Nam Joong Jeon, et al. "Voltage output of efficient perovskite solar cells with high open-circuit voltage and fill factor". In: *Energy Environ. Sci.* Vol.7.Nr.8 (2014), pp. 2614–2618 (cit. on p. 75).

[273] Hak Beom Kim, Yung Jin Yoon, Jaeki Jeong, et al. "Peroptronic devices: Perovskite-based light-emitting solar cells". In: *Energy and Environmental Science* Vol.10.Nr.9 (2017), pp. 1950–1957 (cit. on p. 75).

[274] Jianli Miao and Fujun Zhang. "Recent progress on highly sensitive perovskite photodetectors". In: *Journal of Materials Chemistry C* Vol.7.Nr.7 (2019), pp. 1741–1791 (cit. on p. 75).

[275] Qi Chen, Nicholas De Marco, Yang (Michael) Yang, et al. "Under the spotlight: The organicinorganic hybrid halide perovskite for optoelectronic applications". In: *Nano Today* Vol.10.Nr.3 (June 2015), pp. 355–396 (cit. on p. 75).

[276] Xing Zhao and Nam-Gyu Park. "Stability Issues on Perovskite Solar Cells". In: *Photonics* Vol.2.Nr.4 (Nov. 2015), pp. 1139–1151 (cit. on p. 75).

[277] Soranyel Gonzalez-Carrero, Raquel E. Galian, and Julia Pérez-Prieto. "Maximizing the emissive properties of CH 3 NH 3 PbBr 3 perovskite nanoparticles". In: *Journal of Materials Chemistry A* Vol.3.Nr.17 (2015), pp. 9187–9193 (cit. on pp. 76, 107).

[278] Heinz G. O. Becker. *Organikum*. Ed. by G.O. Heinz Becker, Werner Berger, Günter Domschke, et al. 21st ed. Weinheim, Germany: Whiley-VCH, 2001, p. 852 (cit. on p. 76).

[279] Soranyel Gonzalez-Carrero, Raquel E. Galian, and Julia Pérez-Prieto. "Maximizing the emissive properties of $CH_3NH_3PbBr_3$ perovskite nanoparticles". In: *Journal of Materials Chemistry A* Vol.3.Nr.17 (2015), pp. 9187–9193 (cit. on pp. 77, 78, 81, 87, 88, 105–107, 109).

[280] Soranyel Gonzalez-Carrero, Raquel E. Galian, and Julia Pérez-Prieto. "Organic-inorganic and all-inorganic lead halide nanoparticles [Invited]". In: *Optics Express* Vol.24.Nr.2 (Jan. 2016), A285 (cit. on p. 77).

[281] David B. Williams and C. Barry Carter. *Transmission Electron Microscopy*. Boston, MA: Springer US, 2009, p. 9 (cit. on p. 79).

[282] Mieko Takagi. "Electron-Diffraction Study of Liquid-Solid Transition of Thin Metal Films". In: *Journal of the Physical Society of Japan* Vol.9.Nr.3 (May 1954), pp. 359–363 (cit. on p. 79).

[283] A. Poglitsch and D. Weber. "Dynamic disorder in methylammoniumtrihalogenoplumbates (II) observed by millimeterwave spectroscopy". In: *The Journal of Chemical Physics* Vol.87.Nr.11 (Dec. 1987), pp. 6373–6378 (cit. on pp. 79, 82, 83, 88, 92–96, 106–108).

[284] Hendrik Heinz, Chandrani Pramanik, Ozge Heinz, et al. "Nanoparticle decoration with surfactants: Molecular interactions, assembly, and applications". In: *Surface Science Reports* Vol.72.Nr.1 (Feb. 2017), pp. 1–58 (cit. on p. 80).

[285] H. Abid, A. Trigui, A. Mlayah, E.K. Hlil, and Y. Abid. "Phase transition in organicinorganic perovskite $(C_9H_19NH_3)_2PbI_2Br_2$ of long-chain alkylammonium". In: *Results in Physics* Vol.2 (2012), pp. 71–76 (cit. on pp. 80, 89, 91, 105–107, 111).

[286] H. Bloom, J. O.M. Bockris, N. E. Richards, and R. G. Taylor. "Vapor Pressure and Heat of Vaporization of Some Simple Molten Electrolytes". In: *Journal of the American Chemical Society* Vol.80.Nr.9 (May 1958), pp. 2044–2046 (cit. on p. 81).

[287] G. P. Nagabhushana, Radha Shivaramaiah, and Alexandra Navrotsky. “Direct calorimetric verification of thermodynamic instability of lead halide hybrid perovskites”. In: *Proceedings of the National Academy of Sciences* Vol.113.Nr.28 (July 2016), pp. 7717–7721 (cit. on p. 81).

[288] Noriko Onoda-Yamamuro, Osamu Yamamuro, Takasuke Matsuo, and Hiroshi Suga. “p-T phase relations of $CH_3NH_3PbX_3$ (X = Cl, Br, I) crystals”. In: *Journal of Physics and Chemistry of Solids* Vol.53.Nr.2 (Feb. 1992), pp. 277–281 (cit. on pp. 82, 83).

[289] H Mashiyama, Y Kawamura, and Y. Kubota. “The Anti-Polar Structure of $CH_3NH_3PbBr_3$”. In: *Journal of the Korean Physical Society* Vol.51.Nr.92 (Aug. 2007), p. 850 (cit. on p. 83).

[290] R. Pynn. “Incommensurable structures”. In: *Nature* Vol.281.Nr.5731 (Oct. 1979), pp. 433–437 (cit. on p. 83).

[291] Francesca Tancini, Thomas Gottschalk, W. Bernd Schweizer, François Diederich, and Enrico Dalcanale. “Ion-Pair Complexation with a Cavitand Receptor”. In: *Chemistry - A European Journal* Vol.16.Nr.26 (June 2010), pp. 7813–7819 (cit. on p. 85).

[292] John A. Noël, Laurent Kreplak, Nuwansiri Nirosh Getangama, John R. de Bruyn, and Mary Anne White. “Supercooling and Nucleation of Fatty Acids: Influence of Thermal History on the Behavior of the Liquid Phase”. In: *The Journal of Physical Chemistry B* Vol.122.Nr.51 (Dec. 2018), pp. 12386–12395 (cit. on p. 85).

[293] J Tsau and D Gilson. “Polymorphism in n-Alkylammonium Halides. A Differential Scanning Calorimetric Study”. In: *The Journal of Physical Chemistry* Vol.72.Nr.12 (Nov. 1968), pp. 4082–4085 (cit. on p. 85).

[294] Kazuya Saito, Mayumi Ikeda, and Michio Sorai. “Thermodynamic implication of the dependence of mesomorphic transition entropy on chain-length smectic A - Nematic phase transition”. In: *Journal of Thermal Analysis and Calorimetry* Vol.70.Nr.2 (2002), pp. 345–352 (cit. on p. 85).

[295] P. S. Whitfield, N. Herron, W. E. Guise, et al. “Structures, Phase Transitions and Tricritical Behavior of the Hybrid Perovskite Methyl Ammonium Lead Iodide”. In: *Scientific Reports* Vol.6 (Dec. 2016), p. 35685 (cit. on p. 88).

[296] Jun Hong Noh, Sang Hyuk Im, Jin Hyuck Heo, Tarak N. Mandal, and Sang Il Seok. “Chemical Management for Colorful, Efficient, and Stable InorganicOrganic Hybrid Nanostructured Solar Cells”. In: *Nano Letters* Vol.13.Nr.4 (Apr. 2013), pp. 1764–1769 (cit. on pp. 88, 97).

[297] Gert J. Kruger, Dave G. Billing, and Melanie Rademeyer. “Polymorphism in Long-Chain N-Alkylammonium Halides”. In: *Models, Mysteries and Magic of Molecules*. Ed. by Jan C.A. Boeyens and J.F. Ogilvie. Dordrecht: Springer Netherlands, 2008, pp. 219–231 (cit. on pp. 89, 112).

[298] E. J. Gabe. “The crystal structure of methylammonium bromide”. In: *Acta Crystallographica* Vol.14.Nr.12 (Dec. 1961), pp. 1296–1296 (cit. on p. 89).

[299] Gregor Kieslich, Jonathan Michael Skelton, Jeff Armstrong, et al. “Hydrogen Bonding versus Entropy: Revealing the Underlying Thermodynamics of the Hybrid OrganicInorganic Perovskite $[CH_3NH_3]PbBr_3$”. In: *Chemistry of Materials* Vol.30.Nr.24 (Dec. 2018), pp. 8782–8788 (cit. on p. 91).

[300] Jasmina A. Sichert, Annick Hemmerling, Carlos Cardenas-Daw, Alexander S. Urban, and Jochen Feldmann. “Tuning the optical bandgap in layered hybrid perovskites through variation of alkyl chain length”. In: *APL Materials* Vol.7.Nr.4 (Apr. 2019), p. 041116 (cit. on pp. 93, 97, 104, 105, 108, 109, 111).

[301] G. R. Strobl. “A new method of evaluating slit-smeared small-angle X-ray scattering data”. In: *Acta Crystallographica Section A* Vol.26.Nr.3 (May 1970), pp. 367–375 (cit. on p. 98).

[302] P. M. Voyles, N. Zotov, S. M. Nakhmanson, et al. “Structure and physical properties of paracrystalline atomistic models of amorphous silicon”. In: *Journal of Applied Physics* Vol.90.Nr.9 (Nov. 2001), pp. 4437–4451 (cit. on p. 99).

[303] R. J. Elliott. “Intensity of Optical Absorption by Excitons”. In: *Physical Review* Vol.108.Nr.6 (Dec. 1957), pp. 1384–1389 (cit. on pp. 100, 101, 108).

[304] Michele Saba, Michele Cadelano, Daniela Marongiu, et al. “Correlated electronhole plasma in organometal perovskites”. In: *Nature Communications* Vol.5.Nr.1 (Dec. 2014), p. 5049 (cit. on p. 100).

[305] Hideyuki Kunugita, Tsubasa Hashimoto, Yuki Kiyota, et al. “Excitonic Feature in Hybrid Perovskite $CH_3NH_3PbBr_3$ Single Crystals”. In: *Chemistry Letters* Vol.44.Nr.6 (June 2015), pp. 852–854 (cit. on pp. 101, 103).

[306] Xin Fang, Kun Zhang, Yanping Li, et al. “Effect of excess $PbBr_2$ on photoluminescence spectra of $CH_3NH_3PbBr_3$ perovskite particles at room temperature”. In: *Applied Physics Letters* Vol.108.Nr.7 (Feb. 2016), p. 071109 (cit. on p. 101).

[307] Clemens Burda, Xiaobo Chen, Radha Narayanan, and Mostafa A. El-Sayed. “Chemistry and Properties of Nanocrystals of Different Shapes”. In: *Chemical Reviews* Vol.105.Nr.4 (Apr. 2005), pp. 1025–1102 (cit. on p. 106).

[308] Anirban Dutta, Sumit K. Dutta, Samrat Das Adhikari, and Narayan Pradhan. “Phase-Stable $CsPbI_3$ Nanocrystals: The Reaction Temperature Matters”. In: *Angewandte Chemie International Edition* Vol.57.Nr.29 (July 2018), pp. 9083–9087 (cit. on p. 112).

[309] David P. Nenon, Jeffrey A. Christians, Lance M. Wheeler, et al. “Structural and chemical evolution of methylammonium lead halide perovskites during thermal processing from solution”. In: *Energy & Environmental Science* Vol.9.Nr.6 (2016), pp. 2072–2082 (cit. on p. 113).

[310] Rachel E. Beal, Daniel J. Slotcavage, Tomas Leijtens, et al. “Cesium Lead Halide Perovskites with Improved Stability for Tandem Solar Cells”. In: *The Journal of Physical Chemistry Letters* Vol.7.Nr.5 (Mar. 2016), pp. 746–751 (cit. on p. 113).

[311] D. M. Trots and S. V. Myagkota. “High-temperature structural evolution of caesium and rubidium triiodoplumbates”. In: *Journal of Physics and Chemistry of Solids* Vol.69.Nr.10 (May 2008), pp. 2520–2526 (cit. on p. 113).

[312] CHR. KN. MØLLER. “Crystal Structure and Photoconductivity of Cæsium Plumbohalides”. In: *Nature* Vol.182.Nr.4647 (Nov. 1958), pp. 1436–1436 (cit. on p. 113).

[313] Yuanyuan Zhou and Yixin Zhao. “Chemical stability and instability of inorganic halide perovskites”. In: *Energy & Environmental Science* Nr.1 (2019) (cit. on p. 113).

[314] Qi Wang, Xiaopeng Zheng, Yehao Deng, et al. “Stabilizing the α-Phase of $CsPbI_3$ Perovskite by Sulfobetaine Zwitterions in One-Step Spin-Coating Films”. In: *Joule* Vol.1.Nr.2 (Oct. 2017), pp. 371–382 (cit. on p. 114).

[315] Pushan Ayyub, V. R. Palkar, Soma Chattopadhyay, and Manu Multani. “Effect of crystal size reduction on lattice symmetry and cooperative properties”. In: *Physical Review B* Vol.51.Nr.9 (Mar. 1995), pp. 6135–6138 (cit. on p. 114).

[316] Abhishek Swarnkar, Ashley R. Marshall, Erin M. Sanehira, et al. “Quantum dot-induced phase stabilization of α-$CsPbI_3$ perovskite for high-efficiency photovoltaics”. In: *Science* Vol.354.Nr.6308 (2016), pp. 92–95 (cit. on pp. 114, 116, 117, 122, 123, 132, 134, 137, 138, 147–149, 153–156, 165, 167–173, 176–178, 180).

[317] Anirban Dutta and Narayan Pradhan. “Phase-Stable Red-Emitting $CsPbI_3$ Nanocrystals: Successes and Challenges”. In: *ACS Energy Letters* Vol.4.Nr.3 (2019), pp. 709–719 (cit. on pp. 114, 133, 168).

[318] Miriam Koolyk, Daniel Amgar, Sigalit Aharon, and Lioz Etgar. “Kinetics of cesium lead halide perovskite nanoparticle growth; focusing and defocusing of size distribution”. In: *Nanoscale* Vol.8.Nr.12 (2016), pp. 6403–6409 (cit. on p. 117).

[319] João Borges, José A. Ribeiro, Elisa M. Pereira, et al. “Preparation and characterization of DNA films using oleylamine modified Au surfaces”. In: *Journal of Colloid and Interface Science* Vol.358.Nr.2 (June 2011), pp. 626–634 (cit. on p. 121).

[320] Stefanos Mourdikoudis and Luis M. Liz-Marzán. “Oleylamine in Nanoparticle Synthesis”. In: *Chemistry of Materials* Vol.25.Nr.9 (May 2013), pp. 1465–1476 (cit. on p. 121).

[321] Sergii Yakunin, Loredana Protesescu, Franziska Krieg, et al. “Low-threshold amplified spontaneous emission and lasing from colloidal nanocrystals of caesium lead halide perovskites”. In: *Nature Communications* Vol.6 (2015), pp. 1–8 (cit. on pp. 123, 165).

[322] Patrick Cottingham and Richard L. Brutchey. “Compositionally Dependent Phase Identity of Colloidal $CsPbBr_3 - xI_x$ Quantum Dots”. In: *Chemistry of Materials* Vol.28.Nr.21 (Nov. 2016), pp. 7574–7577 (cit. on pp. 123, 165).

[323] Younghoon Kim, Emre Yassitepe, Oleksandr Voznyy, et al. “Efficient Luminescence from Perovskite Quantum Dot Solids”. In: *ACS Applied Materials & Interfaces* Vol.7.Nr.45 (Nov. 2015), pp. 25007–25013 (cit. on pp. 123, 165).

[324] Alexander N. Beecher, Octavi E. Semonin, Jonathan M. Skelton, et al. “Direct Observation of Dynamic Symmetry Breaking above Room Temperature in Methylammonium Lead Iodide Perovskite”. In: *ACS Energy Letters* Vol.1.Nr.4 (2016), pp. 880–887 (cit. on pp. 124, 165, 166).

[325] Omer Yaffe, Yinsheng Guo, Liang Z. Tan, et al. “Local Polar Fluctuations in Lead Halide Perovskite Crystals”. In: *Physical Review Letters* Vol.118.Nr.13 (2017), pp. 1–6 (cit. on p. 124).

[326] Challa S.S.R. Kumar, ed. *X-ray and Neutron Techniques for Nanomaterials Characterization*. Berlin, Heidelberg: Springer Berlin Heidelberg, 2016 (cit. on p. 124).

[327] Henrik Nikola Krøyer. *On the structure of caesium hexahalogeno-plumbates(II)*. https://www.biodiversitylibrary.org/bibliography/13024 — "Vid. Sel. naturvid. og mathem. Afh., VII Deel." Copenhagen, Denmark :Kongelige Danske videnskabernes selskab, 1960, p. 124 (cit. on pp. 125, 166).

[328] Julia Zimdars and Michael Bredol. “On the influence of coordinating solvents on the reduction of selenium for the phosphine-free synthesis of metal selenide nanoparticles”. In: *New Journal of Chemistry* Vol.40.Nr.2 (2016), pp. 1137–1142 (cit. on p. 127).

[329] James B. Pawley, ed. *Handbook Of Biological Confocal Microscopy*. Boston, MA: Springer US, 2006 (cit. on p. 127).

[330] David Morgan and David F. Kelley. “Spectroscopy of Surface-State p-Doped CdSe/CdS Quantum Dots”. In: *The Journal of Physical Chemistry Letters* Vol.9.Nr.15 (Aug. 2018), pp. 4160–4165 (cit. on pp. 131, 167).

[331] V Babin, P Fabeni, M Nikl, et al. “Luminescent $CsPbI_3$ and Cs_4PbI_6 Aggregates in Annealed CsI:Pb Crystals”. In: *physica status solidi (b)* Vol.226.Nr.2 (Aug. 2001), pp. 419–428 (cit. on pp. 131, 167).

[332] Eline M. Hutter, Rebecca J. Sutton, Sanjana Chandrashekar, et al. “Vapour-Deposited Cesium Lead Iodide Perovskites: Microsecond Charge Carrier Lifetimes and Enhanced Photovoltaic Performance”. In: *ACS Energy Letters* Vol.2.Nr.8 (Aug. 2017), pp. 1901–1908 (cit. on pp. 132, 143, 144, 168).

[333] Jorick Maes, Lieve Balcaen, Emile Drijvers, et al. “Light Absorption Coefficient of $CsPbBr_3$ Perovskite Nanocrystals”. In: *The Journal of Physical Chemistry Letters* Vol.9.Nr.11 (June 2018), pp. 3093–3097 (cit. on pp. 133, 168).

[334] Richard Dalven. “Empirical Relation between Energy Gap and Lattice Constant in Cubic Semiconductors”. In: *Physical Review B* Vol.8.Nr.12 (Dec. 1973), pp. 6033–6034 (cit. on pp. 133, 168).

[335] Graham H. Carey, Ahmed L. Abdelhady, Zhijun Ning, et al. “Colloidal Quantum Dot Solar Cells”. In: *Chemical Reviews* Vol.115.Nr.23 (Dec. 2015), pp. 12732–12763 (cit. on p. 137).

[336] Mark T. Weller, Oliver J. Weber, Jarvist M. Frost, and Aron Walsh. “Cubic Perovskite Structure of Black Formamidinium Lead Iodide, α-$[HC(NH_2)_2]PbI_3$, at 298 K”. In: *The Journal of Physical Chemistry Letters* Vol.6.Nr.16 (Aug. 2015), pp. 3209–3212 (cit. on p. 141).

[337] Shixun Wang, Yu Wang, Yu Zhang, et al. “Cesium Lead Chloride/Bromide Perovskite Quantum Dots with Strong Blue Emission Realized via a Nitrate-Induced Selective Surface Defect Elimination Process”. In: *The Journal of Physical Chemistry Letters* Vol.10.Nr.1 (Jan. 2019), pp. 90–96 (cit. on pp. 141, 144, 170, 171).

[338] Giles E. Eperon, Samuel D. Stranks, Christopher Menelaou, et al. “Formamidinium lead trihalide: a broadly tunable perovskite for efficient planar heterojunction solar cells”. In: *Energy & Environmental Science* Vol.7.Nr.3 (2014), p. 982 (cit. on p. 143).

[339] David Parobek, Yitong Dong, Tian Qiao, Daniel Rossi, and Dong Hee Son. “Photoinduced Anion Exchange in Cesium Lead Halide Perovskite Nanocrystals”. In: *Journal of the American Chemical Society* Vol.139.Nr.12 (Mar. 2017), pp. 4358–4361 (cit. on pp. 147, 156).

[340] Jonathon S. Bechtel and Anton Van Der Ven. “First-principles thermodynamics study of phase stability in inorganic halide perovskite solid solutions”. In: *Physical Review Materials* Vol.2.Nr.4 (2018), pp. 1–7 (cit. on pp. 147, 156).

[341] Mengjin Yang, Taiyang Zhang, Philip Schulz, et al. “Facile fabrication of large-grain $CH_3NH_3PbI_3 - xBr_x$ films for high-efficiency solar cells via CH_3NH_3Br-selective Ostwald ripening”. In: *Nature Communications* Vol.7.Nr.1 (Dec. 2016), p. 12305 (cit. on p. 148).

[342] M. Kállai, Z. Veres, and J. Balla. “Response of flame ionization detectors to different homologous series”. In: *Chromatographia* Vol.54.Nr.7-8 (Oct. 2001), pp. 511–517 (cit. on p. 149).

[343] R Nagarajan. “Molecular Packing Parameter and Surfactant Self-Assembly: The Neglected Role of the Surfactant Tail ”. In: *Langmuir* Vol.18.Nr.1 (Jan. 2002), pp. 31–38 (cit. on pp. 151, 172).

[344] F. Palazon, F. Di Stasio, S. Lauciello, et al. “Evolution of $CsPbBr_3$ nanocrystals upon post-synthesis annealing under an inert atmosphere”. In: *Journal of Materials Chemistry C* Vol.4.Nr.39 (2016), pp. 9179–9182 (cit. on pp. 153, 172).

[345] Zeguo Tang, Takeru Bessho, Fumiyasu Awai, et al. “Hysteresis-free perovskite solar cells made of potassium-doped organometal halide perovskite”. In: *Scientific Reports* Vol.7.Nr.1 (Dec. 2017), p. 12183 (cit. on pp. 153, 172).

[346] Sourav Adhikary and Subhananda Chakrabarti. *Quaternary Capped In(Ga)As/GaAs Quantum Dot Infrared Photodetectors*. Vol. Vol.45. Nr.10. Singapore: Springer Singapore, 2018, pp. 1–63 (cit. on pp. 153, 172).

[347] Guido J. Reiss and Martin Van Megen. “Synthesis, structure and spectroscopy of a new polyiodide in the α,ω-Diazaniumalkane Iodide/Iodine System”. In: *Zeitschrift fur Naturforschung - Section B Journal of Chemical Sciences* Vol.67.Nr.5 (2012), pp. 447–451 (cit. on pp. 155, 156, 173, 179).

[348] Jae Keun Nam, Sung Uk Chai, Wonhee Cha, et al. “Potassium Incorporation for Enhanced Performance and Stability of Fully Inorganic Cesium Lead Halide Perovskite Solar Cells”. In: *Nano Letters* Vol.17.Nr.3 (2017), pp. 2028–2033 (cit. on pp. 156–158, 161, 162, 164, 174, 175, 179).

[349] L. Vegard. “Die Konstitution der Mischkristalle und die Raumfüllung der Atome”. In: *Zeitschrift für Physik* Vol.5.Nr.1 (Jan. 1921), pp. 17–26 (cit. on pp. 157, 175, 180).

[350] Arthur L. Kohl Richard B. Nielsen. *Gas Purification*. Ed. by Arthur L. Kohl Richard B. Nielsen. 5th ed. Houston, 1997, pp. 505–515 (cit. on pp. 158, 174).

[351] Danielle K. Smith and Brian A. Korgel. “The Importance of the CTAB Surfactant on the Colloidal Seed-Mediated Synthesis of Gold Nanorods”. In: *Langmuir* Vol.24.Nr.3 (Feb. 2008), pp. 644–649 (cit. on pp. 158, 174).

[352] Quinten A. Akkerman, Sungwook Park, Eros Radicchi, et al. “Nearly Monodisperse Insulator Cs_4PbX_6 (X = Cl, Br, I) Nanocrystals, Their Mixed Halide Compositions, and Their Transformation into $CsPbX_3$ Nanocrystals”. In: *Nano Letters* Vol.17.Nr.3 (2017), pp. 1924–1930 (cit. on p. 167).

[353] Erin M. Sanehira, Ashley R. Marshall, Jeffrey A. Christians, et al. “Enhanced mobility $CsPbI_3$ quantum dot arrays for record-efficiency, high-voltage photovoltaic cells”. In: *Science Advances* Vol.3.Nr.10 (Oct. 2017), eaao4204 (cit. on p. 170).

[354] Malinda Salim, Hiroyuki Minamikawa, Akihiko Sugimura, and Rauzah Hashim. “Amphiphilic designer nano-carriers for controlled release: from drug delivery to diagnostics”. In: *Med. Chem. Commun.* Vol.5.Nr.11 (2014), pp. 1602–1618 (cit. on p. 172).

[355] Bastian E. Rapp. “Surface Tension”. In: *Microfluidics: Modelling, Mechanics and Mathematics*. Vol. 203. Nr.9. Elsevier, 2017, pp. 421–444 (cit. on p. 172).

[356] Rui A. Gonçalves, B. Lindman, M. G. Miguel, T. Iwata, and Yeng Ming Lam. “Elucidating the effect of additives on the alkyl chain packing of a double tail cationic surfactant”. In: *Journal of Colloid and Interface Science* Vol.528 (2018), pp. 400–409 (cit. on p. 172).

[357] Yuan Fang, Mihaela Cibian, Garry S. Hanan, et al. “Alkyl chain length effects on double-deck assembly at a liquid/solid interface”. In: *Nanoscale* Vol.10.Nr.31 (2018), pp. 14993–15002 (cit. on p. 172).

[358] Rebecca J. Sutton, Giles E. Eperon, Laura Miranda, et al. “Bandgap-Tunable Cesium Lead Halide Perovskites with High Thermal Stability for Efficient Solar Cells”. In: *Advanced Energy Materials* Vol.6.Nr.8 (2016), pp. 1–6 (cit. on p. 174).

[359] Rachel E. Beal, Daniel J. Slotcavage, Tomas Leijtens, et al. “Cesium Lead Halide Perovskites with Improved Stability for Tandem Solar Cells”. In: *The Journal of Physical Chemistry Letters* Vol.7.Nr.5 (2016), pp. 746–751 (cit. on p. 174).

[360] Shouqiang Huang, Bo Wang, Qi Zhang, et al. “Postsynthesis Potassium-Modification Method to Improve Stability of $CsPbBr_3$ Perovskite Nanocrystals”. In: *Advanced Optical Materials* Vol.6.Nr.6 (2018), pp. 1–7 (cit. on pp. 175, 181).

[361] Michael A. Crawford, C. Leigh Broadhurst, Martin Guest, et al. “A quantum theory for the irreplaceable role of docosahexaenoic acid in neural cell signalling throughout evolution”. In: *Prostaglandins Leukotrienes and Essential Fatty Acids* Vol.88.Nr.1 (2013), pp. 5–13 (cit. on p. 180).

[362] MA Crawford, M Thabet, Y Wang, CL Broadhurst, and WF Schmidt. “A theory on the role of π-electrons of docosahexaenoic acid in brain function”. In: *OCL* Vol.25.Nr.4 (July 2018), A403 (cit. on p. 180).

[363] Simon C. Dyall. “Long-chain omega-3 fatty acids and the brain: a review of the independent and shared effects of EPA, DPA and DHA”. In: *Frontiers in Aging Neuroscience* Vol.7 (Apr. 2015), pp. 1–15 (cit. on p. 180).

[364] David Parobek, Yitong Dong, Tian Qiao, and Dong Hee Son. “Direct Hot-Injection Synthesis of Mn-Doped $CsPbBr_3$ Nanocrystals”. In: *Chemistry of Materials* Vol.30.Nr.9 (May 2018), pp. 2939–2944 (cit. on p. 181).

[365] Wasim J. Mir, Abhishek Swarnkar, and Angshuman Nag. “Postsynthesis Mn-doping in $CsPbI_3$ nanocrystals to stabilize the black perovskite phase”. In: *Nanoscale* Vol.11.Nr.10 (2019), pp. 4278–4286 (cit. on p. 181).

List of Figures

2.1 Different solar spectra 7
2.2 Solar cell working principle 11
2.3 Recombination pathways 12
2.4 General Cubic perovskite structure ABX_3 15
2.5 Perovskite crystal structures 16
2.6 Search results "Web of science" Topic: Perovskite solar cell Date: 29.04.2019 17
2.7 Methylammonium triiodoplumbate(II) structure 18
2.8 a) $CsPbX_3$ nanoparticles in dispersion, with different Halides and Halides mixtures under uv-Illumination b) Different measured Pl spectra,indicating different band gaps with permission of ACS publication ref.[23] 19
2.9 TEM-Images of the $CsPbI_3$ quantum dots and an image of a laser beam in the quantum dot dispersion 22
2.10 Surface tension formation due to Interaction in the volume and surface 25
2.11 Surface to volume ratio for different shapes 26
2.12 Bandgap change in with size change of quantum dots adaptation of [145] 27
2.13 Density of states with reduced dimensions in an adaptation of [121] 28
2.14 A) Illustration of a nanoparticle photoluminescence spectrum with the resulting broadening. B) A Low temperature measurement of CdSe/CdS core-shell nanocrystal (solid line) emission of ensemble (dotted line) [150]with permission from AIP Publishing 29
2.15 Approach for nanostructures 31
2.16 Example of a surfactant (Oleylamine) and idealized formation of a reverse micelle 32

2.17 Modified LaMer Model[177, 178] with particle number and Ostwald ripening 34
2.18 Nucleation theory, gibbs free energy with surface and volume energy 35
2.19 LaMer-diagram of the hot injection. Separation of the nucleation and ripening phase with illustration of the particle formation and photos of the "burst" nucleation (t<1sec.) 37

3.1 Measurment with an integration sphere 43
3.2 Radiative and nonradiative PL-pathways in an adaption of [15] 44
3.3 Schematic illustration of the steady-state photoluminescence set-up 45
3.4 Calibrated PLQY setup 47
3.5 TRPL setup and decay 48
3.6 OPTP set-up 49
3.7 1) First teraherz probe pulse 2) Pump pulse with slightly delayed teraherz probe and the resulting pulse 50
3.8 XRF Process 51
3.9 Scattering at device and scattering triangle 54
3.10 Interference on a crystal lattice 55
3.11 X-Ray scattering method overview in an adaptation of [237] B) Sample size 56
3.12 XRD Goniometer 57
3.13 Phase transition in XRD 58
3.14 A) XRR on a one layer system B) resulting scattering pattern . . 61
3.15 A)X-ray reflection on a multilayer system B) resulting XRR pattern 62
3.16 Scheme of a SAXS instrument with X-ray source, collimator, sample environment, flight tube and detector additionally the angle of different scattering methods (i.e. XRD) are shown[237] 65
3.17 Data redurction example 66
3.18 TEM image with FFT and area integral 68
3.19 TG cross section & schematic thermogram 69
3.20 Schematic illustration of a heat flux DSC cross-section 70

3.21 A) Voltage change in the heat flux sensor (HFS) (propotional to the temperature) against time (by a given scan rate) marked T_T transition temperature B) The resulting signal in on the scan with t_1 as temperature onset and t_2 as temperature offset) in a adaptation of [269, 271] 72

4.1 Acid-Base reaction to form alkyleammonium bromide 76
4.2 a) TEM image of the Nanoplatelets b) nanoplatelets standing perpendicular to the TEM Grid and spherical ($PbBr_2$) nanoparticles 78
4.3 Extract of two perovskite layer 79
4.4 Thermo gravimetrie of nanoplatelets 80
4.5 DSC measurement of powder (Bulk) $MaPbBr_3$ and $MaPbBr_3$ Nanoplatelets 82
4.6 DSC measurement of the nanoplatelets 84
4.7 DSC of N-octylammonium bromide 85
4.8 A)Room temperature XRD measurement with calculated structure [283] B)XRD pattern of nanoplatelets synthesized with the protocol, found in literature [117, 279] 88
4.9 A) XRD pattern with included calculated cubic perovskite pattern B) The pure surfactant N-octylammonium bromide with significant signals 89
4.10 A) XRD Pattern extract of the 15° signal with calculated signal B) XRD Pattern extract of the 30.51° signal with calculated signal 90
4.11 Except of the $MaPbBr_3$ structure with additional N-octylammonium ligands on the top and bottom of the structure, additional the interaction radii of the amines are drawn in green 90
4.12 X-ray diffraction pattern of the laboratory device (X-Ray tube) and the synchrotron measurement at room temperature (300 K) additional the calculated pattern.[283] * marks additional or missing signals 92
4.13 Temperature dependent XRD-measurements with temperature scale. 93
4.14 A) Temperature-dependent XRD-measurement extract of the 15° signal with red marked phases transition onsets B) Calculated structures found in literature [283] 94
4.15 A) Extract of the 30° signal from the temperaturdependend XRD measurement B) Calculated structures found in literature [283] 95

4.16 Peakposition of the 30° peak plotted against temperature. The expected phase transitions known from the DSC measurement are implemented 96
4.17 Cell parameter A plotted against the temperature 97
4.18 SAXS Measurment A) desmeared datat B) zoom on the peak at 1.7 nm^{-1} 98
4.19 Resulting SAXS Fit is shown with a peak at 1,7nm^{-1} 99
4.20 Absorption spectrum with a Elliott fit 101
4.21 A) temperature dependend PL (17-319 K) B) excidation dependent Pl data at 17 K 102
4.22 Pl max positions vs temperature of MaPbBr nanoplatelets 103

5.1 A) Equilibrium reaction of caesium carbonate with an organic acid B) Used reaction with the elimination of water and CO_2 during the reaction and shifting the equilibrium on the side of the product. Oleic acid as a molecule is drawn 115
5.2 Oleic acid and oleylamine 116
5.3 $CsPbI_3$ quantum dots (around 8 nm) arranged in a surrounding of the ligand oleylamine (around 2,2 nm 118
5.4 Overview of self-assembled $CsPbI_3$ nanocrystals 119
5.5 Overview $CsPbI_3$ TEM image 120
5.6 Counted size distribution for the $CsPbI_3$quantum dots (n=1000) and the gaps in between the quantum dots 121
5.7 A) Resulting FFT of the overview image B) Area integration over the FFT 122
5.8 Perovskite Phases 123
5.9 GIXRD-Measurement with different fits 124
5.10 XRD pattern of the $CsPbI_3$ quantum dots with the nanotwin fit and additional peaks of the caesium rich Cs_4PbI_6 perovskite . . 125
5.11 XRR-sample and resulting XRR measurment 126
5.12 A) Lasermicroscope example measurement B) profile of the thickness 127
5.13 SLD of nano cuboids 128
5.14 A) Neutron reflectometrie data with fit B) resulting SLD 130

5.15 A) Absorption and emission spectra of a 0,1mg/1mL dispersion of $CsPbI_3$ nanocrystals in octane as dispersion with photo of the emission B) Normalized absorption spectra of the $CsPbI_3$ nanocrystal in comparison to pure oleylamine 131
5.16 Normalized TRPL of $CsPbI_3$ dispersion 132
5.17 Model of the quantum dot for charge carrier dynamics 133
5.18 Comparisson of a $CsPbI_3$ layer and a dispersion 134
5.19 Normalized TRPL measurement of $CsPbI_3$ dispersion and layer . 135
5.20 $CsPbI_3$ quantum dot layer model 136
5.21 Tera hertz spectrum of polycrystaline $CsPbI_3$ and a ligand caped quantum dot assembly 136
5.22 Ligand exchange process 138
5.23 A) Overview of the Self assembled $CsPbI_3$ nano cuboids B) Zoom on 4 $CsPbI_3$ nano cuboids 139
5.24 A)Overview image of the FaI washed sample and a magnification on the quantum dots 139
5.25 Size distribution of the FAI treated sample 140
5.26 Unitcell sizes of treated samples with reference cell sizes 141
5.27 Illustration of the formation of the $FaPbI_3$/CsPbI alloy 142
5.28 Estimated band gaps of the different treated samples 143
5.29 A) Pl signal maximum of the different treated samples compared to the bulk $CsPbI_3$ [332] B) The FWHM of the different treated samples(Spectra in Appendix) 144
5.30 OPTP comparison 145
5.31 TRPL comparisson of $CsPbI_3$ nanocrystals and their treatments . 146
5.32 Structure of octylamine and dioctylamine 149
5.33 Overview and magnification of the N,N-dioctylamine sample . . 150
5.34 XRD pattern of the $CsPbI_3$ nanoparticles with N,N-dioctylamine 151
5.35 Charge carrier mobility inside the N,N-dioctylamine sample . . 152
5.36 TEM-Images of the thermal annealed $CsPbI_3$ quantum dots . . . 153
5.37 XRD of the thermal annealed $CsPbI_3$ nanocrystals 154
5.38 A)1,6-Hexanediamine B)1,4-benzenedimethanamine 155
5.39 TEM-Images of the potassium incorporated $CsPbI_3$ nano cuboids 159
5.40 GIXRD measurement and LeBail fit of the 7.5 mol% sample . . . 160
5.41 Unitcell size of the potassium doped $CsPbI_3$ nano cuboids (All pattern are in the Appendix) 161

5.42 Normalized Pl spectra of the samples with 0, 2.5, 5 and 7.5 mol% potassium content 162
5.43 Normalized Pl Spectrum of $CsPbI_3$ nano cuboids with 7.5 and 20 mol% of potassium 163
.44 TRPL decay of the $CsPbI_3$ dispersion with two non correlating exponential fits 183
.45 FaI treated emission spectrum 183
.46 FaI and $Pb(NO_3)_2$ treated emission spectrum 184
.47 Absorption pure 184
.48 Absorption washed 185
.49 Absorption Fa Treated 185
.50 Absorption FAI+ Pb(NO3)2 treated 186
.51 NMR spectra of FaI 186
.52 Terahertz spectra 187
.53 XRD of the $CsPbI_3$ quantum dots treated with FaI and LeBail fit 187
.54 XRD of the $CsPbI_3$ quantum dots treated with FaI and $Pb(NO_3)_2$ and LeBail fit 188
.55 XRF spectra of 5, 7.5, 10 and 20% K in $CsPbI_3$ Nanoparticles . . 188
.56 XRD of the $CsPbI_3$ quantum dots with the incorporation of 1% potassium and the resulting LeBail fit 189
.57 XRD of the $CsPbI_3$ quantum dots with the incorporation of 2.5% potassium 189
.58 XRD of the $CsPbI_3$ quantum dots with the incorporation of 5% potassium 190
.59 XRD of the $CsPbI_3$ quantum dots with the incorporation of 10% potassium 190
.60 XRD of the $CsPbI_3$ quantum dots with the incorporation of 20% potassium 191

List of Tables

3.1 Elements used to analyse in this thesis in atomic number (Z) order with selected emission lines in keV [225] 51

4.1 Phasetransition Enthalpy and Entropy (calculated as described in 3.3.2Differential scanning calorimetry) 83

5.1 Scattering length density of $CsPbI_3$ and oleylamine 127
5.2 Calculated sizes with Scherrer equation for the different treatments 142
5.3 Quantum yield of the different treated samples 144
5.4 Stability observation of the potassium incorporated $CsPbI_3$ . . . 157
5.5 XRF measurement of the samples 160
5.6 Photoluminicense maximum and FWHM of the potassium doped samples 163

Colophon

This thesis was typeset with LaTeX 2$_\varepsilon$. It uses the *Clean Thesis* style developed by Ricardo Langner. The design of the *Clean Thesis* style is inspired by user guide documents from Apple Inc.

Download the *Clean Thesis* style at `http://cleanthesis.der-ric.de/`.

For all drawings, images and other illustrations the graphical software *Inkscape* and OriginPro2015 were used.

For the Lebail fits the program PowderCell was used.

For the chemical structure editing *MarvinSketch* of ChemAxxon was used.

Erklärung

Erklärung über die selbstständige Anfertigung der Dissertation mit dem Titel "Layer formation from perovskite nanoparticles with tunable optical and electronic properties"

hiermit erkläre ich, dass ich die beigefügte Dissertation selbstständig verfasst und keine anderen als die angegebenen Hilfsmittel genutzt habe. Alle wörtlich oder inhaltlich übernommenen Stellen habe ich als solche gekennzeichnet.
Ich versichere außerdem, dass ich die beigefügte Dissertation nur in diesem und keinem anderen Promotionsverfahren eingereicht habe und, dass diesem Promotionsverfahren keine endgültig gescheiterten Promotionsverfahren vorausgegangen sind.

Berlin, September 1, 2020

Martin Kärgell